

# *Square Planar Metal Complexes with Cyclopeptide and Porphyrin-Based Ligands*

Vom Fachbereich Chemie der Technischen Universität Kaiserslautern zur  
Verleihung des akademischen Grades „Doktor der Naturwissenschaften“

genehmigte Dissertation

DE - 386



Vorgelegt von  
**Lígia Margarida Marques Mesquita**  
geboren in Coimbra, Portugal

Betreuer: Prof. Dr. Stefan Kubik  
Kaiserslautern 2021



Die vorliegende Arbeit wurde unter der Leitung von Prof. Dr. Stefan Kubik im Zeitraum von Oktober 2015 bis April 2019 im Fachbereich Chemie der Technischen Universität Kaiserslautern angefertigt

Dekanin: Prof. Dr. Elke Richling

Betreuer: Prof. Dr. S. Kubik

Datum der Prüfung: 03 Dezember 2021

Prüfungskommission

Vorsitzender: Prof. Dr. Sabine Becker

1. Gutachter: Prof. Dr. Stefan Kubik

2. Gutachter: Prof. Dr. G. Manolikakes



Hiermit versichere ich, dass ich die vorliegende Arbeit selbstständig verfasst und keine anderen als die angegebenen Quellen und Hilfsmittel verwendet habe sowie Literaturzitate kenntlich gemacht wurden. Ich erkläre außerdem, dass diese Dissertation weder in gleicher, noch in anderer Form bereits in einem anderen Prüfungsverfahren vorlag.

Kaiserslautern, den 10 Dezember 2021

Lígia Margarida Marques Mesquita



*“Science knows no country, because knowledge belongs to humanity, and is the torch  
which illuminates the world...”*

**Louis Pasteur**





# Acknowledgements

Through this mean I acknowledge the people that have contributed directly or indirectly to the successful outcome of this work.

First and foremost, to my supervisor, Prof. Dr. Stefan Kubik, thank you for the opportunity to work in his group and for the support and guidance in the planning and conduction of this work.

I would like to thank Prof. Dr. G. Manolikakes and Jun.- Prof. Dr. Sabine Becker for helping with the revision of my thesis.

I wish to express my gratitude to Mrs. Christiana Müller for all the help associated with the NMR measurements, to Daniel Bellaire for the afternoons measuring DOSY NMR and again to Prof. Dr. Sabine Becker for her extensive help in solving challenging crystal structures.

My special thanks to Prof. Dr. Luisa De Cola and Dr. Stephan Sinn for the support during my secondment in Strasbourg, to Dr. Elwin Vrouwe and Dr. Sandro Meucci for the assistance during my time at Micronit Microtechnologies and to Prof. Dr. Arne Lützen and Dr. Jana Anhäuser for the help during my short stay at their lab.

I am also thankful to our chemical store team (Ludvik, Frank, Jürgen). It was always good to remember Portugal with Ludvik whenever I went for chemical orders.

My special thanks to my ResMoSys colleagues and to my co-workers Disha and Daniel for the great friendship and good moments and to Karina Malinowska that went from “student” to dear friend in what felt like seconds. My appreciation also extends to all the other lab members for making the work atmosphere very friendly.

I am overwhelmingly grateful to my family for their endless support, love, and encouragement. I am fully indebted to my friend Yolanda Guastaferrero that pushed me forward when I couldn't move.



# Table of Contents

Acknowledgements .....	I
Table of Contents .....	III
Abbreviations .....	VII
<b>Preface</b> .....	9
<b>1. Metal Directed Self-Assembly of Cyclopeptide-Containing Macrocycles and Cages</b> ....	5
1.1. INTRODUCTION .....	7
1.1.1 Metal Directed Self-Assembly .....	8
1.1.2 Pd(II)-Mediated Assembly of Hollow Supramolecular Structures from Pyridine-Derived Ligands .....	9
1.1.3 Pd(II)-Directed Self-Assembly of Pyridine-Containing Cyclopeptides .....	21
1.2 AIM OF THE PROJECT .....	26
1.3 RESULTS AND DISCUSSION .....	28
1.3.1 Synthesis of the Cyclopeptides and Metal Precursors .....	28
1.3.2 Formation of Hollow Coordination Complexes through Metal-Directed Self-Assembly .....	33
1.3.3 Binding Studies with Cyclopeptide Derived Metal Assemblies.....	53
1.4. CONCLUDING REMARKS .....	68
<b>2. Synthesis and Characterization of Luminescent Neutral Pt(II) Complexes Tethered to Cyclopeptides</b> .....	69
2.1. INTRODUCTION .....	71
2.1.1 Photophysics of Pt(II)-complexes .....	71
2.1.2 <i>N</i> -Metallacycles .....	73
2.2. AIM OF THE PROJECT .....	77

2.3.	RESULTS AND DISCUSSION .....	79
2.3.1	Synthesis of the Azole-based Ligands and Pt(II) Precursors .....	79
2.3.2	Coordination Studies between Pt(II) Complex <b>30</b> and the Cyclopeptides....	81
2.3.3	Coordination Studies Between Pt(II) Complexes of Ligand <b>27b</b> and the Cyclopeptides .....	86
2.3.4	Coordination Studies Between Pt(II) Complexes of Ligand <b>27c</b> and the Cyclopeptides .....	89
2.4.	CONCLUDING REMARKS .....	97
<b>3.</b>	<b>Luminescent Pt(II) Porphyrin Complexes as Oxygen Sensors for Microfluidic Devices</b>	<b>99</b>
3.1.	INTRODUCTION .....	101
3.1.1	Organ-on-a-chip Devices .....	101
3.1.2	OXNANO Nanoparticles .....	108
3.2.	AIM OF THE PROJECT.....	113
3.3.	RESULTS AND DISCUSSION .....	114
3.3.1	Synthesis of the Pt(II) Tetrabenzoporphyrin PtTPTBPF .....	114
3.3.2	Development of Chips Containing OXNANO as Oxygen Sensor Spots.....	116
3.3.3	Development of Chips Containing PtTPTBPF as Oxygen Sensor Spots.....	118
3.3.4	Validation of the Microfluidic Devices.....	123
3.3.5	Oxygen Sensing Studies Using Microfluidic Chip Devices Containing OXNANO 129	
3.3.6	Measurement of the Oxygen Consumption of Cells by Using Microfluidic Chip Devices Containing OXNANO.....	133
3.4.	CONCLUDING REMARKS .....	136
<b>4.</b>	<b>Conclusion and Outlook.....</b>	<b>137</b>
<b>5.</b>	<b>Experimental Procedures.....</b>	<b>141</b>

5.1. Metal Directed Self-Assembly of Cyclopeptide-Containing Macrocycles and Cages	143
5.1.1 Synthetic Procedures	143
5.1.2 Synthesis of the coordination complexes	152
5.1.3 Binding Studies with <b>CP1<sub>2</sub>Pd<sub>2</sub></b>	155
5.1.4 Binding Studies with <b>CP2<sub>2</sub>Pd<sub>3</sub></b>	158
5.2. Synthesis and Characterization of Luminescent Neutral Pt(II) Complexes Tethered to Cyclopeptides	160
5.2.1 Synthetic Procedures	160
5.2.2 Synthesis of the coordination compounds	164
5.3. Luminescent Pt(II) Porphyrin Complexes as Oxygen Sensors for Microfluidic Devices	170
5.3.1 Synthetic Procedures	170
5.3.2 Oxygen detection studies	173
5.3.2.1 Oxygen Meter	173
5.3.2.2 Microfluidic device	176
5.3.2.3 Preparation of Oxygen Sensors	178
5.3.2.4 Preparation of Oxygen Standards	179
5.3.2.5 Signal Intensity and N <sub>2</sub> Sensitivity	180
5.3.2.6 Oxygen Sensors Calibration	180
5.3.2.7 Validation of the Calibration	182
5.3.2.8 N <sub>2</sub> /O <sub>2</sub> exchange through the Hydrophobic Membrane	183
5.3.3 Oxygen Consumption Studies	184
5.3.3.1 Cell Experiments	184
5.3.3.2 Flow effect on the sensor	187
<b>References</b>	<b>189</b>

<b>Appendix I: Additional Images</b> .....	199
Additional Spectra .....	201
PC <sub>12</sub> Pd <sub>2</sub> ·2NDS.....	207
Mean planes (angles and torsions).....	209
<b>Appendix II: Publication and SI</b> .....	217

## Abbreviations

BDS Sodium 1,3-benzenedisulfonate

DCM Dichloromethane

DIPEA *N,N*-Diisopropylethylamine

DMF Dimethylformamide

DMSO Dimethyl sulfoxide

DOSY Diffusion Ordered Spectroscopy

ESI Electrospray Ionization

EtOH Ethanol

HPLC High-Performance Liquid Chromatography

MALDI-TOF Matrix Assisted Laser Desorption Ionization-Time of Flight

MeCN Acetonitrile

MeOH Methanol

MS Mass Spectrometry

NDS Sodium 2,6-naphthalenedisulfonate

NMR Nuclear Magnetic Resonance

NOESY Nuclear Overhauser Effect Spectroscopy

PDMS Polydimethylsiloxane

PyCloP Chlorotripyrrolidinophosphonium hexafluorophosphate

ROESY Rotational Frame Nuclear Overhauser Effect Spectroscopy

TBTU 2-(1*H*-Benzotriazole-1-yl)-1,1,3,3-tetramethylammonium tetrafluoroborate





# Preface



Coordination Chemistry is a branch of chemistry that deals with metal complexes surrounded by ligands that are attached to the metal by dative bonds, also known as coordinate bonds, in which both electrons in the bond are supplied by the same atom on the ligand. The Nobel Prize winner Alfred Werner (1866-1919) established this field by developing in 1913 the coordination theory of metal-ammine complexes, such as  $[\text{Co}(\text{NH}_3)_6\text{Cl}_3]$ .<sup>1</sup> Coordination compounds can be found in Nature, examples are haemoglobin,<sup>2</sup> chlorophyll,<sup>3</sup> Vitamin B-12<sup>4</sup> and hemocyanin.<sup>5</sup> They are also of great importance in many subdisciplines of chemistry, including inorganic and bioinorganic<sup>6</sup> chemistry and polymer<sup>7</sup> and materials science.<sup>8,9</sup>

Recently, it was shown that the coordination of ligands to appropriate metals allows the construction of coordination compounds that are relevant in supramolecular chemistry. Metal-directed self-assembly with metals such as Pd(II) and Pt(II), that prefer a square planar coordination geometry, has been showing remarkable potential to construct supramolecular architectures such as helices,<sup>10</sup> tubes,<sup>11</sup> locks<sup>12</sup> and cages.<sup>13</sup> Some of these complexes have also been shown to assemble by means of metal-metal interactions<sup>14</sup> and, more remarkably, the luminescent properties of certain complexes can also be used for sensing. For instance, Pt(II) and Pd(II) complexes display strong phosphorescence which is strongly reduced in the presence of oxygen.<sup>15</sup>

This thesis is divided into three main chapters dealing with the different properties of Pd(II) and Pt(II) metal complexes. Chapter I was mainly developed at Technische Universität Kaiserslautern with a short partnership with the Kekulé-Institut für Organische Chemie und Biochemie at the Universität Bonn and addressed the construction of coordination macrocycles and cages from suitable Pd(II) sources and cyclopeptide-derived ligands.

In Chapter II, the aggregation abilities and photophysical properties of Pt(II) complexes bearing tridentate-azolate-based ligands and cyclopeptides with peripheral pyridyl moieties were investigated. This project was the result of a short-term secondment developed at the Institut de Science et d'Ingénierie Supramoléculaires in Strasbourg.

Chapter III was the result of a project executed at Micronit Micro Technologies B.V. in Enschede, in which a microfluidic device with oxygen sensing abilities was produced from nanoparticles containing Pt(II)-porphyrins.



# 1. Metal Directed Self-Assembly of Cyclopeptide-Containing Macrocycles and Cages

The project here described was developed as the main topic for this PhD thesis sponsored by the Marie Curie Innovative Training Network ResMoSys. In this chapter, the work developed at the Chemistry Department of the Technische Universität Kaiserslautern (Germany) from October 2015 to April 2019 is described. A short-term partnership was established with the group of Prof. Arne Lützen from the Kekulé-Institut für Organische Chemie und Biochemie, Rheinische Friedrich-Wilhelms-Universität Bonn. The results obtained were published: Mesquita, L. M., Anhäuser, J., Bellaire, D., Becker, S., Lützen, A., Kubik, S. Palladium(II)-Mediated Assembly of a  $M_2L_2$  Macrocycle and  $M_3L_6$  Cage from a Cyclopeptide-Derived Ligand. *Org. Lett.* 2019, 21, 6442-6446. doi:10.1021/acs.orglett.9b02338.



## 1.1. INTRODUCTION

For a long time, chemists strived to attain control over the formation and breaking of the covalent bond to construct new molecules of increasing complexity.<sup>16</sup> However, with the rising interest in creating more diverse and unique chemical architectures, a new paradigm emerged. Referred to as "*the chemistry beyond the molecule*",<sup>16</sup> it took advantage of non-covalent intermolecular interactions to construct complex and functional systems, thus giving rise to the field of Supramolecular Chemistry. Examples of weak and reversible interactions include hydrogen bonds, van-der-Waals forces,  $\pi$ - $\pi$  stacking interactions and other types of interactions.

Even though the use of such interactions to consciously design molecular assemblies is only performed since ca. 50 years, several systems can be found in Nature, in which these intermolecular forces play an important role. For example, the DNA double helix is stabilized by complementary hydrogen bonds and  $\pi$ - $\pi$  stacking interactions between the nucleobases. Also, stabilizing non-covalent forces such as hydrogen bonds and ionic interactions are responsible for the folding of proteins and enzymes into unique three-dimensional structures. It was based on these natural supramolecular mechanisms that the concept of self-assembly<sup>17-19</sup> for the fabrication of artificial systems was developed.

Molecular self-assembly consists of the spontaneous arrangement of suitable building blocks into discrete and often symmetric supramolecular systems.<sup>20</sup> The resulting self-assembled product is stabilized through non-covalent or coordinative interactions, which should be reversible<sup>21</sup> to allow for self-assembly to proceed under thermodynamic control and for any error that may have occurred during the assembly to be corrected immediately ("self-correction").

Mismatched bonds or less stable products will thus dissociate in favour of more stable ones. During self-assembly processes, several reversible reactions may occur simultaneously until an equilibrium is reached and a thermodynamic product is formed ideally in nearly quantitative yield. Changes of the reaction parameters can shift the balance from one product to another that represents the more stable one under the

altered conditions. The used starting compounds are often structurally simple whilst the resulting product has a much more complex architecture.

Self-assembly can be divided into two main types according to the interactions involved between the constituents. The first one is based on H-bonding motifs<sup>22,23</sup> and the second one on metal-ligand interactions.<sup>24,25</sup> The latter was introduced during the 1980s and since then, metal directed self-assembly has been prominent in the creation of supramolecular compounds in which metal atoms and ligands are the primary building blocks and coordinate bonds are the 'glue' that holds these constituents together.<sup>19,26</sup>

### 1.1.1 Metal Directed Self-Assembly

The use of metal ligand interactions is quite appealing for self-assembly since these interactions are stronger than non-covalent interactions and still kinetically labile, allowing for thermodynamic control of the self-assembling process to favour discrete, well-ordered macromolecules over random species. The synthetic efforts to obtain metal directed self-assembled structures are usually low, since the synthesis of the coordination compounds often involves simple building blocks and one-pot procedures to obtain stable albeit dynamic products in high yields.

A fascinating range of structures can be constructed by metal-directed self-assembly that is much more difficult or even impossible to access by covalent chemistry. Some examples include polygons, cages, catenates, knots, rotaxanes, dendrimers and helicates.<sup>16,27,28</sup> Metal atoms function not only as building blocks and orientating centres for the formation of these structures, but also possess properties that are incorporated in the final structure such as electrochemical, photophysical, spectroscopic, magnetic and reactivity properties.<sup>16,27,28</sup> This has resulted in functional metallosupramolecular structures for a large variety of applications including molecular machines.<sup>29-31</sup>

Product formation is determined by the preferred coordination geometry of the metal ion, the structural parameters of the ligand and the metal/ligand ratio.<sup>32</sup> Transition-metal-based systems are particularly interesting for metal directed self-assembly, since they afford predictable structures by adapting the denticities of the ligands to the coordination



numbers of the metals.<sup>26,27</sup> The most stable species eventually dominates the thermodynamic equilibrium.<sup>33</sup>

Amidst the transition metals, palladium(II) centres are particularly attractive components for the synthesis of supramolecular coordination compounds due to their propensity to orient four monodentate ligands at 90° angle in a square planar geometry, their high Lewis acidity, the efficiency which they interact with N or O donor ligands, the intermediate kinetic lability of their complexes, and their diamagnetism that allows the use of NMR spectroscopy for the structural characterization.<sup>34,35</sup>

Considering the predisposition of Pd(II) to interact with N donors, a considerable portion of the discrete organic frameworks so far developed had nitrogen-containing heteroaryls, such as pyridines, as organic building blocks.<sup>33,36–38</sup> On its own, pyridine is not a very good ligand since it only has a single donor atom. However, pyridine moieties can be incorporated into larger molecules, thus creating ligands that are capable of bridging two or more metal atoms to form complex metallostructures.

The outcome of metal-pyridine based self-assembly depends on a variety of factors, the most important of which are the structural parameters of the ligand, the preferred coordination geometry of the acceptor subunit, and external parameters such as temperature, solvent, and the presence of a template.<sup>39,40</sup> The correct coordination angle between the ligands (L-M-L) at the metal centre is paramount for the correct construction of the metal assemblies.

### 1.1.2 Pd(II)-Mediated Assembly of Hollow Supramolecular Structures from Pyridine-Derived Ligands

Supramolecular structures can have highly diverse structures and, among them, supramolecular coordination macrocycles and cages are of great interest due to their potential ability to serve as synthetic receptors.<sup>37,41–43</sup> Such receptors are typically composed of several metal centres joined by organic ligands that create a cavity into which a suitable substrate can be included.

Many of such hollow coordination compounds are positively charged as they are formed from neutral ligands and positively charged metal ions and can contain anions encapsulated inside the void.<sup>44</sup> Their functions can comprise the stabilization of neutral<sup>45,46</sup> or reactive guests<sup>47,48</sup> or the activation of unreactive molecules.<sup>49</sup> Furthermore, they can act as catalysts or sensors,<sup>50-53</sup> can allow gas sequestration,<sup>54</sup> the separation of species from mixtures<sup>45,55</sup> or drug delivery.<sup>56</sup>

Although a handful of these complexes were the result of serendipity, most structures have been obtained by carefully planning and understanding the influence of the individual components on the outcome of the self-assembling process. In addition to the above mentioned parameters, factors like the flexibility of the ligand and the counterions of the metal also have a major impact on the structure and properties of the product.<sup>57</sup>

Metallamacrocycles and cages can be created in a highly diverse range of shapes from symmetric building blocks that often resemble geometric figures or Platonic and Archimedean solids<sup>41,51</sup> (tetrahedron, octahedron, cube, etc) but also other structures such as rings, trigonal bipyramids, trigonal prisms, bowls, etc.

An expert in the construction of such structures is Makoto Fujita, who focuses in his work on the metal-directed self-assembly between appropriately protected square-planar metal ligands and suitable organic building blocks (**Figure 1**, left) for the construction of structurally complex coordination compounds.<sup>37,51</sup> By protecting the metal ion, the number of coordination sites can be reduced, allowing for further control over the number and relative orientation of the organic ligands.<sup>58-63</sup>

One of the synthetic strategies used by Fujita for the design of metallostructures is the directional-bonding approach, in which structurally rigid complementary precursor units with predefined bite angles are used in an appropriate stoichiometric ratio to access a wide variety of supramolecular assemblies in high yields.<sup>64</sup> The symmetry and number of binding sites within the donor ligands and the metal acceptors guide the shape of the target assembly. Following this design strategy, the precursor units normally correspond to the vertices and/or edges of the final supramolecular structures.

The first example of a self-assembled complex obtained by using this strategy was the tetranuclear square **S1**, depicted in **Figure 1**.<sup>65</sup> **S1** contained four cis-protected Pd(II) centres and four 4,4'-bipyridine ligands. The quantitative self-assembly of this complex was observed from the mixture of an equimolar amount of  $[\text{Pd}(\text{en})(\text{NO}_3)_2]$  (en=ethylenediamine) and 4,4'-bipyridine in an aqueous solution at room temperature. The final structure was confirmed by NMR spectroscopy, electrospray ionization mass (ESI-MS) spectrometry, and X-ray crystallography. **S1** possessed a hydrophobic cavity able to recognize neutral aromatic compounds<sup>66</sup> with the highest association constant observed for *N*-(2-naphthyl)acetamide ( $1800 \text{ M}^{-1}$ ).

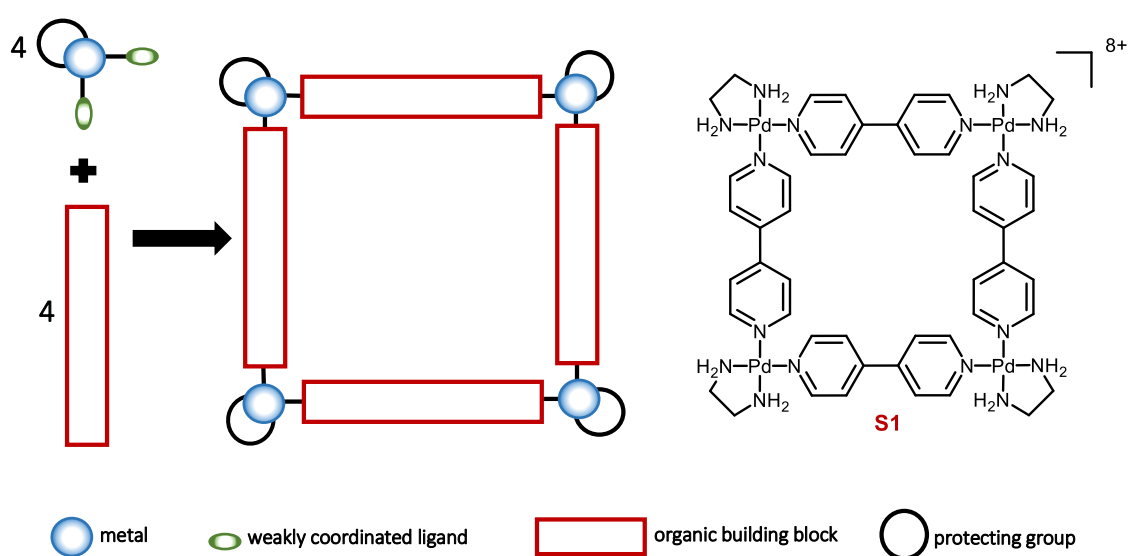


**Figure 1** Left: Schematic representation of the metal-directed self-assembly between a cis-protected metal complex and an organic building block towards the formation of a metallamacrocycle. Charges and counterions are omitted for clarity. Right: Chemical structure of a square framework obtained by reacting an equimolar amount of  $[\text{Pd}(\text{en})(\text{NO}_3)_2]$  and 4,4'-bipyridine.

Henceforth, several metal-directed self-assembly reactions were performed by Fujita's group using the directional-bonding approach. The equilibrium dynamics of such reactions and resulting metallostructures depended on the reaction conditions and the nature of the precursor units.<sup>37,50,51,67–69</sup>

The self-assembly of the Pt(II) analog<sup>67</sup> of **S1** was slow due to the inertness of the Pt(II)–pyridine bond. Initially, a complex product mixture was formed, affording the thermodynamically most stable Pt(II) square only after heating to 100°C for several weeks.

The Pd(II) and Pt(II) squares accordingly exhibited significant differences in their behaviour. While the addition of  $[Pd(en)(NO_3)_2]$  to **S1** shifted the equilibrium and gave rise to a mixture of products, the Pt(II) square remained intact after the addition of  $[Pt(en)(NO_3)_2]$ .

The structure of **S1** was expanded by incorporating suitable spacers into the bipyridine framework.<sup>68</sup> However, with the use of longer linear linking components, the reaction resulted in an equilibrium between molecular squares and triangles (**Figure 2**). The product ratio was dependent of the concentration of the reaction mixture.

At higher concentrations, the ratio shifted towards the formation of the molecular square. This effect indicated that the equilibrium was the result of the balance between enthalpy and entropy, with the less strained molecular square being more stable in terms of enthalpy while entropy favoured the structure consisting of fewer components.

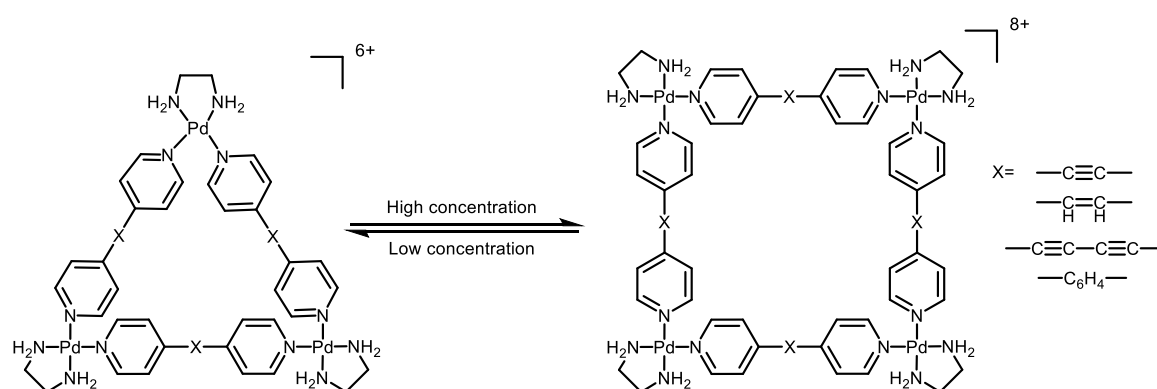


**Figure 2** Equilibrium between the square and the triangle frameworks resulting from the metal-directed self-assembly between an equimolar amount of  $[Pd(en)(NO_3)_2]$  and bipyridine-derived building blocks with incorporated phenylene, ethynylene, or ethynylene spacers.

An analogous behaviour was observed when the ethylenediamine protecting group on Pd(II) was replaced with a more sterically demanding 2,2'-bipyridine group (**Figure 3**).<sup>68</sup> Again, the ratio square:triangle was concentration-dependent and high concentrations favoured the square formation, probably due to steric repulsion between 2,2'-bipyridine and 4,4'-bipyridine subunits.

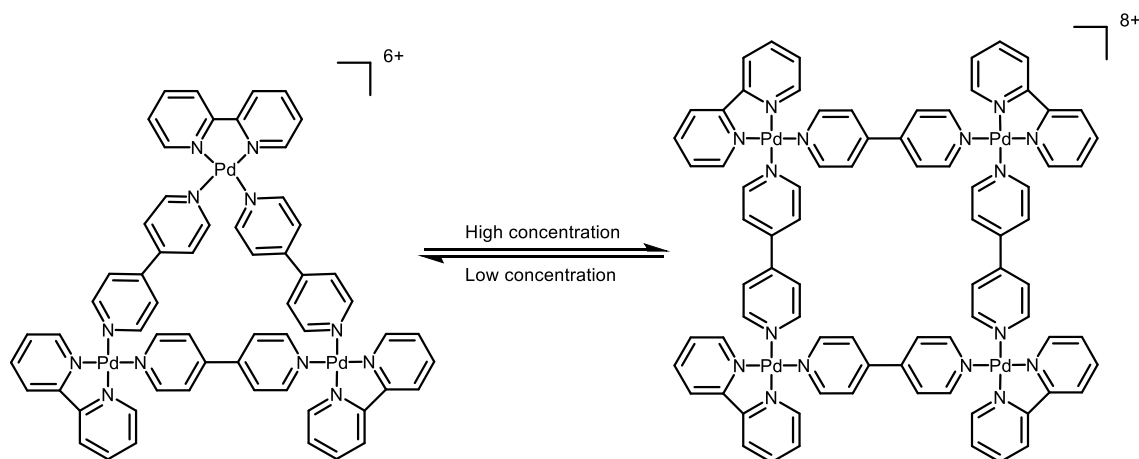


**Figure 3** Equilibrium between the square and the triangle frameworks resulting from the metal-directed self-assembly between an equimolar amount of  $[Pd(2,2'-bipy)(NO_3)_2]$  and 4,4'-bipyridine.

The substitution of 4,4'-bipyridine for more flexible bidentate ligands afforded the macrocyclic dinuclear complexes **M1** to **M8** in the reaction with  $[Pd(en)(NO_3)_2]$  instead of the previously observed larger macrocycles (**Figure 4**).<sup>37,50,51</sup> The structures of the macrocycles **M1**, **M2** ( $ClO_4$  salt), **M3** and **M5** were determined by X-ray crystallography, whilst the others were deduced from NMR spectroscopy and fast atom bombardment mass (FABMS) spectrometry.

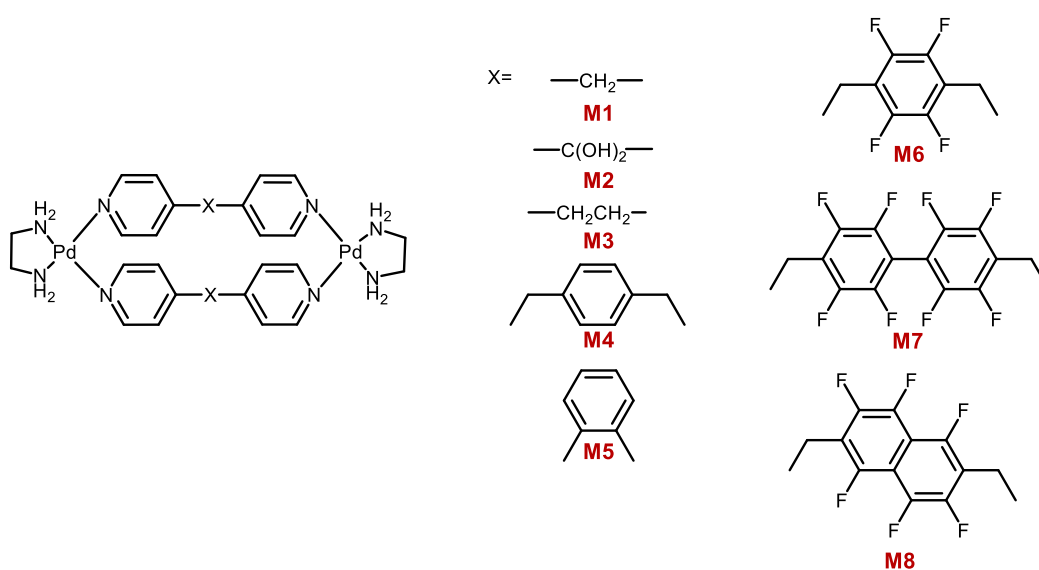


**Figure 4** Examples of self-assembled macrocycles resulting from the reaction between an equimolar amount of  $[Pd(en)(NO_3)_2]$  and different flexible bidentate ligands.

Interestingly, **M7** and **M8** existed in aqueous solution in equilibrium with linear oligomers but dilution of the solution or change of the solvent to methanol shifted the equilibrium ratio towards macrocycle formation.<sup>50</sup>

The strategy shown in **Figure 1** was then extended to the formation of cage-type architectures by reacting tris-(4-pyridylmethyl)benzene (**L1**) with  $[\text{Pd}(\text{en})(\text{NO}_3)_2]$  in a 2:3 ratio.<sup>70</sup> Initially a mixture of oligomeric products was obtained. The presence of suitable neutral or anionic guests such as carboxylates induced, however, the assembly of the complex **C1** (**Figure 5**).

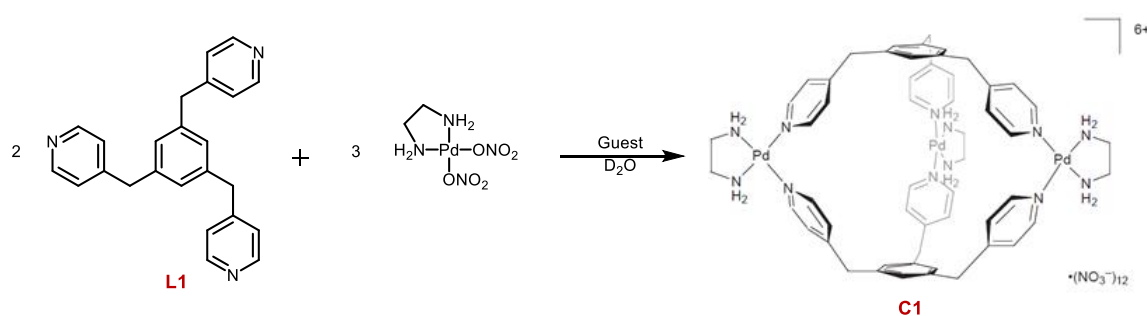


**Figure 5** Trigonal prismatic coordination cage **C1** obtained by reaction of 2 eq of tris-(4-pyridylmethyl)benzene (**L1**) with 3 eq of  $[\text{Pd}(\text{en})(\text{NO}_3)_2]$ . ©The Royal Society of Chemistry 1998.

**C1** exhibited a trigonal prismatic  $D_{3h}$  symmetric structure, which was deduced mainly from NMR spectroscopic and ESI-MS spectrometric measurements. NMR titration experiments showed that **C1** formed 1:1 host-guest complexes with various guests. 1-Adamantanecarboxylic acid and 2-phenylpropionic acid were the templates that produced the cage with the highest yields (> 90%). The manner in which the framework of **C1** assembled is an example for a thermodynamically templated receptor synthesis. Earlier examples of similar templated cage syntheses can be found in the literature.<sup>71,72</sup>

A second approach used for the design of 3D molecular architectures was also pioneered by Fujita and co-workers. In molecular panning, flat, panel-like organic ligands having more than two linking sites are joined using cis-protected square planar Pt(II) or Pd(II) metal centers as corner units. The suitable positioning of the donor binding sites in the panel is vital and guides the final geometry of the resulting architectures. In this method, the organic molecular components were designed to represent basic geometric shapes such as triangles, squares, or rectangles. These molecular panels then react with the metal

centres to create polyhedral self-assembled structures in which the ligands resided on the faces while the metals resided on the vertices or edges.

A variety of nanosized discrete metal-assembled frameworks with structures that can be classified as cages, bowls, tubes, tetrahedra, or octahedra containing pyridine-based molecular panels and cis-protected Pd(II) were constructed by Fujita et al. using this approach.<sup>73</sup> These structures not only recognized and encapsulated more than one substrate, but also often exhibited interesting functions. They were able, for example, to mediate regio- or stereoselective reactions, stabilize reactive molecules and intermediates, act as storage devices, and interact with biologically relevant compounds.<sup>74–78</sup> Cages **C2**, **C3**, and **C4** are good examples of three-dimensional assemblies obtained by molecular panelling.

The highly symmetric nano-sized  $M_6L_4$  adamantoid cage **C2** was constructed by mixing the coplanar 2,4,6-tri-4-pyridyl-1,3,5-triazine (**L2**) and  $[Pd(en)(NO_3)_2]$  in a 2:3 ratio (Figure 6, top).<sup>79</sup> When a 2:4 ratio was used for the self-assembly, only **C2** was formed and the excess of  $[Pd(en)(NO_3)_2]$  remained unused, attesting for the substantial thermodynamic stability of the cage.

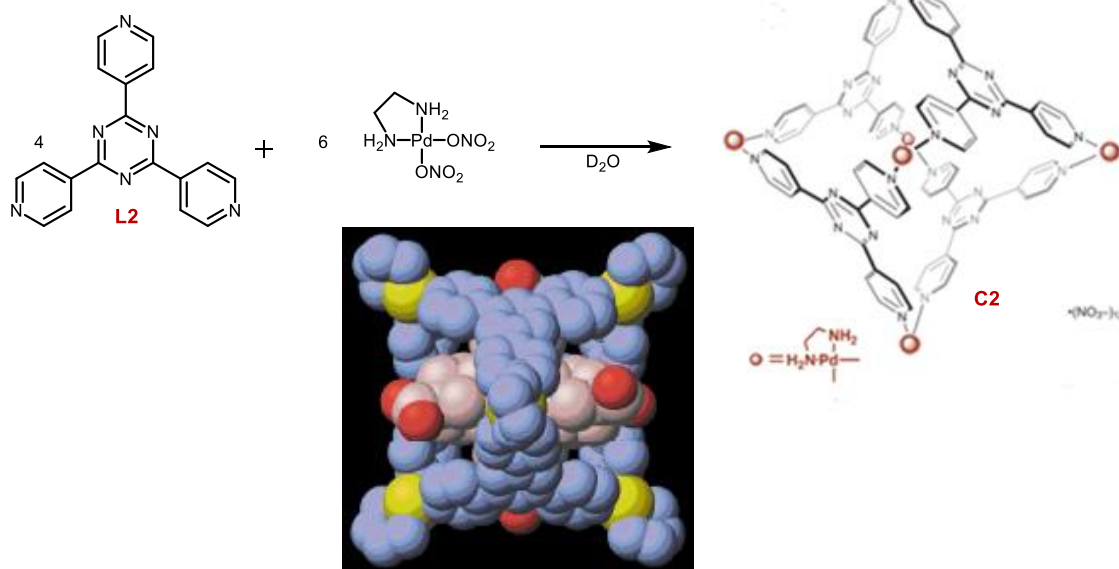


**Figure 6** Top:  $M_6L_4$  adamantoid cage **C2** obtained by reaction of 2eq of 2,4,6-tri-4-pyridyl-1,3,5-triazine (**L2**) with 3eq of  $[Pd(en)(NO_3)_2]$ ; bottom: X-ray crystal structure of **C2** with 4 adamantane carboxylates in the cavity. Hydrogen atoms omitted for clarity. Colour code: blue – **C2** moiety (carbon and nitrogen), Yellow – palladium, light pink – adamantane moiety (carbon), red – oxygen; ©The Royal Society of Chemistry 2001

**C2** possessed an extraordinarily large cavity with a diameter of ca. 11 Å in which four 1-adamantane carboxylate ions were encapsulated. The crystal structure of this complex indicated that the hydrophobic adamantyl groups were located inside the cage's cavity, while the hydrophilic carboxylate groups were located outside (**Figure 6**, bottom). NMR spectroscopic studies showed that the 1:4 host–guest aggregate also existed in solution.

Larger derivatives of **C2** were obtained by using the phenylene- and biphenylene-bridged tridentate ligands **L3** and **L4** (**Figure 7**).<sup>79</sup> Cages **C3**, **C4**, and **C2** were categorized as ultrafine particles since their size reached the nanometre scale (2-5nm) as demonstrated by the volume-weighted distribution analysis of the particle sizes by laser light scattering.

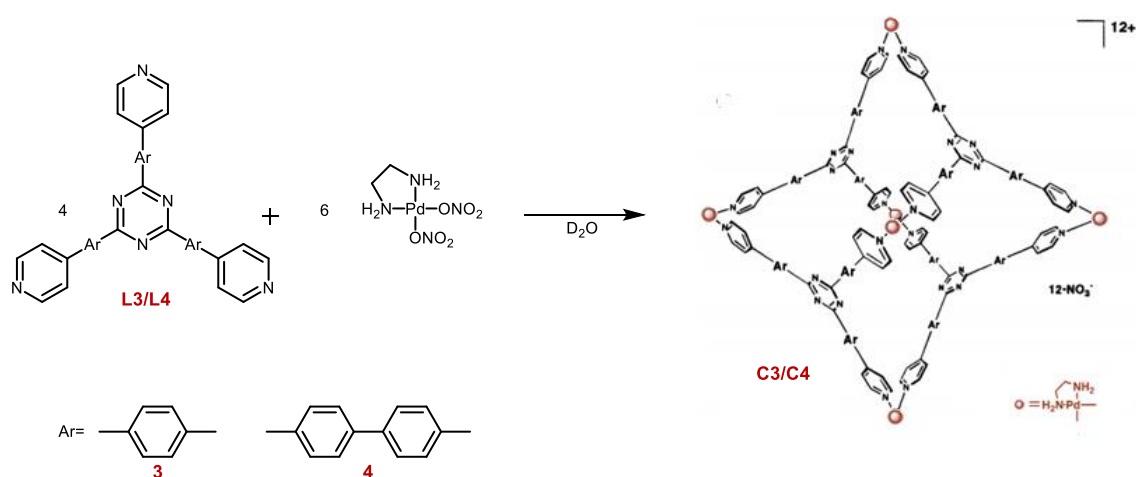


**Figure 7**  $M_6L_4$  adamantanoid cages **C3** and **C4** obtained by reaction of 2eq of the pyridine-based tridentate ligands **L3** and **L4** with 3eq of  $Pd(NO_3)_2(en)$ . © 1995 Nature Publishing Group

Another strategy to obtain large hollow complexes of well-defined shapes and sizes is based on combining metal ions with rigid bent organic ligands. For instance, tetravalent Pd(II) acceptors and C- or banana-shaped pyridine-based bis-monodentate ligands have been used for the coordination-driven self-assembly of three dimensional  $M_nL_{2n}$  assemblies (M=metal, L=ligand) with n ranging from two up to twenty-four.

In general, the nuclearity of the resulting structures depends on the angle at which the ligand orients the donor atoms. It can be predicted by assuming the smallest assembly in which all binding sites are occupied without leading to steric strain (**Figure 8**).<sup>80–82</sup>



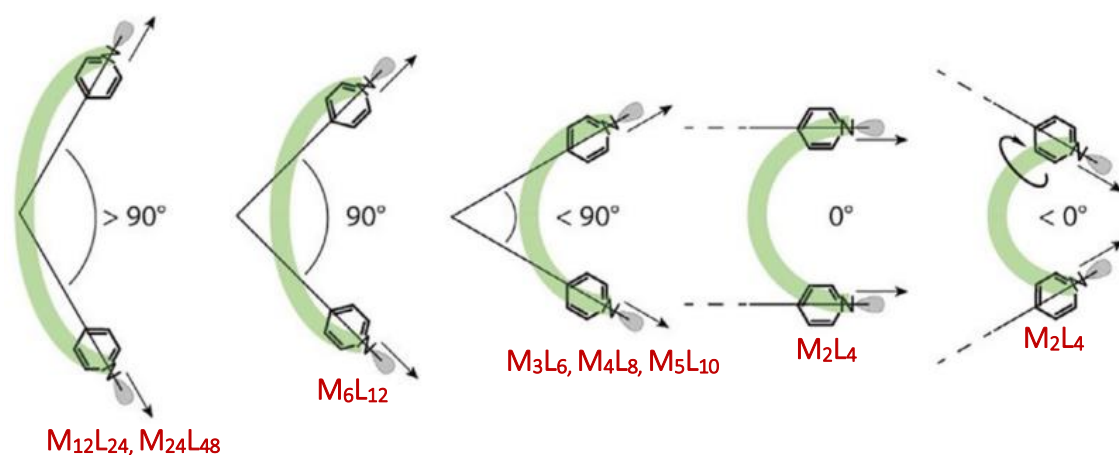


**Figure 8** Relation between the nuclearity of the  $M_nL_{2n}$  assemblies ( $M=\text{Pd(II)}$ ,  $L=\text{pyridine containing bis-monodentate ligand}$ ,  $n=\text{nuclearity}$ ) and the angles between the two donor electron lone pairs of the ligand. © 2018 Elsevier B.V

Ligands that adopt conformations in which the bonding vectors of the two pyridyl donors are collinear ( $0^\circ$ ) or directed towards a common point in space ( $<0^\circ$ ) lead to  $M_2L_4$  assemblies, while structures of higher nuclearity are obtained from ligands in which the bonding vectors are oriented at an angle  $>0^\circ$ . In this case, the size of the metal-complex depends on the angle between the two lone pairs of the donor atoms. For angles smaller than  $90^\circ$ , complexes with three to five metal centres are obtained and for angles larger than  $90^\circ$ , the complexes contain twelve or twenty-four metal ions. Ligands with a  $90^\circ$  bend angle afford  $M_6L_{12}$  complexes (**Figure 8**).

In 1998, the first  $M_2L_4$  cage (**C5**) derived from Pd(II) directed self-assembly and pyridine containing ligands was synthesized by Steel and co-workers (**Figure 9**).<sup>83</sup> **C5** was prepared by mixing 1,4-bis(3-pyridyloxy)-benzene (**L5**) and  $\text{PdI}_2(\text{Py})_2$  in acetonitrile together with silver triflate in order to precipitate the halide anions. The cage was shown to encapsulate one  $\text{PF}_6^-$  anion when  $\text{NH}_4\text{PF}_6$  was present during the reaction.

Lützen et al. reported the formation of the homochiral metallosupramolecular dinuclear  $M_2L_4$  cage **C6** by reacting tetravalent  $[\text{Pd}(\text{CH}_3\text{CN})_4](\text{BF}_4)_2$  with an enantiomerically pure planar chiral ligand based on a [2.2]paracyclophane skeleton ((*Rp*)-**L6**) in deuterated acetonitrile (**Figure 9**).<sup>84</sup> When a racemic mixture of **L6** was exposed to the same reaction conditions the self-assembly reaction occurred without a significant degree of diastereoselectivity, giving rise to a mixture of all possible diastereomeric complexes

$[\text{Pd}_2\{(\text{Rp})\text{-L2}\}_4](\text{BF}_4)_4$  (and its enantiomer),  $[\text{Pd}_2\{(\text{Rp})\text{-L6}\}_3\{(\text{Sp})\text{-L6}\}_1](\text{BF}_4)_4$  (and its enantiomer), *cis*- $[\text{Pd}_2\{(\text{Rp})\text{-L6}\}_2\{(\text{Sp})\text{-L6}\}_2](\text{BF}_4)_4$  and *trans*- $[\text{Pd}_2\{(\text{Rp})\text{-L6}\}_2\{(\text{Sp})\text{-L6}\}_2](\text{BF}_4)_4$ .

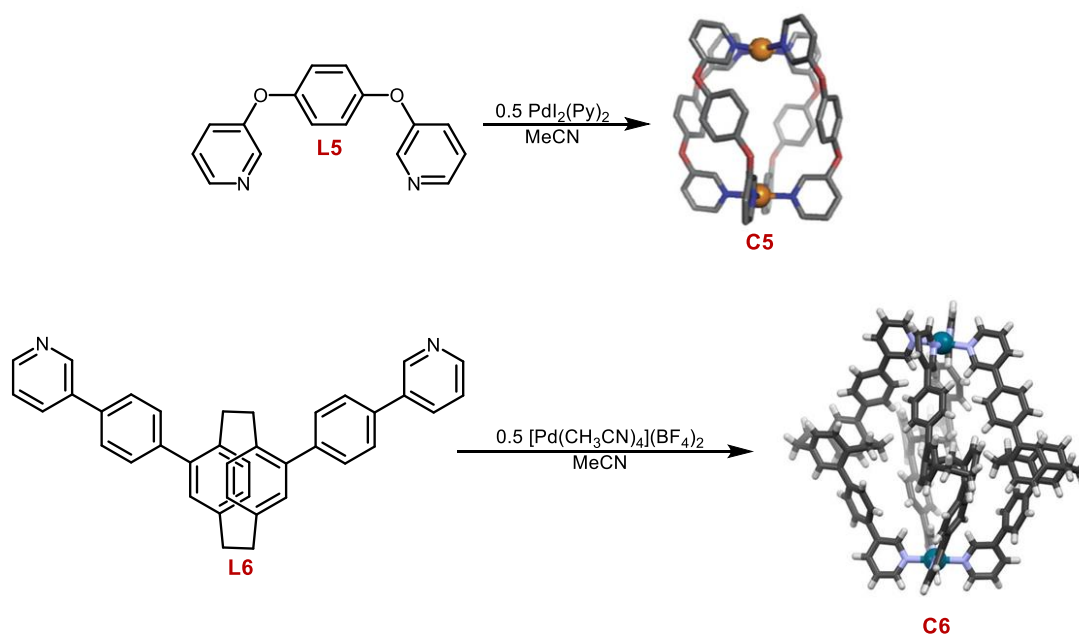


**Figure 9** Examples of  $\text{Pd}_2\text{L}_4$  cages. **C5**: X-ray crystal structure of  $\text{Pd}_2\text{L5}_4 \cdot (\text{PF}_6)_4 \cdot 2\text{MeCN}$ . Hydrogen atoms, counter ions and solvent molecules are omitted for clarity. Colour code: grey – carbon, red – oxygen, blue – nitrogen, orange – palladium. © 2018 Elsevier B.V; **C6**: X-ray crystal structure of homochiral  $\text{Pd}_2\text{L6}_4 \cdot (\text{BF}_4)_4$ . Counter ions omitted for clarity. Colour code: grey – carbon, white – hydrogen, blue – nitrogen, petrol – palladium; © The Royal Society of Chemistry 2019

An unexpected result was obtained by the same group with the dissymmetric bis(3-pyridyl) ligand **L7** based on a BINOL scaffold.<sup>85</sup> Since **L7** had a converging donor vector angle ( $-60^\circ$ )<sup>81</sup> one would expect that self-assembly would give rise to a  $\text{M}_2\text{L}_4$  type cage. The reaction between **L7** and  $[\text{Pd}(\text{CH}_3\text{CN})_4](\text{BF}_4)_2$ , however, afforded the  $\text{M}_4\text{L}_8$  complex **C7** (**Figure 10**) in which the four metal ions were arranged in a distorted tetrahedral fashion. The four ligands of the edges adopted a C-shaped conformation, whereas the other four adopted a twist-folded W-shaped arrangement.

This coordination mode resulted in a structure containing three cavities: two at the outer periphery that hosted two tetrafluoroborate anions, and another central cavity featuring a confined, chiral, and hydrophilic environment that hosted several acetonitrile molecules. This unprecedented structural motif was the result of an efficient template effect of the two tetrafluoroborate counterions encapsulated in the peripheral cavities.

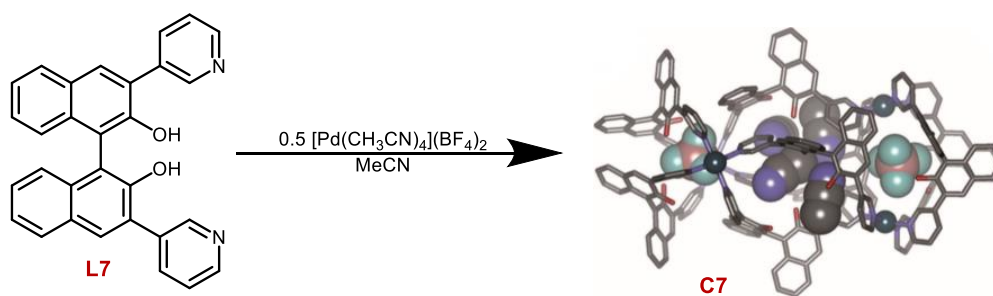


**Figure 10** X-ray crystal structure of  $\text{Pd}_4\text{L7}_8$  (**C7**) including encapsulated  $\text{CH}_3\text{CN}$  molecules and  $\text{BF}_4^-$  anions. Hydrogen atoms and further non-encapsulated tetrafluoroborate ions and solvent molecules are omitted for clarity. Colour code: grey – carbon, red – oxygen, green – fluorine, red-brown – boron, purple – nitrogen, blue – palladium. © 2014 Wiley-VCH Verlag GmbH & Co. KGaA, Weinheim

This example demonstrated that despite a careful ligand design one cannot always predict the most thermodynamically stable assembly due to the different contributions that have to be considered. Nevertheless, the proper understanding of the assembly principles during complex formation allows for the manipulation of the reaction conditions in order to favour the formation of one structure with respect to another, as exemplified by Fujita and co-workers<sup>86</sup> (**Figure 11**).

They reported the self-assembly of a ligand with a fixed angle of approximately  $60^\circ$  (**L8**) with  $\text{Pd}(\text{NO}_3)_2$ , yielding either tubular trigonal  $\text{M}_3\text{L}_6$  (**C8a**) or tetragonal prismatic  $\text{M}_4\text{L}_8$  (**C8b**) coordination cages (**Figure 11**). The exclusive formation of one geometry or the other was determined by the choice of solvent. In  $\text{DMSO-}d_6$ , the tetragonal **C8b** was favoured, whereas in  $\text{CD}_3\text{CN}$ , the trigonal prismatic **C8a** was formed. This was an unexpected result since both cages possessed comparable strain energies, even though the formation of **C8a** should be entropically favoured. Crystal structures offered insight into the reasons for this behaviour. In **C8a**, the cavity was small and filled by one water and two acetonitrile molecules. In the case of **C8b**, however, the cavity contained two nitrate anions and two DMSO molecules, which compensated for the entropic disadvantage of the formation of the larger cage. Interestingly, when acetonitrile was added to the solution of **C8b**, the complete conversion to **C8a** occurred. The equilibrium was again shifted by removal of the acetonitrile.

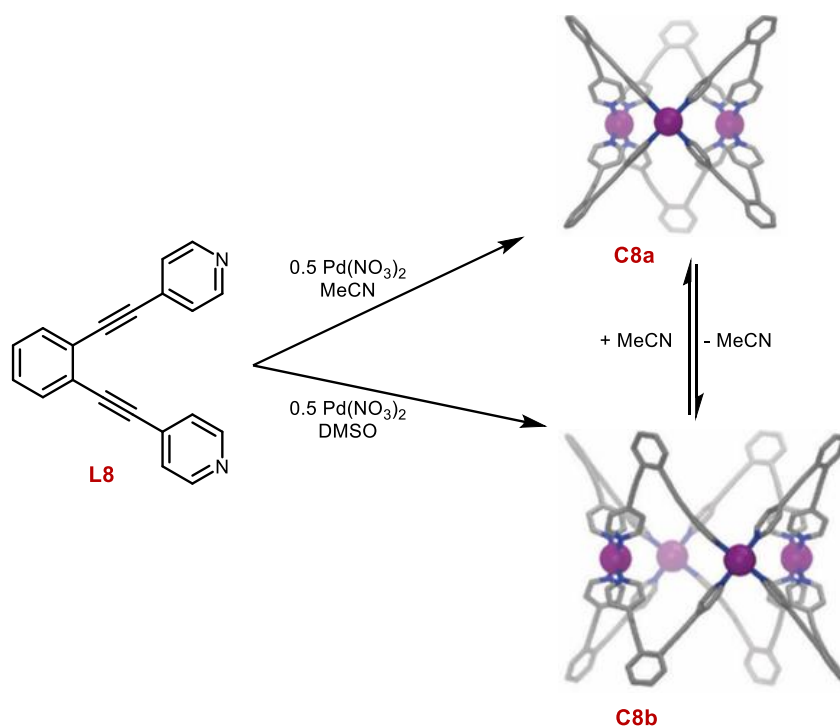


**Figure 11** Solvent controlled assembly of  $Pd_3L_8$  and  $Pd_4L_8$  coordination cages. X-ray crystal structures of tubular trigonal prismatic cage **C8a** and tubular tetragonal prismatic cage **C8b**. Hydrogen atoms, counter anions and solvent molecules omitted for clarity. Colour code: grey – carbon, blue – nitrogen, purple – palladium. ©The Royal Society of Chemistry 2014

In another example by Fujita, structural control of the metal-assembly was dependent on the bend angle of the ligand (**Figure 12**).<sup>87</sup> The thiophene-based ligand **L9** alone afforded a rhombicuboctahedron  $M_{24}L_{48}$  and the furan-derived ligand **L10** a cuboctahedron  $M_{12}L_{24}$  in the presence of  $Pd(NO_3)_2$ . These results were in perfect agreement with the expected ones considering the bend angles of the ligands. Interestingly, the reaction of tetravalent Pd(II) with mixtures of these two ligands in various ratios afforded exclusively either  $M_{12}L_{24}$  (**C10**) or  $M_{24}L_{48}$  (**C9**) structures, but never a mixture of the two.

Cages **C9** and **C10** contained statistical mixtures of the two ligands, in which their average bend angle was determined by the ligand ratio and varied from  $127^\circ$  to  $149^\circ$  (see table in **Figure 12**). Starting from a ratio of **L9**:**L10** of 9:1 and then varying it sequentially to 1:9, **C9** was formed exclusively until a ratio was 2:8 reached, whereupon a threshold was passed and **C10** was exclusively observed (see red square in table from **Figure 12**). The slight

difference in bend angles between the 3:7 and the 2:8 ratios represented the “critical structural switch”, determining the structure of the resulting assembly.

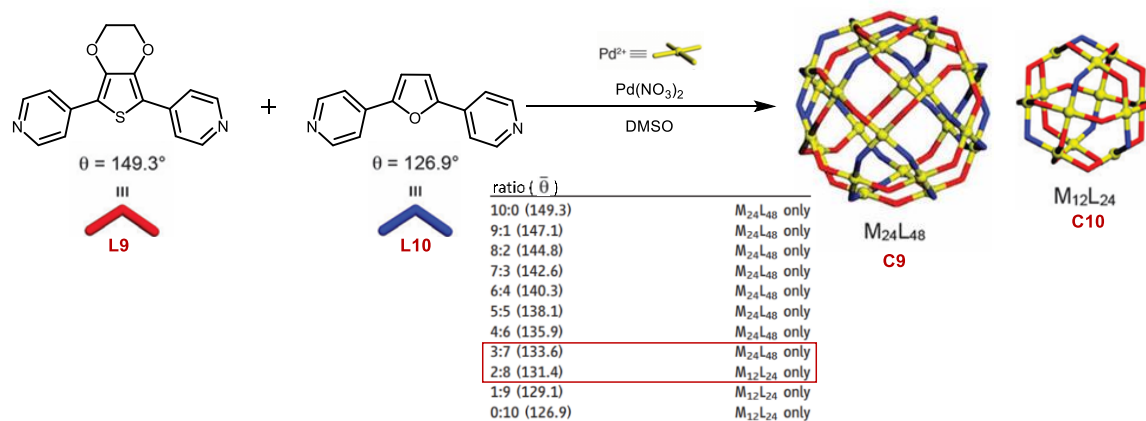


**Figure 12** Self-organization of mixtures of the ligands **L9** and **L10** exclusively into either **C9** or **C10** with a critical structural switch occurring at an average bend angle between 131° and 134° (red square in the table). ©The Royal Society of Chemistry 2013

### 1.1.3 Pd(II)-Directed Self-Assembly of Pyridine-Containing Cyclopeptides

In Nature, metal ions are cofactors for a large number of proteins and often play important catalytic, structural, regulatory, and/or enzymatic roles in biological systems. So it comes as no surprise that chemists have been synthesizing peptide mimics with incorporated natural or non-natural metal binding sites that can imitate natural metalloproteins.<sup>88</sup> The coordination of metal ions can induce conformational changes in the peptide, can dramatically change its properties,<sup>89</sup> or promote self-assembly through metal–ligand interactions, creating nanostructures that are structurally and functionally quite distinct from the original peptide.<sup>90</sup> Substantial advances have been achieved using peptides for the construction of nanostructures, including the fabrication of nanofiber materials for cell culture and tissue engineering,<sup>91</sup> the assembly of peptide nanotubes<sup>92</sup> and helical ribbons among others.

While the self-assembly of cyclopeptides mediated by hydrogen bond formation has been extensively investigated,<sup>93–100</sup> the metal-directed self-assembly of cyclopeptides is less common.

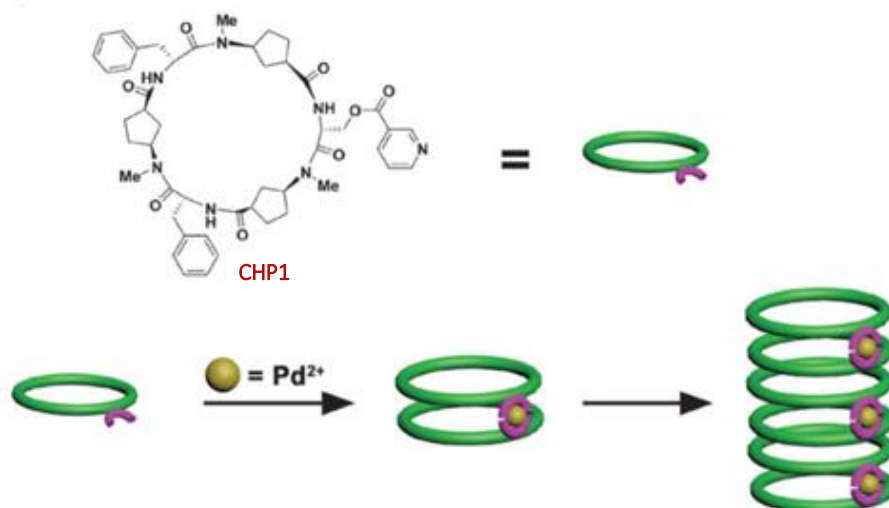


**Figure 13** Top: Chemical structure of cyclohexapeptide **CHP1**. Bottom: Proposed model for the formation of the molecular pom-poms formed by self-assembly. © 2013, Wiley-VCH Verlag GmbH & Co. KGaA

Cyclopeptides represent, however, attractive building blocks in this context because of their structural versatility, chirality and the possibility to control their preferred conformation by the structures of their subunits.<sup>101–104</sup> Thus, cyclic peptides have the potential to give rise to coordination compounds that combine synthetic supramolecular aspects with natural product chemistry.

Among the examples of cyclopeptide-derived coordination compounds,<sup>92,102–107</sup> those obtained by Pd(II) mediated self-assembly of pyridine containing cyclopeptides are especially scarce.<sup>92,104</sup> One example was described by Panciera et al., comprising the formation of “pom-pom” like molecular structures from the  $\alpha,\gamma$ -cyclic hexapeptide **CHP1** with nicotinic acid residues in the periphery (**Figure 13**).<sup>92</sup>

The coordination of these moieties to Pd(II) centres was confirmed by <sup>1</sup>H-NMR spectroscopy but, unfortunately, the obtained spectrum was more complex than expected. The broadening of the signals, in particular, indicated the formation of polymeric structures.

Further investigations allowed to conclude that upon complexation, **CHP1** formed dimers that self-organized in a hierarchical process (**Figure 13**, bottom) to form spherical structures covered by needle-shaped crystals, giving the appearance of “molecular pom-poms”.

Scanning electron microscopy (SEM) showed that these spheres consisted of two main parts, a dense and compact central core and a cortex where the nanocrystals grew. Due to their porous composition, these materials were able to encapsulate and subsequently liberate small molecules.

In another example, Jolliffe obtained an infinite coordination polymer by coordinating the tripodal pyridyl containing Lissoclinum-type cyclic hexapeptide **CHP2** (Figure 14) to [1,3-bis(diphenylphosphino)propane]palladium(II) triflate (Pd(dppp)OTf<sub>2</sub>).<sup>104</sup> Two nitrogen donor atoms from different cyclopeptides were coordinated to dppp-protected Pd(II), forming a linear polymer that extended along the crystallographic  $\alpha$ -axis, with each metal centre possessing square planar geometry.

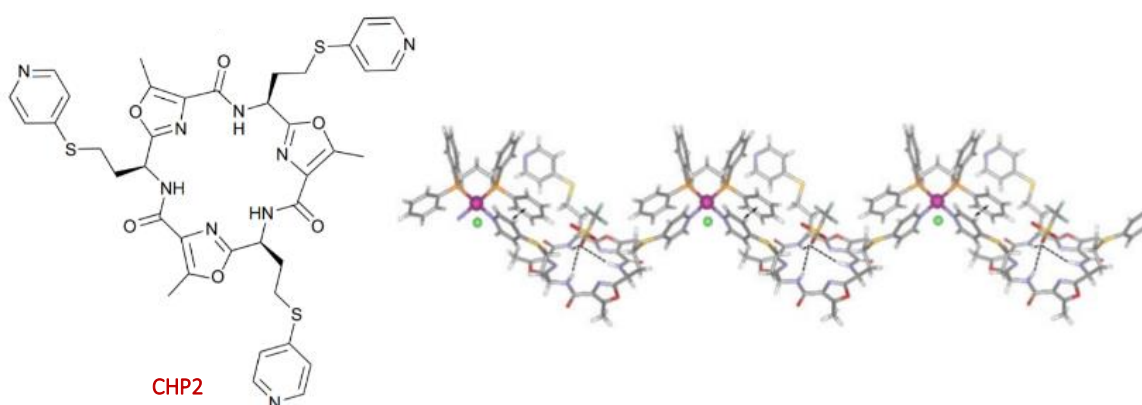


**Figure 14** Left: Chemical structure of hexacyclopeptide **CHP2**. Right: Part of the infinite 1D coordination polymer in the crystal structure of  $\{[Pd(dppp)CHP2] \cdot OTf \cdot Cl \cdot 3MeOH \cdot 3Et_2O\}_n$ . Dashed lines represent hydrogen bonds, and double-headed arrows represent  $\pi$ - $\pi$  interactions. Regions of disorder removed for clarity. Colour code: white – hydrogen, grey – carbon, blue – nitrogen, Yellow – sulphur, violet – palladium, red – oxygen, orange – phosphorus, green – chlorine; © 2012 Taylor & Francis

It was observed that  $\pi \cdots \pi$  interactions existed between the coordinated pyridyl substituents and the neighbouring aromatic residues of the dppp ligand. In addition, intramolecular hydrogen bonds stabilized the planar geometry adopted by the **CHP2** ring. The positively charged coordination polymer was bound to chloride counterions through electrostatic interactions near the metal centre (Figure 14, green) and to triflate anions through hydrogen bonds in the cyclopeptide ring. One pyridyl group per cyclopeptide

remained coordinatively unsaturated, resulting in the loss of the  $C_3$  symmetry present in the original ring.

When **CHP2** was reacted with silver nitrate instead of  $\text{Pd(dppp)OTf}_2$ , the  $L_2M_3$  type metallocage **C11** was obtained (**Figure 15**). Crystallization was not possible, but the modelled structure indicated that the cage possessed a  $C_3$  symmetric structure with a slight helical twist, due to the chiral nature of the cyclohexapeptide. Prior to the work performed in this thesis, **C11** was the only cyclohexapeptide derived coordination cage described.

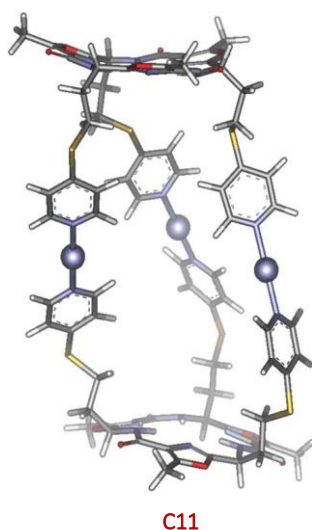


**Figure 15** Molecular structure of **C11** capsule  $[(L_2Ag_3)^{3+}]$  modelled with SPARTAN 10 (AM1). Colour code: white – hydrogen, grey – carbon, blue – nitrogen, Yellow – sulphur, purple – palladium, red – oxygen; © 2012 Taylor & Francis

Kubik et al. have shown that the tetracyclopeptide **CP1** (**Figure 16**) with two diverging pyridyl units forms coordination polymers with  $\text{CdCl}_2$  and  $\text{HgCl}_2$ .<sup>102</sup> The X-ray crystal structure analysis of the metal-free ligand **CP1** showed that the peptide adopted a V-shaped conformation with the two pyridyl units pointing to the same side of the cyclopeptide ring. The angle between the mean planes of the two phenyl units amounted to  $52.32^\circ$  and the pyridyl units were rotated by  $38.07^\circ$  with respect to the neighbouring benzene ring.



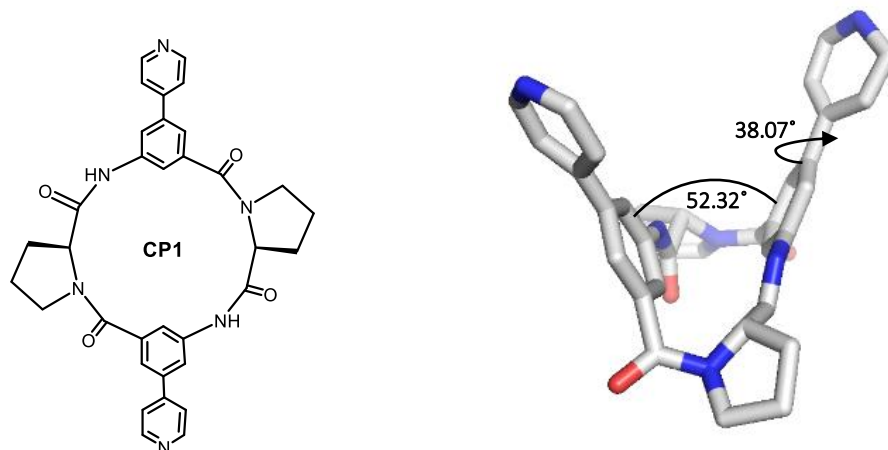


**Figure 16** Left: Chemical structure of the cyclic tetrapeptide **CP1**. Right: X-ray crystal structure of  $\text{CP1}\cdot 2\text{H}_2\text{O}\cdot \text{EtOH}$ . Hydrogen atoms and solvent molecules omitted for clarity. Colour code: grey – carbon, blue – nitrogen, red – oxygen;

The coordination of **CP1** to cadmium(II) or mercury(II) ions resulted in the formation of homochiral coordination polymers (**Figure 17**) in which the metal centres adopted a slightly distorted tetrahedral geometry and were bound to two pyridyl moieties of two different cyclopeptide rings and two chloride ions. In both structures, **CP1** adopted a V-shaped conformation similar to the one of the free form but with angles between the mean planes of the phenyl units of almost  $90^\circ$ . Also, the torsion angle of the pyridine rings was slightly smaller. These structural changes indicated that **CP1** was able to adapt its conformation according to the requirements of metal coordination.

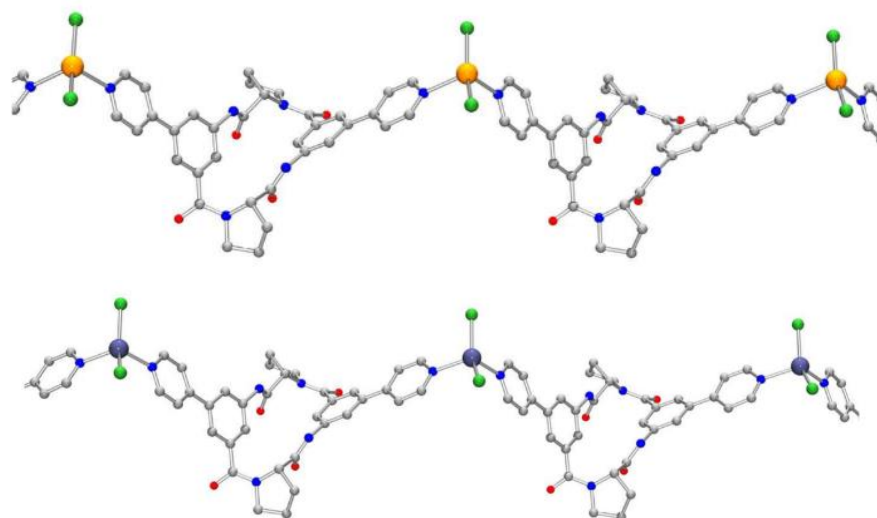


**Figure 17** Crystal structure of the 1D coordination polymers  $[\text{CP1}\cdot \text{HgCl}_2]_n$  (top) and  $[\text{CP1}\cdot \text{CdCl}_2]_n$  (bottom). Hydrogen atoms omitted for clarity. Colour code: grey – carbon, blue – nitrogen, red – oxygen, orange – mercury, purple – cadmium, green – chlorine.

## 1.2 AIM OF THE PROJECT

This project focuses on the synthesis of discrete coordination complexes derived from pyridyl containing cyclopeptides by Pd(II)-mediated self-assembly and the study of the receptor properties of these complexes.

Given the known ability of **CP1** to coordinate to metal ions, this cyclopeptide was chosen as one of the building blocks for the targeted metal assemblies. This cyclopeptide has the advantage that it allows using the strategy described by Fujita to create discrete coordination complexes with suitable palladium(II) precursors.<sup>37,51</sup>

One goal of the work was therefore to investigate the coordination between **CP1** and  $[\text{Pd}(\text{en})(\text{NO}_3)_2]$  (**Figure 18**). Even though the final structure of this reaction cannot be predicted with certainty, considering that **CP1** is more flexible than most of the ligands used by Fujita, one would expect a macrocyclic complex with the composition  $\text{CP1}_2\text{Pd}_2$  to be the thermodynamically most stable product.

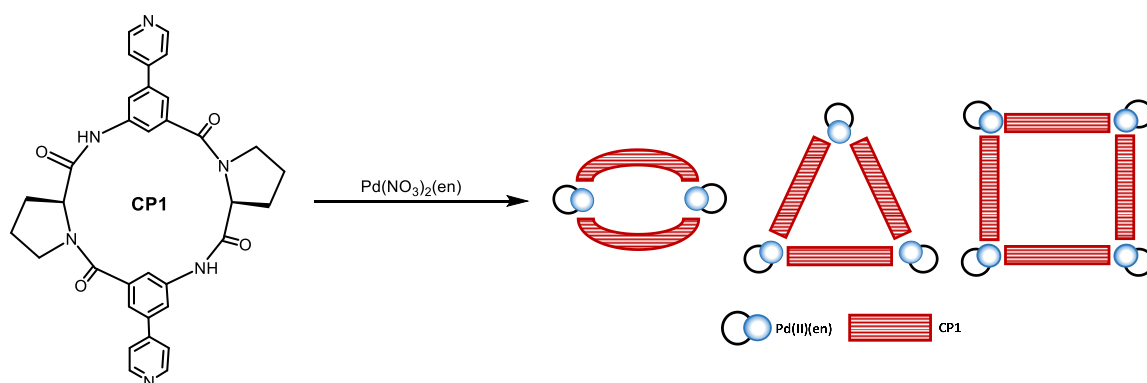


**Figure 18** Schematic representation of possible products resulting from the metal-directed self-assembly of a cis-protected Pd(II) complex and **CP1**.

To evaluate whether such cyclopeptides also allow accessing three dimensional structures by the same route, the complexation between  $[\text{Pd}(\text{en})(\text{NO}_3)_2]$  and the corresponding cyclohexapeptide **CP2** was targeted (**Figure 19**). Preliminary calculations provided information that **CP2** might be suitable for this purpose. These calculations were based on the crystal structure of the parent cyclohexapeptide **CP3** composed of (L)-proline and 3-aminobenzoic acid subunits.<sup>108</sup> **CP3** adopted a conformation in which all the proline amides

had *trans* conformation and the aromatic rings were tilted in the same direction. The structure did not exhibit an ideal  $C_3$  symmetry, however, since the NH and CO groups of the amide bonds were not all arranged in the same way (black arrows in the crystal structure of **CP3** in **Figure 19**). Since **CP3** adopted an average  $C_3$  symmetric conformation in solution, only symmetric structures were considered in the calculations performed on **CP2**.

The thus resulting structure had a deeper cavity than **CP3**, exhibiting a cone-shaped conformation with all the pyridyl units pointing to the same side of the cyclic peptide. A  $83.02^\circ$  mean angle between the phenyl units with a  $52.52^\circ$  torsion of the pyridyl rings with respect to the neighbouring aromatic subunits was observed. From the calculated structure, it could thus be expected that **CP2** could form a cage when interacting with  $[\text{Pd}(\text{en})(\text{NO}_3)_2]$  with the composition  $\text{CP}_2_2\text{Pd}_3$ . A flatter cyclopeptide conformation could alternatively afford the larger  $\text{CP}_2_4\text{Pd}_6$  complex.

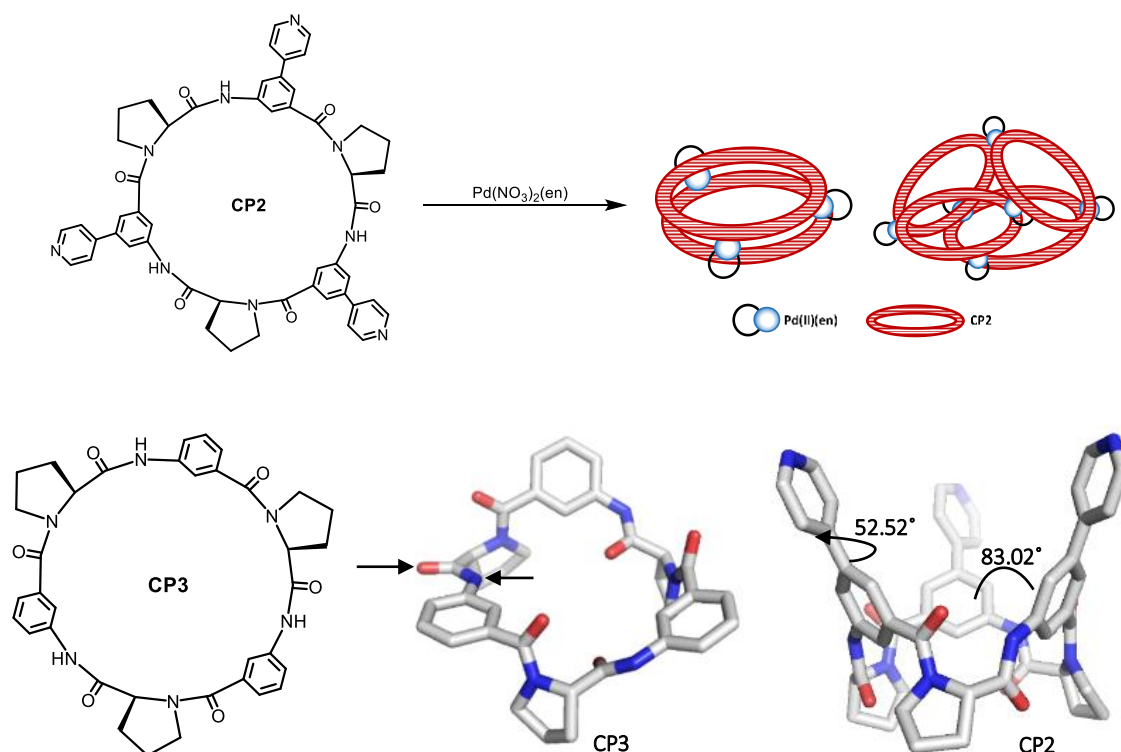


**Figure 19** Top: Schematic representation of metal-directed self-assembly between a *cis*-protected  $\text{Pd}(\text{II})$  complex and **CP2** giving rise to coordination cages. Bottom: Chemical structure of **CP3** (left), x-ray crystal structure of  $\text{CP}_3 \cdot 3\text{CH}_3\text{OH}$  (middle) and modelled structure of **CP2** (right) calculated by using Avogadro with the MMFF force field and without considering solvent molecules. Hydrogen atoms and solvent molecules omitted for clarity. Colour code: grey – carbon, blue – nitrogen, red – oxygen;

The use of tetravalent Pd(II) and **CP1** to obtain cage like structures was also planned (**Figure 20**). Considering the 52.32° bend angle of **CP1**, the cages **CP1<sub>6</sub>Pd<sub>3</sub>**, **CP1<sub>8</sub>Pd<sub>4</sub>** and **CP1<sub>10</sub>Pd<sub>5</sub>** are all possible outcomes of the corresponding coordination-driven self-assembly.<sup>81</sup> Binding studies were also planned to assess whether the obtained cyclopeptide-derived metallostructures could serve as receptors.

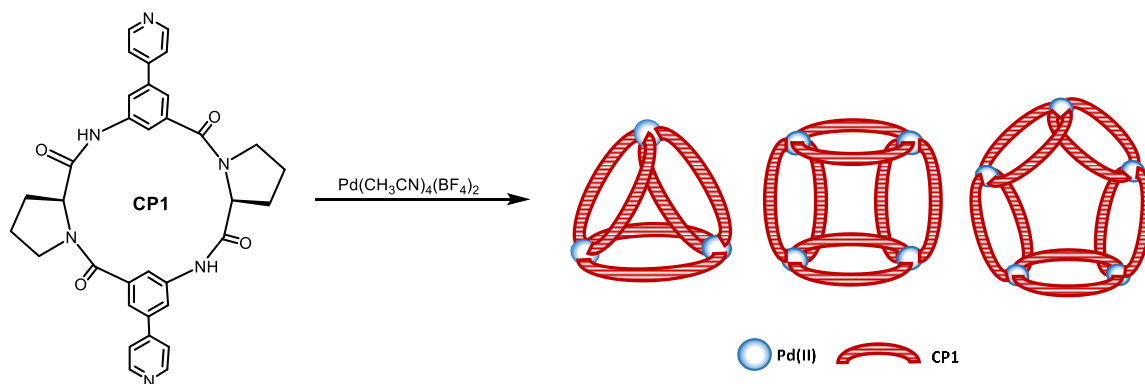


**Figure 20** Schematic representation of metal-directed self-assembly between tetravalent Pd(II) centres and **CP1** towards the formation of coordination cages.

## 1.3 RESULTS AND DISCUSSION

### 1.3.1 Synthesis of the Cyclopeptides and Metal Precursors

The synthesis of cyclopeptide **CP1** was performed as previously described.<sup>102</sup> It began with the esterification of 3-amino-5-bromobenzoic acid (**1**, **Figure 21**) in *n*-butanol. The butyl ester was chosen to avoid the transesterification under the basic conditions of the Suzuki coupling at a later stage of the synthesis that is performed in *n*-butanol. The esterified compound **2** was then reacted with Boc-L-proline (**3**) in dichloromethane with chlorotripyrrolidinophosphonium hexafluorophosphate (PyCloP) as the coupling agent under basic conditions to afford the dipeptide **4** (**Figure 21**).

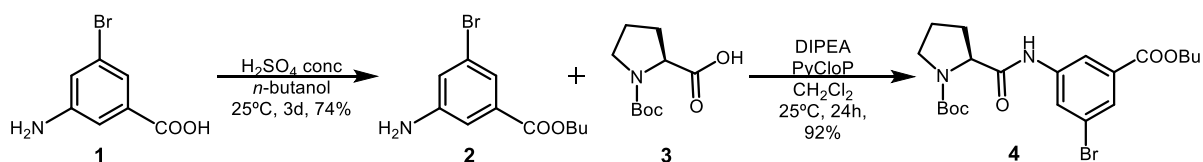


**Figure 21** Synthetic scheme for the synthesis of dipeptide **4** from the commercially available starting materials 3-amino-5-bromobenzoic acid (**1**) and Boc-L-proline (**3**).

The introduction of a pyridyl subunit into dipeptide **4** was achieved through a Suzuki coupling by reaction with 4-pyridinyl boronic acid in *n*-butanol, yielding dipeptide **5**. This dipeptide was then saponified to afford dipeptide **6** (Figure 22).

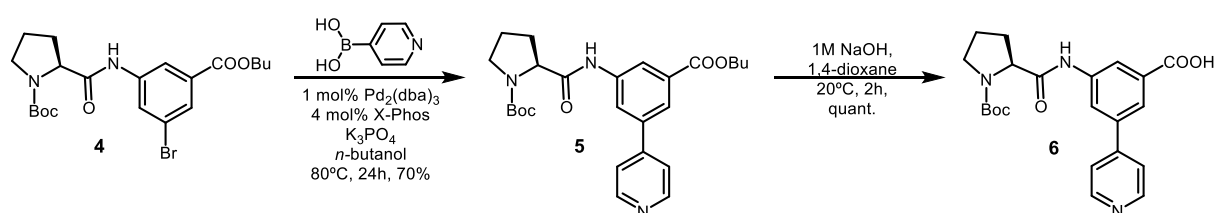


**Figure 22** Synthetic scheme for the synthesis of dipeptide **6** from dipeptide **4**.

This peptide was converted into the benzyl ester **7** by reaction with benzyl alcohol and 2-(1*H*-benzotriazole-1-yl)-1,1,3,3-tetramethylamminium tetrafluoroborate (TBTU) and deprotected at the *N*-terminus under acidic conditions to afford dipeptide **8** (Figure 23).

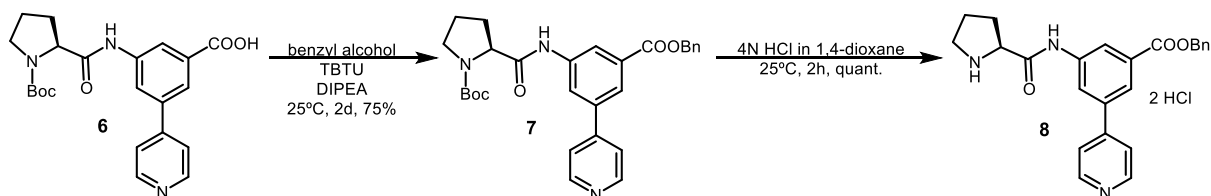


**Figure 23** Synthetic scheme for the synthesis of dipeptide **8** from dipeptide **6**.

Equimolar amounts of the dipeptides **6** and **8** were reacted in the presence of PyCloP as the coupling agent, yielding the tetrapeptide **9**. This compound was then deprotected first at the *C*-terminus and then at the *N*-terminus to yield the fully deprotected tetrapeptide **10**. Cyclization was carried out under high dilution conditions to afford the cyclotetrapeptide **CP1** with a yield of 20% (Figure 24).

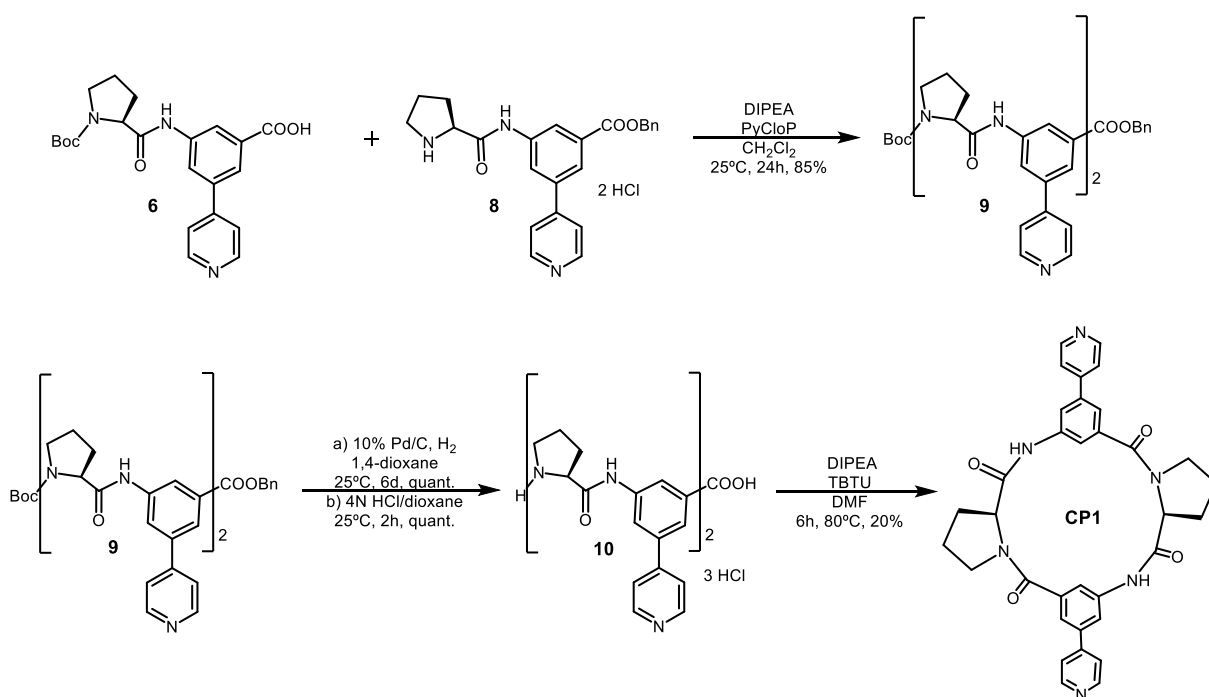


**Figure 24** Synthetic scheme for the synthesis of cyclopeptide **CP1** from dipeptides **6** and **8**.

The corresponding cyclohexapeptide **CP2** was prepared by also using a previously established synthetic route.<sup>109</sup> Specifically, tetrapeptide **9** was deprotected at the *N*-terminus (**11**) and coupled with dipeptide **6** to afford hexapeptide **12**, which was then cleaved at both ends to yield the fully deprotected hexapeptide **13** (Figure 25).

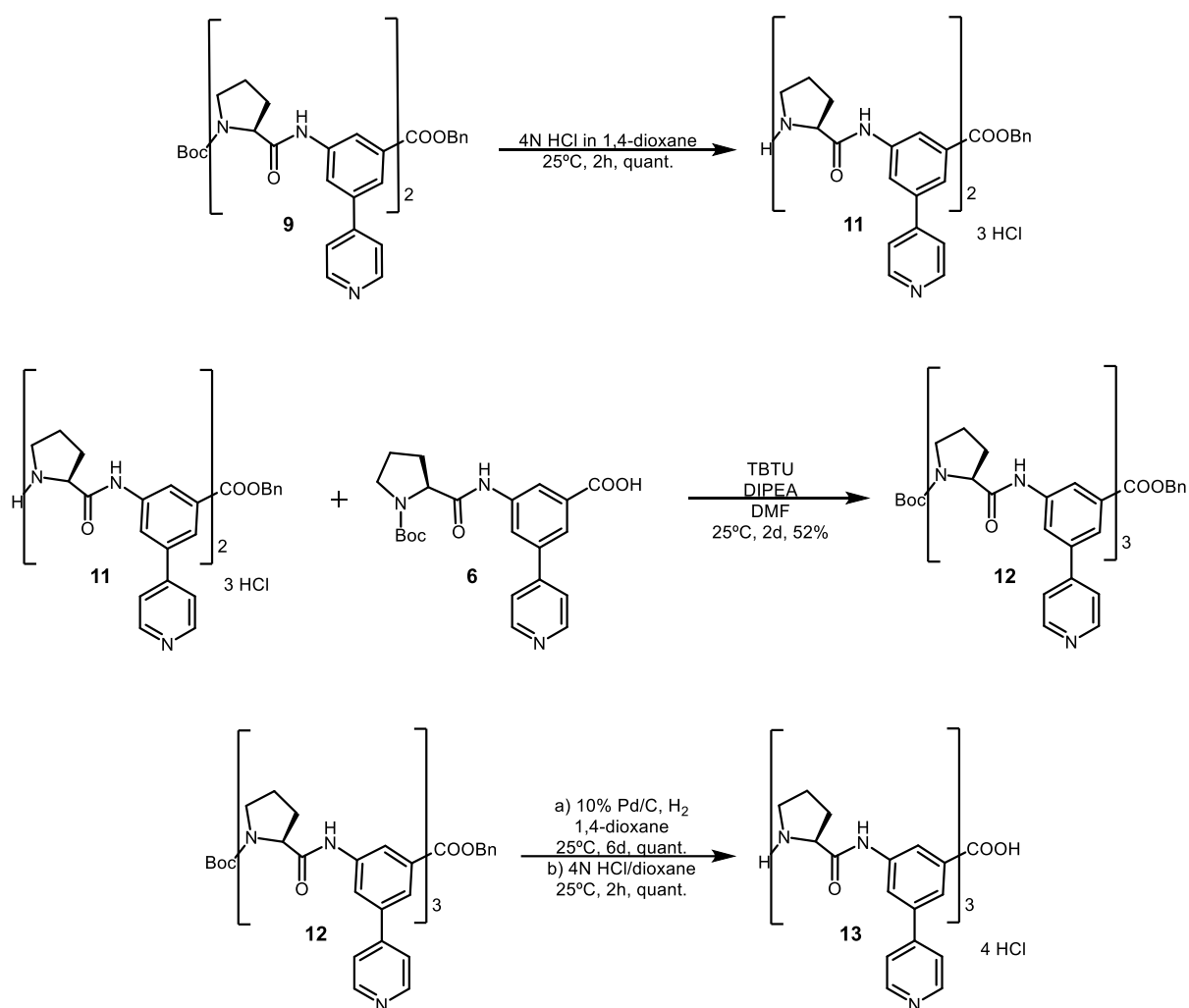


**Figure 25** Synthetic scheme for the synthesis of deprotected hexapeptide **13** from the linear tetrapeptide **9**.

The cyclization in the original synthesis of **CP2** was achieved by the drop-wise addition of a solution of **13** and *N,N*-diisopropylethylamine (DIPEA) in DMF to a solution of TBTU and DIPEA in DMF over the course of 4h at 80°C, followed by 2h of stirring at 80°C. Unfortunately, this method only afforded **CP2** in a yield of 3%. Based on previous work,<sup>110</sup> the reaction conditions were therefore altered and the addition of hexapeptide **13** was performed at 25°C. This change in the synthetic procedure resulted in a marked improvement of the amount of isolated product, which was eventually obtained in a yield of 43% (**Figure 26**).

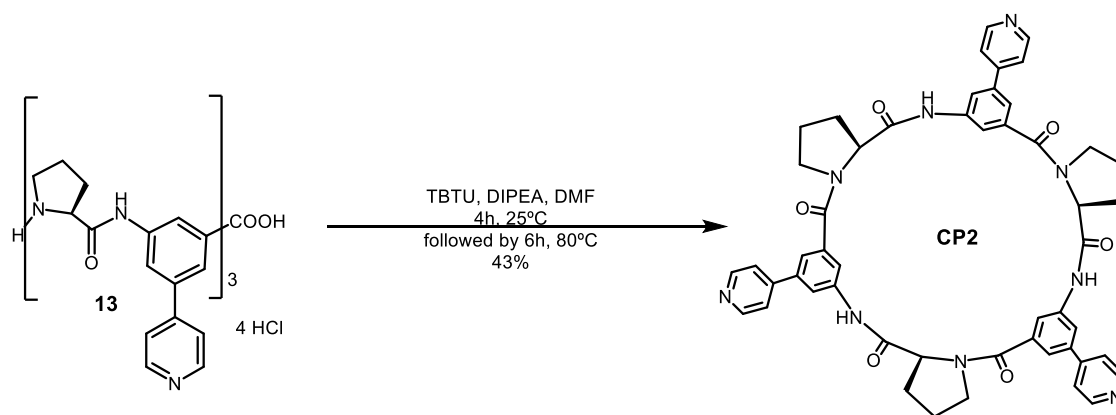


**Figure 26** Synthetic scheme for the synthesis of cyclohexapeptide **CP2** from the deprotected hexapeptide **13**.

The metal complexes  $[\text{Pd}(\text{NO}_3)_2(\text{en})]$  (**15**),  $[\text{Pt}(\text{NO}_3)_2(\text{en})]$  (**17**) and  $[\text{Pd}(\text{NO}_3)_2(2,2'\text{-bipyridine})]$  (**19**) that were used for the reaction with the cyclopeptides were prepared by following literature procedures,<sup>111–113</sup> which involved exchanging the chloride ions from the commercially available chloro complexes  $[\text{PdCl}_2(\text{en})]$ ,  $[\text{PtCl}_2(\text{en})]$  and  $(2,2'\text{-bipyridine})\text{dichloropalladium(II)}$  for nitrate anions by treatment with silver(I) nitrate (**Figure 27**).

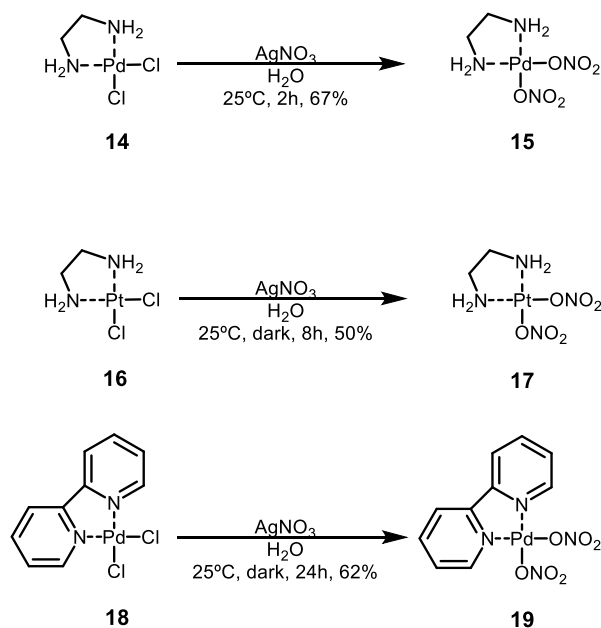


**Figure 27** Synthetic schemes for the synthesis of the metal complexes  $[\text{Pd}(\text{NO}_3)_2(\text{en})]$  (**15**),  $[\text{Pt}(\text{NO}_3)_2(\text{en})]$  (**17**), and  $[\text{Pd}(\text{NO}_3)_2(2,2'\text{-bipyridine})]$  (**19**) from the the commercially available chloro complexes  $[\text{PdCl}_2(\text{en})]$ ,  $[\text{PtCl}_2(\text{en})]$ , and  $(2,2'\text{-bipyridine})\text{dichloropalladium(II)}$ , respectively.



### 1.3.2 Formation of Hollow Coordination Complexes through Metal-Directed Self-Assembly

To get acquainted with the procedures described by Fujita for the preparation of palladium(II) complexes, the molecular box **21** was synthesized by reacting  $[\text{Pd}(\text{NO}_3)_2(\text{en})]$  (**15**) with 4,4'-bipyridine (**20**) according to the described procedure (Figure 28).<sup>68</sup>

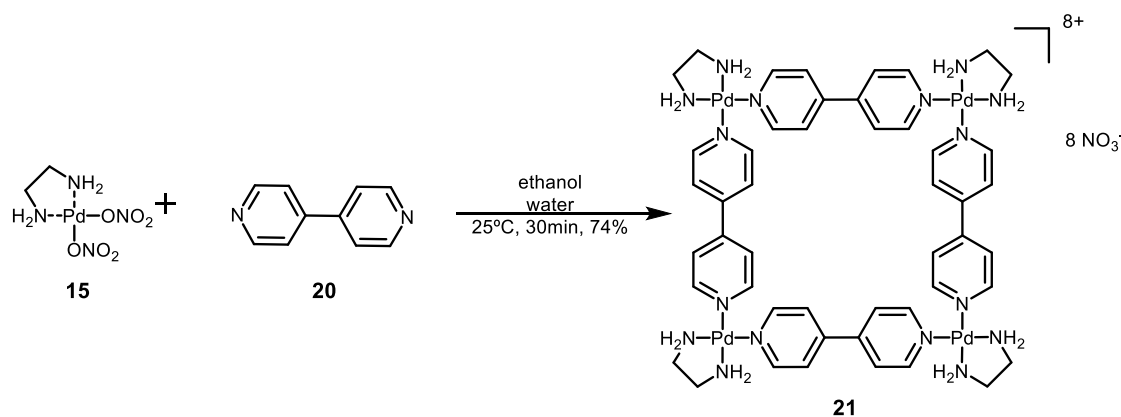


**Figure 28** Synthetic scheme for the synthesis of the Fujita square (**21**) from  $[\text{Pd}(\text{NO}_3)_2(\text{en})]$  (**15**) and 4,4'-bipyridine (**20**).

This reaction failed with commercially available  $[\text{Pd}(\text{NO}_3)_2(\text{en})]$ , which is why the required Pd(II) complex was synthesized. Its reaction with **20** afforded the expected product **21** with a yield of 74%. The compound was structurally characterized by  $^1\text{H}$  NMR spectroscopy and elemental analysis, the results of which compared favourably with the reported ones.

In the  $^1\text{H}$  NMR spectrum, each set of chemical equivalent protons afforded one signal, illustrating the symmetrical structure of **21**. The deshielding of the pyridyl protons with respect to the chemical shifts of the protons in the free ligand confirmed the successful metal coordination (Figure 29).

Based on these results, the synthesis of analogous metal complexes from the CP1 and CP2 was pursued.

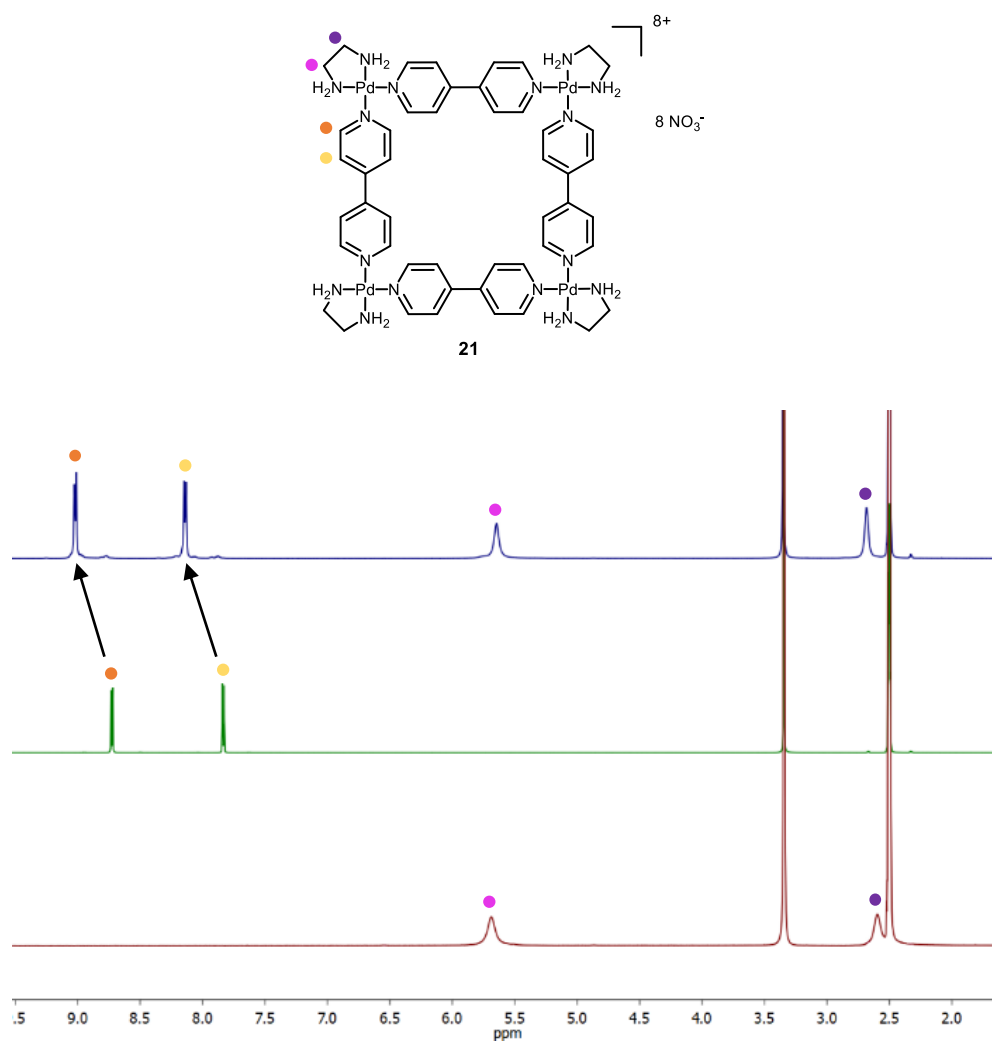


**Figure 29**  $^1\text{H}$  NMR spectra in  $\text{DMSO-}d_6$  of  $[\text{Pd}(\text{NO}_3)_2(\text{en})]$  **15** (red spectrum), 4,4'-bipyridine **20** (green spectrum) and molecular box **21** (blue spectrum).

Two routes were investigated for the coordination of **CP1** to  $[\text{Pd}(\text{NO}_3)_2(\text{en})]$  (**15**) (**Figure 30**). In the first one, **CP1** was reacted with **15** in the required 1:1 ratio. The second approach consisted in adding further bis(monodentate) ligands that could serve to enlarge potentially resulting rings. In this case, a 1:2:1 ratio between **CP1**, **15** and the additional ligands was chosen. The use of a spacer molecule could be advantageous for metallamacrocycle formation in case the cyclopeptide does not adopt the correct conformation for complexation to occur. 4,4'-Bipyridine (**20**) was chosen as the spacer molecule since it was frequently used by Fujita for the synthesis of coordination compounds.<sup>114</sup>

Potential products resulting from both approaches are shown in **Figure 30**, although the formation of alternative structures cannot be ruled out.

Other metal precursors than  $[\text{Pd}(\text{en})(\text{NO}_3)_2]$  (**15**) were also used for the reactions, specifically  $[\text{Pd}(\text{NO}_3)_2(2,2'\text{-bipyridine})]$  (**19**) and  $[\text{Pt}(\text{en})(\text{NO}_3)_2]$  (**17**) since Pt(II) and Pd(II) complexes are usually isostructural. The inertness of Pt(II) complexes was expected to allow the isolation of the final products, which could present an advantage for subsequent studies. (**Figure 30**).

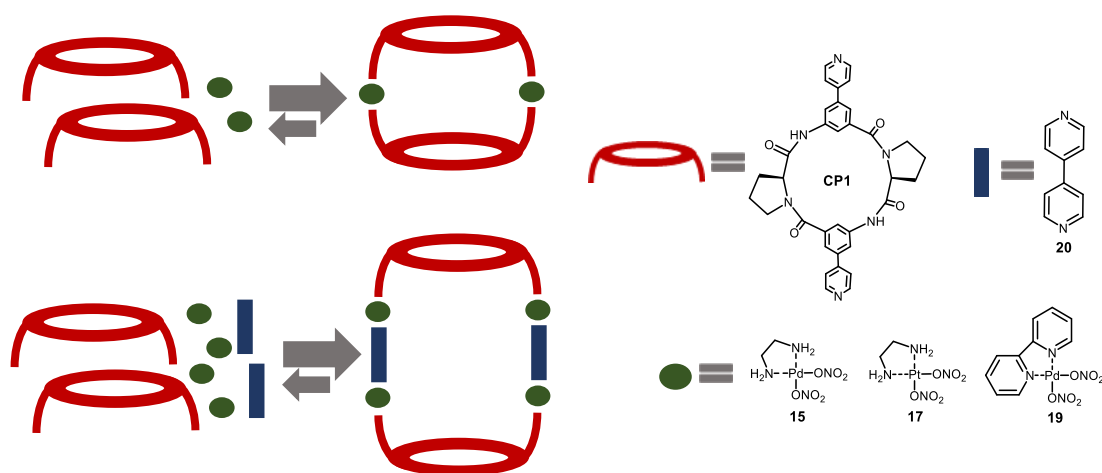


**Figure 30** Schematic representation of the pursued strategies to obtain metallamacrocycles from **CP1** by the Fujita approach.

A set of experiments was performed to identify suitable reaction conditions for metallamacrocyclic formation (**Figure 31**). Each metal precursor ( $[\text{Pd}(\text{en})(\text{NO}_3)_2]$  (**15**),  $[\text{Pd}(\text{NO}_3)_2(2,2'\text{-bipyridine})]$  (**19**) and  $[\text{Pt}(\text{en})(\text{NO}_3)_2]$  (**17**)) was reacted with **CP1** in a 1:1 ratio at 25°C or 60°C. Reactions between **CP1**, the metal precursors and 4,4'-bipyridine (**20**) in a 1:2:1 ratio were also performed at 25°C or 60°C. All reactions were performed in different deuterated solvents in NMR tubes to allow following product formation by  $^1\text{H-NMR}$  spectroscopy.  $^1\text{H-NMR}$  measurements of each sample were made at different reaction times (1h, 5h, 12h, 24h, 48h, 72h, 5d, and 7d).

**CP1** was insoluble in most solvents (except for  $\text{DMF-}d_7$ ), but the formation of discrete complexes was expected to lead to soluble products. Therefore, the experiments in which the cyclopeptide did not dissolve were not investigated further because they likely did not afford a discrete product. This was observed with the samples containing 4,4'-bipyridine

(**20**) and/or  $[\text{Pd}(\text{NO}_3)_2(2,2'\text{-bipyr})]$  (**19**).  $^1\text{H-NMR}$  measurements of these samples confirmed that the cyclopeptide was never in solution in these reactions.

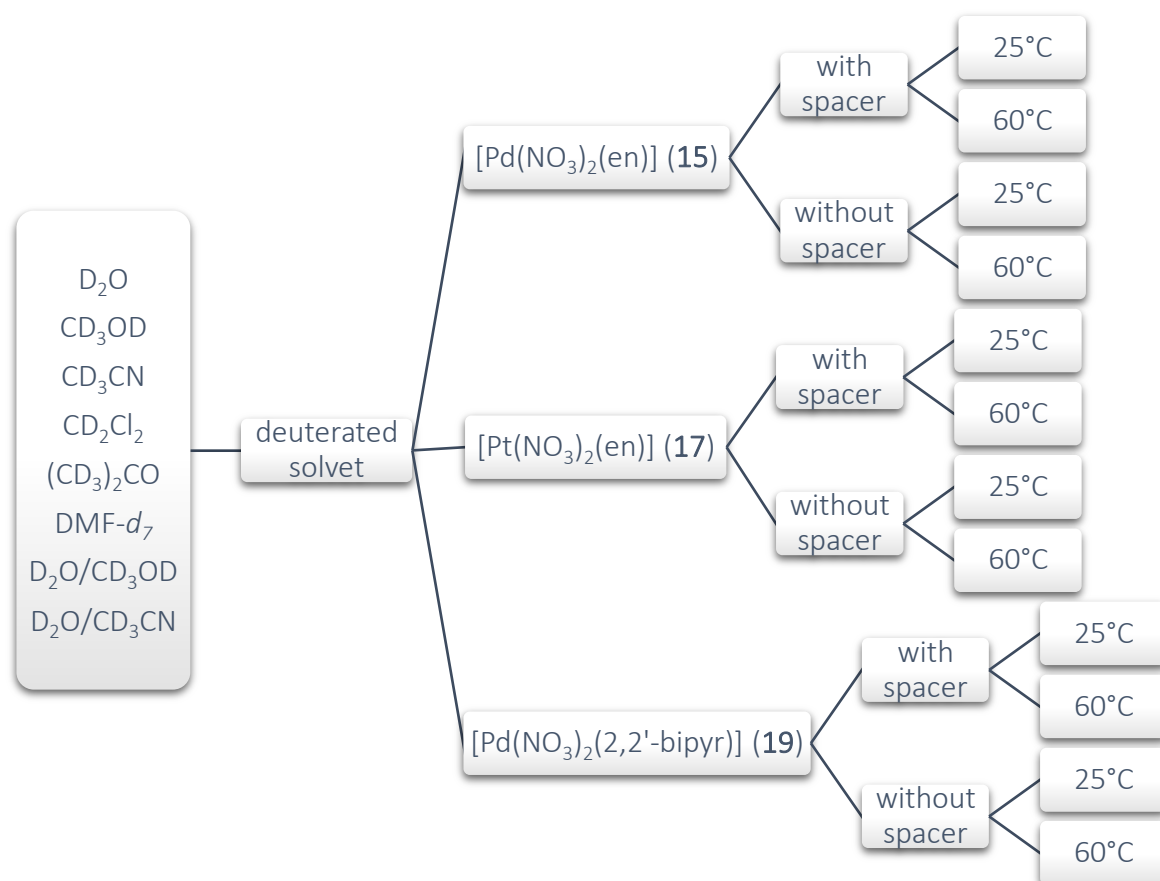


**Figure 31** Diagram of the different reaction conditions used to assess the coordination of **CP1** with  $[\text{Pd}(\text{en})(\text{NO}_3)_2]$  (**15**),  $[\text{Pt}(\text{en})(\text{NO}_3)_2]$  (**17**) and  $[\text{Pd}(\text{NO}_3)_2(2,2'\text{-bipyr})]$  (**19**).

Complex  $^1\text{H-NMR}$  spectra indicated that the reaction conditions were unsuitable to afford a discrete and presumably symmetric product. Complex spectra resulted in all reactions performed at  $60^\circ\text{C}$ , from which could be concluded that  $25^\circ\text{C}$  was a more suitable temperature for the formation of the desired products.

The complexation between  $[\text{Pt}(\text{en})(\text{NO}_3)_2]$  and **CP1** was slow and never went to completion. A minimum of two days was needed for the cyclopeptide to be completely in solution in these experiments and the  $^1\text{H NMR}$  spectra were always complex, preventing peak assignment.

Among the samples containing only **CP1** and [Pd(en)(NO<sub>3</sub>)<sub>2</sub>] at 25°C, the ones in DMF-*d*<sub>7</sub>, D<sub>2</sub>O/CD<sub>3</sub>OD, and D<sub>2</sub>O/CD<sub>3</sub>CN yielded simple <sup>1</sup>H-NMR spectra, suggesting the formation of a single species. The presence of a metal complex of **CP1** in these samples was confirmed by ESI-MS spectrometry.

The sample in D<sub>2</sub>O/CD<sub>3</sub>OD afforded a clear <sup>1</sup>H-NMR spectrum after 5h of reaction time and no changes in the spectrum occurred during the 7 days of the experiment, suggesting that the thermodynamic equilibrium was rapidly reached under these conditions. The reaction mixture in DMF-*d*<sub>7</sub> needed 72h to afford the final product and the one in D<sub>2</sub>O/CD<sub>3</sub>CN needed 12h. In this case, the formation of a precipitate was observed after 48h that, according to the <sup>1</sup>H-NMR measurements, seemed to represent a degradation product. These results indicated that D<sub>2</sub>O/CD<sub>3</sub>OD was the best solvent mixture for complex formation.

These experiments demonstrated that Fujita's approach gave rise to the formation of Pd(II) complexes of **CP1**. The most promising results were obtained when the cyclotetrapeptide was treated with [Pd(en)(NO<sub>3</sub>)<sub>2</sub>] in D<sub>2</sub>O/CD<sub>3</sub>OD at 25°C. These reaction conditions were subsequently further optimized.

The optimized procedure involved adding 1.1 equivalents of [Pd(en)(NO<sub>3</sub>)<sub>2</sub>] in D<sub>2</sub>O/CD<sub>3</sub>OD, 1:1 (v/v) to solid **CP1** to achieve a final concentration of the presumed 2:2 complex of 1 mM and treating the suspension in an ultrasound bath at 25 °C until it was a clear solution. The formed product was structurally characterized directly from the reaction mixture by means of NMR spectroscopy and ESI-TOF MS spectrometry.

Information about the success of metal coordination was derived by ESI-TOF MS spectrometry. In the ESI-TOF mass spectrum, a peak was observed at  $m/z = 815.13$ , which corresponds to the ion  $\{[\mathbf{CP1}_2 \cdot (\text{Pd(en)})_2] (\text{NO}_3)_2\}^{2+}$  (**Figure 138**, page 203). The isotope pattern of this peak confirmed that it belonged to a doubly charged ion. Thus, the expected smallest possible dimetallic complex was the major product of the reaction. Other prominent peaks appeared at  $m/z$  ratios of 376.05, 587.21, and 669.17 that were assigned to  $[\mathbf{CP1} \cdot \text{Pd(en)}]^{2+}$ , protonated **CP1** and  $[\mathbf{CP1}_2 \cdot \text{Pd(en)}]^{2+}$ , respectively. The fragments containing only one metal centre could have been formed during ionization or the dilution of the sample prior to measuring the mass spectrum.

The  $^1\text{H}$  NMR spectrum of the obtained solution is depicted in **Figure 32**. The spectrum is similar to that of the free cyclopeptide which is, however, not soluble in the respective solvent mixture. Each set of chemically equivalent protons appears in this spectrum as one signal, indicating the formation of a symmetrical product.

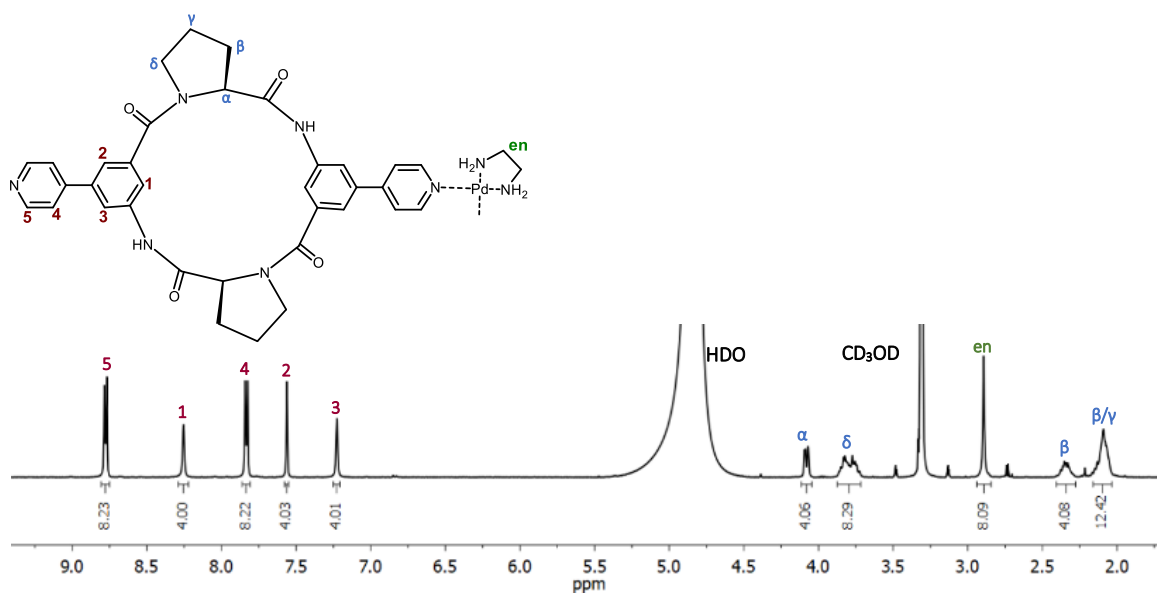


**Figure 32**  $^1\text{H}$  NMR spectrum in  $\text{D}_2\text{O}/\text{CD}_3\text{OD}$ , 1:1 (v/v) of the product resulting from the reaction between **CP1** and  $[\text{Pd}(\text{en})(\text{NO}_3)_2]$ .

Metal coordination is usually inferred from the deshielding of the pyridyl protons upon complex formation, but a reliable comparison of the  $^1\text{H}$  NMR spectra of **CP1** prior and after complex formation could not be made because of the insolubility of the cyclopeptide in the solvent mixture.

Successful complex formation could, however, be inferred from the presence of a crosspeak in the NOESY NMR spectrum between the proton signals of the  $\text{CH}_2$  groups in the ethylenediamine ligand (“en”) and the signals of the protons in 2-position of the ring nitrogen atoms (**Figure 33**). This crosspeak indicated that the ethylenediamine ligands and the pyridyl residues of **CP1** were in close proximity, confirming that Pd(II) was indeed coordinated as anticipated.

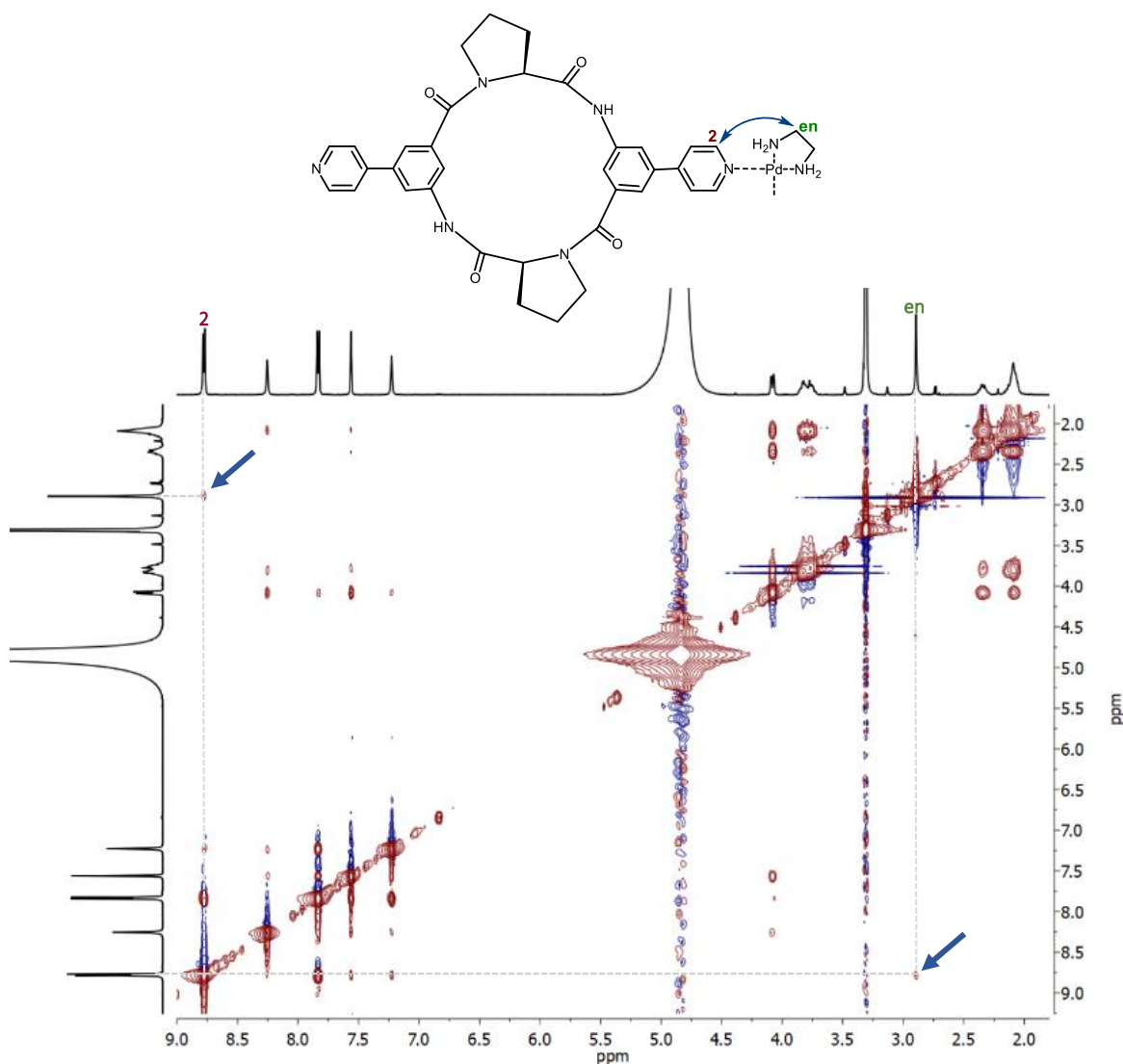


**Figure 33** NOESY NMR spectrum in  $D_2O/CD_3OD$ , 1:1 (v/v) of the product formed between **CP1** and  $[Pd(en)(NO_3)_2]$ . Crosspeaks between the signal of the ethylamine ligand “en” and of the one of the protons in 2- position of the pyridyl groups are highlighted with blue arrows.

Information about the structural integrity of the reaction product and its size was derived from DOSY NMR experiments. The cyclopeptide and ethylenediamine signals appeared as a single trace in the DOSY NMR spectrum, showing that the components of the complex diffuse at the same rate and that they therefore belong to the same compound (**Figure 34**). Also, the presence of only one trace of signals in the spectrum indicated that the complex was the only species in the equilibrium. The value derived from this spectrum for the diffusion coefficient ( $D = 1.103 \times 10^{-10} \text{ m}^2\text{s}^{-1}$ ) allowed estimating a hydrodynamic diameter of the product of 22.9 Å according to the Stokes-Einstein equation.

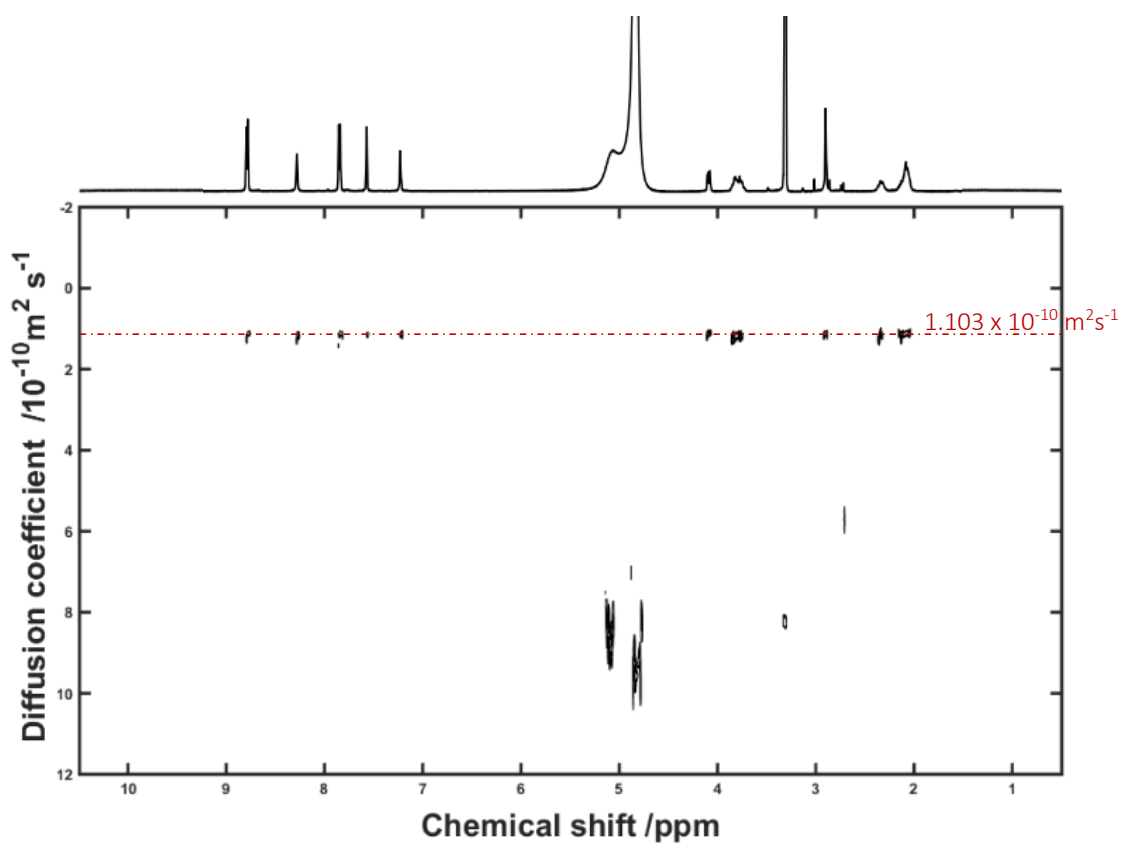


**Figure 34** DOSY NMR spectrum in  $\text{D}_2\text{O}/\text{CD}_3\text{OD}$  (1:1 v/v) of the product obtained in the reaction between **CP1** and  $[\text{Pd}(\text{en})(\text{NO}_3)_2]$ .

In combination, the experimental results suggest that reaction between **CP1** and  $[\text{Pd}(\text{en})(\text{NO}_3)_2]$  afforded the metallamacrocycle **CP1<sub>2</sub>Pd<sub>2</sub>** depicted in **Figure 35**.

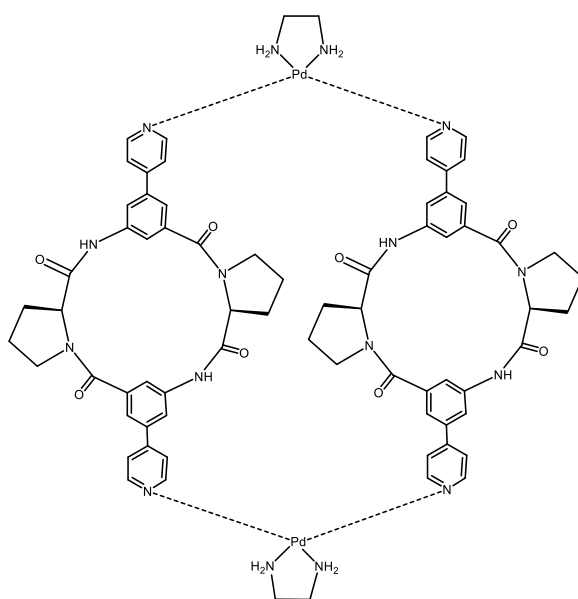


**Figure 35** Structure of the metallamacrocycle **CP1<sub>2</sub>Pd<sub>2</sub>**.



Attempts to crystallize  $\text{CP1}_2\text{Pd}_2$  were unsuccessful, only yielding crystals of free  $\text{CP1}$ , so that information about the structure of  $\text{CP1}_2\text{Pd}_2$  was obtained from semi-empirical calculations, which were based on the crystal structure of  $\text{CP1}$  (Figure 36).

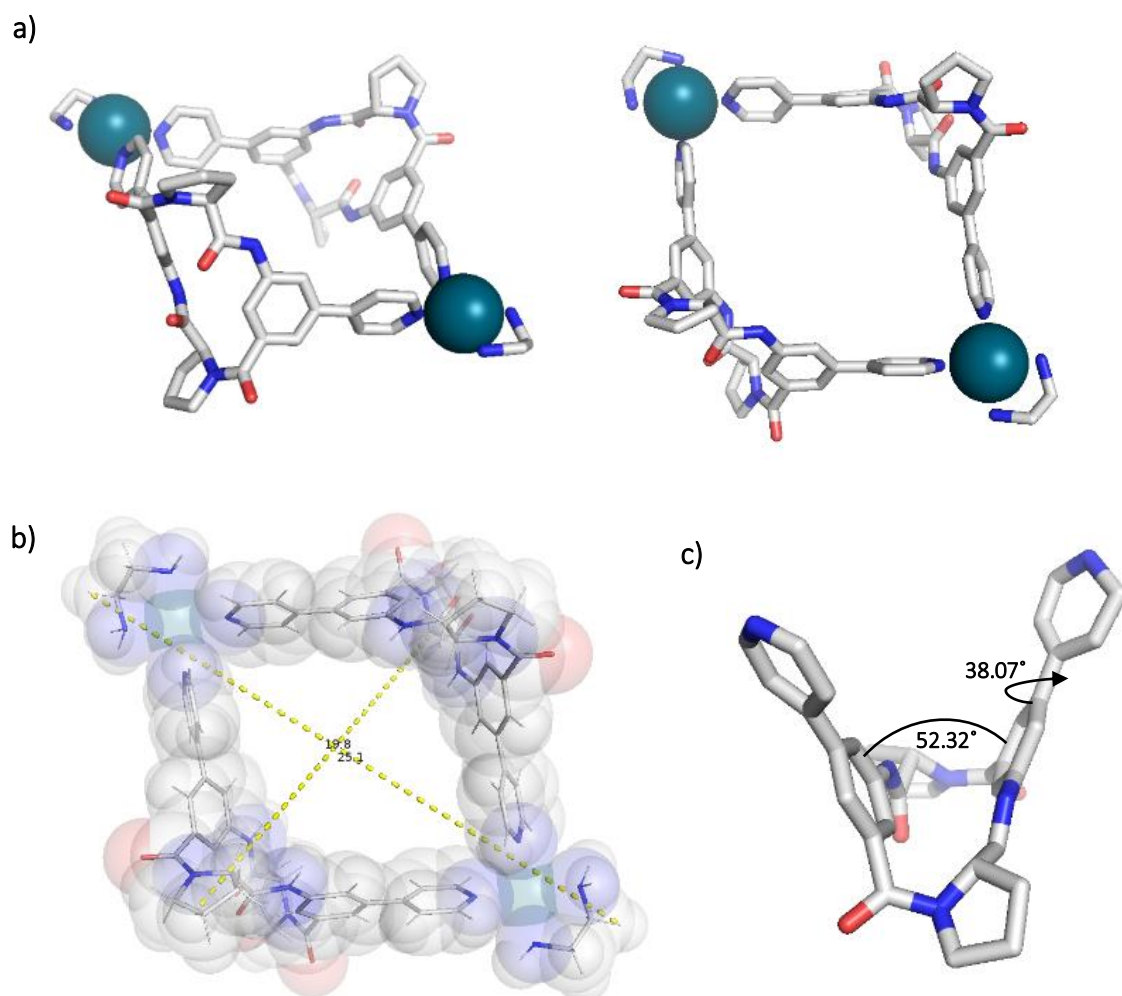


**Figure 36** a) Calculated structure of  $\text{CP1}_2\text{Pd}_2$ . The geometry optimization was performed at the semi-empirical PM6 level as implemented in Spartan 18, Wavefunction Inc. Hydrogen atoms are omitted for clarity. b) Estimated molecular dimensions of the calculated structure. From the marked distances of hydrogen atoms, an average diameter of 25.4 Å can be estimated when considering the van-der-Waals radii of hydrogen atoms (1.1 Å). c) Crystal structure of  $\text{CP1}\cdot 2\text{H}_2\text{O}\cdot \text{CH}_3\text{CN}$ . Solvent molecules and hydrogen atoms are omitted for clarity.

The calculated structure showed that  $\text{CP1}_2\text{Pd}_2$  is on average  $D_2$  symmetric, consistent with its simple  $^1\text{H}$  NMR spectrum. The angle between the aromatic subunits ( $83.83^\circ$ ) of the cyclopeptide in  $\text{CP1}_2\text{Pd}_2$  is larger than the  $52.32^\circ$  observed in the crystal structure of  $\text{CP1}$ , indicating that  $\text{CP1}$  was not optimally preorganized for palladium coordination. The strain in  $\text{CP1}_2\text{Pd}_2$  is likely small, however, since related cyclopeptides have been shown to adopt

conformations with varying arrangements of the aromatic subunits.<sup>115</sup> The peptide NH groups of the cyclotetrapeptide rings are facing toward the interior of the metallamacrocycle cavity, which suggests that **CP1<sub>2</sub>Pd<sub>2</sub>** may be suitable for anion binding.

An average diameter of 25.4 Å was calculated from this structure when considering the van-der-Waals radii of the hydrogen atoms (**Figure 36c**). This value was in reasonable agreement with the hydrodynamic radius estimated from DOSY NMR spectroscopy, considering the oblong shape of the complex and the fact that its structure was calculated in the gas phase. This result thus confirmed the assigned complex composition since larger complexes would have larger radii.

Based on these analytical results it can be concluded that the treatment of **CP1** with [Pd(en)(NO<sub>3</sub>)<sub>2</sub>] yielded the metallamacrocycle **CP1<sub>2</sub>Pd<sub>2</sub>**. It was subsequently tested if a coordination cage would also be accessible in a similar way by using the larger cyclohexapeptide **CP2**.

A similar approach to the one used for the synthesis of **CP1<sub>2</sub>Pd<sub>2</sub>** was employed to convert **CP2** into a metal complex. Experiments were executed to assess complex formation by again pursuing two routes (**Figure 43**). In the first one, **CP2** was reacted with the metal precursor to create a 2:3 complex and in the second one the formation of a 2:6:3 complex between **CP2**, the metal precursor and 4,4'-bipyridine (**20**) as spacer was investigated.

Reaction conditions analogous to the ones used for **CP1** were evaluated (different deuterated solvents, temperatures, with/without spacer) and the same metal precursors ([Pd(en)(NO<sub>3</sub>)<sub>2</sub>] (**15**), [Pd(NO<sub>3</sub>)<sub>2</sub>(2,2'-bipyr)] (**19**) and [Pt(en)(NO<sub>3</sub>)<sub>2</sub>] (**17**)) and spacer (4,4'-bipyridine (**20**)) were used. Again, the evolution of the reactions was followed by <sup>1</sup>H NMR spectroscopy after 1h, 5h, 12h, 24h, 72h, 5d, and 7d.

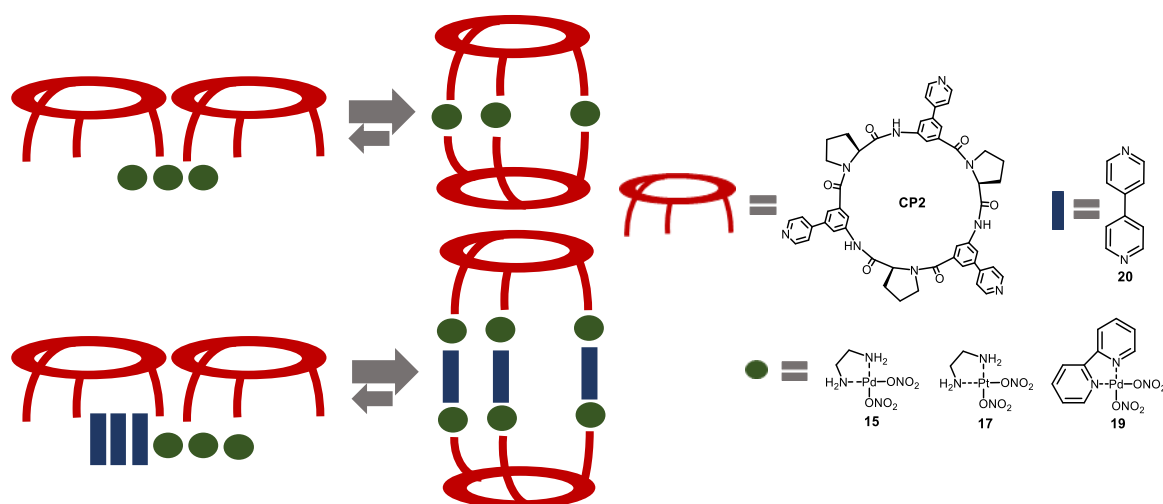


**Figure 37** Schematic representation of the potential structures resulting from **CP2** in the presence of square planar metal complexes and bis(monodentate) ligands.

Like **CP1**, **CP2** was insoluble in most of the solvents studied except for  $\text{DMF-}d_7$ , but metal interaction also promoted the dissolution. The results of the experiments were similar to the ones obtained for **CP1**, with the most promising ones resulting from the samples in which **CP2** reacted with  $[\text{Pd}(\text{en})(\text{NO}_3)_2]$  at  $25^\circ\text{C}$  to create a 2:3 complex.

Information about the self-assembly was again derived from  $^1\text{H}$  NMR spectroscopy and ESI-TOF MS spectrometry. Complex formation was mainly studied in  $\text{D}_2\text{O}/\text{CD}_3\text{CN}$  since reactions took considerably longer when they were performed in  $\text{DMF-}d_7$  or  $\text{D}_2\text{O}/\text{CD}_3\text{OD}$ .

The most favourable conditions for cage formation were achieved by adding 1.5 equivalents of  $[\text{Pd}(\text{en})(\text{NO}_3)_2]$  in  $\text{D}_2\text{O}/\text{CD}_3\text{CN}$ , 1:1 (v/v) to solid **CP2** at  $25^\circ\text{C}$ . The solution was stirred until it was clear to achieve a final concentration of a potential 2:3 complex of 1 mM. This complex was characterized in the same solution in which it was prepared.

Peaks at  $m/z = 376.9$  and  $464.3$  were observed in the ESI-TOF mass spectrum (**Figure 143**, page 206), corresponding to the ions  $\{[\text{CP2}_2 \cdot (\text{Pd}(\text{en}))_3]\}^{6+}$  and  $\{[\text{CP2}_2 \cdot (\text{Pd}(\text{en}))_3] (\text{NO}_3)\}^{5+}$ , respectively, thus confirming the presence of expected 3:2 complex in solution.

The  $^1\text{H}$  NMR spectrum of the product is depicted in **Figure 38**. The high symmetry of the product was again evidenced by the simplicity of the  $^1\text{H}$  NMR spectrum.

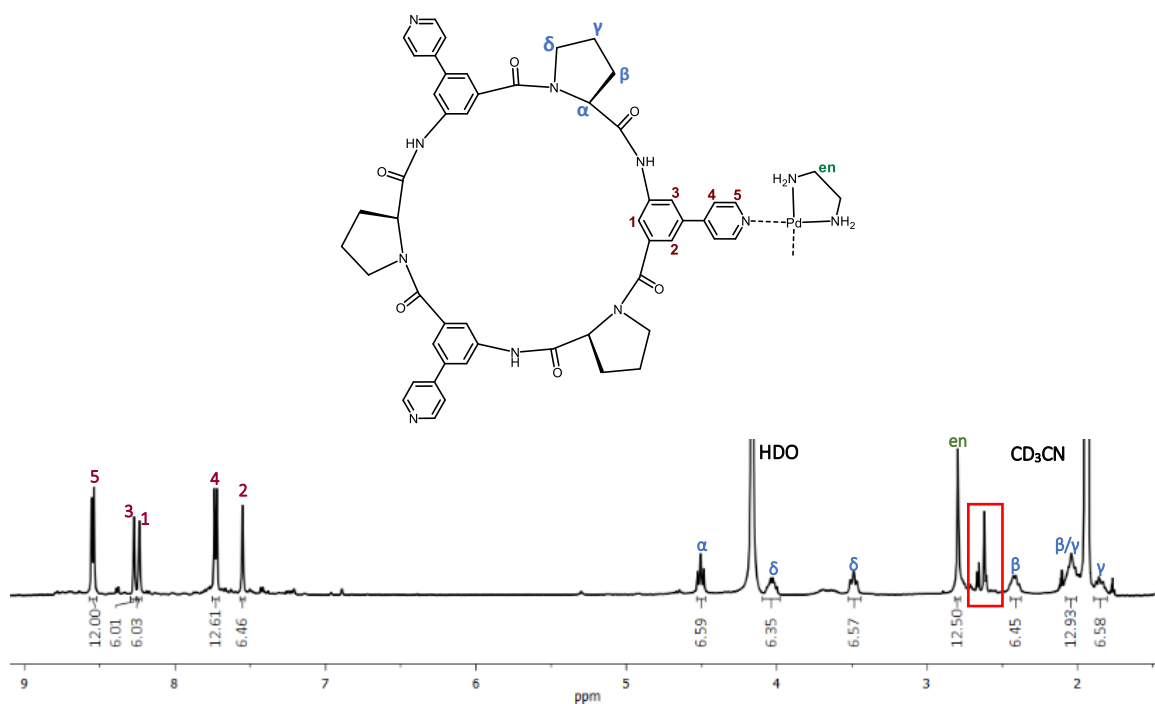


**Figure 38**  $^1\text{H}$  NMR spectrum in  $\text{D}_2\text{O}/\text{CD}_3\text{CN}, 1:1$  (v/v) of the cage product resulting from the treatment of **CP2** with  $[\text{Pd}(\text{en})(\text{NO}_3)_2]$ . The peaks highlighted with a red rectangle in the spectrum were due to an impurity from  $\text{CD}_3\text{CN}$  that was present in all available batches of this solvent during the course of this work.

Again, a comparison of the  $^1\text{H}$  NMR spectra of **CP2** prior and after complex formation could not be made but the presence of a crosspeak between the proton signals of the ethylenediamine (“en”) and the ones in the 2-positions of the pyridyl groups in the NOESY NMR spectrum suggested complex formation also in this case (**Figure 39**).

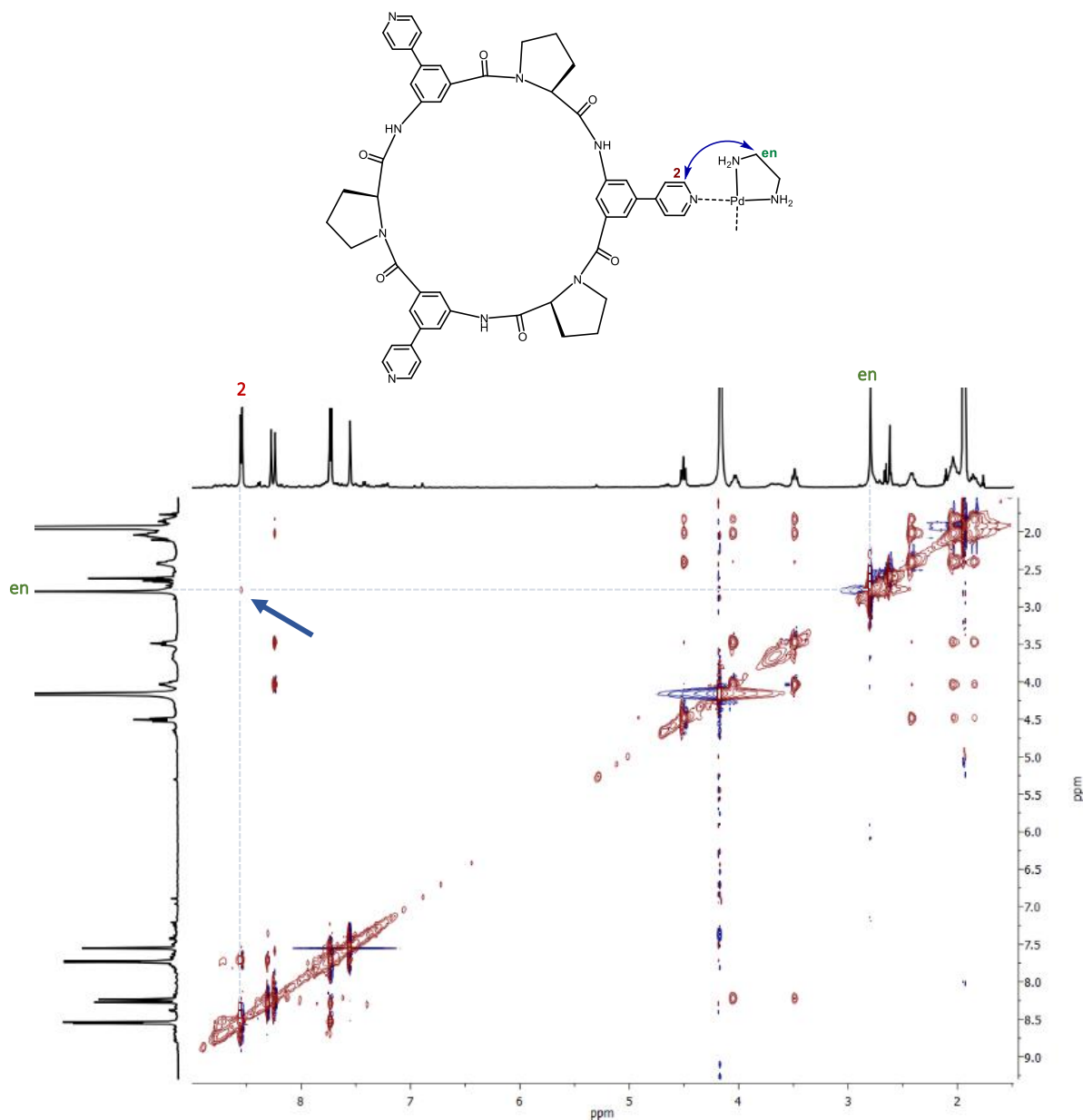


**Figure 39** NOESY NMR spectrum in  $D_2O/CD_3OD$ , 1:1 (v/v) of the product formed between **CP2** and  $[Pd(en)(NO_3)_2]$ . The crosspeak between the signal of the ethylenediamine ligand “en” and of the one of the protons in 2-position of the pyridyl groups is highlighted with a blue arrow.

Confirmation that complex formation indeed occurred and that only one species was present in solution was obtained from the DOSY NMR spectrum. Only a single trace appeared for the cyclopeptide and ethylenediamine signals, which means that both components diffused at the same rate and therefore belonged to the same compound (**Figure 40**). A hydrodynamic diameter of 23.4 Å for the complex was estimated from the obtained diffusion coefficient ( $D = 2.300 \times 10^{-10} \text{ m}^2\text{s}^{-1}$ ).

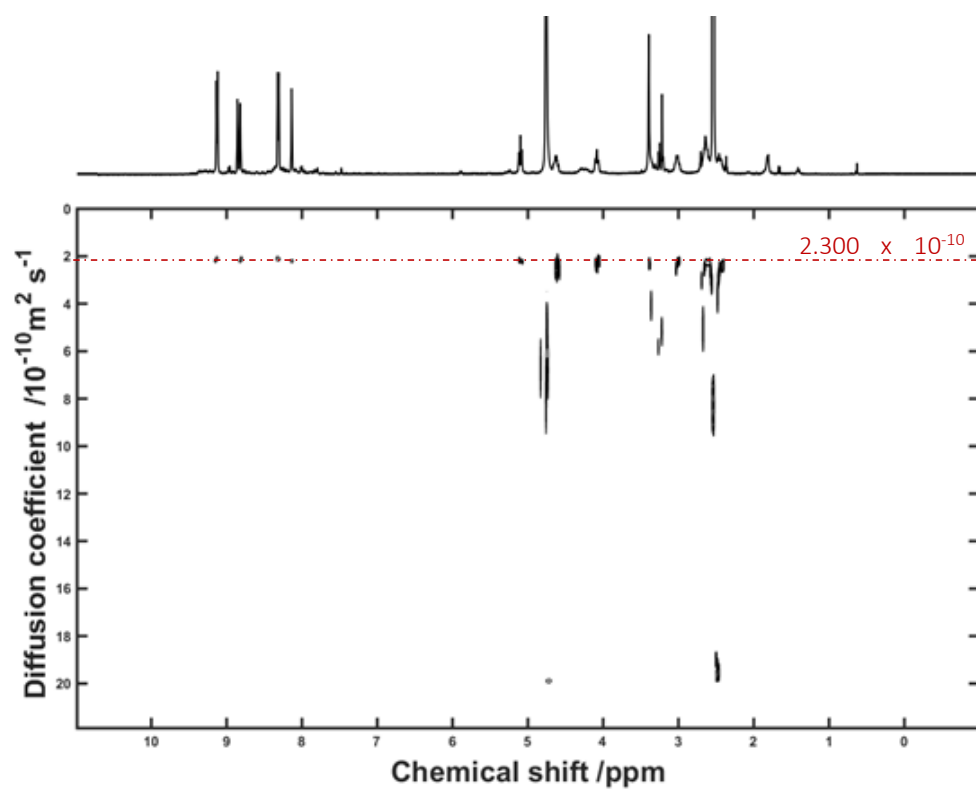


**Figure 40** DOSY NMR spectrum in  $D_2O/CD_3OD$  (1:1 v/v) of the product obtained in the reaction between **CP2** and  $[Pd(en)(NO_3)_2]$ .

The aforementioned experimental results indicated that the cage **CP2<sub>2</sub>Pd<sub>3</sub>** depicted in **Figure 41** was most likely the final product of the reaction between **CP2** and  $[Pd(en)(NO_3)_2]$ .

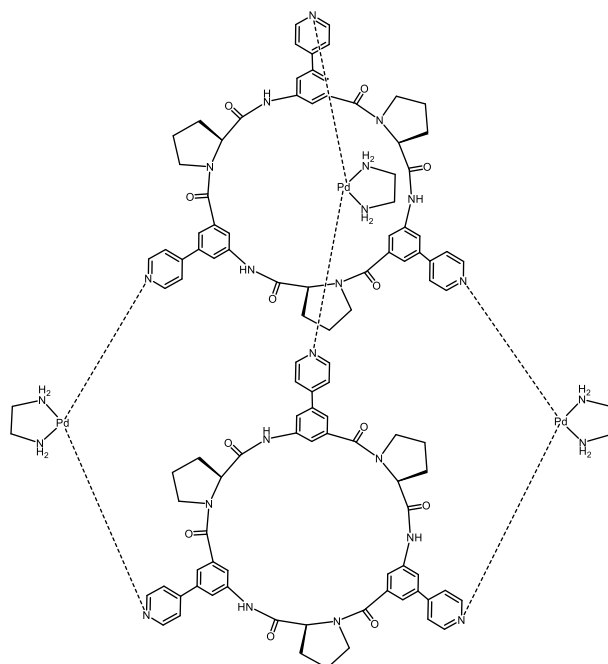


**Figure 41** Structure of the metallacage **CP2<sub>2</sub>Pd<sub>3</sub>**.

Crystallization attempts of both  $\text{CP2}_2\text{Pd}_3$  and  $\text{CP2}$  were unsuccessful. So, information about the cage's structure was derived from semi-empirical calculations (**Figure 42**) based on the previously modelled structure of  $\text{CP2}$ . The calculated structure of  $\text{CP2}_2\text{Pd}_3$  had  $D_3$  symmetry, consistent with the simple  $^1\text{H}$  NMR spectrum. The mean angles of the aromatic subunits in the cage amounted to only  $57.90^\circ$  as opposed to the  $83.02^\circ$  found in the calculated structure of the free cyclopeptide  $\text{CP2}$  (**Figure 42c**). The pyridine subunits are also less tilted in the complex. From this structure, an average diameter of  $25.1 \text{ \AA}$  was estimated which was in accordance with the experimental result obtained from the DOSY NMR experiment ( $23.4 \text{ \AA}$ ), confirming the complex composition. Contrarily to the cyclotetrapeptide in  $\text{CP1}_2\text{Pd}_2$ , the oxygen atoms of the cyclohexapeptide rings were oriented towards the cavity of the cage in the calculated structure, suggesting that  $\text{CP2}_2\text{Pd}_3$  could potentially interact with cationic guests.

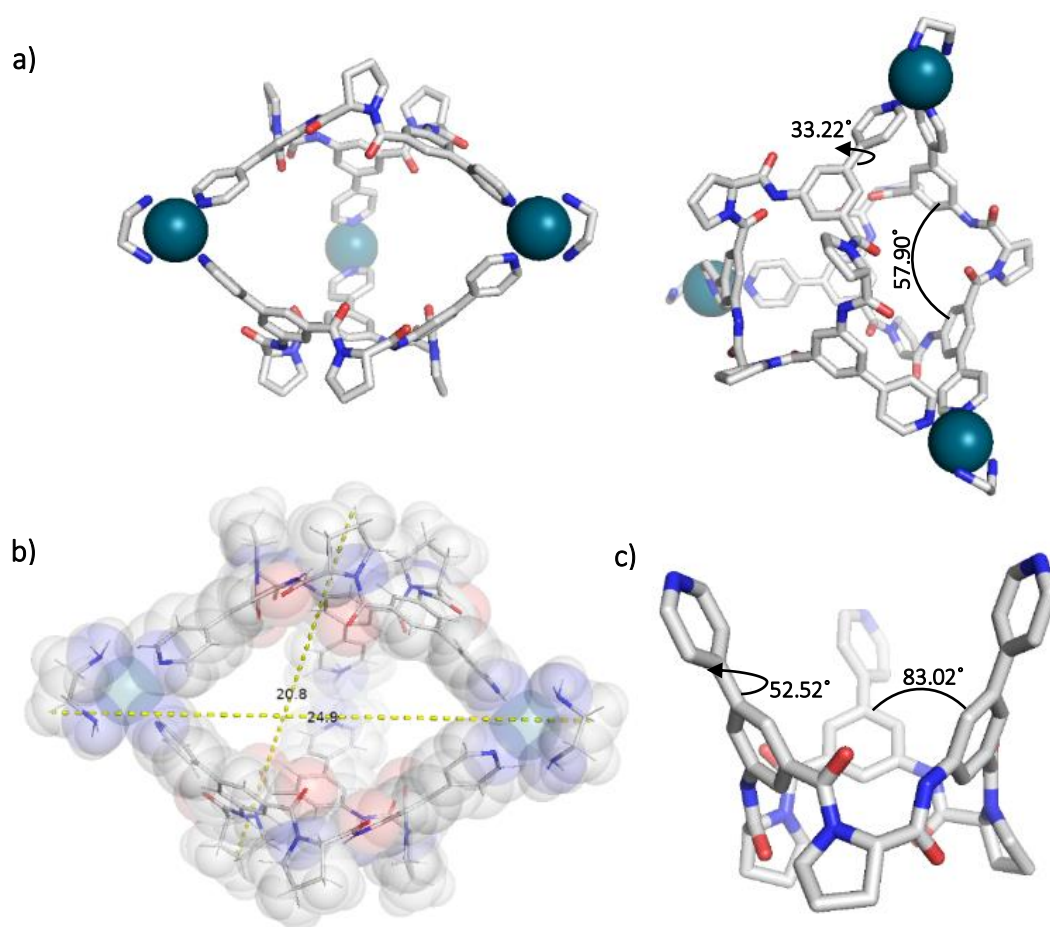


**Figure 42** a) Calculated structure of  $\text{CP2}_2\text{Pd}_3$ . The geometry optimization was performed at the semi-empirical PM6 level as implemented in Spartan 18, Wavefunction Inc. Hydrogen atoms are omitted for clarity. b) Estimated molecular dimensions of the calculated structure. From the marked distances of hydrogen atoms, an average diameter of  $25.1 \text{ \AA}$  was estimated when considering the van-der-Waals radii of hydrogen atoms ( $1.1 \text{ \AA}$ ). c) Calculated structure of  $\text{CP2}$ .

**CP1<sub>2</sub>Pd<sub>2</sub>** and **CP2<sub>2</sub>Pd<sub>3</sub>** were similar in size even though a larger cyclopeptide was used in the latter case. To access a larger metallocsupramolecular structure, the use of tetravalent Pd(II) ions was subsequently tested. To this end, **CP1** was reacted with [Pd(CH<sub>3</sub>CN)<sub>4</sub>](BF<sub>4</sub>)<sub>2</sub> in a 2:1 ratio.

As stated previously, the composition of such coordination complexes is dependent on the ligand's bend angle and can be predicted by assuming that the smallest assembly respecting the maximum occupancy rule is the most likely product. For bend angles lower than 90°, complexes with three to five metal centres should be favoured.

Considering that the angle between the aromatic subunits of **CP1** is 52.32° (< 90°), one would therefore expect **CP1<sub>6</sub>Pd<sub>3</sub>** as the smallest structure possible in which six **CP1** ligands coordinate three Pd(II) centres (**Figure 43**). **CP1<sub>8</sub>Pd<sub>4</sub>** or **CP1<sub>10</sub>Pd<sub>5</sub>** could also be possible or even larger complexes respecting a **CP1<sub>2n</sub>Pd<sub>n</sub>** ratio since the angle between the aromatic subunits in **CP1** is rather variable.<sup>84,85,116,117</sup>

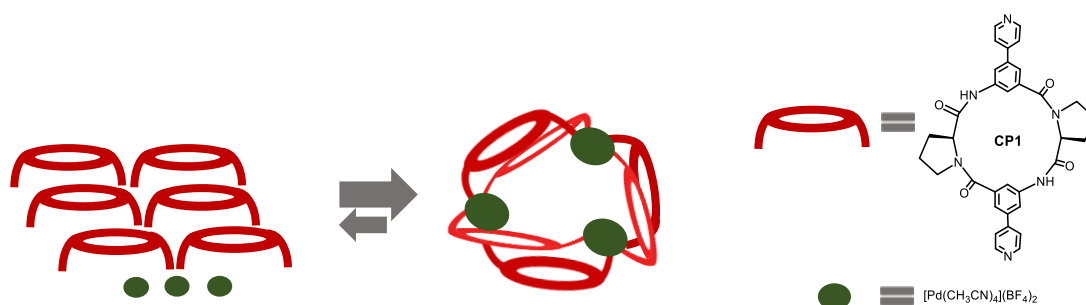


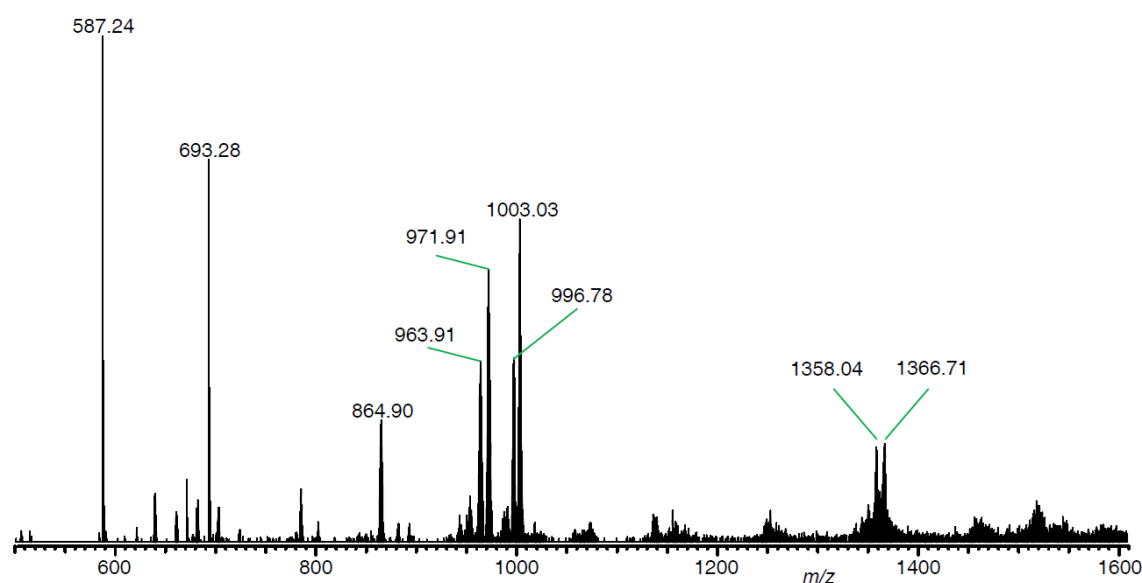
**Figure 43** Schematic representation of the approach to obtain a cage by reacting **CP1** with [Pd(CH<sub>3</sub>CN)<sub>4</sub>](BF<sub>4</sub>)<sub>2</sub> in a 2:1 ratio.

The reaction between **CP1** and the palladium(II) salt was performed for 4 h at 60 °C in DMSO-*d*<sub>6</sub>. Other solvents and temperatures were also tested, but the cyclopeptide never dissolved under these conditions. The complex was prepared on the NMR scale and characterized in solution without isolation.

Prominent peaks were visible at *m/z* ratios of 996.78, 1003.03, 1358.04 and 1366.40 in the ESI mass spectrum (**Figure 44**) of the reaction mixture that indicate the formation of a



product with the composition **CP1<sub>6</sub>Pd<sub>3</sub>**. Trace amounts of the **CP1<sub>4</sub>Pd<sub>2</sub>** complex could also be detected ( $m/z$  864.90).



		$m/z$ calcd.	$m/z$ exp.
$[\text{CP1}+\text{H}]^+$	$\text{C}_{34}\text{H}_{30}\text{N}_6\text{O}_4 + \text{H}^+$	587.24	587.24
$[\text{CP1}_4\text{Pd}_2+\text{Cl}]^{3+}$	$\{[\text{Pd}_2(\text{C}_{34}\text{H}_{30}\text{N}_6\text{O}_4)_4]\text{Cl}\}^{3+}$	864.90	864.90
$[\text{CP1}_6\text{Pd}_3+\text{BF}_4+\text{NO}_3]^{4+}$	$\{[\text{Pd}_3(\text{C}_{34}\text{H}_{30}\text{N}_6\text{O}_4)_6](\text{BF}_4)(\text{NO}_3)\}^{4+}$	996.78	996.78
$[\text{CP1}_6\text{Pd}_3+2\text{BF}_4]^{4+}$	$\{[\text{Pd}_3(\text{C}_{34}\text{H}_{30}\text{N}_6\text{O}_4)_6](\text{BF}_4)_2\}^{4+}$	1003.03	1003.03
$[\text{CP1}_6\text{Pd}_3+2\text{BF}_4+\text{NO}_3]^{3+}$	$\{[\text{Pd}_3(\text{C}_{34}\text{H}_{30}\text{N}_6\text{O}_4)_6](\text{BF}_4)_2(\text{NO}_3)\}^{3+}$	1358.04	1358.04
$[\text{CP1}_6\text{Pd}_3+3\text{BF}_4]^{3+}$	$\{[\text{Pd}_3(\text{C}_{34}\text{H}_{30}\text{N}_6\text{O}_4)_6](\text{BF}_4)_3\}^{3+}$	1366.38	1366.38

**Figure 44** ESI-TOF MS spectrum (positive mode) of the reaction mixture containing **CP1** and  $[\text{Pd}(\text{CH}_3\text{CN})_4](\text{BF}_4)_2$  in a 2:1 ratio.

The  $^1\text{H}$  NMR spectrum of the solution was clearly different from the spectrum of free **CP1** in the same solvent, suggesting that metal coordination had taken place (**Figure 45**). Upfield shifts of the signals in the aromatic region of the spectrum were, for example, clear indication that the pyridyl units of **CP1** engaged in interactions with the metal. The complexity of the resulting spectrum suggested the presence of a mixture of species, with a prominent product exhibiting a set of characteristic peaks.

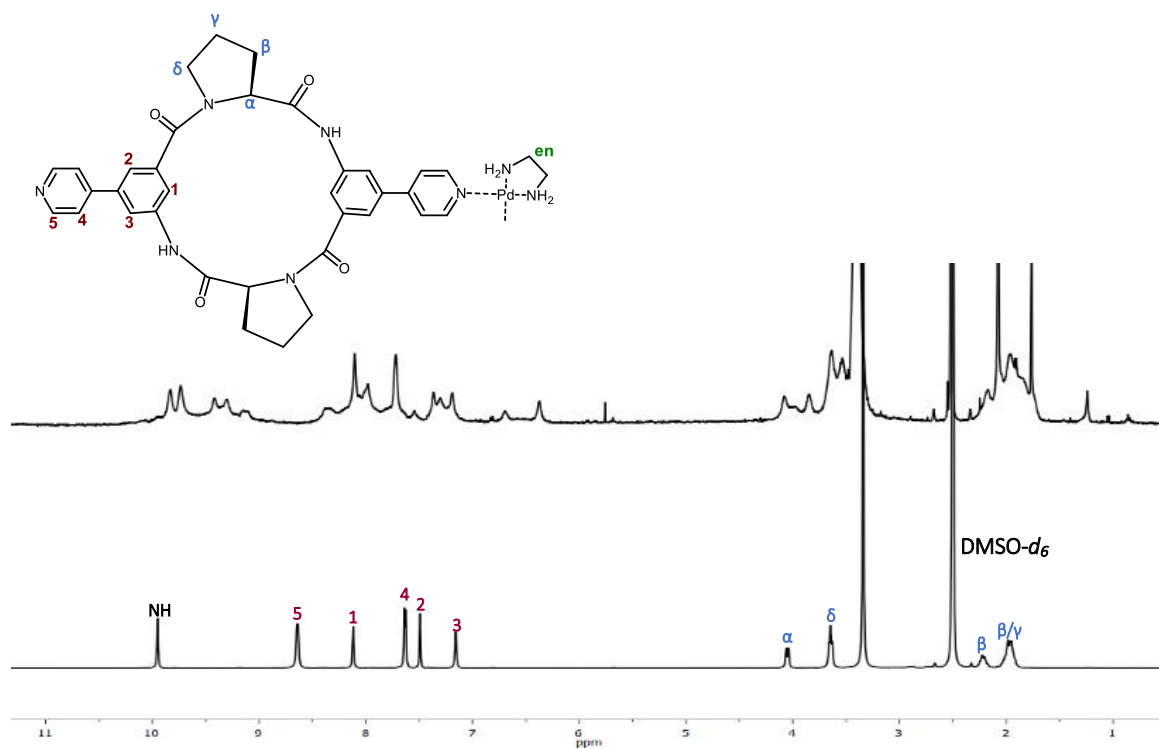


**Figure 45** Top: <sup>1</sup>H NMR spectrum of the reaction solution of **CP1** and [Pd(CH<sub>3</sub>CN)<sub>4</sub>](BF<sub>4</sub>)<sub>2</sub> in a 2:1 ratio in DMSO-d<sub>6</sub>. Bottom: <sup>1</sup>H NMR spectrum of a solution of **CP1** in DMSO-d<sub>6</sub>. The NH signal in the spectrum of **CP1** at 9.55 ppm was not visible in the spectrum of the cage because of H/D exchange.

Satisfactory <sup>13</sup>C NMR and 2D NMR spectra could not be obtained from the reaction solution, preventing the peak assignment, but DOSY NMR spectroscopy confirmed that the major peaks in the spectrum indeed belonged to a single species with a diffusion coefficient *D* of  $0.733 \times 10^{-10} \text{ m}^2\text{s}^{-1}$ , corresponding to a hydrodynamic diameter of 27.2 Å (**Figure 46**).

The results obtained were strong evidence that the expected cage **CP1<sub>6</sub>Pd<sub>3</sub>** was the main product obtained.

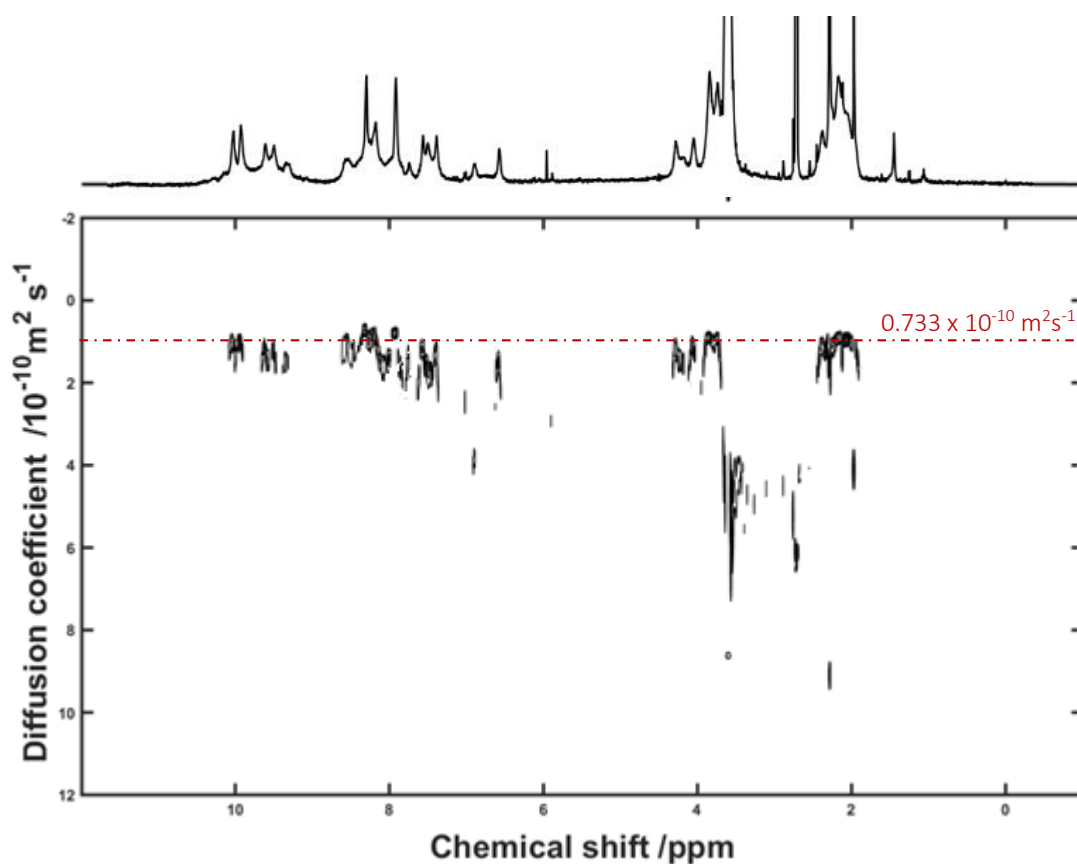


**Figure 46** DOSY NMR spectrum of the reaction mixture containing **CP1** and  $[Pd(CH_3CN)_4](BF_4)_2$  in a 2:1 ratio in  $DMSO-d_6$ .

Unfortunately, crystallization attempts failed, but structural information about **CP1<sub>6</sub>Pd<sub>3</sub>** was obtained by semi-empirical calculations based on the crystal structure of **CP1** (Figure 47). The calculated structure showed that the complex displays a  $D_3$  symmetric structure in which each Pd(II) centre connects four equivalent subunits of **CP1**. Even though all six **CP1** molecules are thus equivalent, the symmetry within each ring is lost, explaining the complex signal pattern observed in the  $^1H$  NMR spectrum. The average diameter of **CP1<sub>6</sub>Pd<sub>3</sub>** was estimated to amount to 28.8 Å, which was in good agreement with the one obtained from the DOSY NMR experiments, confirming the expected composition of the cage. The angles between the aromatic subunits of the cyclopeptide also required some adjustment for palladium coordination to occur but, as expected for this structure, their values were smaller than 90°.

The results thus indicated that the treatment of **CP1** with  $[\text{Pd}(\text{CH}_3\text{CN})_4](\text{BF}_4)_2$  generated a coordination cage with the composition **CP1<sub>6</sub>Pd<sub>3</sub>**, potentially with the smaller complex **CP1<sub>4</sub>Pd<sub>2</sub>** as a side product.

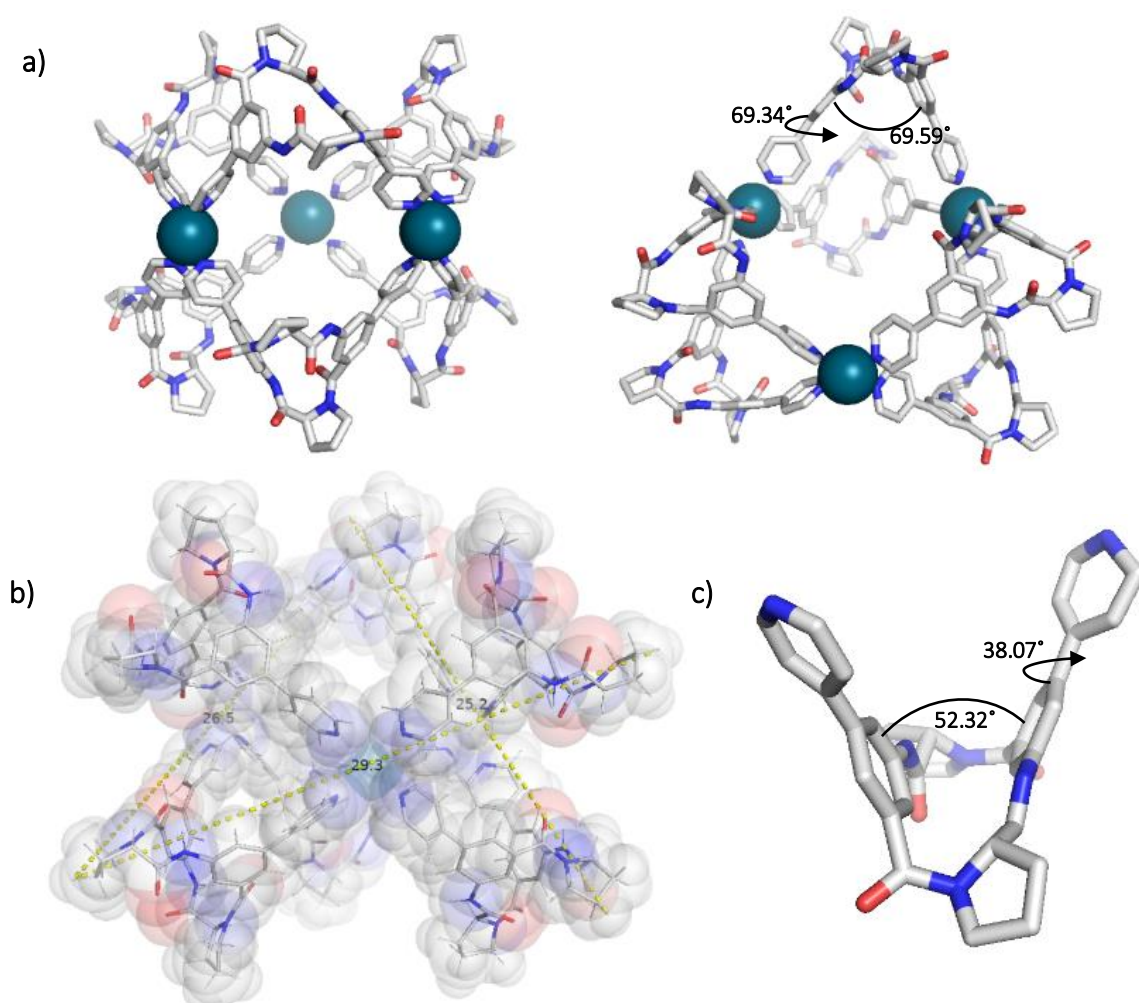


**Figure 47** a) Calculated structure of **CP1<sub>6</sub>Pd<sub>3</sub>**. The geometry optimization was performed at the semi-empirical PM6 level as implemented in Spartan 18, Wavefunction Inc. Hydrogen atoms are omitted for clarity. b) Estimated molecular dimensions of the calculated structure. From the marked distances of hydrogen atoms, an average diameter of 28.8 Å was estimated when considering the van-der-Waals radii of hydrogen atoms (1.1 Å). c) Crystal structure of **CP1·2H<sub>2</sub>O·CH<sub>3</sub>CN**. Solvent molecules and hydrogen atoms are omitted for clarity.

### 1.3.3 Binding Studies with Cyclopeptide Derived Metal Assemblies

Investigations were subsequently performed to evaluate whether the cavities of the prepared coordination compounds would be available for guest binding. The focus was in this context to use dicarboxylates as guest molecules since they had previously been shown to interact with some of Fujita's coordination compounds.<sup>118</sup>

**CP1<sub>2</sub>Pd<sub>2</sub>** was selected as host since the macrocyclic structure of this metal compound suggested that it could be especially suitable for anion binding. The structure of the terephthalate complex of **CP1<sub>2</sub>Pd<sub>2</sub>** was calculated to gain insight into possible binding modes and the size fit of this guest in the cavity of the metallamacrocycle (**Figure 48**).

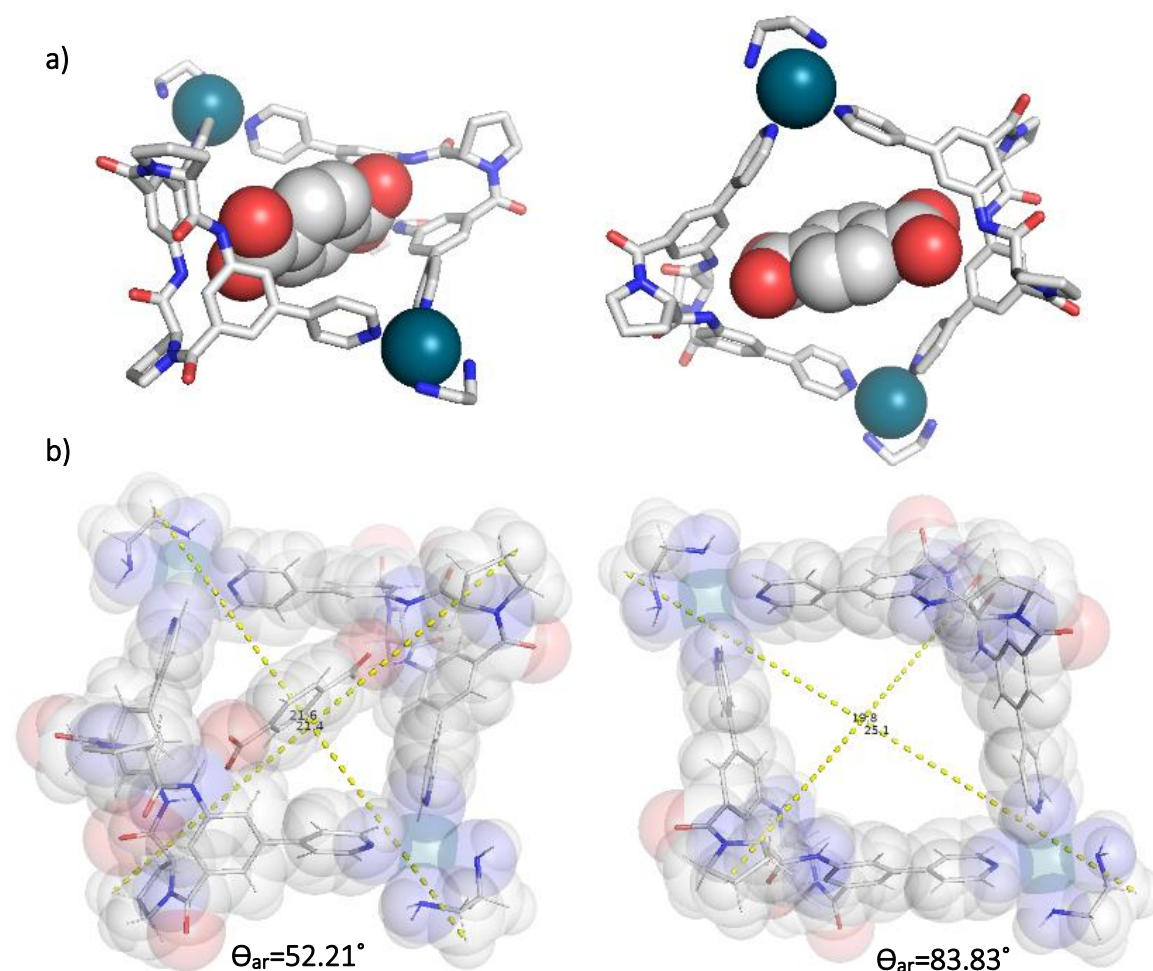


**Figure 48** a) Calculated structure of the terephthalate complex of **CP1<sub>2</sub>Pd<sub>2</sub>**. The geometry optimization was performed at the semi-empirical PM6 level as implemented in Spartan 18, Wavefunction Inc. Hydrogen atoms are omitted for clarity. b) Estimated molecular dimensions of the calculated structure (left) and **CP1<sub>2</sub>Pd<sub>2</sub>** (right). From the marked distances of hydrogen atoms, an average diameter of 23.8 Å was estimated for the complex when considering the van-der-Waals radii of hydrogen atoms (1.1 Å).

According to the modelled structure (**Figure 48**), **CP1<sub>2</sub>Pd<sub>2</sub>** should be able to incorporate terephthalate into its cavity, which could afford a complex in which the negatively charged carboxylate groups from the guest interact with the amide NH groups of the cyclopeptide rings.

An average diameter of 23.8 Å was estimated for this complex, which was smaller than the diameter of the free metallamacrocycle (25.4 Å). Also, the angle between the aromatic subunits of **CP1** was smaller in the calculated structure of the complex (52.21°) than for **CP1<sub>2</sub>Pd<sub>2</sub>** (83.83°). The distances between hydrogen atoms of the two ethylenediamine ligands (21.6 vs 25.1) and of the proline groups of the two **CP1** subunits (21.4 vs 19.8) also differed in the structures obtained for the complex and the free metallamacrocycle.

Since the calculations suggested that anion recognition was indeed possible, qualitative binding studies were performed by comparing the <sup>1</sup>H NMR spectra of various sodium dicarboxylates in D<sub>2</sub>O/CD<sub>3</sub>OD, 1:1 (v/v) in the absence and the presence of 1 equivalent of **CP1<sub>2</sub>Pd<sub>2</sub>** (**Figure 49**). The dicarboxylates were obtained by reacting the corresponding carboxylic acids (terephthalic acid, isophthalic acid, diphenic acid, 2,6-naphthalene dicarboxylic acid, adipic acid, and glutaric acid) with an equimolar amount of Na<sub>2</sub>CO<sub>3</sub>.

The pronounced upfield shifts of the signals of the chosen guests in the <sup>1</sup>H-NMR spectra induced by the presence of **CP1<sub>2</sub>Pd<sub>2</sub>** indicated that an interaction took place (**Figure 49**). The direction of the shifts suggested the incorporation of the dicarboxylates into the **CP1<sub>2</sub>Pd<sub>2</sub>** cavity where they experienced the shielding of the surrounding aromatic rings.

Since only a single set of averaged signals was observed for host and guest, complex formation was fast on the NMR time-scale. Based on this qualitative evidence for complex formation, quantitative binding studies were subsequently performed. These experiments required the use of buffers in order to maintain a constant basic pH throughout the NMR titration and promote deprotonation of the dicarboxylic acids. Carbonate/bicarbonate and borate buffers were considered to ensure a pH of ca. 9.

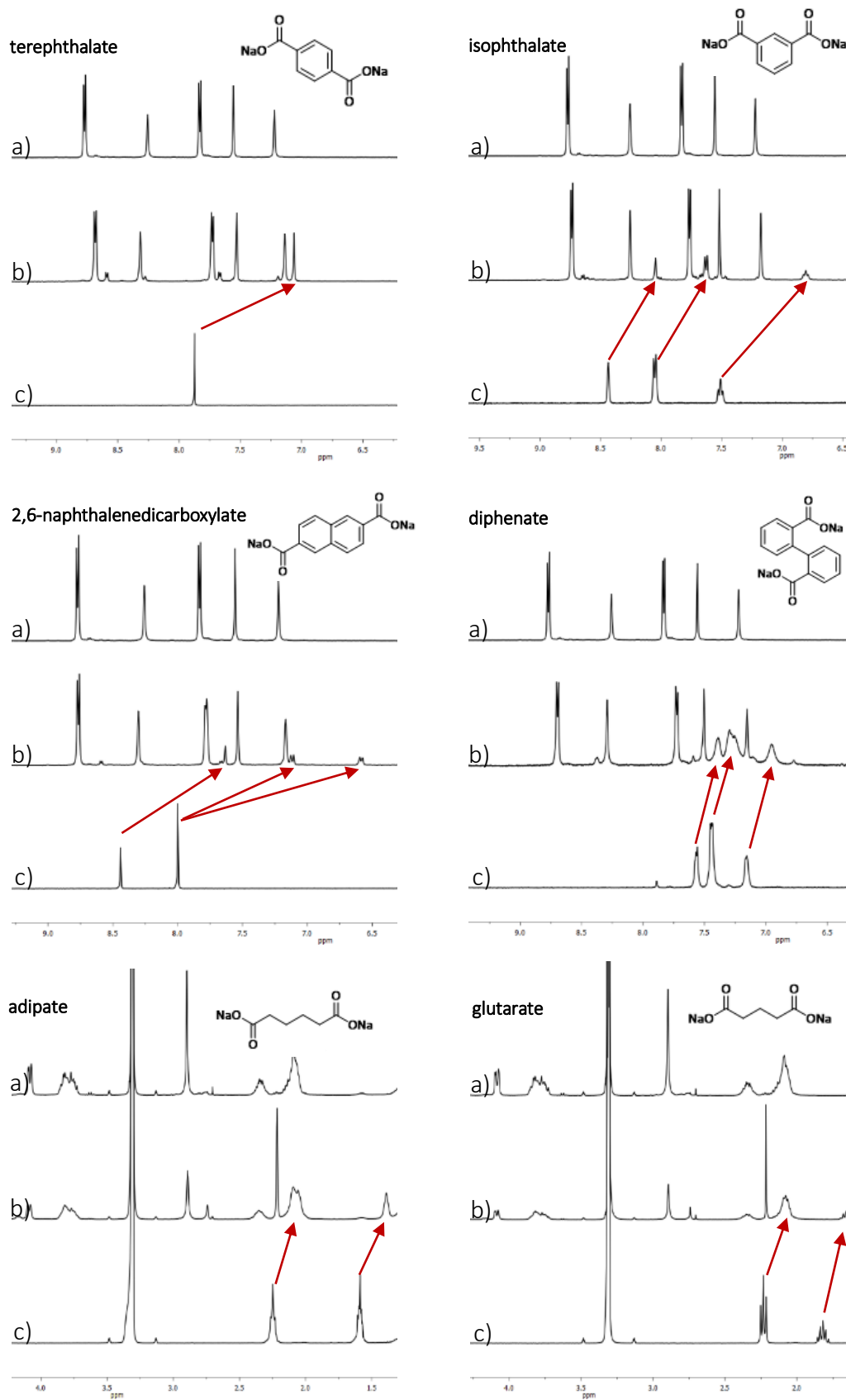


**Figure 49**  $^1\text{H}$  NMR spectra of  $\text{CP1}_2\text{Pd}_2$  (0.5 mM) (a), of a dicarboxylic acid (0.5 mM) (c), and of equimolar mixtures of  $\text{CP1}_2\text{Pd}_2$  and a dicarboxylic acid (each 0.5 mM) (b) in a solution of  $\text{Na}_2\text{CO}_3$  (0.5 mM) in  $\text{CD}_3\text{OD}/\text{D}_2\text{O}$ , 1:1 (v/v).

To assess whether **CP1<sub>2</sub>Pd<sub>2</sub>** was stable under these conditions, the <sup>1</sup>H-NMR spectrum of a **CP1<sub>2</sub>Pd<sub>2</sub>** solution (0.5 mM) in CD<sub>3</sub>OD/D<sub>2</sub>O, 1:1 (v/v) was compared with the spectra of the solutions of the metallamacrocycle (0.5 mM) in buffered media (pD = 9.8).

**Figure 50** shows that the buffers had a detrimental effect on the structural integrity of **CP1<sub>2</sub>Pd<sub>2</sub>**. When using borate buffer (blue spectrum), the signals in the <sup>1</sup>H-NMR spectrum of the metallamacrocycle split and over time became less defined. These spectral changes were accompanied by precipitate formation, indicating that this buffer caused decomposition of the metallamacrocycle.

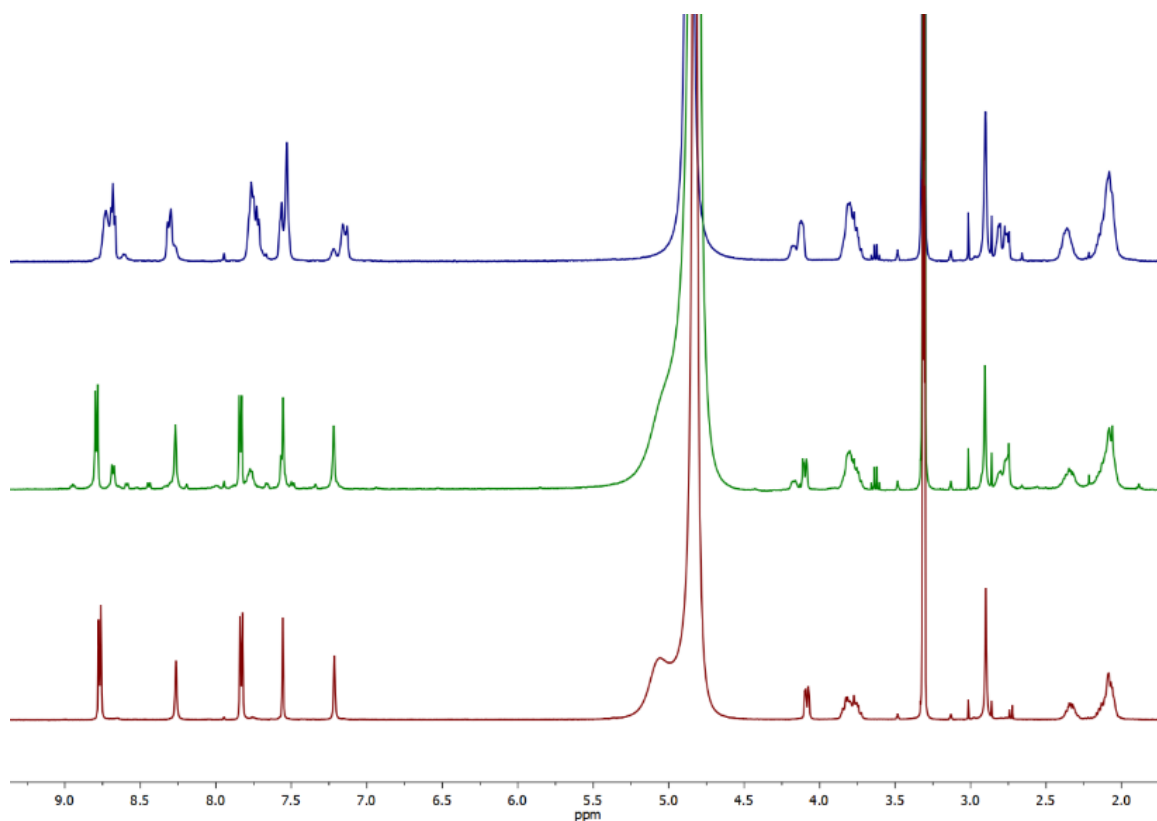


**Figure 50** <sup>1</sup>H NMR spectra of **CP1<sub>2</sub>Pd<sub>2</sub>** (0.5 mM) (red), of **CP1<sub>2</sub>Pd<sub>2</sub>** (0.5 mM) in carbonate/bicarbonate buffer solution ( $C_{Na} = 0.01$  M) (green) and of **CP1<sub>2</sub>Pd<sub>2</sub>** (0.5 mM) in borate buffer solution ( $C_{Na} = 0.01$  M) (blue) in CD<sub>3</sub>OD/D<sub>2</sub>O, 1:1 (v/v).

The proton NMR spectrum of the carbonate/bicarbonate buffered solution of **CP1<sub>2</sub>Pd<sub>2</sub>** (green in **Figure 50**) contained additional signals that were not present in the spectrum of the metallamacrocycle (red) in the absence of buffer, also suggesting a potential interaction of the buffer components and **CP1<sub>2</sub>Pd<sub>2</sub>**.



Since no changes were observed in this spectrum over time and no precipitate appeared, experiments were performed to test if the stability of the dicarboxylate complexes of **CP1<sub>2</sub>Pd<sub>2</sub>** could be quantified in this buffer.

To that end, NMR samples in D<sub>2</sub>O/CD<sub>3</sub>OD (1:1, v/v) were prepared by adding increasing amounts of a terephthalate solution corresponding to 0.5, 1, 1.5 and 2 equivalents to a **CP1<sub>2</sub>Pd<sub>2</sub>** solution (0.5 mM) in a carbonate/bicarbonate buffered medium (C<sub>Na</sub> = 0.01 M) (**Figure 51**).

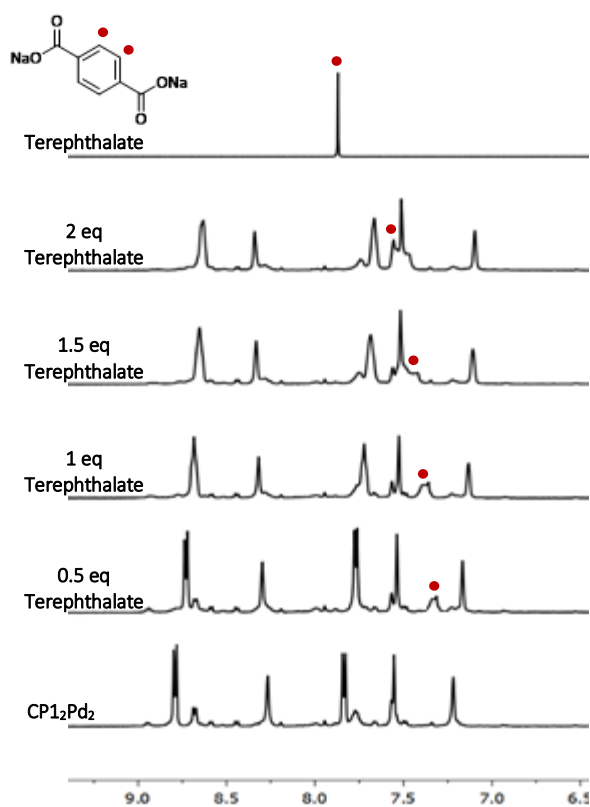
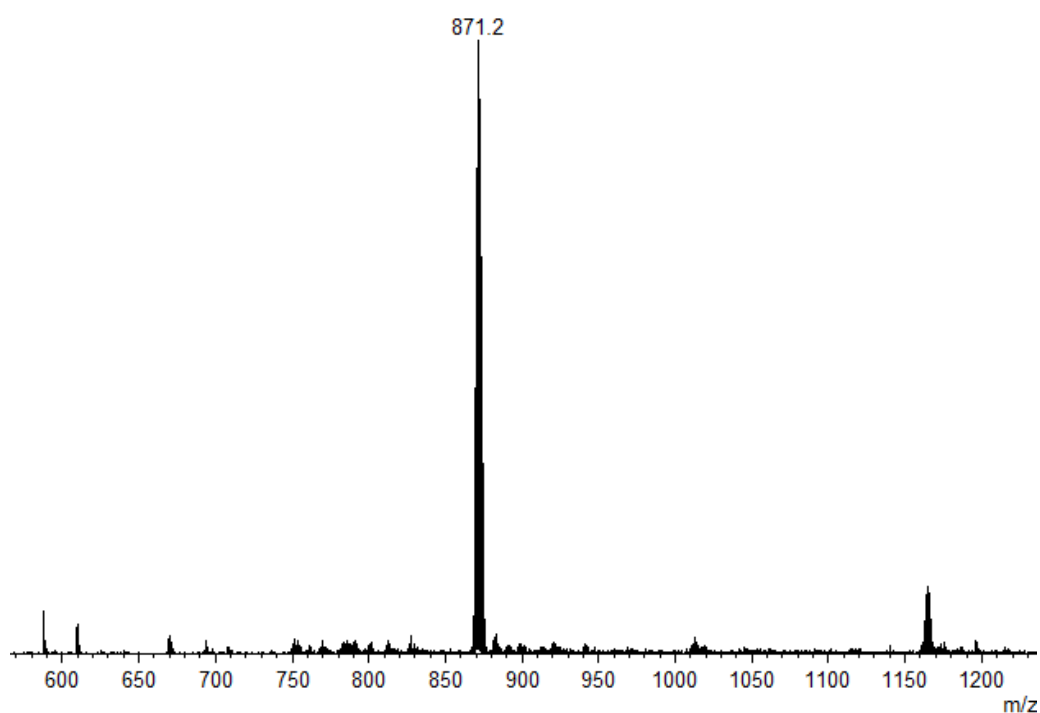


**Figure 51** <sup>1</sup>H NMR spectra of the carbonate/bicarbonate buffered solution (C<sub>Na</sub> = 0.01 M) of **CP1<sub>2</sub>Pd<sub>2</sub>** (0.5 mM) in D<sub>2</sub>O/CD<sub>3</sub>OD (1:1, v/v) at 22°C with increasing amounts of terephthalate.

The <sup>1</sup>H NMR spectra of these samples exhibited additional signals and the broadening of most signals with increasing amount of terephthalate (**Figure 51**), indicating that partial decomposition of **CP1<sub>2</sub>Pd<sub>2</sub>** could not be ruled out and that the buffer components potentially interfered in the binding equilibrium.

In light of these results, the use of buffer in the binding studies should be avoided and the attention was therefore directed toward the use of disulfonates as guests, which are fully deprotonated at neutral pH, eliminating the need to use buffers.

As a potential guest, sodium 1,3-benzenedisulfonate (BDS) was originally chosen. Equimolar amounts of BDS and **CP1<sub>2</sub>Pd<sub>2</sub>** were equilibrated in D<sub>2</sub>O/CD<sub>3</sub>OD, 1:1 (v/v) and the product formed was characterized directly from the reaction mixture by means of NMR spectroscopy and ESI-TOF MS spectrometry. The ESI-TOF mass spectrum (**Figure 52**) exhibited a single peak at  $m/z = 871.20$ , corresponding to the doubly positively charged complex of **CP1<sub>2</sub>Pd<sub>2</sub>** with one BDS molecule.



		<i>m/z calcd.</i>	<i>m/z exp.</i>
$[\text{CP1}_2\text{Pd}_2 + \text{BDS}]^{2+}$	$\text{C}_{72}\text{H}_{76}\text{N}_{16}\text{O}_8\text{Pd}_2^{4+} + \text{C}_6\text{H}_4\text{O}_6\text{S}_2^{2-}$	871.2	871.1

**Figure 52** ESI-TOF MS spectrum (positive mode) of an equimolar mixture of **CP1<sub>2</sub>Pd<sub>2</sub>** and BDS.

The  $^1\text{H}$  NMR spectra of  $\text{CP1}_2\text{Pd}_2$ , BDS and of an equimolar mixture of both compounds in  $\text{D}_2\text{O}/\text{CD}_3\text{OD}$ , 1:1 (v/v) are shown in **Figure 53**.

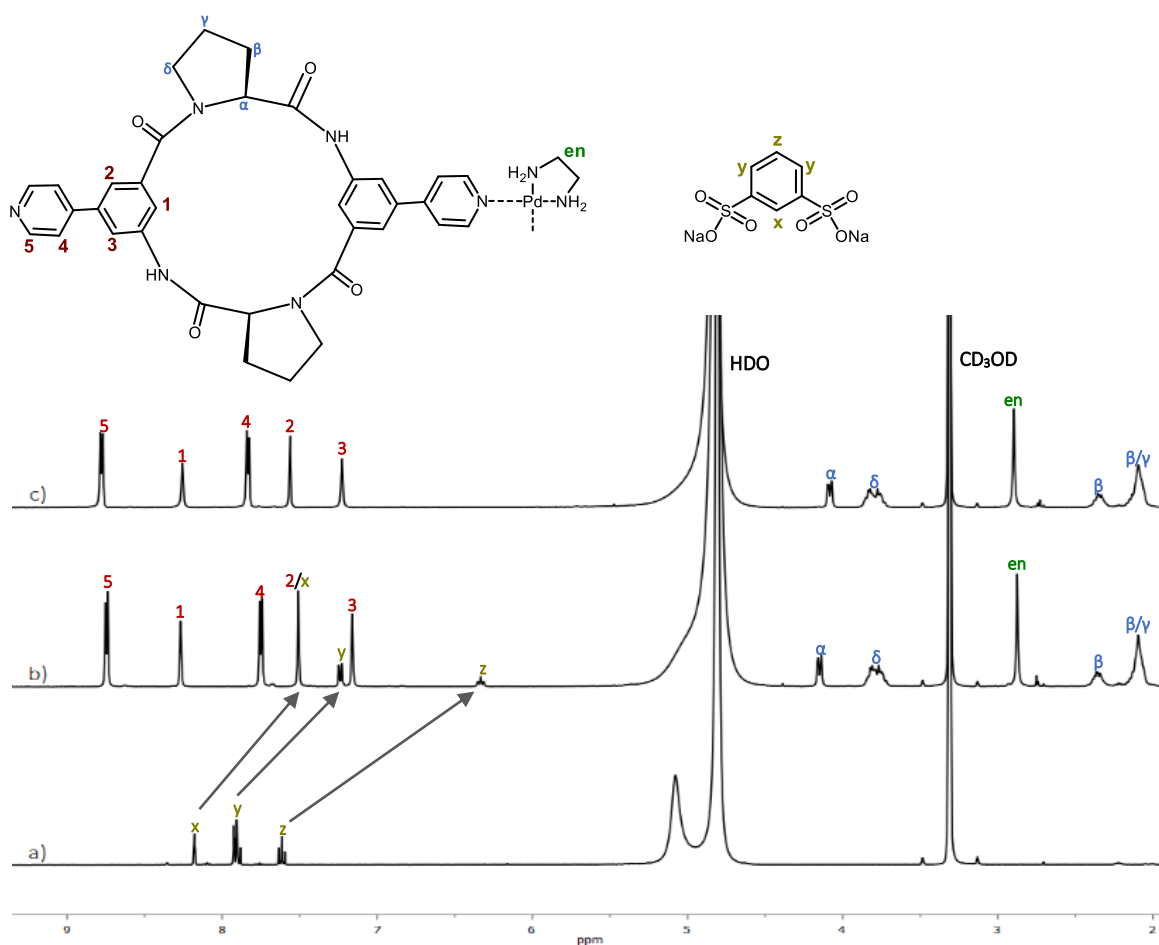


**Figure 53**  $^1\text{H}$  NMR spectra of BDS (0.5 mM) (a), of an equimolar mixture of  $\text{CP1}_2\text{Pd}_2$  and BDS (each 0.5 mM) (b) and of  $\text{CP1}_2\text{Pd}_2$  (0.5 mM) (c) in  $\text{CD}_3\text{OD}/\text{D}_2\text{O}$ , 1:1 (v/v).

The presence of  $\text{CP1}_2\text{Pd}_2$  again caused a pronounced upfield shift of the guest signals, which suggested complex formation. Similar to the experiments with dicarboxylates, complex formation was fast on the NMR time-scale since only a single set of averaged signals was observed for  $\text{CP1}_2\text{Pd}_2$  and BDS.

In this case, complex formation was also investigated by DOSY NMR spectroscopy (**Figure 54**). In the DOSY NMR spectrum of a 1:1 mixture of  $\text{CP1}_2\text{Pd}_2$  and BDS, the signals of both components appeared as a single trace, showing that host and guest diffuse at the same rate and that they therefore interact.

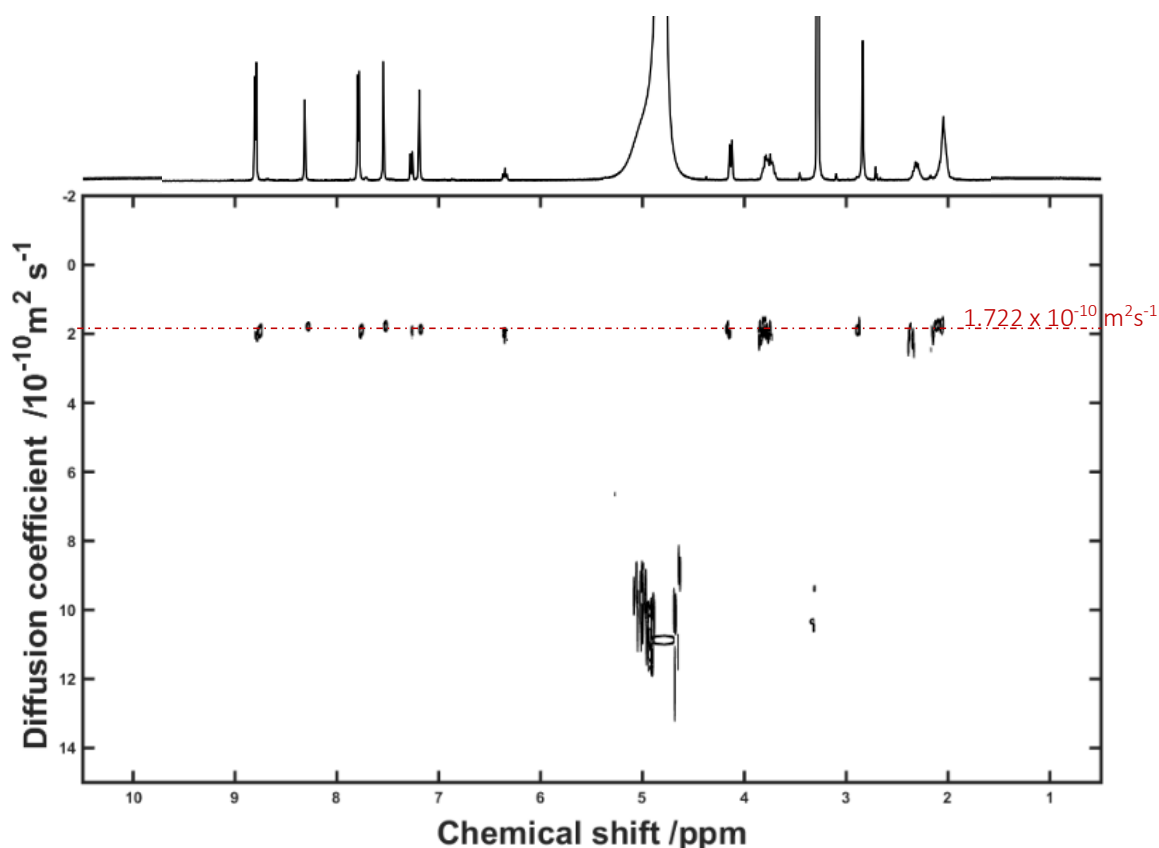


**Figure 54** DOSY NMR spectrum in  $D_2O/CD_3OD$  (1:1 v/v) of an equimolar mixture of  $CP1_2Pd_2$  and BDS (each 0.5 mM).

A hydrodynamic diameter of 14.6 Å was determined for the respective complex from the diffusion coefficient ( $D=1.722 \times 10^{-10} \text{ m}^2\text{s}^{-1}$ ). Assuming that the structure of the BDS complex is similar to the one modelled for terephthalate (see b in **Figure 55**), the experimental diameter was substantially smaller than the calculated one. The reason for this discrepancy is the fast rate of complex formation. If the solution contains a mixture of the complex and the free binding partners, the observed signals represent an average of the signals of three interconverting species: the complex, the host and the guest. Since BDS is much smaller than the other components, it diffuses faster, thus apparently increasing the diffusion coefficient and reducing the size of  $CP1_2Pd_2$ .

Since a crystal structure could not be obtained, structural information about  $CP1_2Pd_2 \cdot BDS$  was acquired from force field calculations (**Figure 55**). The calculated structure was, as expected, rather similar to the one of the terephthalate complex in its symmetry (both  $D_2$  symmetric), molecular dimensions (see b in **Figure 55**), and average diameter (22.4 Å for  $CP1_2Pd_2 \cdot BDS$  and 23.8 Å for the dicarboxylate complex).

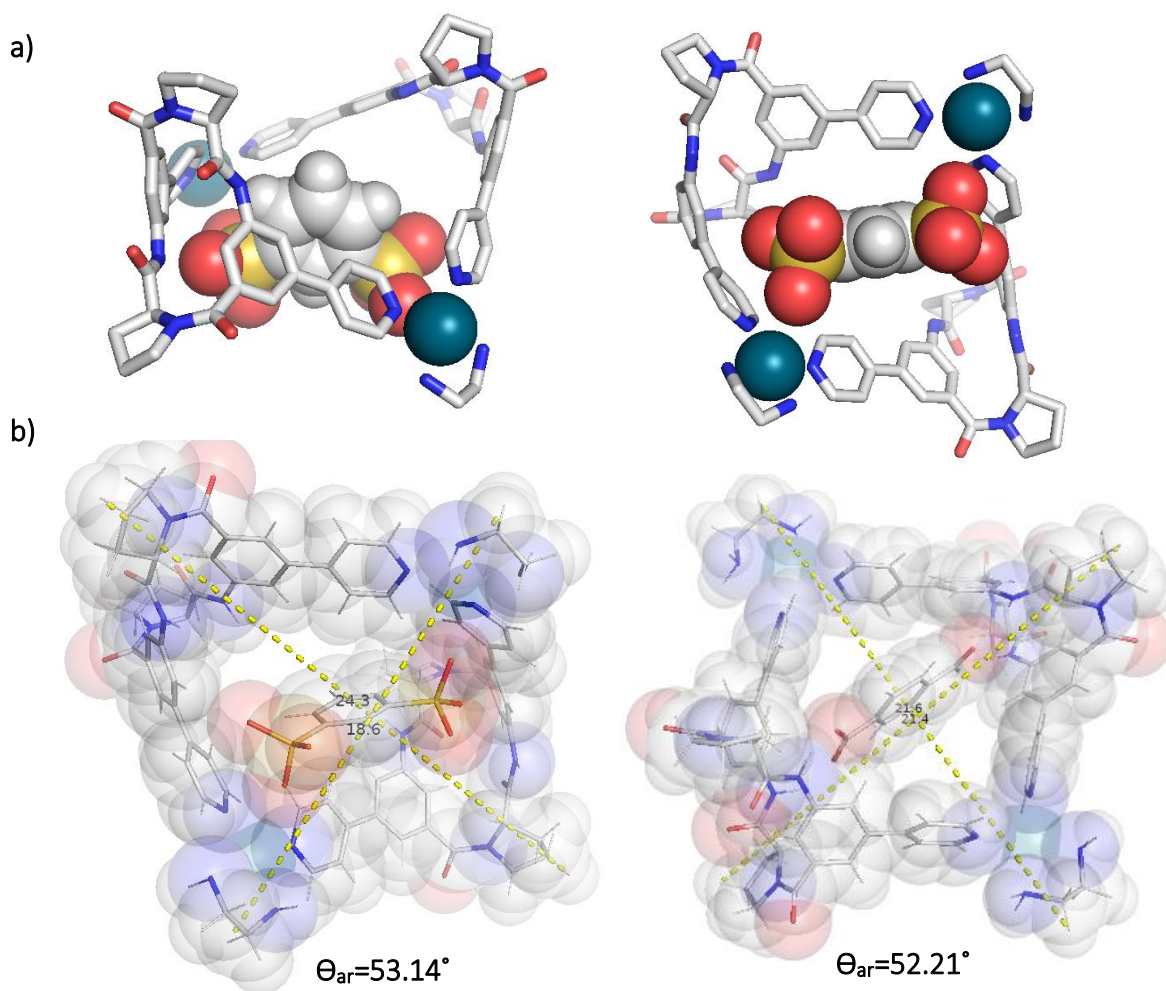


**Figure 55** a) Calculated structure of  $CP1_2Pd_2.BDS$ . The geometry optimization was performed with Universal Force Field (UFF) Algorithm as implemented in Avogadro. Hydrogen atoms are omitted for clarity. b) Estimated molecular dimensions of the calculated structure (left) and the terephthalate complex of  $CP1_2Pd_2$  (right). From the marked distances of hydrogen atoms, an average diameter of 22.4 Å can be estimated for the BDS complex when considering the van-der-Waals radii of hydrogen atoms (1.1 Å).

NMR titrations were performed to obtain information about the stability of the BDS complex by observing the effects of the gradual addition of  $CP1_2Pd_2$  to a solution of BDS in  $D_2O/CD_3OD$  (1:1 v/v) (**Figure 56**) on the  $^1H$  NMR spectrum.

Since binding of BDS was fast on the NMR time-scale, the binding isotherms were constructed from the gradual shifts of the guest signals observed when increasing the amount of  $CP1_2Pd_2$ .

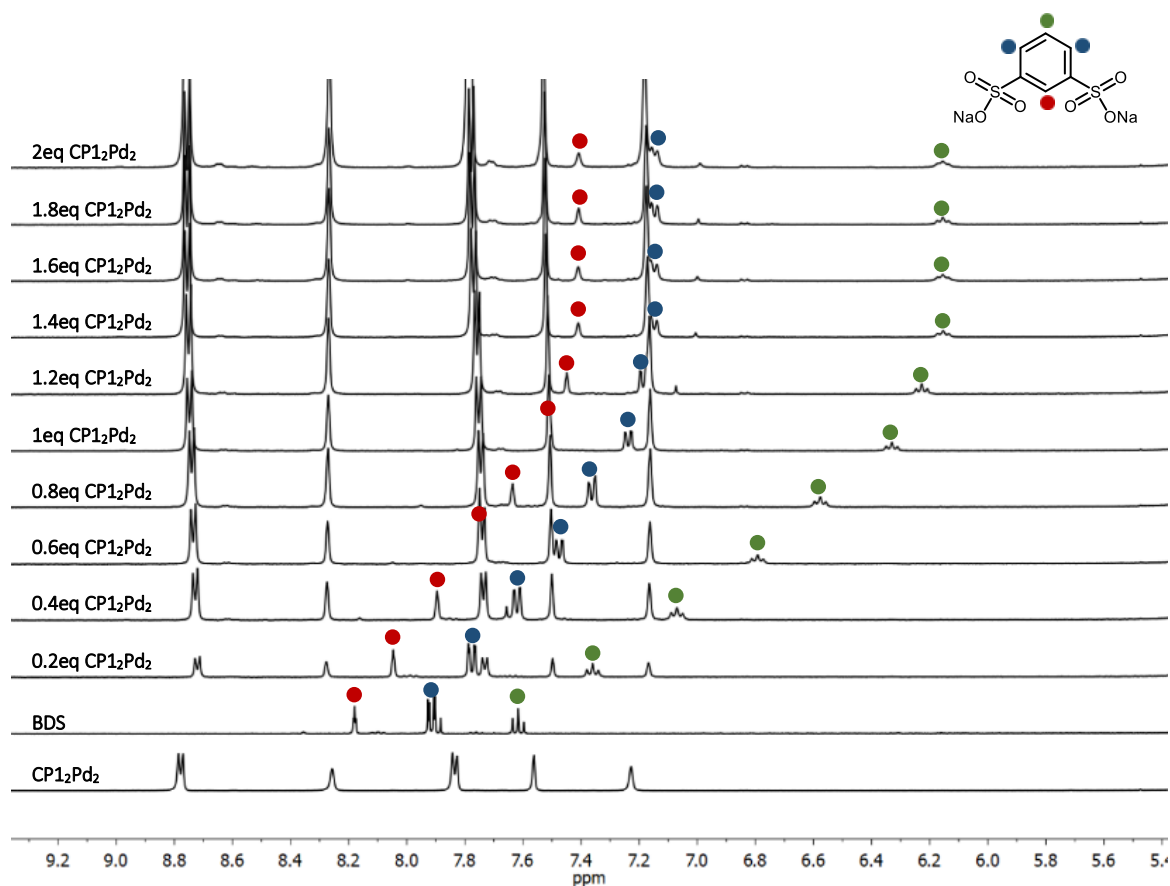


**Figure 56** <sup>1</sup>H NMR spectra of the NMR titration of sodium 1,3-benzenedisulfonate BDS (0.5mM) in D<sub>2</sub>O/CD<sub>3</sub>OD (1:1, v/v) at 22°C with increasing amounts of CP<sub>12</sub>Pd<sub>2</sub>. The signals of the guest are marked with coloured dots.

The isotherms obtained from the shifts were globally fitted to different binding models using HypNMR2008 (**Figure 123**, page 157), but only the 1:1 model afforded a good fit between the experimental and the calculated results, confirming the results of ESI-TOF MS spectrometry. Accordingly, the log  $K_a$  of the complex amounted to  $4.8 \pm 0.2$ , which showed that the complex had a considerable stability in the aqueous solvent mixture.

Taken together, the analytical results thus demonstrate that the metallamacrocycle CP<sub>12</sub>Pd<sub>2</sub> formed a stable host-guest complex in which one molecule of BDS was included in the host cavity.

In addition, it was investigated whether the larger sodium 2,6-naphthalenedisulfonate (NDS) would also be a suitable guest. Initially, the effects of increasing amounts of NDS on the <sup>1</sup>H NMR spectrum of CP<sub>12</sub>Pd<sub>2</sub> were again evaluated (**Figure 57**).

In this case, complex formation proceeded differently than that of BDS. A new set of signals in the  $^1\text{H}$  NMR spectra appeared in the presence of NDS that progressively became more pronounced as the amount of the disulfonate increased. The signals of  $\text{CP1}_2\text{Pd}_2$  concomitantly became less intensive until they disappeared at an NDS/ $\text{CP1}_2\text{Pd}_2$  ratio of 2:1 (red boxes in **Figure 57**). Further addition of NDS caused the appearance of the signals of the free guest (blue boxes). These results indicated that NDS binding was slow on the NMR time-scale and likely involved the complexation of two NDS molecules.

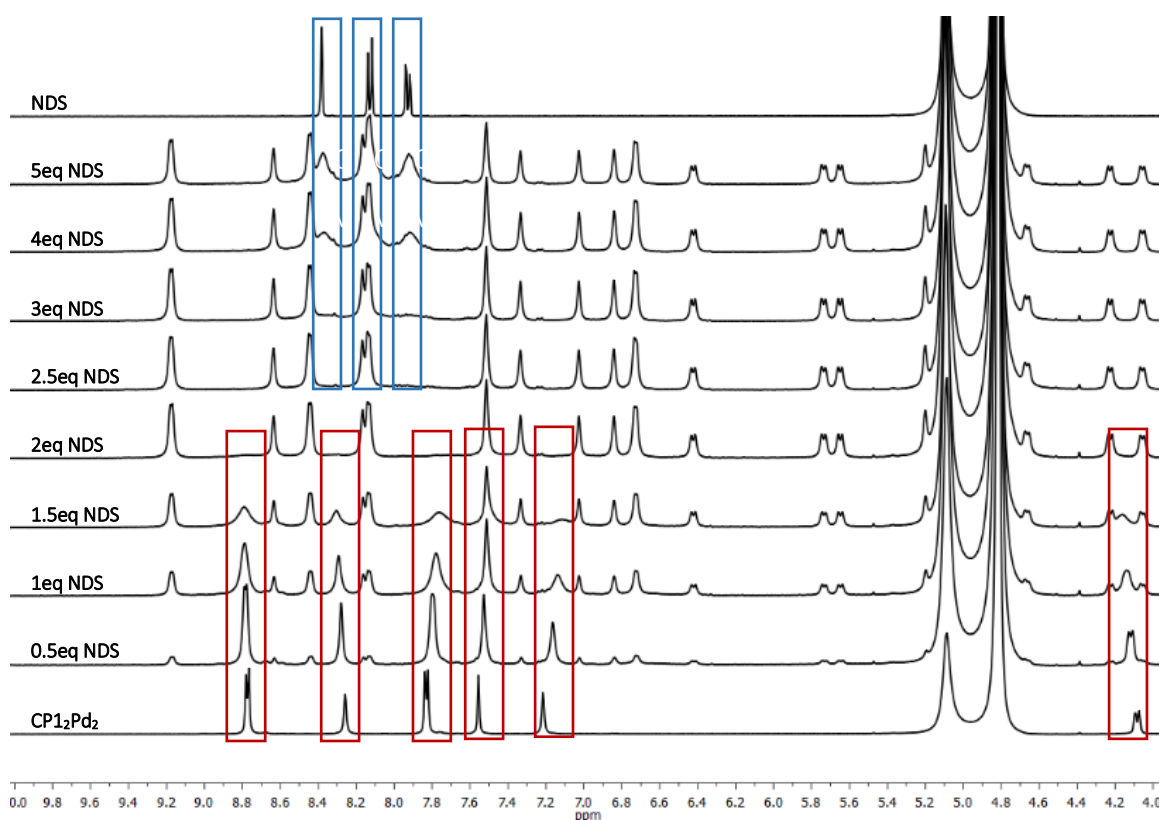


**Figure 57**  $^1\text{H}$  NMR spectra of the NMR titration of  $\text{CP1}_2\text{Pd}_2$  (1.0 mM) in  $\text{CD}_3\text{OD}/\text{D}_2\text{O}$ , 1:1 (v/v) with increasing amounts of 2,6-naphthalenedisulfonate NDS (22 °C). The spectrum of NDS is shown on the top. The signals of disappearing  $\text{CP1}_2\text{Pd}_2$  and those of appearing free NDS are marked with red and blue boxes, respectively.

The signals in the NMR spectrum of the complex could mostly be assigned by using 2D NMR techniques, demonstrating that some of the guest signals experienced pronounced upfield shifts upon complex formation of almost 4 ppm (**Figure 58**). Splitting of the signals of the equivalent protons of  $\text{CP1}_2\text{Pd}_2$  and NDS was indicative that these protons had different environments in the complex and that the complex accordingly had a lower symmetry than  $\text{CP1}_2\text{Pd}_2$  alone.

Unfortunately, NOESY NMR spectra showed no intermolecular crosspeaks between signals of **CP1<sub>2</sub>Pd<sub>2</sub>** and NDS, which would have provided information about the structure of the complex in solution (**Figure 146** page 208).

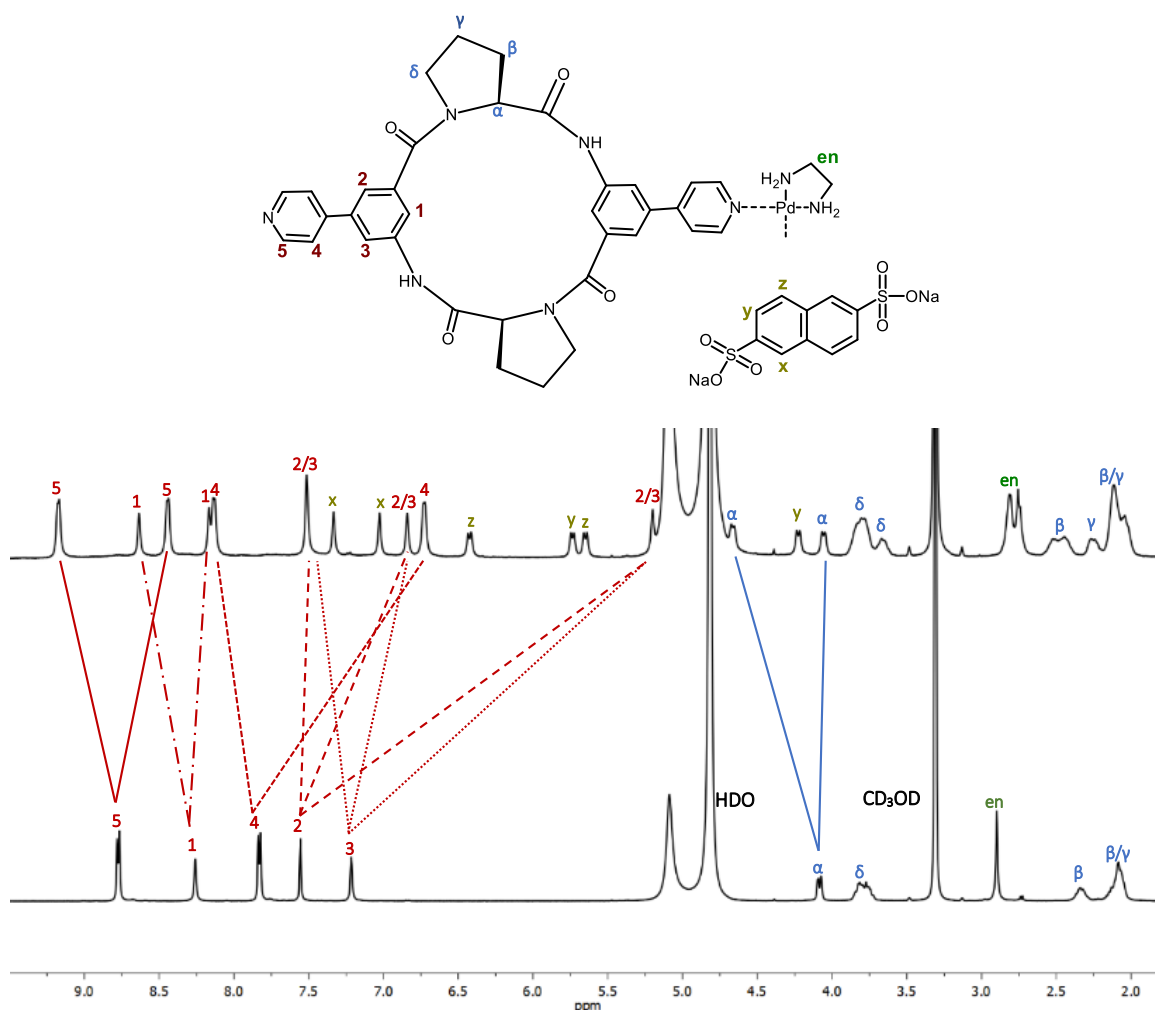


**Figure 58** <sup>1</sup>H NMR spectra of a mixture of **CP1<sub>2</sub>Pd<sub>2</sub>** (1mM) and NDS (2 mM) (top) and <sup>1</sup>H NMR spectra of **CP1<sub>2</sub>Pd<sub>2</sub>** (1mM) (bottom) in CD<sub>3</sub>OD/D<sub>2</sub>O, 1:1 (v/v).

DOSY NMR spectroscopy demonstrated that the signals deriving from **CP1<sub>2</sub>Pd<sub>2</sub>** and those of NDS were part of a single species with a diffusion coefficient  $D = 1.261 \times 10^{-10} \text{ m}^2\text{s}^{-1}$  and a corresponding hydrodynamic diameter of 20.0 Å (**Figure 59**).

In the ESI-TOF mass spectrum of the **CP1<sub>2</sub>Pd<sub>2</sub>**/NDS solution, no signal was observed that could be attributed to the complex, likely because the binding of the two molecules of NDS to **CP1<sub>2</sub>Pd<sub>2</sub>** afforded a neutral compound.



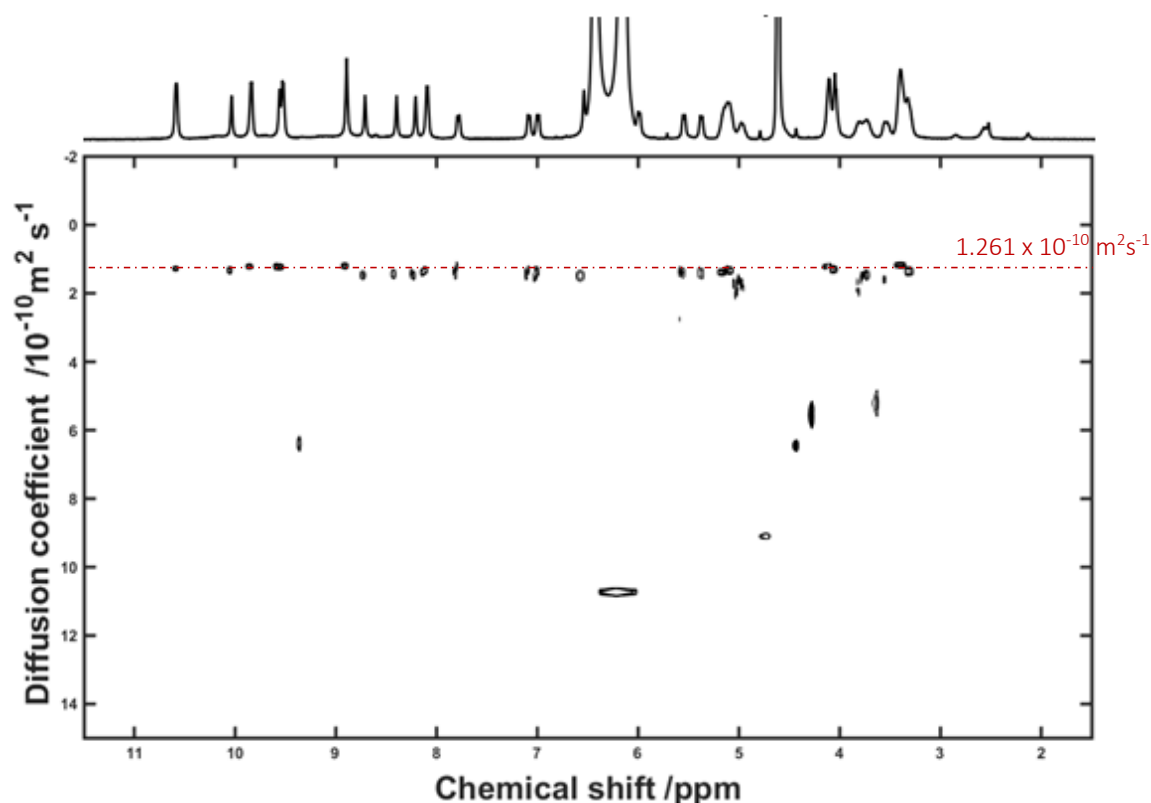


**Figure 59** DOSY NMR spectra of a mixture of  $\text{CP}_{12}\text{Pd}_2$  (1mM) and NDS (2 mM) in  $\text{CD}_3\text{OD}/\text{D}_2\text{O}$ , 1:1 (v/v).

Fortunately, a crystal structure of the corresponding complex was obtained from a mixture of  $\text{CP}_{12}\text{Pd}_2$  (1mM) and NDS (2 mM) in  $\text{CD}_3\text{OD}/\text{D}_2\text{O}$ , 1:1 (v/v) by slow diffusion with  $\text{CD}_3\text{CN}$ . This structure confirmed the expected composition, with two molecules of NDS included in the cavity of  $\text{CP}_{12}\text{Pd}_2$  (Figure 60).

The metallamacrocycle alone had a structure similar to the calculated one, but the included guest molecules reduced the symmetry of the structure to  $C_2$ , providing an explanation for the signal splitting observed in the  $^1\text{H}$  NMR spectrum. Specifically, the pyridyl units facing the edges of the included guests had a different environment than those aligned along the faces.

The two NDS molecules were arranged in a parallel fashion, with some of their protons residing within the clefts produced by the aromatic units along the cyclopeptide rings, explaining the considerable shielding in the NMR.

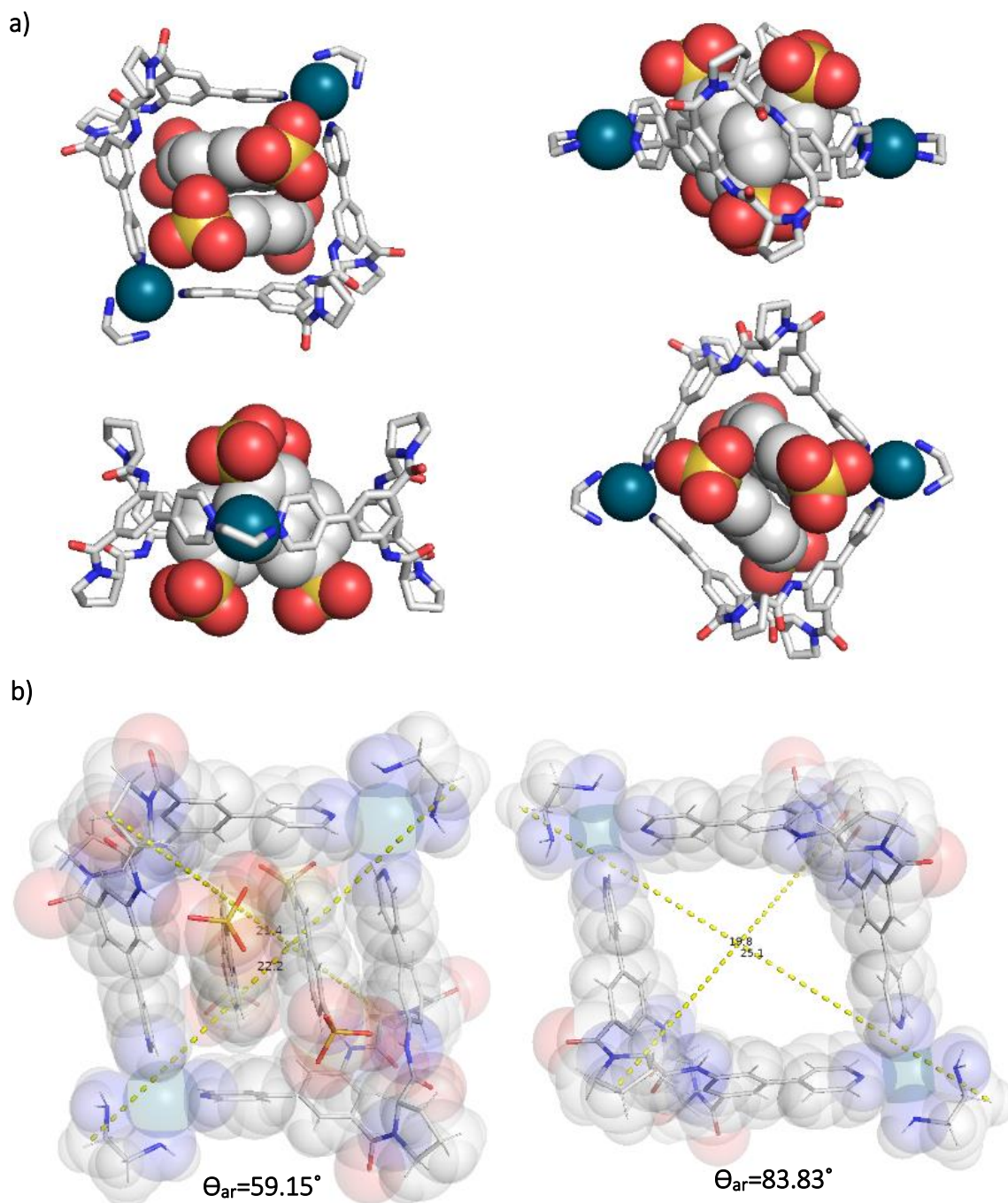


**Figure 60** a) Crystal structure of  $CP1_2Pd_2 \cdot 2NDS$ . Hydrogen atoms are omitted for clarity. b) Estimated molecular dimensions of  $CP1_2Pd_2 \cdot 2NDS$  from the crystal structure (left) and of the calculated structure of  $CP1_2Pd_2$  (right). From the marked distances of hydrogen atoms, an average diameter of 24.1 Å was estimated when considering the van-der-Waals radii of hydrogen atoms (1.1 Å).

A slight contraction of **CP1<sub>2</sub>Pd<sub>2</sub>** (diameter of 25.4 Å) was observed with respect to the calculated structure of the metallamacrocycle upon NDS binding, leading to an average diameter of 24.1 Å (**Figure 60**), consistent with the increase of the diffusion coefficient upon complex formation. The difference was less pronounced than expected from the hydrodynamic diameter resulting from the DOSY NMR experiment, but it suggested a structural change of **CP1<sub>2</sub>Pd<sub>2</sub>** induced by guest binding.

The close proximity of the anionic sulfonate groups of the guests is noteworthy, but their Coulomb repulsion was likely compensated by the sum of the interactions stabilizing the complex ( $\pi$ - $\pi$  stacking and [C-H $\cdots$  $\pi$ ] interactions), including the attractive electrostatic interactions with the metal centres. The strong mutual stabilization of the eight components in **CP1<sub>2</sub>Pd<sub>2</sub>**·2NDS likely explains why both NDS molecules were strongly bound without any evidence for an intermediate 1:1 complex.

Unfortunately, the complexity of the binding equilibrium, involving two stability constants, prevented the quantitative assessment of complex stability from NMR titrations. Nonetheless, since the equilibrium was slow on the NMR time-scale and the complex was fully formed once the required two equivalents of the guest were present in solution, a high stability of **CP1<sub>2</sub>Pd<sub>2</sub>**·2NDS is very likely.

These binding studies thus confirmed that **CP1<sub>2</sub>Pd<sub>2</sub>** provided a suitable environment for hosting anionic guests, leading to stable host-guest complexes. With confirmation of disulfonate incorporation, qualitative binding studies using BDS and NDS and the cage **CP2<sub>2</sub>Pd<sub>3</sub>** obtained from the larger cyclohexapeptide were performed. NMR samples in CD<sub>3</sub>CN/D<sub>2</sub>O, 1:1 (v/v) were prepared by adding increasing amounts of the guest solutions to a **CP2<sub>2</sub>Pd<sub>3</sub>** solution (0.5 mM). Unfortunately, precipitate formation was observed even with only 0.1 equivalents of the guests present in solution and host-guest complex formation could not be evaluated due to the complex <sup>1</sup>H NMR spectra obtained from these samples. The precipitates formed were redissolved in DMSO-*d*<sub>6</sub> but no information could be obtained from the <sup>1</sup>H NMR and ESI MS spectra of the samples. Since reaction between **CP1** and tetravalent Pd (II) did not provide **CP1<sub>6</sub>Pd<sub>3</sub>** as a single product and purification or NMR peak assignment were not successful, no binding studies were performed with this cage.

## 1.4. CONCLUDING REMARKS

During the experimental work of this chapter, two cyclopeptides (**CP1** and **CP2**) were synthesized accordingly to previous established synthetic procedures. In the case of **CP2**, the synthesis was improved in the last step, affording the product in a yield of 43% instead of 3%.

Both cyclopeptides afforded discrete hollow coordination complexes when reacting with the Pd(II) ligands  $[\text{Pd}(\text{NO}_3)_2(\text{en})]$  and  $[\text{Pd}(\text{CH}_3\text{CN})_4](\text{BF}_4)_2$ , demonstrating that appropriately designed cyclopeptides could serve as ligands for the generation of chiral coordination compounds, the structure and composition of which depends on the nature of the metal nodes. Such metal complexes featured functional groups along their surfaces that could induce interesting receptor properties. Indeed, the metallamacrocycle **CP1<sub>2</sub>Pd<sub>2</sub>**, resulting from the reaction between **CP1** and  $[\text{Pd}(\text{NO}_3)_2(\text{en})]$ , possessed a pronounced affinity for anionic substrates in aqueous solvents.

While the binding of sodium 1,3-benzenedisulfonate (BDS) led to the formation of a 1:1 complex in  $\text{D}_2\text{O}/\text{CD}_3\text{OD}$ , 1:1 (v/v) that had a stability  $\log K_a$  of 4.8, the complexation of the larger sodium 2,6-naphthalenedisulfonate (NDS) was rather unusual. In this case, the equilibrium was slow on the NMR time-scale and yielded an overall neutral complex with two guest molecules residing in the host cavity.

This work thus demonstrated for the first time that cyclopeptides represent suitable scaffolds for accessing coordination cages and the interesting receptor properties of some of these compounds.

## **2. Synthesis and Characterization of Luminescent Neutral Pt(II) Complexes Tethered to Cyclopeptides**

This project was developed during a secondment within the Marie Curie Innovative Training Network ResMoSys. In this chapter, the work developed at the Supramolecular Science and Engineering Institute – ISIS (Strasbourg, France) from November 2016 to December 2016 is described. The synthesis and characterization of the compounds required for this project were executed prior and after the stay at the Chemistry Department of the TU Kaiserslautern.



## 2.1. INTRODUCTION

The development of new light-emitting materials made possible innovations with a wide range of high-tech applications. For this reason, research on luminescent materials is performed world wide<sup>119,120</sup> specifically on materials containing transition-metal complexes (TMCs) due to their particularly promising photophysical properties. Such materials have been applied in several fields such as photocatalysis,<sup>121</sup> artificial photosynthesis,<sup>122</sup> dye-sensitized solar cells,<sup>123</sup> optoelectronics,<sup>124,125</sup> electrochemieluminescence (ECL),<sup>126</sup> non-linear optical materials,<sup>127</sup> sensing,<sup>128</sup> and bioimaging.<sup>129</sup>

Among the different TMCs, significant attention is being devoted to luminescent platinum(II) complexes due to their attractive chemical and photophysical properties such as high stability, emission in the visible region, high photoluminescence quantum yields, long excited-state lifetimes, and high tendency to self-assemble in supramolecular structures that possess enhanced luminescence intensity and tuneable properties.

### 2.1.1 Photophysics of Pt(II)-complexes

Pt(II)-complexes have a square-planar geometry with a coordination number of four.<sup>130</sup> This geometry enables stacking of the complexes, driven by dipole-dipole and quadrupole ( $\pi$ - $\pi$ ) interactions in combination with solvophobic effects and dispersion interactions (London forces). The formation of the corresponding aggregates produces a dramatic change of the photophysical properties (**Figure 61**).<sup>131</sup>

Typically, luminescent platinum(II) compounds in a molecularly dissolved state (monomeric form) possess the lowest-unoccupied molecular orbital (LUMO) with ligand  $\pi^*$  character whereas the highest-occupied molecular orbital (HOMO) is predominantly of ligand  $d\pi$  character. In this case, excited states resulting from metal-perturbed ligand centred (MP-LC) and metal-to-ligand charge transfer (MLCT) transitions are responsible for the emission.<sup>132,133</sup>

On the basis of the ligand field theory, Pt(II) centres with a square-planar arrangement of the coordinating ligands possess occupied  $d_{z^2}$  orbitals normal to the plane of the molecule which do not (or only weakly) interact with the coordination sphere of the ligand. They are thus prone to interact with surrounding species such as solvent molecules or  $d_{z^2}$  orbitals from other metal complexes.<sup>131</sup> Orbital mixing of two platinum(II) centres stacking on top of each other (close proximity of 3.5 Å = van der Waals radius) leads to the destabilization of one filled  $d_{z^2}$  orbital (Figure 61).

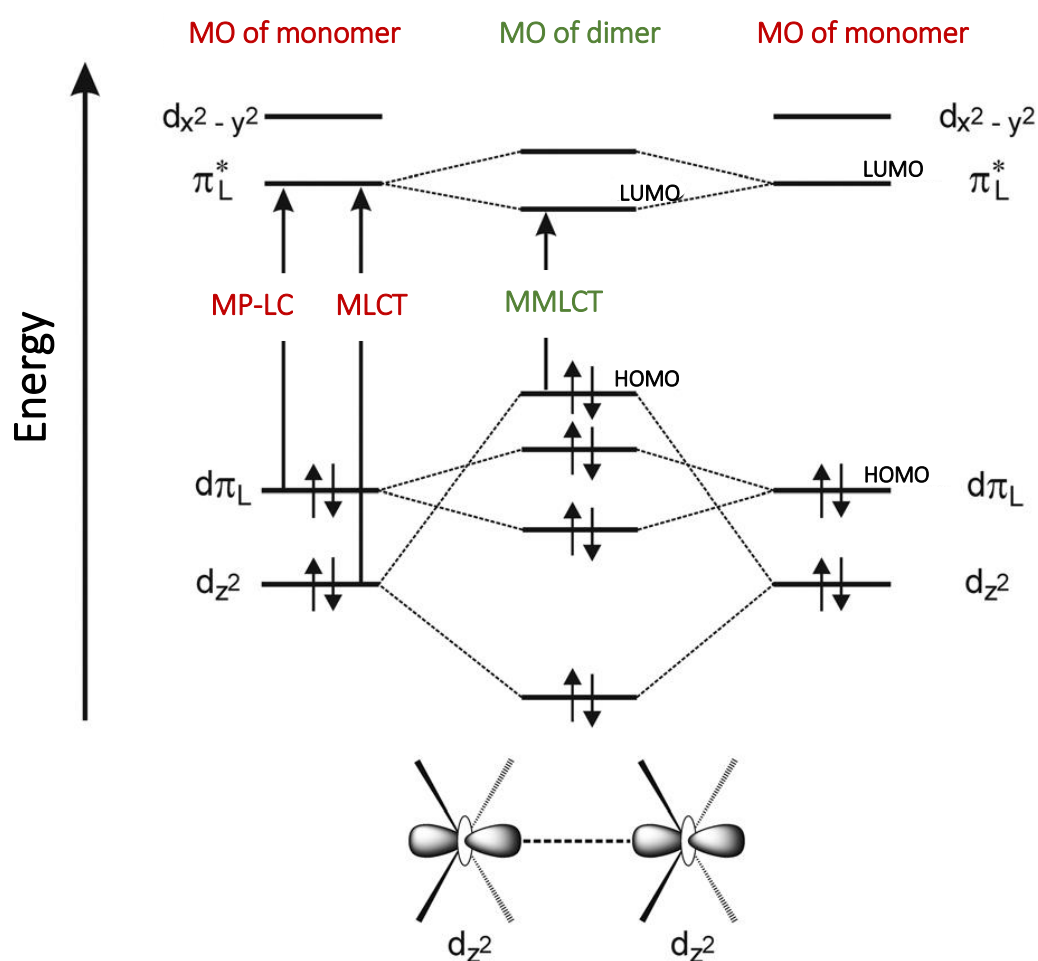


**Figure 61** Simplified molecular orbital diagram of a monomeric square-planar Pt(II)-complex featuring ligands with a  $\pi$ -system. Upon dimer formation/aggregation of Pt(II)-complexes, their  $d_{z^2}$  orbitals interact with each other, resulting in novel transitions (MMLCT) that require less energy than the excitation of the monomeric species (MP-LC, MLCT).



As a consequence, a metal-metal-to-ligand charge transfer (MMLCT) transition becomes possible that requires less energy than the excitation of the monomeric form. The absorption leading to this new charge transfer state and its luminescence is significantly shifted to larger wavelengths with respect to the monomeric parent Pt(II) complex and features stronger emission intensity with extraordinary long excited-state lifetimes at room temperature. Moreover, considering that the energy of the HOMO-LUMO gap depends on the Pt-Pt distance, these spectral changes can be used as a readout of the aggregation. Accordingly, different modes of aggregation result in different energy gaps and thus in different emission wavelengths.

### 2.1.2 *N*-Metallacycles

Bi-, ter- and tetradentate chelating ligands with a  $\pi$ -conjugated system are frequently utilized for the construction of luminescent Pt(II)-complexes.<sup>134</sup> In comparison to bidentate ligands, terdentate ligands generally afford Pt(II)-complexes of high thermodynamic and kinetic stability. Tetradentate ligands provide even more rigid supramolecular building blocks than the terdentate analogues. In this Chapter, the focus will be on the spectroscopic and luminescent properties of Pt(II)-complexes derived from terdentate ligands, specifically of those derived from bis(tetrazolate)-pyridine.

Neutral luminescent Pt(II)-complexes based on terdentate dianionic bis(tetrazolate)-pyridine ligands have been intensely studied because their large planar aromatic surfaces allow the formation of non-covalent adducts (dimers, aggregates, etc) where the emerging metal-metal interactions of the Pt(II) centres strongly augment the emission properties of the complexes.<sup>14,135–139</sup>

These complexes contain a terdentate ligand with a central pyridine unit bearing 1*H*-1,2,4 triazolyl groups in positions 2 and 6, a Pt(II) metal centre and an ancillary ligand. The triazolyl flanking groups can be substituted in 5-position with different groups. The deprotonation upon *N*-metallacyclation is often facilitated by the addition of a base.

By altering the ancillary ligand one can tune the self-assembly properties, while preserving the chromophoric system that is defined by the terdentate dianionic ligand. Thus, the ancillary ligand enables the control of the self-assembly process by adjusting its solubility

and bulkiness and by introducing further supramolecular motifs. It is therefore easily possible to tune these complexes for different applications by just exchanging the ligand.

Pyridine based compounds are quite effective as ancillary ligands since they afford thermodynamically stable and planar complexes. These complexes exhibit room temperature emission in organic solvents such as tetrahydrofuran (THF) or dichloromethane (DCM), featuring an emission band ( $^3\text{LC}$  based) around 460 nm (blue). Upon aggregation, the luminescence is strongly enhanced with a bathochromically shifted emission peak ( $^3\text{MMLCT}$  based).<sup>120</sup>

The ability of neutral platinum(II) complexes with a tridentate bis(triazolate)pyridine ligand to self-assemble, creating luminescent nanostructures in cellular compartments, was demonstrated by De Cola and co-workers (Figure 62).<sup>140</sup> Both complexes shown in Figure 62 display a strong yellow luminescence in their aggregated form, arising from  $^3\text{MMLCT}$  emission.

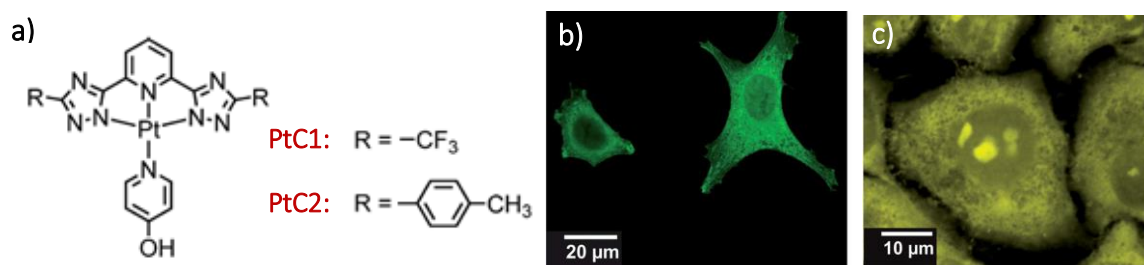


**Figure 62** a) Molecular structures of neutral Pt(II) complexes with a tridentate bis(triazolate)pyridine ligand; b) Luminescence confocal microscopy images showing the distribution of complex **PtC2** inside HeLa cells; c) Luminescence confocal microscopy images showing the distribution of complex **PtC1** inside HeLa cells; © 2014 Royal Chemical Society

According to cell internalization and localization experiments, the tridentate ligand coordinated to the platinum dictated the target areas of the cells where the assemblies occur. Aggregates containing **PtC2** were mainly observed in the cytoplasmic region of the cells (Figure 62b), while the **PtC1**-containing complexes were only partially distributed in this region, but bright aggregates were observed inside the nucleus (Figure 62c). These aggregates appeared to remain intact inside the cell.

In a different study by the same group, micrometre-long and highly crystalline fibres were constructed by the solvent-assisted self-assembly of the blue-emitting neutral Pt(II)-complex **PtC3** based on a tridentate dianionic bis(triazolate)pyridine ligand decorated with bulky electron-withdrawing trifluoromethyl groups (**Figure 63**). The aggregates showed highly efficient (quantum yield up to 74%) polarized yellow-orange light emission, as a consequence of their high degree of supramolecular order imparted by weak non-covalent intermolecular (metal-metal and  $\pi$ - $\pi$ ) interactions.<sup>14</sup>

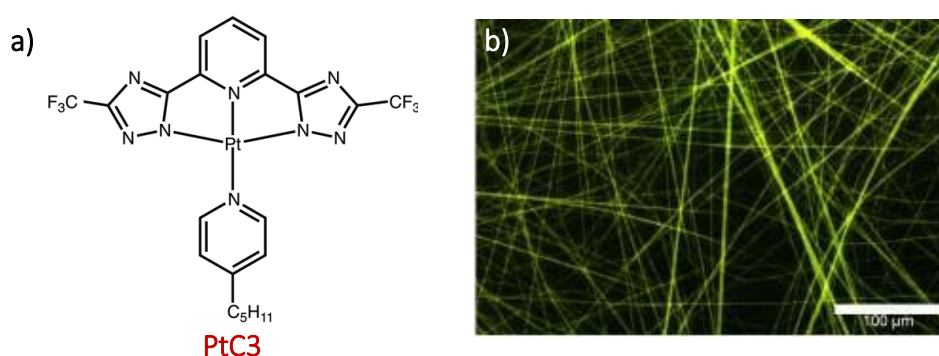


**Figure 63** a) Molecular structures of neutral Pt(II) complexes with a tridentate bis(triazolate)pyridine ligand; b) Luminescent fibers formed from a self-assembled neutral Pt(II)-complex. © 2014 Royal Chemical Society

The mechanochromic responsiveness of the Pt(II)-complex **PtC4** with the same trifluoromethyl terdentate ligand and a different ancillary pyridine ligand was also investigated by De Cola and co-workers (**Figure 64**). Changes in the luminescence were observed in hydrostatic pressure experiments (24.2 kbar) using a diamond anvil cell. An AFM tip served as writing pencil on a blue emissive fibre to induce emission colour changes. Upon scratching with the tip, the emission colour changed to yellow and the thus written message could be erased by a photoconversion reaction induced with a 405 nm excitation.<sup>141</sup>

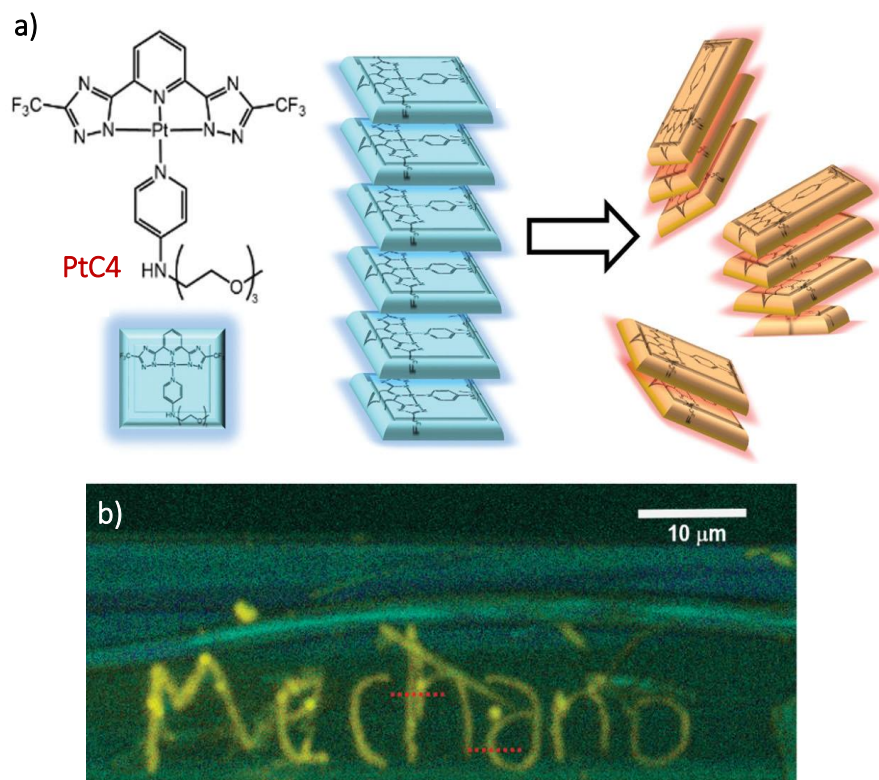


**Figure 64** a) Chemical structure of the neutral tridentate Pt(II) complex and cartoon showing the principle of its mechanochromism, where a long crystalline domain with largely spaced adjacent Pt(II) complexes is transformed into smaller aggregates with poor crystallinity and shorter Pt...Pt distance; b) Nanolithography on ultralong ribbons. Confocal spectral images of ribbons engraved with a seven-letter long word ("Mechano") by means of AFM nanolithography conducted at  $10 \mu\text{m s}^{-1}$  maximum scan rate, with constant force =  $24 \mu\text{N}$ . Excitation wavelength, emission spectral window, and objective used are 488 nm, 490–700 nm,  $63\times$  NA 1.3, respectively. © 2016 WILEY-VCH Verlag GmbH & Co. KGaA, Weinheim.

A ratiometric chemosensor for potassium was obtained by using a bipyridine-containing *cis*-substituted crown ether as ancillary ligand (**Figure 65**). In its unfolded state, **PtC5** displayed a blue emission, but when the Pt(II) centres approached each other, a bathochromic shift of the emission occurred and the complexes became strongly orange emissive (folded state). Potassium binding to the folded state caused unfolding and was thus accompanied with pronounced changes in the emission properties of the complex from orange to blue. The process was reversed by the addition of 18-crown-6.<sup>142</sup>

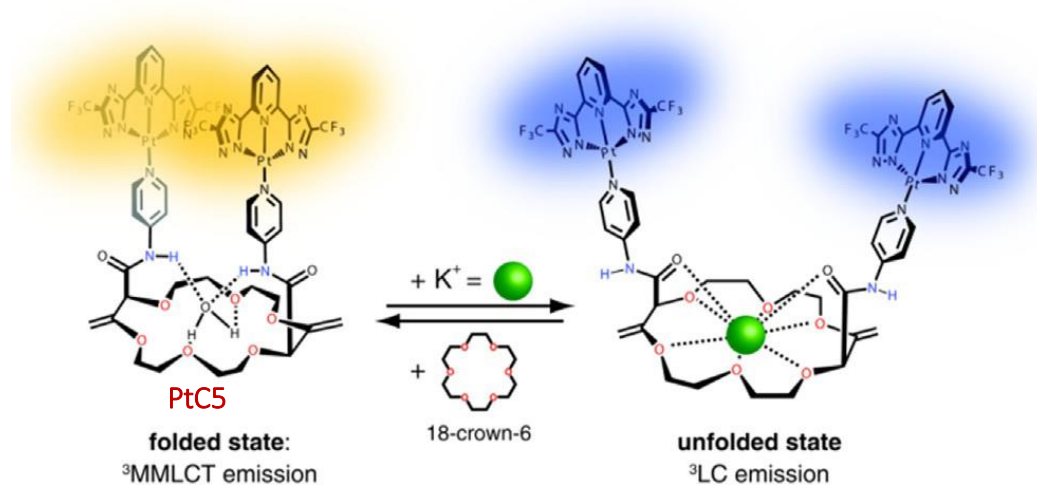


**Figure 65** Reversible emission-color switch of Pt–dye pendant crown ether upon addition of potassium salts and by extraction of the metal ion with unsubstituted 18-crown-6. © 2016 Wiley-VCH Verlag GmbH & Co. KGaA, Weinheim.

## 2.2. AIM OF THE PROJECT

In this project, cyclopeptides bearing pyridyl pendant arms should be used as scaffolds to arrange two or three square planar platinum(II) complexes in space and the stacking/aggregation properties of these compounds and the concomitant changes of the luminescence properties investigated.

As cyclopeptides, **CP1** and **CP2** with two or three peripheral pyridyl units should be used, which were also employed for the construction of coordination cycles and cages (Chapter 1). These peptides should be coordinated to appropriate platinum(II) precursors to afford the products shown in **Figure 66**. After the preparation of the products, their aggregation properties and photophysical behaviour should be characterized.

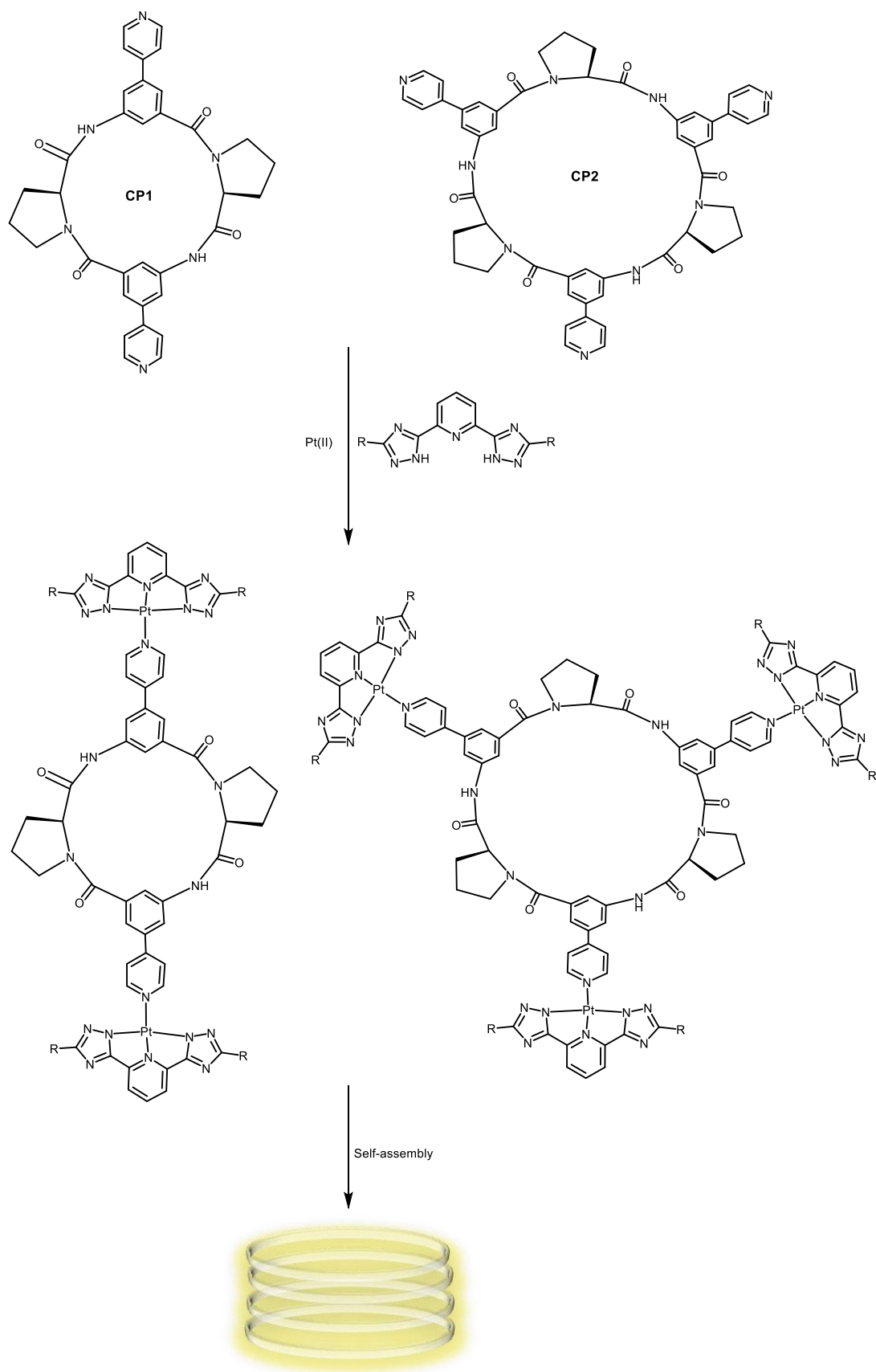


**Figure 66** General structures of the diplatinum(II) and triplatinum(II) complexes that should be prepared from CP1 and CP2.

## 2.3. RESULTS AND DISCUSSION

### 2.3.1 Synthesis of the Azole-based Ligands and Pt(II) Precursors

The synthesis of the different tridentate azole-based ligands used was performed according to described procedures.<sup>142</sup> It started with the aminoamidine formation by reacting pyridine-2,6-dicarbonitrile (**22**) with hydrazine monohydrate (**23**) in ethanol to obtain the pyridine-2,6-bis(carboximidhydrazide) **24** (Figure 67).

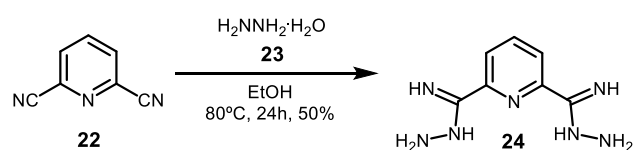


**Figure 67** Synthetic scheme for the synthesis of pyridine-2,6-bis(carboximidhydrazide) **24** from pyridine-2,6-dicarbonitrile **22**.

The final tridentate ligands **27a,b,c** were obtained in a two-step reaction, starting with the acylation of the NH<sub>2</sub> groups of **24** by the appropriate carboxylic acids **25a,b,c** at 80°C to obtain the intermediates **26a,b,c**, followed by 1,2,4-triazole formation in the presence of ethylene glycol (Figure 68).

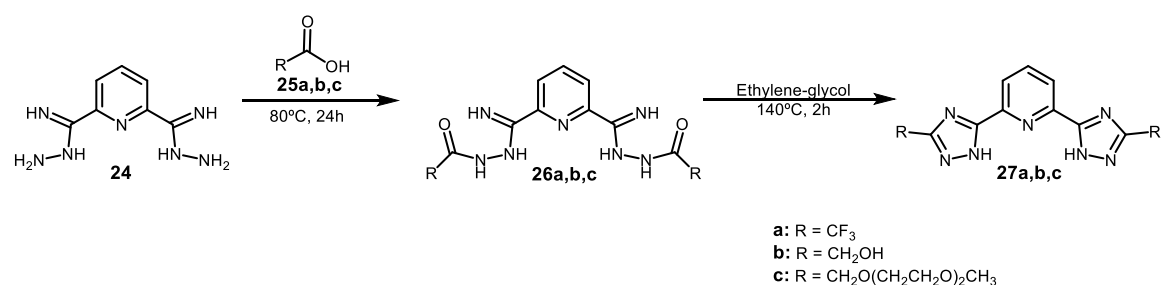


**Figure 68** Synthetic scheme for the synthesis of the three tridentate 1,2,4-triazole-based ligands **27a,b,c**.

Specifically, the ligand **27a** was synthesized by dissolving compound **24** (Figure 68) in trifluoroacetic acid **25a**. Purification was achieved by adding an excess of water to the reaction mixture to obtain **27a** as the precipitate.

Since it was expected that the CF<sub>3</sub> groups in **27a** reduce the solubility of the ligands in the polar solvents required to dissolve the cyclopeptides,<sup>143</sup> the ligands **27b** and **27c** with polar substituents were also prepared. These ligands were synthesized by reacting compound **24** (Figure 68) with glycolic acid **25b** or 2-(2-(2-methoxyethoxy)ethoxy)acetic acid **25c**, respectively.

The purification of these compounds was more demanding than that of **27a**. The addition of water to the reaction mixture of **27b** only precipitated some impurities and no precipitate was formed from the solution of **27c**. Since the purification of the products could not be achieved by simple precipitation, they were purified chromatographically.

Thus, **27b** was obtained by preparative reversed-phase (RP8) column chromatography with minor impurities that were removed by precipitation with chloroform. Ligand **27c** could not be purified by using this chromatographic method, but purification was accomplished by preparative high performance liquid chromatography (HPLC) on a reversed-phase.

The Pt(II) precursor [Pt(DMSO)<sub>2</sub>Cl<sub>2</sub>] (**29**) that was used for the coordination between the cyclopeptides and the tridentate azole-based ligands was prepared by exchanging two chloride ions of the commercially available potassium tetrachloroplatinate(II) K<sub>2</sub>PtCl<sub>4</sub> (**28**) for DMSO (Figure 69) as described in the literature.<sup>142</sup>

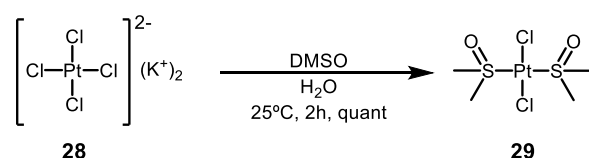


**Figure 69** Synthetic scheme for the synthesis of the Pt(II) precursor, [Pt(DMSO)<sub>2</sub>Cl<sub>2</sub>] (**29**), from the commercially available potassium tetrachloroplatinate(II) K<sub>2</sub>PtCl<sub>4</sub> (**28**).

The complex **30** was prepared by treating **27a** and **29** in DMF at 75°C (Figure 70).<sup>144</sup> Unfortunately, attempts to obtain the analogous complexes from **27b** and **27c** did not afford the desired products. No evidence of the successful formation of the Pt(II)



complexes of **27b** and **27c** was found in the ESI-TOF mass spectra of the respective reaction mixtures even after 7d and the use of an excess of  $[\text{Pt}(\text{DMSO})_2\text{Cl}_2]$  (**29**).

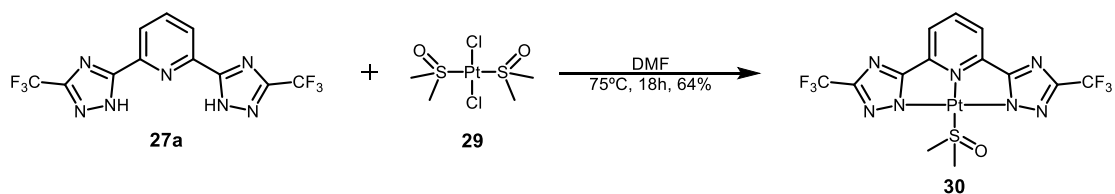


**Figure 70** Synthetic scheme describing the preparation of the Pt (II) complex **30**.

### 2.3.2 Coordination Studies between Pt(II) Complex **30** and the Cyclopeptides

The preparation of the target complexes **PtCF<sub>3</sub>-CP1** and **PtCF<sub>3</sub>-CP2** (**Figure 71**) was initially attempted by adding 3.3 equivalents of **30** to cyclotetrapeptide **CP1** in acetonitrile or 5.0 equivalents of **30** to cyclohexapeptide **CP2** (**Figure 72**).

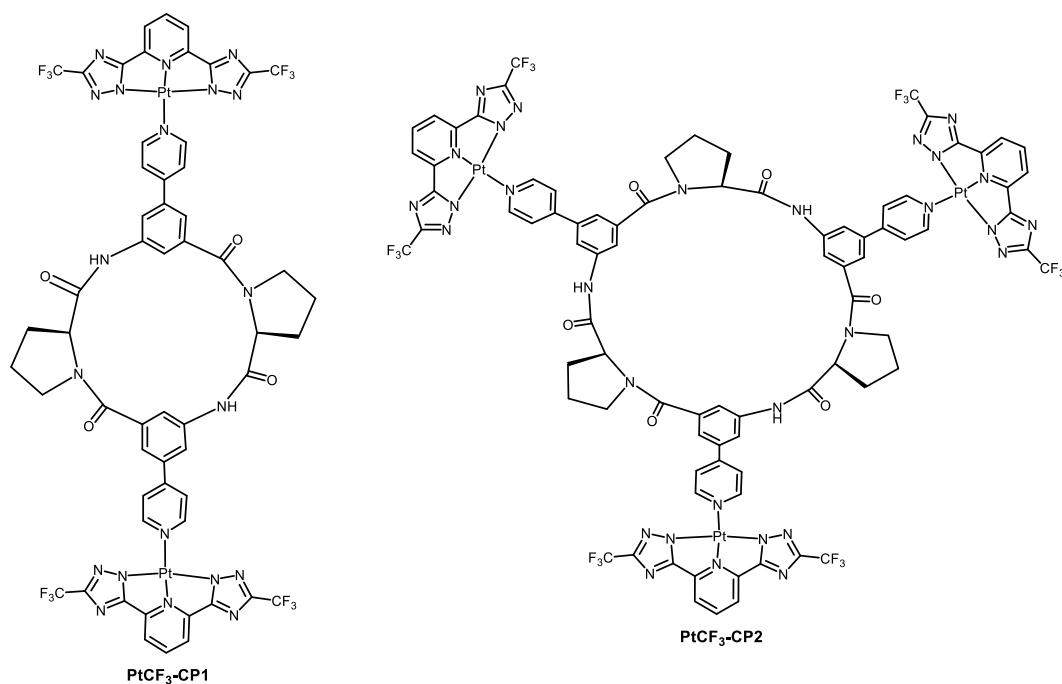


**Figure 71** Structures of the target complexes **PtCF<sub>3</sub>-CP1** and **PtCF<sub>3</sub>-CP2** from the reactions between the cyclopeptides **CP1** or **CP2** and Pt(II) complex **30**.

The suspensions were left stirring at room temperature until the solvent was completely evaporated. Acetonitrile was then added, the suspensions were centrifuged, and the supernatant discarded. This process was repeated four times with acetonitrile, two times with methanol and one time with dichloromethane (**Figure 72**). The resulting precipitates were analysed by NMR spectroscopy and ESI-MS spectrometry.

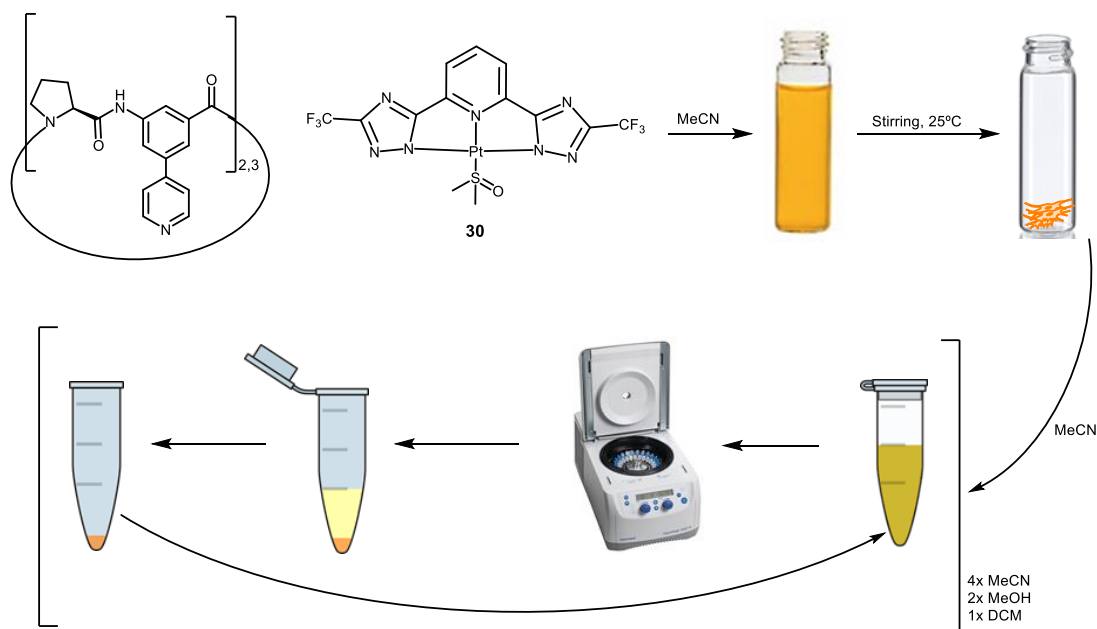


**Figure 72** Schematic representation of the initial attempt to obtain metal complexes from cyclopeptides **CP1** and **CP2** and the Pt(II) complex **30**.

Unfortunately, the expected coordination complexes were not obtained under these conditions. The ESI-MS spectra of the precipitates contained peaks corresponding to compound **30**, free **27a** and free cyclopeptides but no peaks that indicated complexation. The <sup>1</sup>H NMR spectra exhibited complex sets of signals inconsistent with the symmetric structures of the expected products.

To exclude that this result was due to the solvent, analogous experiments were performed also in DMF (**Figure 73**). The solutions were left stirring for 48h, followed by the addition of water to precipitate potential products. The precipitates were centrifuged and subjected to several washing cycles with different solvents (**Figure 73**).

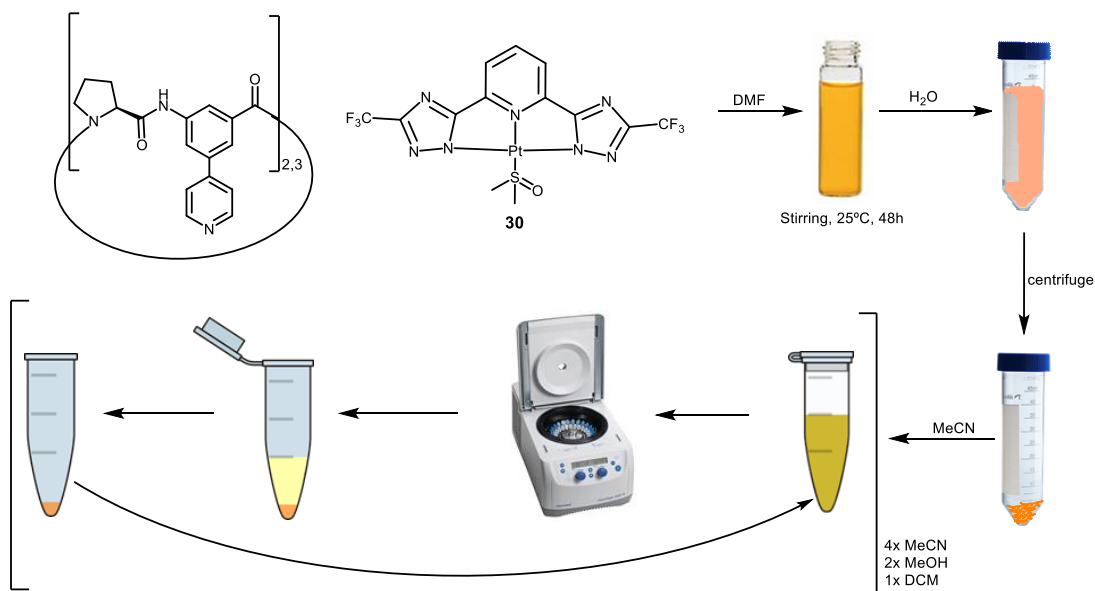
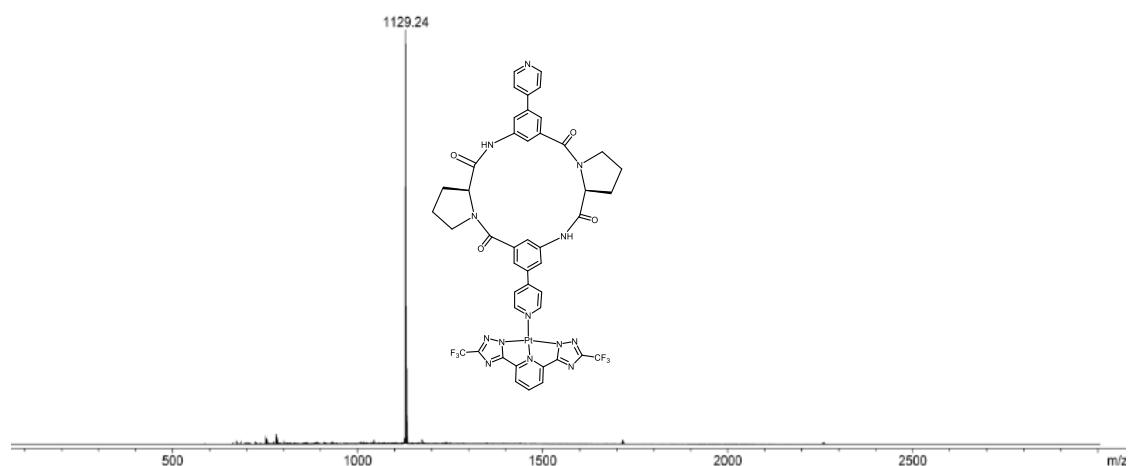


**Figure 73** Schematic representation of the subsequent attempts to obtain metal complexes from the cyclopeptides **CP1** and **CP2** and the Pt(II) complex **30**.

The thus obtained solids had an extreme low solubility, especially in deuterated solvents. Accordingly, NMR spectroscopic characterization was not possible. However, information about complex formation could be derived from ESI-TOF MS spectrometry and from the luminescent properties of the precipitates.

As shown in **Figure 74**, the ESI-TOF MS spectrum of the precipitates resulting from the reaction between **CP1** and **30** contained a single peak at  $m/z = 1129.24$ , which corresponded to the mass of protonated **CP1** with only one pyridine ring coordinated to a platinum(II) centre. The reaction conditions were altered to test whether complete conversion could be achieved by prolonging the reaction time or performing the reaction at higher temperatures. In all cases, only the monometallic complex was obtained.

Considering that **30** was present in excess in all experiments, the failure to obtain the dimetallic complex was attributed to steric effects that prevent both pyridine units of **CP1** to coordinate to a platinum complex.

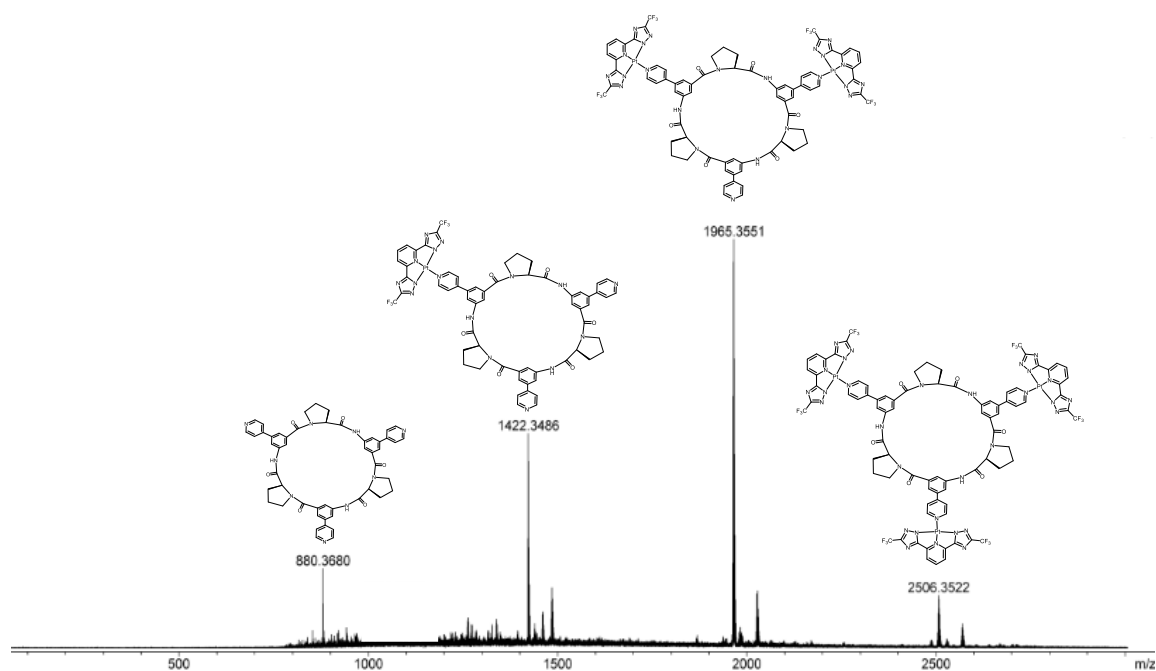


		<i>m/z calcd.</i>	<i>m/z exp.</i>
[CP1·30]+H <sup>+</sup>	C <sub>45</sub> H <sub>33</sub> F <sub>6</sub> N <sub>13</sub> O <sub>4</sub> Pt + H <sup>+</sup>	1129.24	1129.24

**Figure 74** ESI-TOF MS spectrum of the reaction between **CP1** and **30**.

The use of the larger cyclopeptide **CP2** was therefore expected to facilitate product formation. Indeed, the ESI-TOF MS spectrum of the reaction mixture containing **CP2** and **30** in DMF contained peaks corresponding to complexes of **CP2** with different levels of complexation. The peaks at  $m/z = 880.37$ ,  $1422.35$  and  $1965.36$  were assigned to protonated forms of free **CP2** and **CP2** containing one and two tridentate ligands (**Figure 75** ESI-TOF MS spectrum of the reaction between **CP2** and **30**). More importantly, the peak at  $m/z = 2506.35$  was assigned to the protonated target complex [**CP2·30**<sub>3</sub>], indicating that the cyclohexapeptide **CP2** allowed accessing a trimetallic platinum(II) complex.

Since NMR characterization was not possible, elemental analysis was used to assess whether a pure compound was isolated and the different peaks in the mass spectrum were due to fragmentation or whether the isolated material was indeed a mixture of products. Unfortunately, the products resulting from the reaction even after further varying the time and conditions were never pure according to ESI-TOF MS spectrometry and elemental analysis. Since purification was not possible due to the extremely low solubility of the Pt(II) complexes, only the luminescence of the mixture could be qualitatively investigated.



		<i>m/z calcd.</i>	<i>m/z exp.</i>
[CP2+H] <sup>+</sup>	C <sub>51</sub> H <sub>45</sub> N <sub>9</sub> O <sub>6</sub> + H <sup>+</sup>	880.36	880.37
[CP2·30]+H <sup>+</sup>	C <sub>62</sub> H <sub>48</sub> F <sub>6</sub> N <sub>16</sub> O <sub>6</sub> Pt + H <sup>+</sup>	1422.36	1422.35
[CP2·30 <sub>2</sub> ]+H <sup>+</sup>	C <sub>73</sub> H <sub>51</sub> F <sub>12</sub> N <sub>23</sub> O <sub>6</sub> Pt <sub>2</sub> + H <sup>+</sup>	1965.52	1965.36
[CP2·30 <sub>3</sub> ]+H <sup>+</sup>	C <sub>84</sub> H <sub>54</sub> F <sub>18</sub> N <sub>30</sub> O <sub>6</sub> Pt <sub>3</sub> + H <sup>+</sup>	2506.36	2505.35

**Figure 75** ESI-TOF MS spectrum of the reaction between **CP2** and **30**

When a suspension of **30** in DMF was exposed to UV light ( $\lambda_{\text{exc}}=366\text{nm}$ ), orange emission was observed, typical for intermolecular Pt...Pt interactions due to aggregate formation (**Figure 76a**).<sup>142</sup> The solids obtained from the reaction between **CP1** and **30** (**Figure 73**) were also suspended in DMF and in this case blue emission was observed after UV exposure (**Figure 76b**), characteristic for ligand-centred (LC) transitions. If stacked aggregates would be present in this solution, the emerging intermolecular metal...metal interactions of the Pt(II) centres should change the emission to yellow.<sup>145</sup>

The DMF suspension of the solids obtained from the reaction between **CP2** and **30**, however, displayed bright yellow emission after UV exposure (**Figure 76c**), indicating that

intramolecular<sup>142</sup> or intermolecular<sup>145</sup> Pt...Pt interactions arising from aggregation occur in this system.

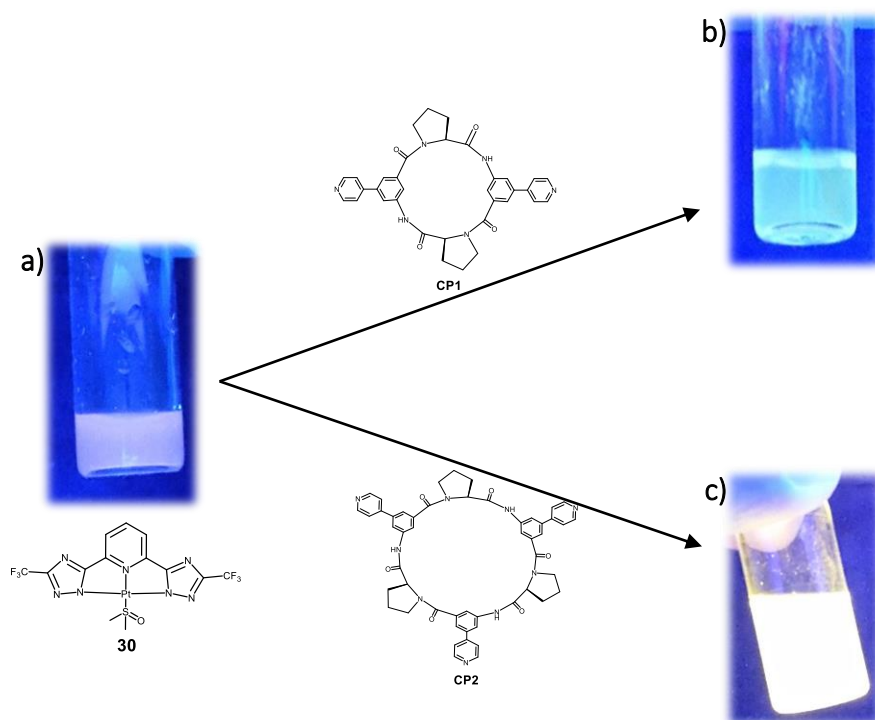


**Figure 76** Luminescent properties of DMF suspensions of compound **30** (a), of the precipitate resulting from the reaction between **CP1** and **30** (b) and of the precipitate resulting from the reaction between **CP2** and **30** (c) when excited at 366nm.

Although these results demonstrated that **CP1** and **CP2** coordinate to platinum(II) centres, the derived complexes could not be isolated in pure form. Both cyclopeptides influence the luminescence properties of complex **30** but no clear evidence for an aggregation was obtained.

### 2.3.3 Coordination Studies Between Pt(II) Complexes of Ligand **27b** and the Cyclopeptides

To address the solubility issues observed for the Pt(II) complexes containing the ligand **27a**, the preparation of analogous cyclopeptide complexes containing the more polar ligand **27b** was attempted. Since the synthesis of the corresponding precursor corresponding to the Pt(II) complex **30** was unsuccessful, a one-pot synthesis using a non-nucleophilic base

(DIPEA),  $[\text{Pt}(\text{DMSO})_2\text{Cl}_2]$  (**29**), **27b** and the cyclopeptides was used to obtain the target compounds.<sup>145</sup>

In the case of **CP1**, equimolar amounts of **27b** and  $[\text{Pt}(\text{DMSO})_2\text{Cl}_2]$  (**29**) were heated in DMF at 80°C prior to the addition of 0.3 equivalents of **CP1** (Figure 77).

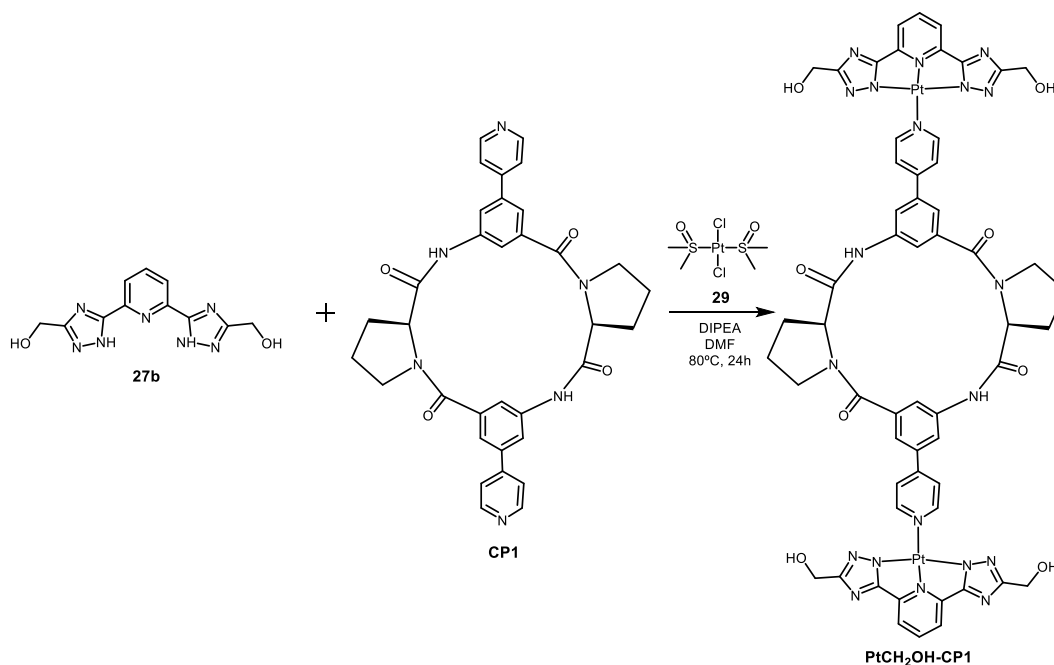


**Figure 77** One-pot procedure for the attempted synthesis of the cyclopeptide-containing dimetallic platinum(II) complex **PtCH<sub>2</sub>OH-CP1**.

For **CP2**, the procedure was the same, but the ratio of the compounds was accordingly adapted (Figure 78). After 24h, a sample of both reaction mixtures was collected and analysed by ESI-TOF and MALDI-TOF mass spectrometry. No peaks were present in the spectra of both reactions that could be assigned to the expected products. The mixtures were therefore allowed to react for six more days and samples were collected and analysed by mass spectrometry every 24h. In none of the obtained mass spectra, peaks of the target compounds were observed, even after the addition of further equivalents of **27b**,  $[\text{Pt}(\text{DMSO})_2\text{Cl}_2]$  and DIPEA.

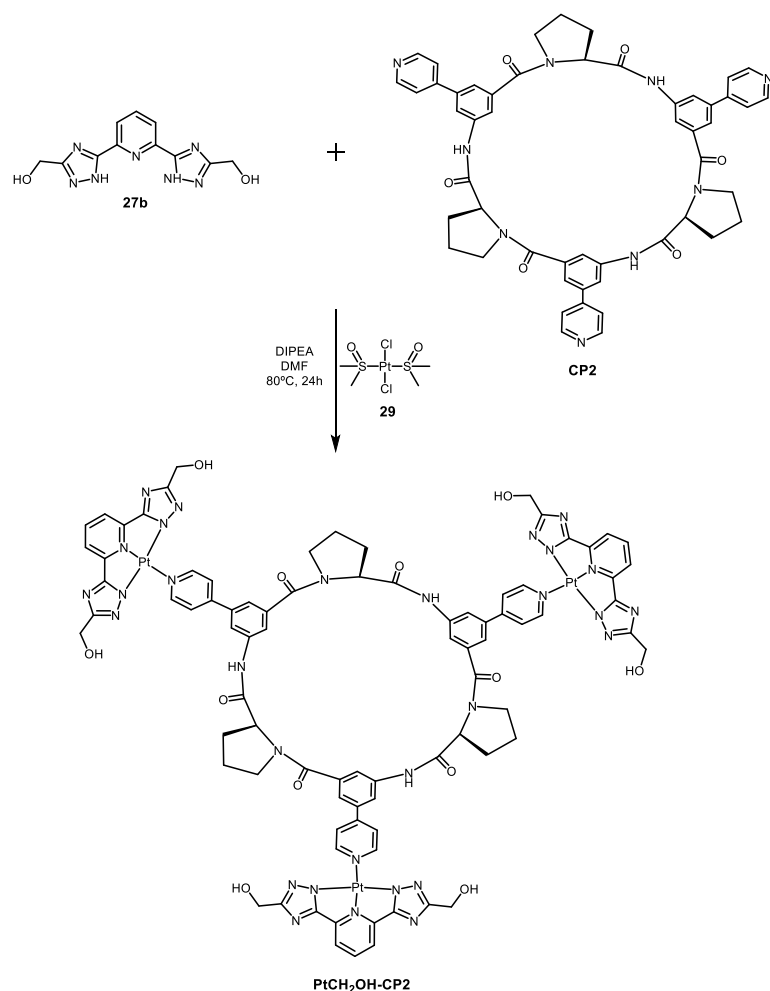


**Figure 78** One-pot procedure for the attempted synthesis of the cyclopeptide-containing trimetallic platinum(II) complex **PtCH<sub>2</sub>OH-CP2**.

To assess whether the reaction conditions are suitable for the attempted synthesis, a coordination reaction containing **27b**, [Pt(DMSO)<sub>2</sub>Cl<sub>2</sub>], DIPEA and pyridine was performed under the same conditions (**Figure 79**). Again, a sample was collected and analysed by mass spectrometry. No peaks corresponding to the expected product **31** were observed even after prolonged reaction times. From these results it could be concluded that Pt(II) complexation involving **27b** was probably not possible. An explanation for the failed coordination could be the basic conditions necessary for this reaction, under which also the OH groups could be partially deprotonated, creating a coordination site that competes with the deprotonated triazole rings for the metal centres.



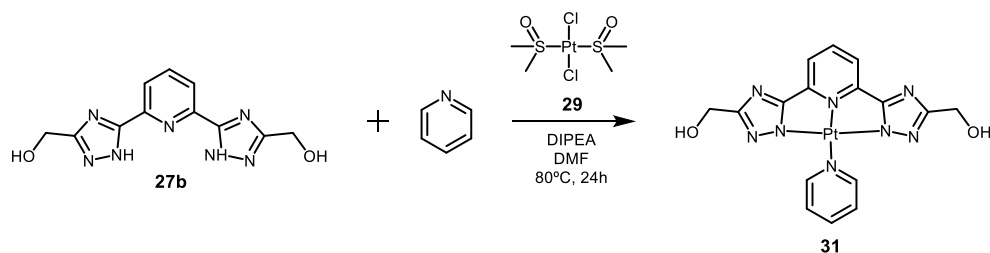


**Figure 79** One-pot procedure for the attempted synthesis of the pyridine containing platinum(II) complex **31**.

### 2.3.4 Coordination Studies Between Pt(II) Complexes of Ligand **27c** and the Cyclopeptides

The tridentate ligand **27c** was synthesized to circumvent the potential deprotonation issues associated with **27b**. To test if complexation would be possible with this ligand, the one-pot synthesis of the pyridine complex **32** was initially tested (**Figure 80**). An equimolar amount of **27c** and  $[Pt(DMSO)_2Cl_2]$  were dissolved in DMF, treated with DIPEA and subsequently with pyridine.

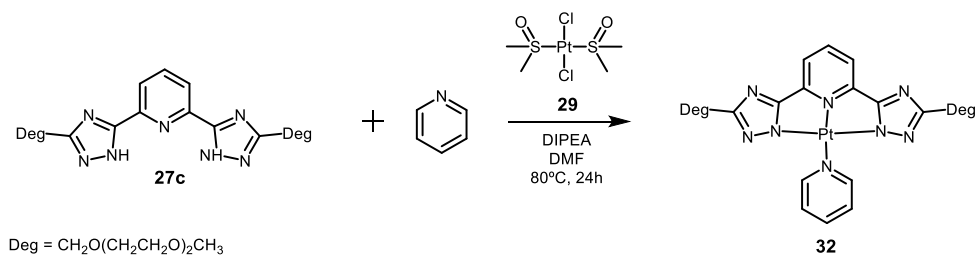
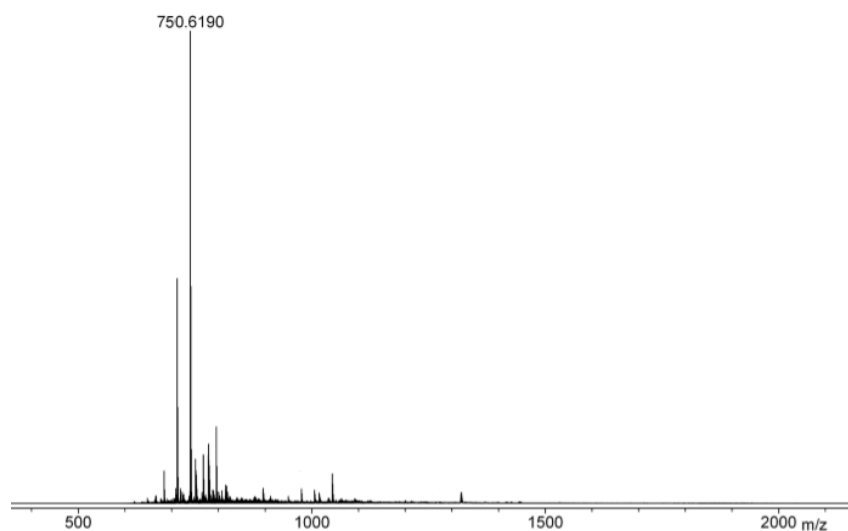


**Figure 80** One-pot synthetic procedure for the formation of the pyridine-derived neutral platinum(II) complex **32**.

The ESI-TOF MS spectrum (**Figure 81**) of the reaction mixture in this case contained a prominent peak at  $m/z$  750.62, corresponding to the protonated complex **32**. Thus, Pt(II) coordination was successful in this case.



		<i>m/z</i> calcd.	<i>m/z</i> exp.
[ <b>32</b> +H] <sup>+</sup>	C <sub>26</sub> H <sub>34</sub> N <sub>8</sub> O <sub>6</sub> Pt + H <sup>+</sup>	750.23	750.62

**Figure 81** ESI-TOF MS spectrum of the reaction mixture resulting from treating **27c**, [Pt(DMSO)<sub>2</sub>Cl<sub>2</sub>] and pyridine.

Since complex formation seems to be possible in this case, the same conditions were used to react **27c**, [Pt(DMSO)<sub>2</sub>Cl<sub>2</sub>] and **CP1** (**Figure 82**).

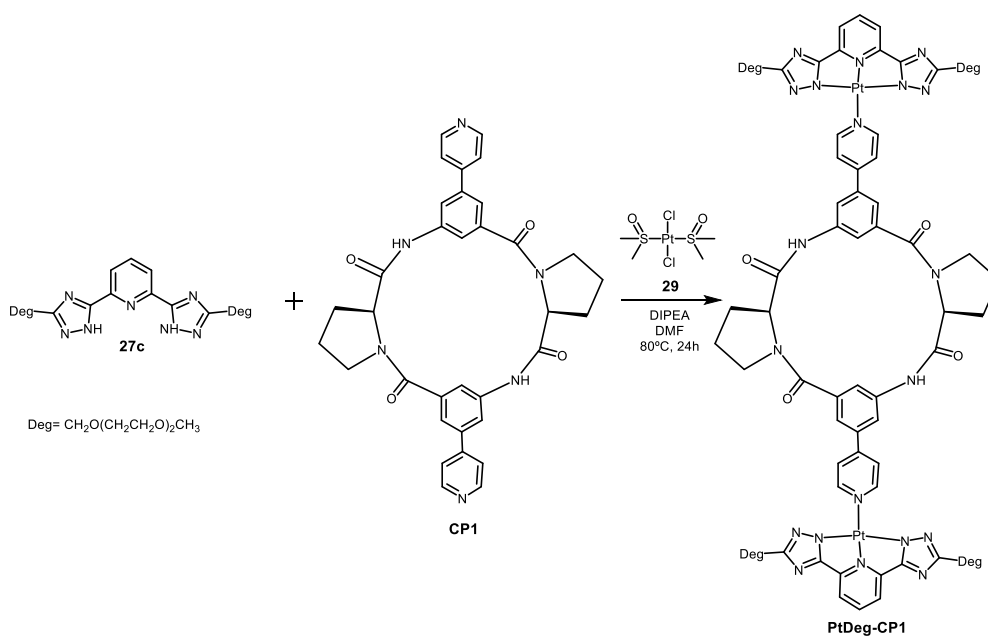


**Figure 82** Attempted one-pot synthesis of the cyclopeptide-containing dimetallic platinum(II) complex **PtDeg-CP1**.

In an analogous fashion, **CP2** was reacted with **27b**, [Pt(DMSO)<sub>2</sub>Cl<sub>2</sub>] and DIPEA in DMF (**Figure 83**).

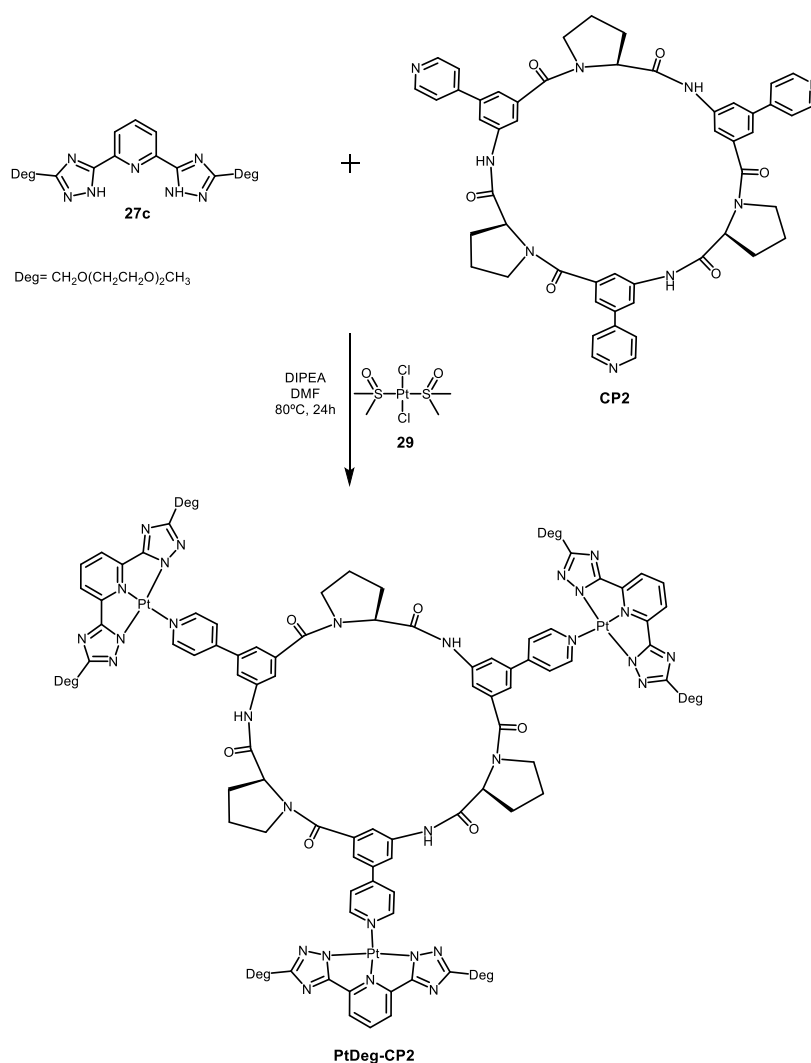


**Figure 83** Attempted one-pot synthesis of the cyclopeptide-containing trimetallic platinum(II) complex **PtDeg-CP2**.

Samples from both reactions were analysed by mass spectrometry after 24h. Neither the ESI-TOF nor the MALDI-TOF mass spectra contained peaks corresponding to the target compounds **PtDeg-CP1** or **PtDeg-CP2**. The samples were allowed to react for six more days, during which more equivalents of **27c**, [Pt(DMSO)<sub>2</sub>Cl<sub>2</sub>] and DIPEA were added.

No significant changes were visible in the mass spectra, so the reactions were stopped, the solvents evaporated and the residues dried under vacuum. The high luminescence observed for the aqueous solutions of the crude products when exposed to UV light ( $\lambda_{\text{exc}} =$

366 nm) (**Figure 84**) was indirect evidence that Pt(II) complexation occurred since, on their own, **27c**,  $[\text{Pt}(\text{DMSO})_2\text{Cl}_2]$ , **CP1** or **CP2** had no luminescent properties.

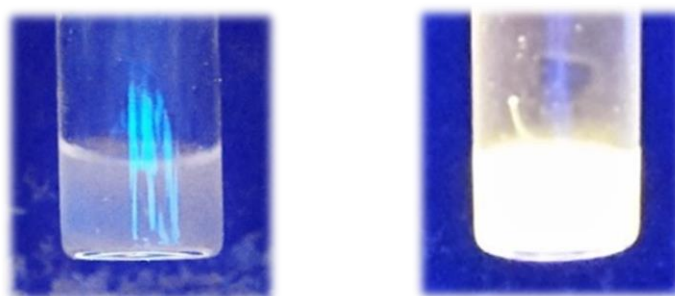


**Figure 84** Luminescent properties of the aqueous solutions of the crude products resulting from the reactions between **27c**,  $[\text{Pt}(\text{DMSO})_2\text{Cl}_2]$  and a) **CP1**, b) **CP2**, under UV light ( $\lambda_{\text{exc}} = 366 \text{ nm}$ ).

The fact that the emission was orange for the sample containing **CP1** (**Figure 84a**) was promising, since it suggested that with this ligand, contrarily to what was observed for **27a**, both pyridine residues might engage in Pt(II) coordination or that aggregation occurred.

The crude products containing **27c** were highly soluble in a wide range of solvents, including in water. Therefore, a separation was attempted by using reversed-phase chromatography on a RP8 column.

The RP-TLC (Reverse Phase Thin Layer Chromatography) plates from the crude samples with **CP1** and **CP2** exhibited different spots of which only one was orange emissive when excited at 366nm. The fractions containing this product after separation on a column were combined and isolated. Subsequently, the  $^1\text{H}$  NMR spectra of the obtained substances were recorded in  $\text{D}_2\text{O}$  and compared with the spectrum of the free ligand **27c** (**Figure 85**).

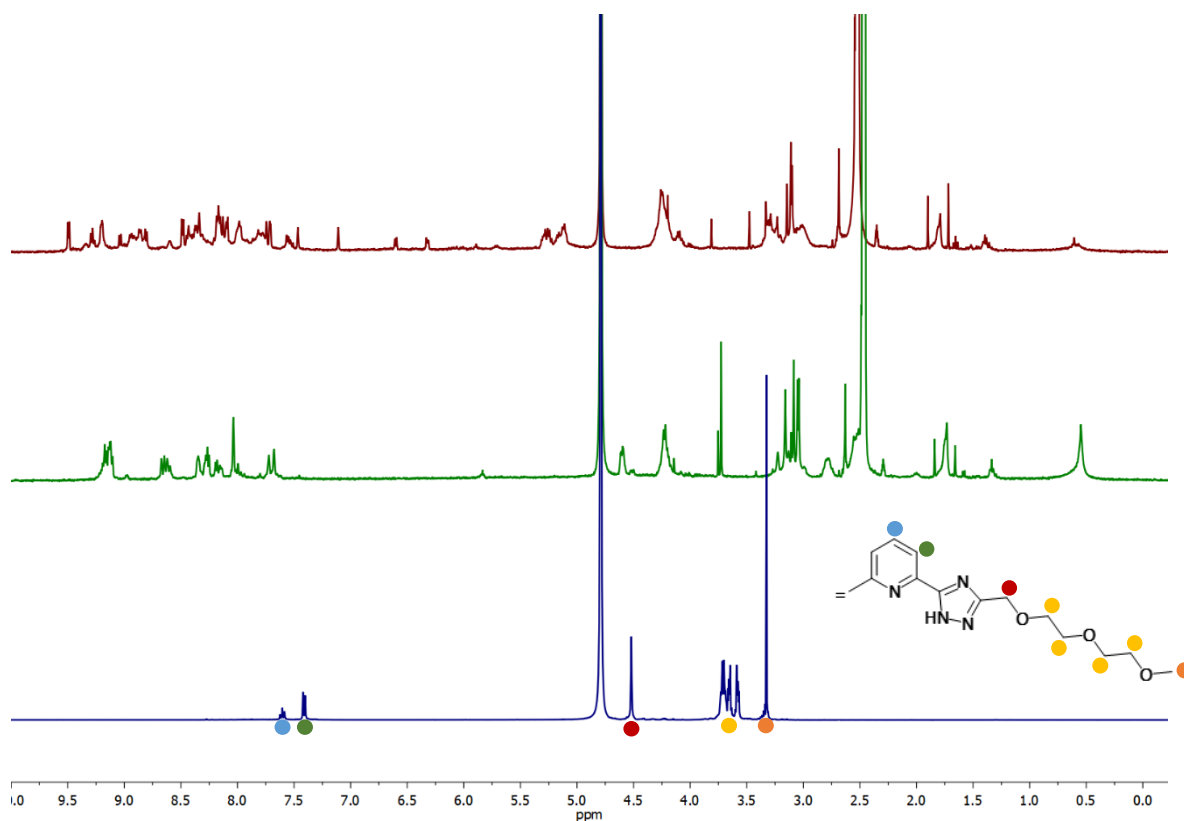


**Figure 85**  $^1\text{H}$  NMR spectra of **27c** (blue) and of the Pt(II) complexes purified by RP8 column chromatography of **CP1** (green) or **CP2** (red).

The target complexes of **CP1** and **CP2** are symmetric structures and therefore simple  $^1\text{H}$  NMR spectra were expected. However, the spectra of the purified samples were both complex (**Figure 85**). The integration of the peaks moreover did not afford results that were consistent with the expected number of protons in the products, suggesting that the products were still not pure. Thus, purification was attempted by preparative HPLC.

As can be observed in **Figure 86**, the HPLC chromatograms of the samples contained several peaks confirming that the products indeed had a more complex composition than expected from the RP8 column. Fractions corresponding to each signal were collected, evaporated and dried under vacuum.

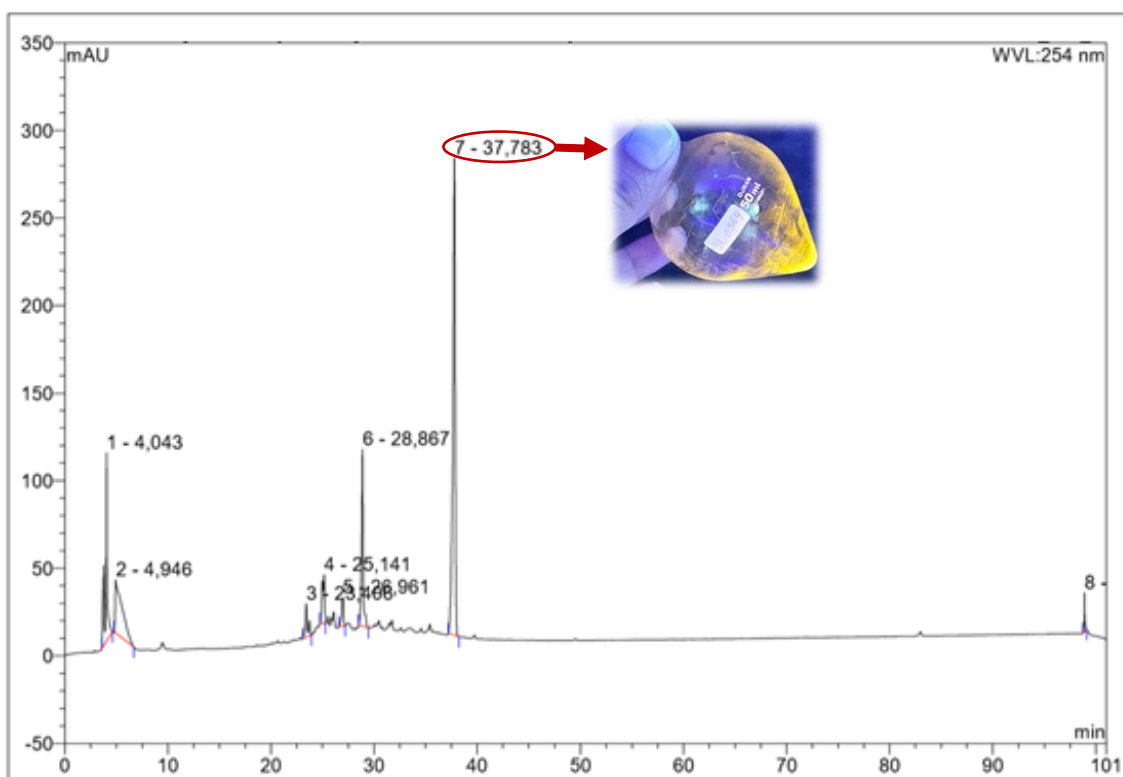
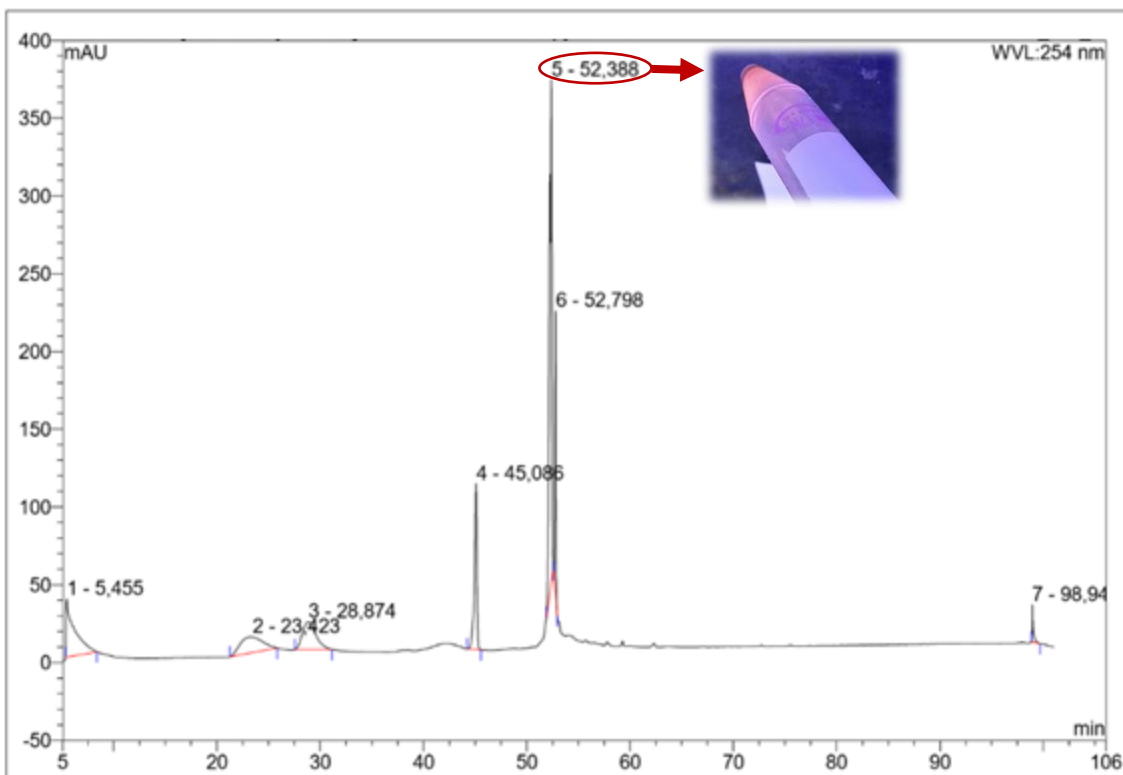


**Figure 86** HPLC chromatograms of the Pt(II) complexes purified by RP8 column chromatography containing CP1 (top) or CP2 (bottom). Luminescent properties of the products obtained from the marked fractions under UV light ( $\lambda_{exc} = 366$  nm).

Due to the small scale in which these reactions were performed, NMR spectroscopy and elemental analysis could not be used to characterize the products. However, when the different dried products were exposed to UV light ( $\lambda_{\text{exc}} = 366 \text{ nm}$ ), only two exhibited luminescence (**Figure 86**). From the sample containing **CP1**, solely the product from the fraction corresponding to the peak at the retention time 52.4 min was orange emissive, and from the sample with **CP2** the product at the signal with a retention time of 37.8 min was yellow emissive. This was strong evidence that these peaks corresponded to Pt(II) complexes.

ESI-TOF MS spectra of the products did not contain peaks corresponding to the expected products. However, trace amounts of these compounds were observed by MALDI-TOF MS.

The MALDI-TOF MS spectrum (**Figure 87**) from the HPLC product obtained from **CP1** contained peaks at  $m/z = 1257.43$  and  $1927.64$ , which corresponded to the masses of the singly protonated complexes of **CP1** with one pyridine coordinated to Pt(II) and **27c** and the expected dimetallic complex **PtDeg-CP1**, respectively.

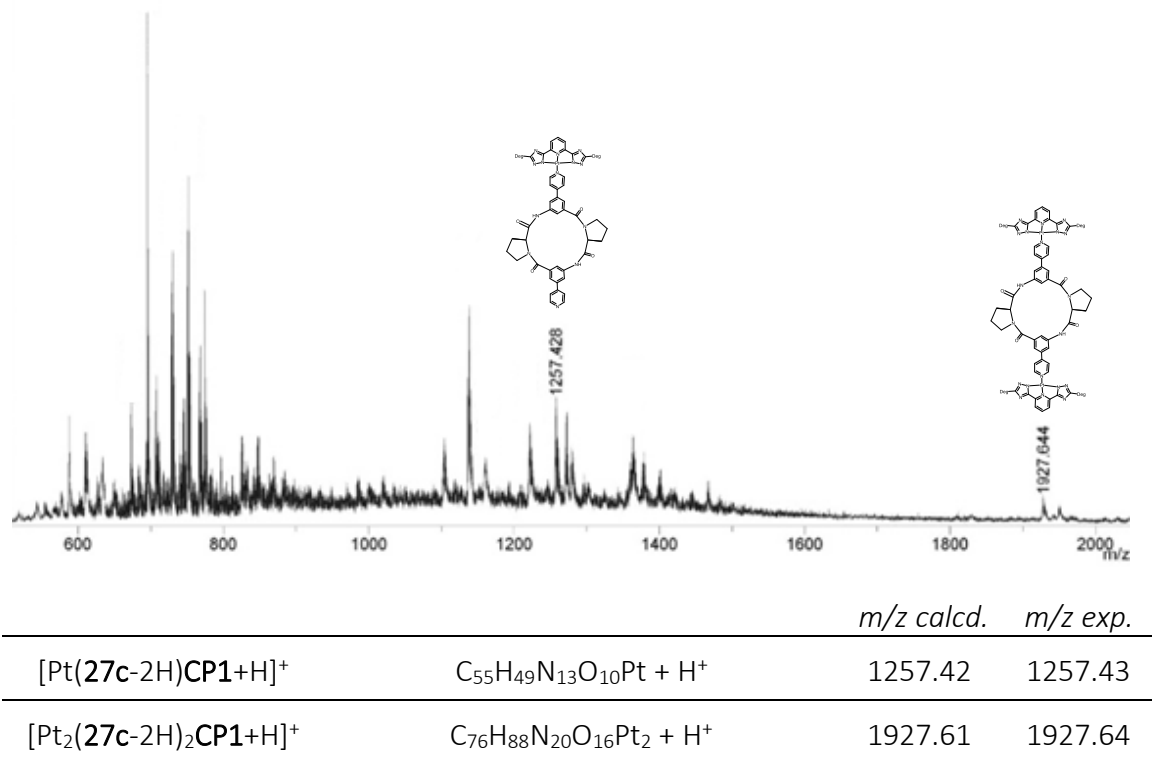
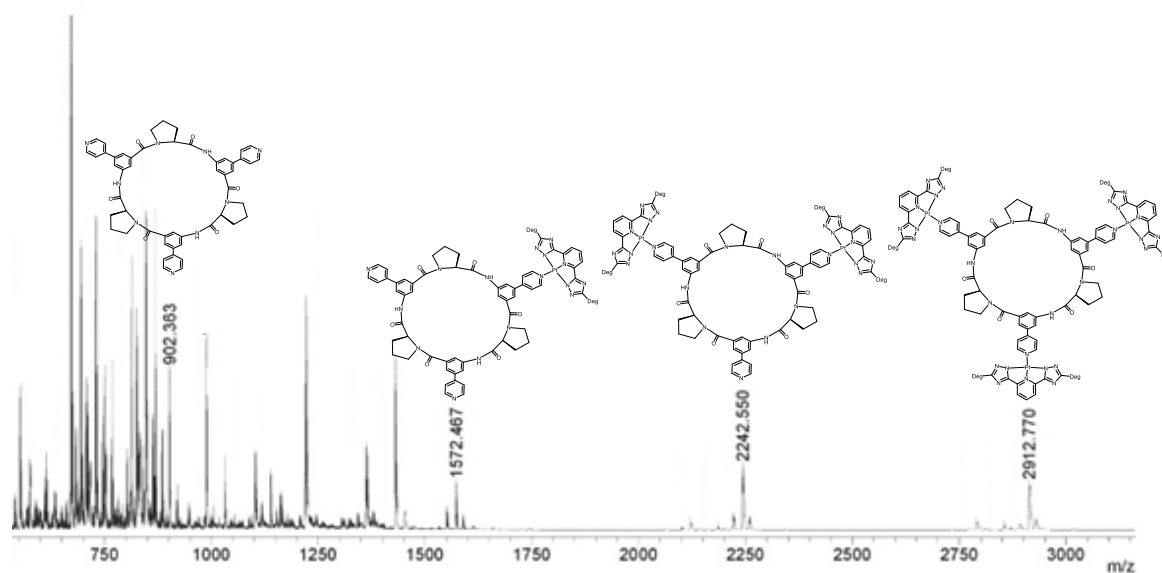


**Figure 87** MALDI-TOF MS spectrum of the product isolated by HPLC that gave a peak in the chromatogram at retention time 52.4 min.

The spectrum of the sample with **CP2** (**Figure 88**) contained peaks at  $m/z = 902.36$ , 1572.47 and 2242.55 that were assigned to the  $\text{Na}^+$  adducts of **CP2** and the mono- and dimetallic Pt(II) complexes of **CP2**, respectively. The peak at  $m/z = 2912.77$  corresponded to the  $\text{Na}^+$  adduct of the trimetallic target complex **PtDeg-CP2**.



		<i>m/z calcd.</i>	<i>m/z exp.</i>
$[\text{CP2}+\text{Na}]^+$	$\text{C}_{51}\text{H}_{45}\text{N}_9\text{O}_6 + \text{Na}^+$	902.34	902.36
$[\text{Pt}(\text{27c-2H})\text{CP2}+\text{Na}]^+$	$\text{C}_{72}\text{H}_{74}\text{N}_{16}\text{O}_{12}\text{Pt} + \text{Na}^+$	1572.52	1572.47
$[\text{Pt}_2(\text{27c-2H})_2\text{CP2}+\text{Na}]^+$	$\text{C}_{93}\text{H}_{103}\text{N}_{23}\text{O}_{18}\text{Pt}_2 + \text{Na}^+$	2242.70	2242.55
$[\text{Pt}_3(\text{27c-2H})_3\text{CP2}+\text{Na}]^+$	$\text{C}_{114}\text{H}_{132}\text{N}_{30}\text{O}_{24}\text{Pt}_3 + \text{Na}^+$	2912.89	2912.77

**Figure 88** MALDI-TOF MS spectrum of the product isolated by HPLC that gave a peak in the chromatogram at 37.8 min.

Even though MALDI-TOF MS confirmed the presence of the target complexes **PtDeg-CP1** and **PtDeg-CP2** in the products obtained by HPLC, the intensity of the peaks corresponding to these species was quite low and both spectra contained many other signals, which could be due to fragmentation during ionization or an indication that the products were impure. To address this issue, the reactions would have to be repeated at a larger scale to allow characterization of the products by means of NMR spectroscopy and elemental analysis. If it would turn out that the products after HPLC were indeed impure, then the next step for



purification could be to use size exclusion column chromatography to separate the target complexes from the ones in which Pt(II) complexation was incomplete.

The scale-up of the reactions and the further characterization of the Pt(II) complexes were not performed during these studies. Thus, the results only provided qualitative evidence that the formation of the neutral Pt(II) coordination compounds **PtDeg-CP1** and **PtDeg-CP2** is indeed possible by using ligand **27c** and the developed one-pot synthesis.

## 2.4. CONCLUDING REMARKS

During the project described in this chapter, the new ligands **27b** and **27c** were successfully synthesized and characterized, and the known Pt(II) complex **30** prepared.

Even though qualitative evidence was obtained that the complexes **PtCF<sub>3</sub>-CP2**, **PtDeg-CP1** and **PtDeg-CP2** could be prepared, their purification and full characterization could not be achieved. Thus, the characterization of the photophysical properties or aggregation behaviour of cyclopeptide-containing Pt(II) complexes could not be performed.

The work can be regarded as a proof-of-concept that emissive neutral Pt(II) complexes bearing tridentate ligands are accessible from cyclopeptides containing pyridyl units. Further investigations must show whether these luminescent cyclopeptides potentially have sensing abilities.



# **3. Luminescent Pt(II) Porphyrin Complexes as Oxygen Sensors for Microfluidic Devices**

This project was performed during the industrial secondment as part of the Marie Curie Innovative Training Network ResMoSys. In this chapter, the work developed at Micronit Micro Technologies B.V (Enschede, The Netherlands) in the months from January 2018 to April 2018 is described. The synthesis and characterization of the compounds required for this project were executed prior to the stay at the Chemistry Department of the TU Kaiserslautern. Biological assays were performed at the University of Twente (BIOS Laboratories). The results obtained were presented by Sandro Meucci, R&D scientist at Micronit, in a talk entitled "Tailoring the extracellular environment of in vitro systems" for the conference Advances in Cell & Tissue Culture (ACTC 2018).



## 3.1. INTRODUCTION

The difficulties associated with drug research and development coupled with rising costs constitute substantial challenges to the pharmaceutical industry.<sup>146</sup> Poor predictive power of existing preclinical models is the primary reason for drug failures in clinical trials, creating a critical need for new testing approaches to improve the effectiveness of preclinical predictions of drug efficacy and safety in humans.<sup>147,148</sup>

Microengineered cell culture may present a solution to this need. Cutting edge microfluidic fabrication have led to the development of chip technologies that replicate the complex structure, microenvironment, and physiological functionality of living human organs.<sup>149–151</sup> These organ-on-a-chip devices present new opportunities of applications ranging from preclinical drug discovery, such as target identification and validation, to target-based screening and phenotypic screening.

### 3.1.1 Organ-on-a-chip Devices

Key functions of human organs can be mimicked by engineered microsystems consisting of transparent 3D polymeric microchannels lined by living human cells. These artificial models are fabricated in such a way that they can replicate three important aspects of intact organs: the 3D microarchitecture defined by the spatial distribution of multiple tissue types, the functional tissue–tissue interfaces, and the complex organ-specific mechanical and biochemical microenvironments.<sup>149,151–155</sup>

These organ-on-a-chip systems provide specialized *in vitro* models for complex biological processes, allowing their simulation, mechanistic investigation, and pharmacological modulation. Over the last years, organ-on-a-chip devices have been used in the development of models that can mimic the structural and functional complexity of human organs such as the liver, heart, lung, intestine, kidney and the brain.<sup>149,156–158</sup>

Other than improving research and development efficiency, organ-on-a-chip devices could be useful to support and accelerate efforts in development treatments for rare diseases, or in stratified medicine and nanomedicine. In addition, they could be viable alternatives

to animal models since they enable direct real-time visualization and quantitative high-resolution analysis of diverse biological processes without requiring large amounts of costly reagents or scale-up.<sup>159</sup> Thus, they may play a pivotal role in streamlining clinical trial processes.<sup>160</sup>

Microfluidic platforms are also powerful tools for studying organic reactions,<sup>161</sup> enzyme kinetics,<sup>162,163</sup> and cells<sup>164,165</sup> at the micro- or nanoscale. However, due to their reduced dimensions, finding new methods to accurately determine analytes is challenging in this context. The use of luminescent chemical sensors integrated into organ-on-a-chip devices has proven to be an effective technique for obtaining online and real-time analytical data at such a small scale.<sup>166</sup>

Amongst the different chemical sensors used, luminescent oxygen sensors<sup>167</sup> are particularly promising due to their high sensitivity, ability for contactless readout, ease of miniaturization, ease of integration, low cost, and the fact that they do not deplete oxygen during the measurements like other types of chemical sensors. Sin et al.<sup>168</sup> were one of the firsts to integrate luminescent oxygen sensors into microfluidic devices.

They developed a silicon based three-chamber “lung-liver-other-on-a-chip” cell culture system (**Figure 89**, left) for mammalian cells that could replace whole animals in the toxicological and pharmacological testing of chemicals. A resin-adsorbed Ru(II) complex was applied at the bottom layer of the chip and coated with poly(dimethylsiloxane) (PDMS) to create an oxygen sensor patch that would monitor whether the oxygen supply for the cells is adequate (**Figure 89**, right).<sup>168</sup>

This type of microfluidic sensor chemistry was also used in differential oxygenators for cell culture<sup>169,170</sup> to determine the oxygen consumption rates of single cells,<sup>171</sup> and in the monitoring of oxygen during microbial fermentations.<sup>172,173</sup>

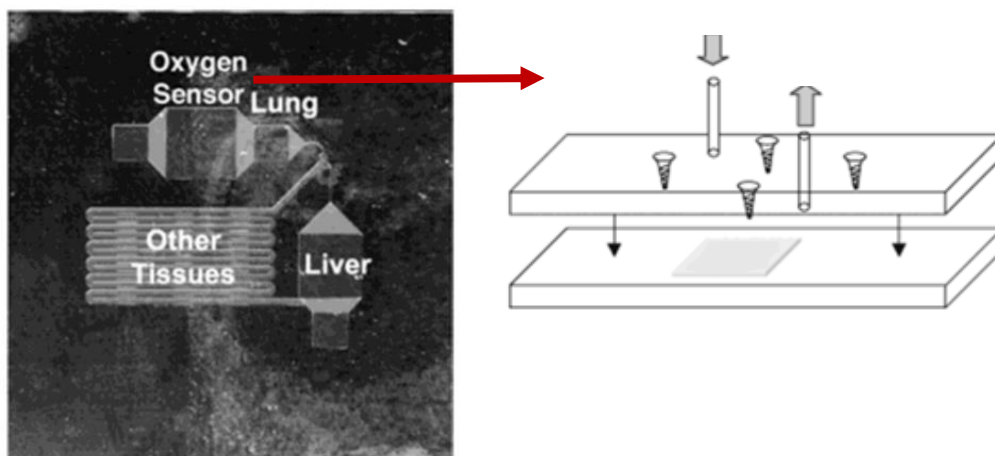


**Figure 89** Left: Photograph of a silicon-based “lung-liver-other-on-a-chip system”. Right: Schematic of the investigated oxygen sensor chip house. © 2004 American Chemical Society and American Institute of Chemical Engineers

Platinum(II) benzo-<sup>174</sup> and naphthoporphyrins<sup>174–176</sup> are among the most popular luminophores for the production of oxygen indicators in organ-on-a-chip devices due to their photostability, strong phosphorescence at room temperature, moderate to high molar absorption coefficients, large Stokes’ shifts and long phosphorescence lifetimes (microsecond to millisecond). Also, these complexes belong to a class of  $\pi$ -extended porphyrins that are characterized by an extended aromatic fragment fused on the porphyrin core, which is responsible for a bathochromic shift of the absorption and emission bands towards the red part of the electromagnetic spectrum.

These red-excitable and NIR emitting indicators are strongly preferred to indicators that absorb light in the UV–vis region for the development of optical oxygen sensors since the latter present some drawbacks like 1) a high level of background noise upon excitation in the UV–vis due to the presence of many natural compounds (such as nucleotides FAD and NAD) present in biological samples that are also fluorescent, 2) low performance in measurements in scattering media such as marine sediments or tissues and 3) unsuitability to be used in implantable sensors since blood efficiently absorbs in the visible region. Since organ-on-a-chip devices mimic biological samples like blood, cells or tissues, the use of the red-excitable Pt(II) porphyrins is highly advantageous for optical oxygen sensing in these media.<sup>177</sup>

An example of the application of red-excitable Pt(II) porphyrins as oxygen indicators in organ-on-a-chip devices was reported by Vollmer *et al.*<sup>169</sup> Pt(II) octaethylporphine ketone **PtOEPK** pads deposited on a microfluidic device acted as luminescent oxygen sensors, allowing the precise real-time detection of gaseous and/or dissolved oxygen (**Figure 90**). The optical sensors were evaluated by using both gaseous and aqueous samples and they exhibited a good linearity, optical stability, resolution, sensitivity and accuracy, with their performance being comparable to known sensors of similar nature.<sup>178–180</sup>

The simple, rapid and inexpensive fabrication protocol combined with a flexible platform for the detection of both gaseous or dissolved oxygen and the biocompatibility of the PDMS material<sup>181</sup> made this microfluidic device ideally suited to be used in different biological applications, ranging from tissue engineering and cell culturing in a microfluidic environment to real-time blood gas detection in a clinical environment or even extracorporeal oxygenation in a surgical setting.

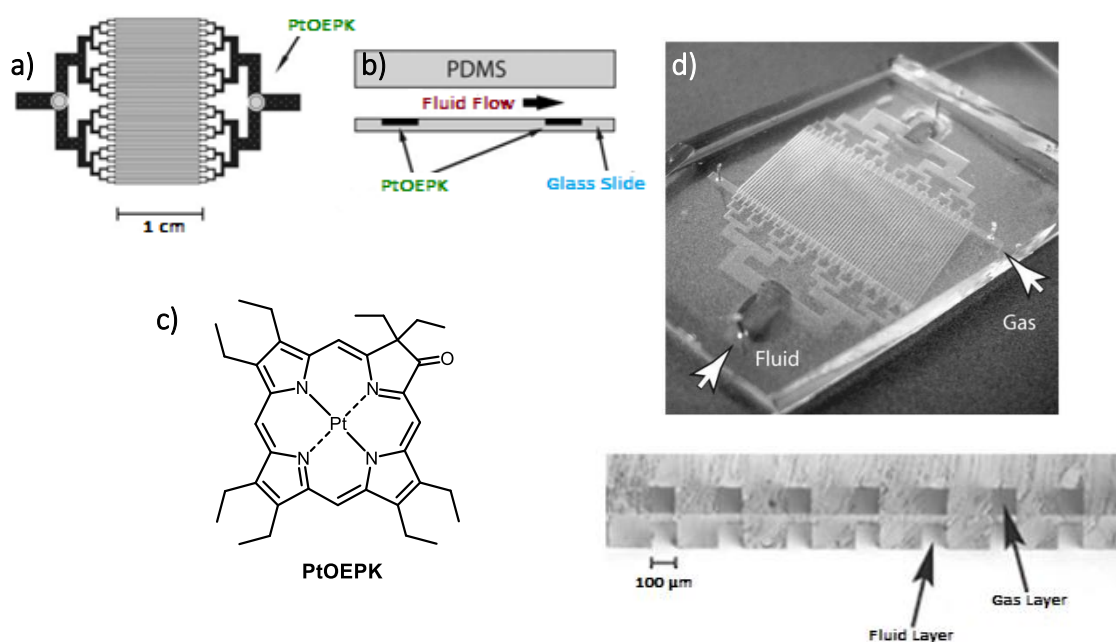


**Figure 90** a) Lithography mask of the capillary structure, showing the location of O<sub>2</sub> sensors. b) Microfluidic device cross section, showing the position of the **PtOEPK** dye sensor pads etched in the glass substrate. c) Chemical structure of the Pt(II) octaethylporphine ketone **PtOEPK**. d) Image showing the location of the sensor pads in an actual device as well as the inlet locations for fluid and gas flow (arrows). e) Cross section view showing the vertical alignment of fluidic and gas channels. The channels are separated by a 20 nm membrane created by spin coating. © The Royal Society of Chemistry 2005



Thomas *et al.*<sup>182</sup> developed a microfluidic system that provided on-chip oxygen control while simultaneously mitigating pervaporation and so avoiding substantial changes in the osmotic pressure of the solution present within the fluidic chambers of the device (**Figure 91**, left). In order to understand how the changes in oxygen level propagated throughout the entire microfluidic system, oxygen sensing films obtained by mixing Pt(II) mesotetrakis(pentafluorophenyl) porphine **PtTFPP** (**Figure 91**, right) with PDMS were integrated into the floor of the microfluidic device, allowing real time, *in situ* monitoring of the oxygen partial pressure.

While other techniques addressed oxygen regulation and pervaporation control separately, this was the first microfluidic approach with the ability to simultaneously regulate the oxygen level and reduce solution evaporation using water-filled control lines.

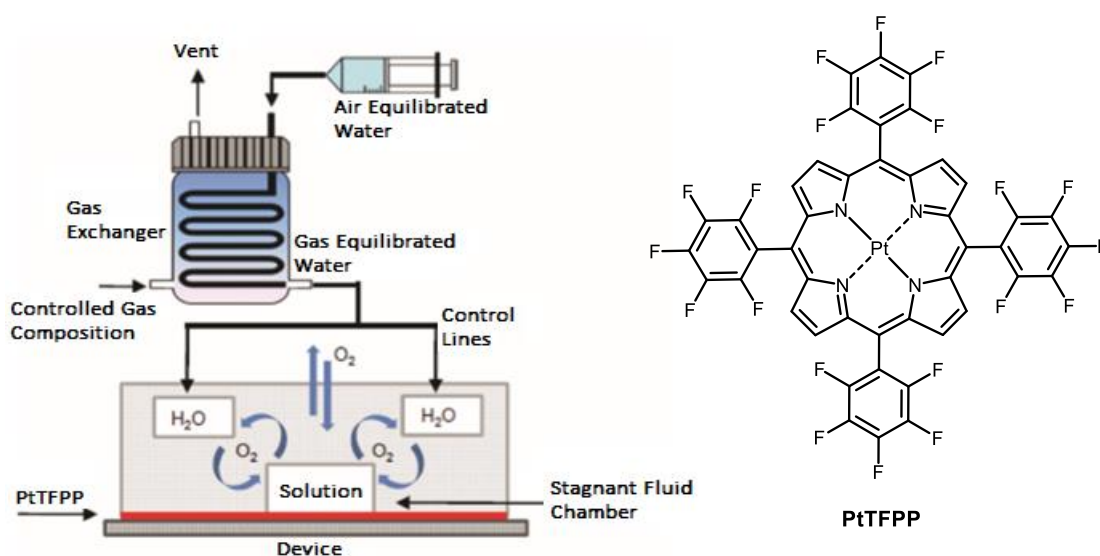


**Figure 91** Left: Schematic of the microfluidic device setup for on-chip oxygen regulation. Water was pumped through the gas exchanger where the partial pressure of oxygen ( $pO_2$ ) in the liquid was reduced via equilibration with the controlled gas composition. This solution then entered the microfluidic control lines flanking the fluid chamber of the device. **PtTFPP** sensor film integrated into the floor of the device (red) measured changes of  $pO_2$  as the dissolved oxygen in the control lines diffused through the PDMS and into the adjacent fluid chamber. © 2011 American Chemical Society. Right: Chemical structure of Pt(II) mesotetrakis(pentafluorophenyl) porphine **PtTFPP**.

A multi-gradient integration in a single microfluidic device for tissue-mimicked cell research was described by Wang *et al.*<sup>183</sup> In this study, an oxygen gradient was generated in a chamber by exchange between the aerial oxygen and the oxygen-free gas-permeable PDMS channel and a chemical concentration gradient was formed using a special channel-branched device between adjacent chambers. The on-chip integration of oxygen and chemical concentration gradients allowed for the evaluation of the antitumor effects of both hypoxia-specific and normoxia-dependent drugs on different types of tumour cells using the microfluidic set-up.

The device (**Figure 92**, left) encompassed a disk-shaped top layer, which included a microchannel network, eight microchambers, two inlets and eight outlets, a glass slide bottom layer, and an oxygen sensor film consisting of Pt(II) octaethylporphyrin **PtOEP** in the middle (**Figure 92**, right). It allowed for the real-time visualization of the hypoxia dynamics and proved to allow establishing an oxygen gradient within the chamber.

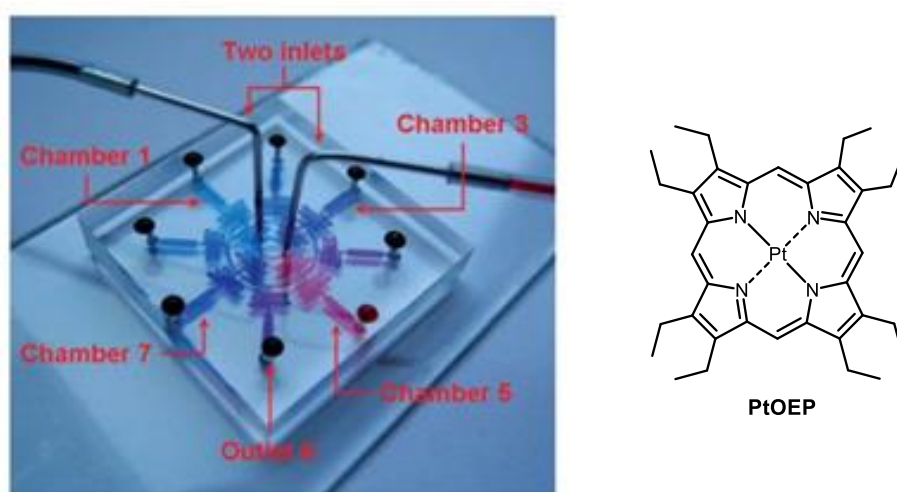


**Figure 92** Left: Microfluidic device. Two dye solutions (red and blue) were loaded into the device from the two inlets at 2 mL/min. The gradual change of colours within the terminal chambers confirmed the chemical concentration gradient between these chambers. © The Royal Society of Chemistry 2012. Right: Chemical structure of Pt(II) octaethylporphyrin **PtOEP**.

Bolivar *et al.*<sup>184</sup> used microfluidic flowcells featuring integrated optical oxygen sensing layers containing platinum(II) meso-tetra(4-fluorophenyl) tetrabenzoporphyrin **PtTPTBPF** (**Figure 93**) to determine the enzymatic activity of glucose oxidase. The enzyme was

immobilized on chemically modified glass surfaces and luminescence lifetime measurements were used for the accurate on-line monitoring of the oxygen consumption of the enzyme. The results obtained through this method were in good agreement with reported ones, providing a proof-of-concept that these devices could be tailor-made by surface modifications for enzymatic studies. Pre-fabricated sensor layers containing such complexes were also used in microfluidic devices for regulating oxygen levels<sup>182,185</sup> and for cell culture.<sup>186</sup>

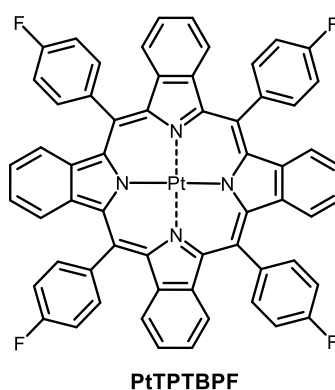
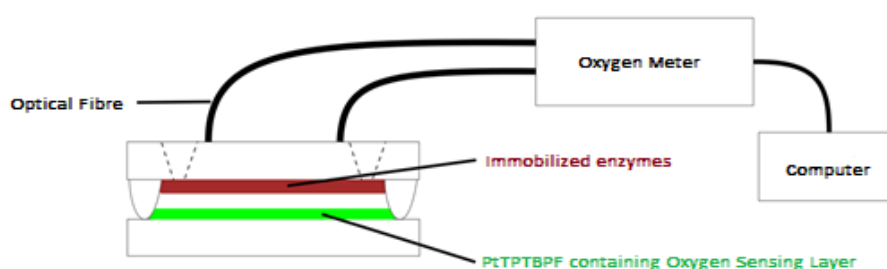


**Figure 93** Top: Schematic set-up for the on-line detection of oxygen consumption. Optical fibres connected the spots of interest to the read-out device through the top of the holder and the signals were monitored in real-time. Bottom: Chemical structure of the Pt(II) meso-tetra(4-fluorophenyl)tetrabenzoporphyrin **PtTPTBPF**.

In the examples discussed above, the oxygen indicators were incorporated into a host polymer, for example PDMS, to create the sensor layers or pads. Various oxygen-permeable polymeric matrices such as polystyrene,<sup>187,188</sup> sol-gels,<sup>189,190</sup> polyvinylchloride<sup>191</sup> and poly(1-trimethylsilyl-1-propyne)<sup>192</sup> can be used to immobilize Pt(II) porphyrins and create chemical sensors. Among the different host materials available, oxygen sensitive nanoparticles (ONPs) have been very successfully used because they enable micro- and

nanostructured systems such as cells, tissue, or nanoscale devices to be studied. Due to their small size, there is also virtually no diffusion barrier for oxygen. Thus, the response is fast.

The most direct approach to obtain nanosensors for oxygen is to entrap the indicator inside an appropriate nanoparticle. Precipitation is a simple method to convert conventional bulk polymers into nanosized particles<sup>193</sup> since it only requires the oxygen indicators and polymers to be dissolved in a solvent, usually a water-miscible one, followed by precipitation of the nanoparticles by the slow addition of water. Borisov *et al.*<sup>194</sup> incorporated Pt(II) and Pd(II) benzoporphyrins into polysulfone nanobeads in this way, for example.

Oxygen nanosensors can also be fabricated from commercially available polymer nanoparticles that are swollen in an organic solvent containing the oxygen indicator. The indicator is thus taken up by the nanoparticles to give oxygen-sensitive nanobeads. In this way, **PtTFPP (Figure 91, right)** was encapsulated in carboxylated microbeads of polystyrene by Schmäzlin *et al.*<sup>195,196</sup> and used to determine dissolved oxygen in plant cells. The hydrophobic and inert nature of polystyrene prevented dye leakage, and the beads were well compatible with living cells.

Commercially available poly(styrene-co-vinylpyrrolidone) nanoparticles are excellent matrices for the simple preparation of optical nanosensors since they are uncharged, do not aggregate at high ionic strength, are stable even in complex media, and are available with a suitable size. The incorporation of the indicator is easy and can either occur within the hydrophobic polystyrene core or along the hydrophilic shell consisting of poly(vinylpyrrolidone).<sup>197</sup> Hydrophobic oxygen indicators prefer the hydrophobic polystyrene core, while hydrophilic probes prefer the shell. In this thesis, the focus will be on a specific type of such core-shell nanoparticles termed OXNANO.

### 3.1.2 OXNANO Nanoparticles

OXNANO is the commercial name given by Pyroscience (Aachen, Germany) to nanoparticles that have a core-shell structure in which nonpolar polystyrene blocks with

immobilized **PtTPTBPF** (Figure 93, bottom) form the core and hydrophilic poly(vinylpyrrolidone) blocks form the interfacial region. These nanoparticles are synthesized by adding a solution of the Pt(II) porphyrin in THF to a stirred solution of poly(styrene-block-vinylpyrrolidone) nanobeads in water/THF. Undissolved material is removed by centrifugation and the dried OXNANO nanoparticles are obtained by freeze-drying the mixture.

The OXNANO nanoparticles are excitable with orange-red light ( $\lambda=610-630$  nm) and show an oxygen-dependent luminescence in the near infrared ( $\lambda=760-790$  nm), allowing them to act as optical oxygen sensors. A quenching effect on the indicator's luminescence is observed by collision between oxygen molecules and the immobilized **PtTPTBPF**. In simpler terms, a higher amount of oxygen results in a lower emission signal.

Since these nanoparticles are dispersible in aqueous solutions or culture media, they are well suited for dissolved oxygen measurements in liquid samples within closed transparent systems (plastic or glass) and possess advantages over the more conventional dissolved oxygen measurement *via* fixed sensor spots.<sup>198-200</sup> A simple batch calibration of the OXNANO dispersion allows read-out at various locations along the sample container or in different samples containing the same dispersion. For these reasons, OXNANO nanoparticles have been used for measurements of oxygen levels in setups such as bioreactors, ecosystems, or cultures and of cells growth experiments, microbes, fungi, plankton, aquatic animals, and plants.

The applicability of the nanoparticles for online dissolved oxygen tension (DOT) monitoring systems in shaken cultivation flasks was demonstrated by Flitsch *et al.*<sup>201</sup> In this experiment a solution of OXNANO nanoparticles was added to the cultivation broth. DOT measurements from the suspended nanoparticles were compared with the DOT measurements from fixed sensor spots in the same flask (Figure 94), revealing erroneous measurements for the sensor spots but not for the nanoparticles. Thus, these oxygen-sensitive nanoparticles represent a robust, reliable and easy to use DOT measurement system.

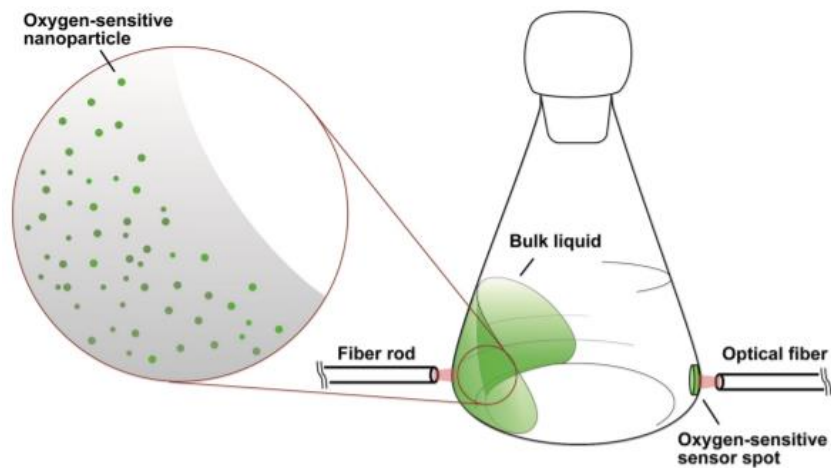


**Figure 94** Setup for simultaneous DOT measurements via oxygen-sensitive nanoparticles and an oxygen-sensitive sensor spot. © 2016 Flitsch et al.

Due to their ultra-fast response time, OXNANO nanoparticles allow real-time oxygen monitoring and high-throughput screening. Since they are also suited for contactless measurements of fast processes in small sample volumes and within complex geometries, the OXNANO nanoparticles can be quite useful in the fields of microfluidics and lab-on-a-chip devices.

Micronit Microtechnologies (Enschede, Netherlands) is a major actor in the design, development, and manufacturing of these microfluidics devices. Their portfolio of products includes flow cells, lab-on-a-chip, and organ-on-a-chip devices where they can perform reactions, mixing, analysis of cellular processes, and cell culture experiments on a single chip at the microliter scale.

Recent efforts were directed by Micronit to integrate an oxygen sensor in an organ-on-a-chip and monitor the oxygen pressure (or concentration) *in-situ*. To that end, sensor spots based on the oxygen sensitive nanoparticles OXNANO were fabricated and incorporated into microfluidic chip devices and their oxygen sensing abilities were evaluated by comparison with chips produced with the commercially available sensor foil OXFOIL (Pyroscience).<sup>202</sup>

The OXNANO sensor spots were created by directly depositing on the surface of the bottom layer of a three-layer microfluidic chip drops of a dispersion of the nanoparticles in water

(Figure 95a). The solvent was removed by using a hot plate at 70°C and PDMS was blade-coated over the nanoparticles, immobilizing them on the glass surface.

The geometry of the sensor spots was controlled by using a Kapton tape stencil and curing of the PDMS was made by placing the sensor layer in an oven at 70°C overnight. OXFOIL is a polyethyleneterephthalat (PET) foil with a layer of oxygen sensitive dye embedded in its matrix, covered by a black optical isolation, reducing the interference from ambient light. This sensor foil was glued to the bottom glass of the three-layer chip (Figure 95b) by using Elastosil®E43 (Wacker, Germany), a one-component silicone rubber and cured by atmospheric moisture. Three sensor spots were cut using a scalpel and glued on the bottom of the microfluidic chip.<sup>202</sup>

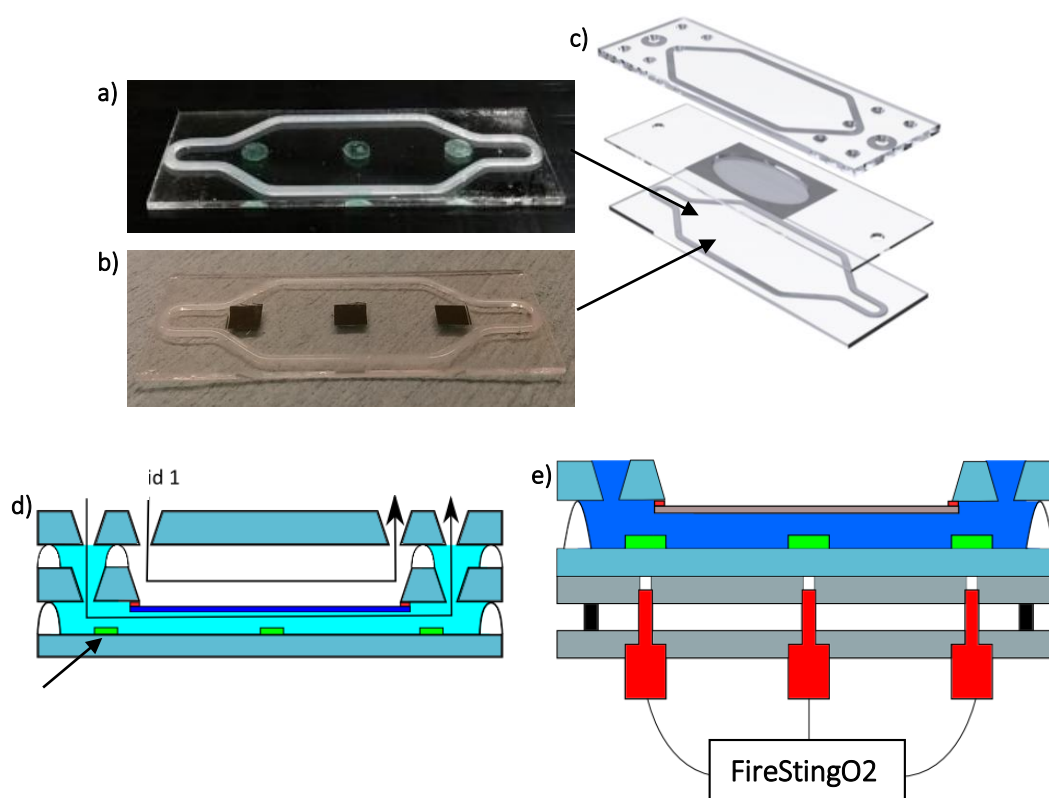


**Figure 95** a) Photograph of the bottom layer of a standard three-layer microfluidic chip from Micronit with three OXNANO sensor spots. b) Photograph of the bottom layer of a standard three-layer microfluidic chip from Micronit with three OXFOIL sensor spots. c) Standard three-layer microfluidic chip from Micronit. d) Schematic representation of the microfluidic device. e) Schematic representation of the contactless fibre-optics sensing system.

The three stacked layers of the organ-on-a-chip (**Figure 95c**) created two channels in which different fluids could flow. A permeable membrane in the middle layer allowed for gas exchange between the channels. Experiments to evaluate the responsiveness of both the OXNANO and the OXFOIL chips to alterations of the concentration of oxygen were performed by flowing oxygen-saturated water through the lower channel of the chips and gaseous nitrogen through the upper channel (**Figure 95d**). Contactless sensing was achieved through the glass bottom layer of the chip (**Figure 95e**) by exciting the sensors with the help of fibre optics ( $\lambda=620$  nm), collecting the emitted light ( $\lambda=760$  nm), and processing the results with an oxygen meter (FireStingO2). The reduction of the excited state lifetime of the sensors in the presence of oxygen was used to quantify the oxygen amount in the sample. The measuring principle was based on frequency resolved measurements (**Figure 96a**), where an intensity sinusoidally modulated red excitation light resulted in a phase-shifted sinusoidally modulated emission in the NIR. The FireStingO2 measured this phase shift (termed “dphi” in the software) and converted it internally into oxygen units using the Stern-Vollmer equation (**Figure 96b,c**).<sup>202</sup>

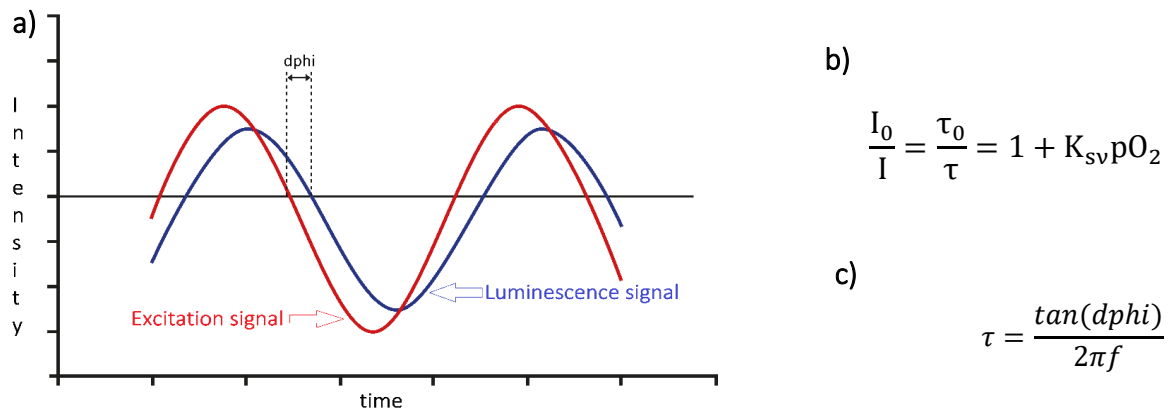


**Figure 96** a) Frequency-resolved lifetime measurements. b) Stern – Volmer equation.  $I$  and  $I_0$  represent the luminescence intensities in the presence and absence of quencher;  $\tau$  and  $\tau_0$  are the lifetimes of the luminophore in the presence and absence of the quencher,  $K_{sv}$  is the Stern–Volmer quenching constant and  $pO_2$  is the oxygen’s partial pressure. c) Relation between lifetime ( $\tau$ ) and phase shift ( $dphi$ ).



The measurements performed with the OXNANO chips showed a good correlation between the measured and actual oxygen content inside the three-layer microfluidic chip, also following the same trend as obtained for the OXFOIL chips. The results thus indicated that the nanoparticles were applicable for use in the microfluidic device. However, because the OXNANO nanoparticles were not soluble in water and the sensor spots were created from a suspension, all the sensors showed inhomogeneous distribution of the nanoparticles inside the sensor spots (**Figure 97**), resulting in a variation of the signal intensities from one sensor to the other and even between sensor spots in the same chip, which reduced the reproducibility of the results.<sup>202</sup>

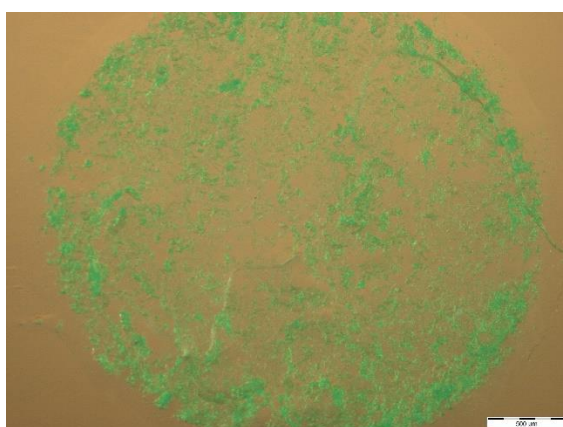


*Figure 97* Photograph of a microscopic image (4x) of a sensor spot produced from a 1 mg/mL dispersion of OXNANO in water.

## 3.2. AIM OF THE PROJECT

The project developed in this chapter had three main goals. The first one was to improve the OXNANO-containing chip devices previously developed at Micronit by obtaining homogeneous sensor spots, which should lead to an increase of the reproducibility of the oxygen measurements. The second was to synthesize and characterize **PtTPTBPF (Figure 93)** and investigate if this compound is suitable for oxygen sensing after incorporation into a microfluidic device. The final aim was to compare the oxygen sensing abilities of the different chips obtained and identify the best sensor for biological assays.

### 3.3. RESULTS AND DISCUSSION

#### 3.3.1 Synthesis of the Pt(II) Tetrabenzoporphyrin PtTPTBPF

The synthesis of the fluorinated tetrabenzoporphyrin Pt(II) complex **PtTPTBPF** was performed according to a literature procedure.<sup>203</sup> Initially, an exchange reaction between zinc acetate (**33**) and 4-fluorophenylacetic acid (**34**) in methanol afforded the Zn(II) salt **35** (Figure 98).

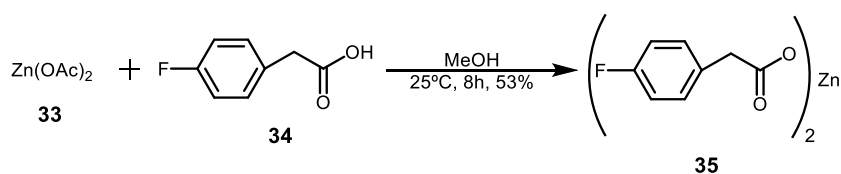


**Figure 98** Synthetic scheme of the synthesis of the Zn(II) complex **35** from the commercially available starting materials zinc acetate (**33**) and 4-fluorophenylacetic acid (**34**).

Subsequently, this salt was used as a template to obtain, in a single step, the Zn(II) complex of the fluorinated tetrabenzoporphyrin **37** from 4-fluorophenylacetic acid (**34**) and phthalimide (**36**) (Figure 99). Compounds **34**, **35**, and **36** were mixed and ground in a mortar, transferred to a round bottom flask and melted at 360°C, forming a dark green slurr that was allowed to react for 2 hours. After work-up, **37** was obtained as dark green crystals in a yield of 7%.

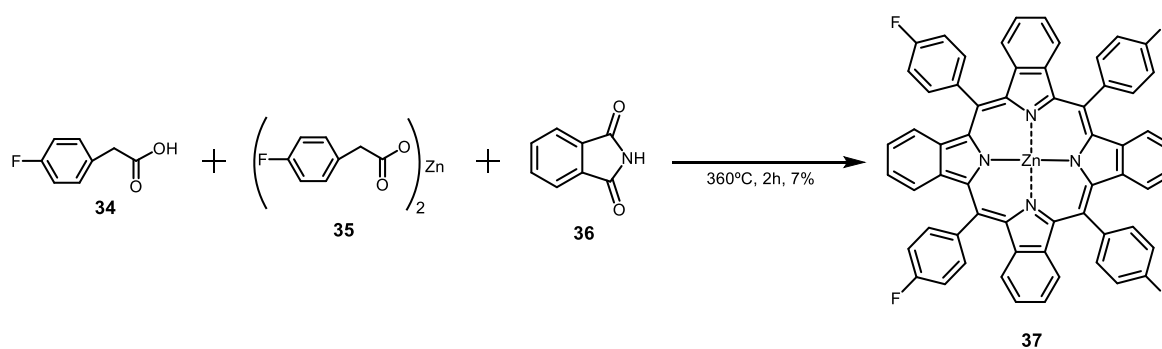


**Figure 99** Synthetic scheme for the synthesis of the Zn(II) fluorinated tetrabenzoporphyrin **37** from 4-fluorophenylacetic acid (**34**), phthalimide (**36**), and the Zn(II) salt **35**.

The Zn(II) complex **37** was then dissolved in THF and converted into the free fluorinated tetrabenzoporphyrin **38** by adding methanesulfonic acid. The product **39** was obtained as a dark green powder (**Figure 100**).

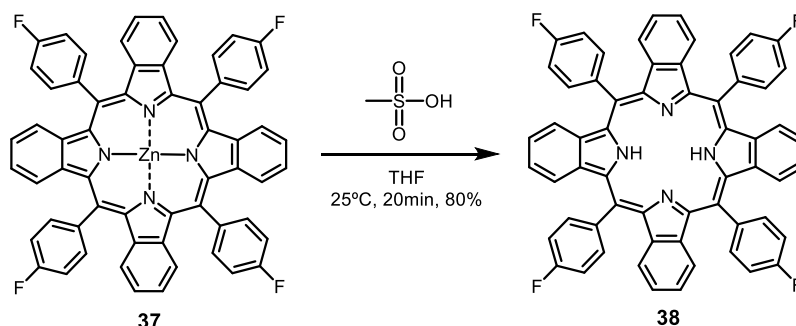


**Figure 100** Synthetic scheme for the synthesis of the free fluorinated tetrabenzoporphyrin **38** from the Zn(II) complex **37**.

Platinum(II) coordination was achieved by adding a hot solution of PtCl<sub>2</sub> in benzonitrile (PhCN) to a solution of **38** in diphenylether (DPE), affording the corresponding Pt(II) complex **PtTPTBPF** as a sticky green precipitate (**Figure 101**) via the intermediate complex [Pt(PhCN)<sub>2</sub>Cl<sub>2</sub>].

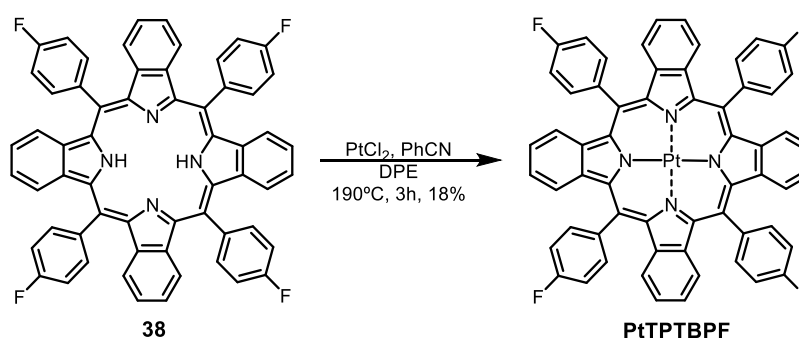


**Figure 101** Synthesis of the Pt(II) complex **PtTPTBPF** from the fluorinated tetrabenzoporphyrin **38**.

### 3.3.2 Development of Chips Containing OXNANO as Oxygen Sensor Spots

A standard three-layer microfluidic chip from Micronit (**Figure 102d**) was used to assemble the oxygen sensor containing OXNANO nanoparticles. This chip comprised three stacked layers, creating two channels in which different solutions can flow. A permeable membrane in the middle layer allowed for gas exchange between the channels. A perfluorinated elastomer was used as a gasket, ensuring the sealing of the two channels. Oxygen sensor spots were created in the bottom layer of the chip.

The proper position of the sensor spots was ensured by covering the bottom layer with a kapton tape containing three spherical cut-outs into which aliquots of the sensor solution were added (**Figure 102a**). The spots were immobilized to the glass surface by blade coating the layer with poly(dimethylsiloxane)<sup>169,170</sup> (PDMS), the kapton was removed (**Figure 102b**), and the gasket was dispensed on the glass (**Figure 102c**).

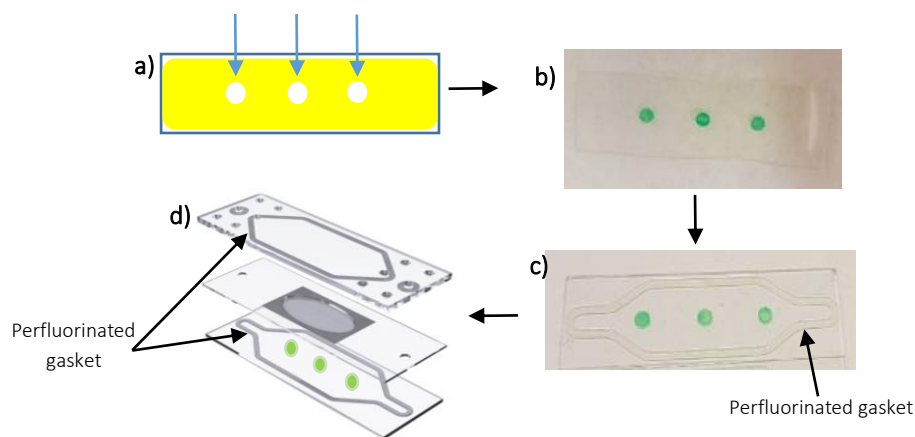


**Figure 102** Preparation of oxygen sensor chips. The sensor solution was applied on a simple glass bottom layer with Kapton tape stencil glued on it (a). After PDMS coating, the Kapton was removed (b) and the gasket was added (c). A standard three-layer microfluidic chip setup was used for the final assembly (d).

As mentioned previously, related oxygen sensor chips containing OXNANO nanoparticles were developed at Micronit. The drawbacks of these chips were inhomogeneities in the sensor spots (**Figure 103a**), which prevented quantitative measurements. The reason for these inhomogeneities was likely the fact that the spots were created by using an aqueous suspension of the nanoparticles. Accordingly, some spots contained more nanoparticles than others.

To address this issue, the use of a homogeneous nanoparticle solution in an organic solvent was considered for the preparation of the spots. In this way, the concentration of the nanoparticles in the spots could be precisely controlled. Due to the good solubility of OXNANO nanoparticles in dichloromethane, this solvent was used to prepare the respective solution.

Different conditions were tested to create uniform sensor spots, at the same time ensuring a sufficiently high signal intensity in the presence of oxygen and a marked drop in intensity when oxygen was replaced by a nitrogen rich medium.

The best sensor spots were obtained when 2  $\mu\text{L}$  aliquots of a 10 mg/mL solution of OXNANO in dichloromethane were added five times per spot (total of 10  $\mu\text{L}$ ) directly on the glass bottom layer. Each aliquot was added once the solvent of the previous addition had evaporated. Addition of aliquots with larger volumes than 2  $\mu\text{L}$  resulted on an overflow of the sensor solution whilst lower volumes did not completely fill the circles in the kapton. When more than five additions were applied per spot or a higher concentration of sensor solution was used, agglomerates of nanoparticles were formed after solvent evaporation. Less than five additions per spot or the use of a sensor solution with a lower concentration resulted in sensor spots that did not produce a high enough signal intensity when subjected to oxygen.

Thus prepared OXNANO sensor spots (**Figure 103a**) featured a homogeneous and smooth surface with evenly distributed nanoparticles, which was a substantial improvement with respect to the spots obtained by using aqueous nanoparticle suspensions (**Figure 103b**). Also, they produced high signal intensities when in oxygen rich environments, while subjecting them to a nitrogen-rich environment caused a significant drop of emission

intensity. Various OXNANO chips were made by using this procedure, and all of them had comparable characteristics (**Figure 103c**).

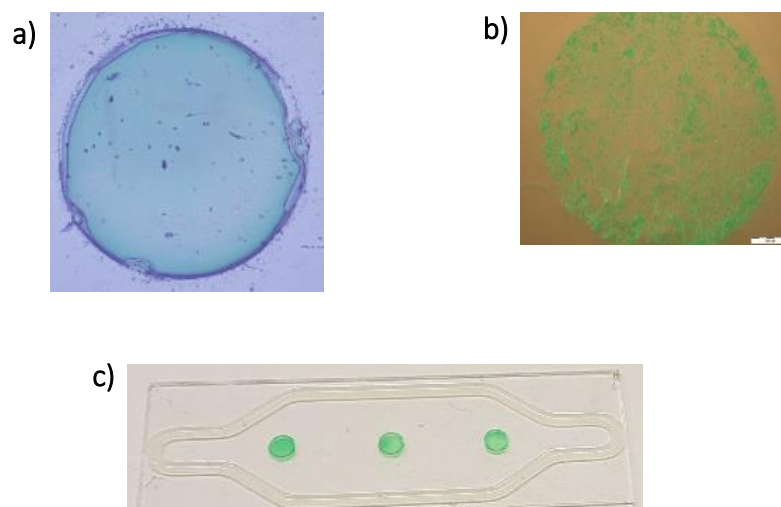


**Figure 103** OXNANO Sensor. a) Photograph of a microscopic image (4x) of a sensor spot produced from a 10 mg/mL sensor solution of OXNANO in dichloromethane. b) Photograph of a microscopic image (4x) of a sensor spot produced from a 1 mg/mL dispersion of OXNANO in water. c) Photograph of the bottom layer of the three-layer microfluidic chip produced by using the nanoparticle solution in dichloromethane, showing the three OXNANO sensor spots.

### 3.3.3 Development of Chips Containing PtTPTBPF as Oxygen Sensor Spots

Chips containing free **PtTPTBPF** instead of the **PtTPTBPF**-containing nanoparticles were also prepared (**Figure 104**). In this case, 5  $\mu\text{L}$  of a solution of the Pt(II) complex in dichloromethane was applied to each spot three times (total of 15  $\mu\text{L}$ ). Each 5  $\mu\text{L}$  aliquot was added once the previous one was dried. The spots were then coated with PDMS and cured overnight at 70°C. Different concentrations, amounts and number of additions of the sensor solution were tested but only the described procedure afforded a sufficiently high signal intensity in the presence of oxygen. These chips turned out to be not suitable for the measurements since the spots had no smooth surface and the **PtTPTBPF** complex was not evenly distributed (**Figure 104c**). In addition, the thus produced sensor spots exhibited no change in emission intensity when the oxygen in the medium was replaced by nitrogen.

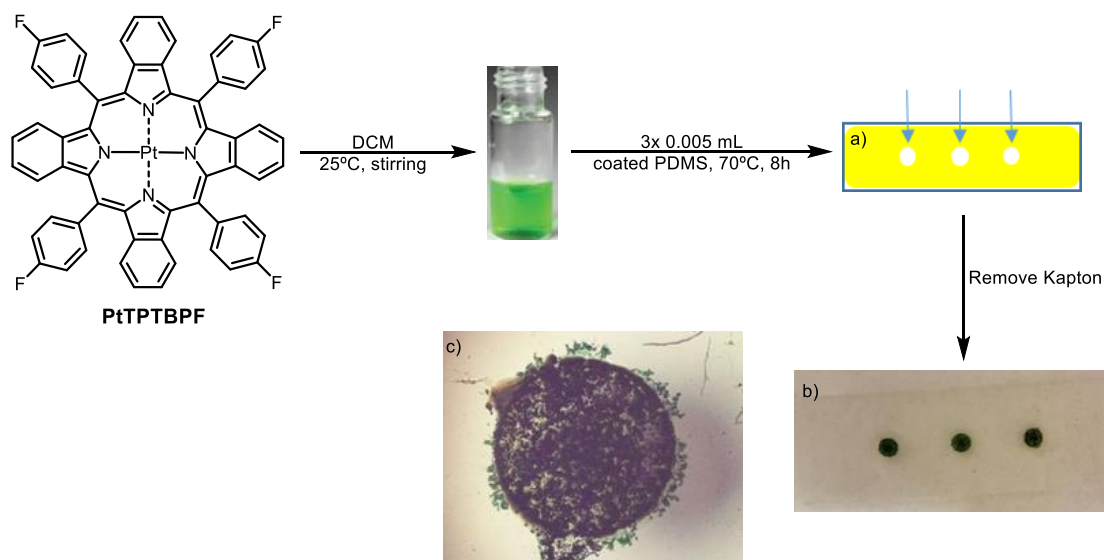


**Figure 104** Preparation of **PtTPTBPF** sensor chips. a) The sensor solution was applied to a glass bottom layer with Kapton tape stencil glued to it, coated with PDMS followed by removal of the Kapton. b) Photograph of a glass bottom layer with three **PtTPTBPF** spots. c) Photograph of a microscopic image(4x) of a **PtTPTBPF** spot.

Since the sensing abilities of **PtTPTBPF** improve when incorporating this compound in a polymeric matrix, chips were also prepared by mixing the Pt(II) complex with polystyrene,<sup>177</sup> PDMS<sup>204,205</sup> and Elastosil®E43.<sup>206</sup>

For the preparation of the PDMS containing chips, a solution of PDMS and **PtTPTBPF** in dichloromethane was used. This solution was applied to each spot twice in aliquots of 3  $\mu\text{L}$ . The second addition was made once the first solution was fully dried. Afterwards, the spots were cured overnight at 70°C. The perfluorinated gasket was dispensed on the glass after confirmation that the chip was sensitive to the oxygen content of the medium (**Figure 105**).

Different conditions were tested but at higher concentrations of the Pt(II) complex the solution became difficult to apply, while the signal intensity was not sufficient when the concentration was too low. Also, when larger volumes of the solutions were applied to the sensor spots, the spots became too thick and easily detached from the bottom layer.

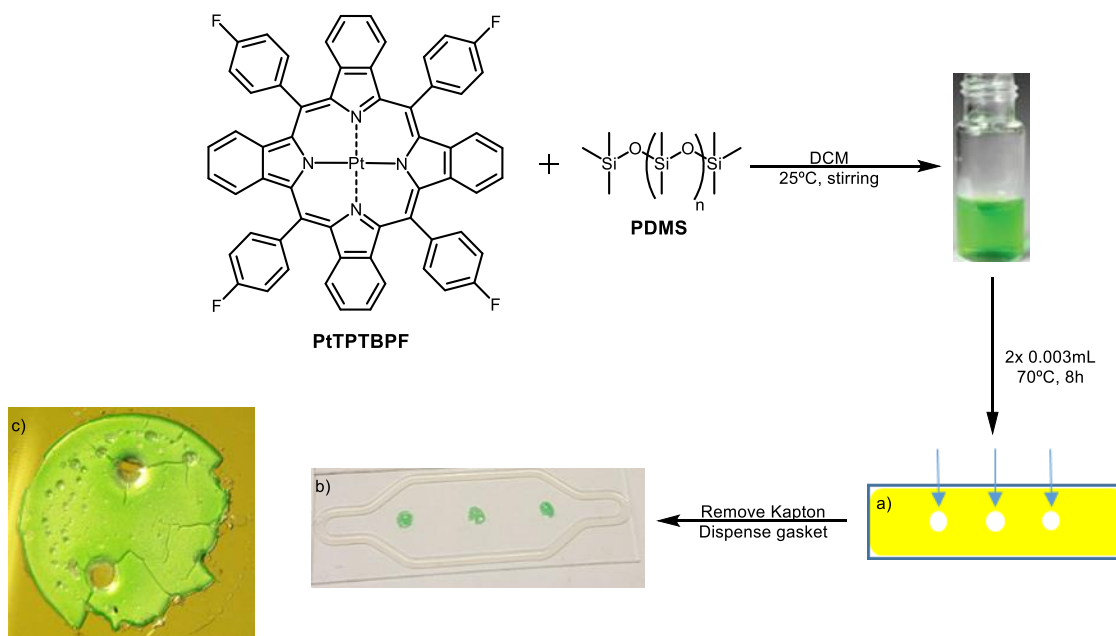


**Figure 105** Preparation of PDMS sensor Chips. a) The sensor solution was applied to a glass bottom layer with a Kapton tape stencil glued to it, cured at 70°C, followed by removal of the Kapton and the addition of the gasket. b) Photograph of a bottom layer of the three-layer microfluidic chip with three **PtTPTBPF**/PDMS sensor spots. c) Photograph of a microscopic image (4x) of a **PtTPTBPF**/PDMS sensor spot.

As shown in **Figure 105c**, the sensor spots became considerably brittle after curing and broke easily when the Kapton was removed. This made it difficult to obtain bottom layers with suitable sensor spots (**Figure 105b**). Also, holes were present in the spots due to the formation of bubbles during the curing that could affect the flow of the solution in the lower channel and potentially produce false intensity readings. Bubble formation could not be avoided by using different curing temperatures or times.

Chips containing the one-component acetoxy-cure silicone rubber Elastosil®E43 were prepared in a similar manner by using a solution of E43 and **PtTPTBPF** in dichloromethane for creating the sensor spots. The susceptibility to the oxygen content of the medium was confirmed before dispensing the perfluorinated gasket (**Figure 106**). Again, different conditions were tested for the manufacturing of these chips to identify which conditions produced spots that were thin enough and at the same time gave a sufficiently intensive signal.



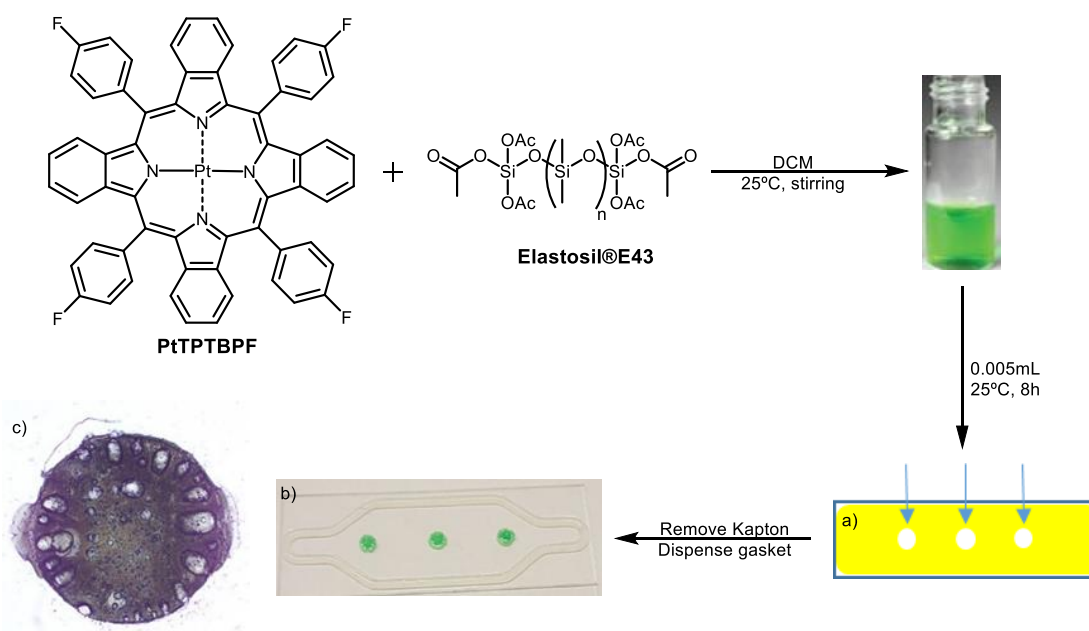


**Figure 106** Preparation of Elastosil®E43 sensor Chips. a) The sensor solution was applied on a simple glass bottom layer with Kapton tape stencil glued on it, cured at 25°C the Kapton was removed and the gasket added. b) Photograph of a bottom layer of the three-layer microfluidic chip with three PtTPTBPF/E43 sensor spots. c) Photograph of a microscopic view (4x) from a PtTPTBPF/E43 sensor spot.

The thus obtained sensor spots also featured holes due to bubble formation during curing (Figure 107a). Smooth surface spots were obtained by drying the spots in the fridge (Figure 107b), but the low temperatures decreased the adhesion of the spots to the bottom layer. As a consequence, the spots detached from the glass when they came in contact with the test solutions, rendering these conditions unsuitable for chip formation.

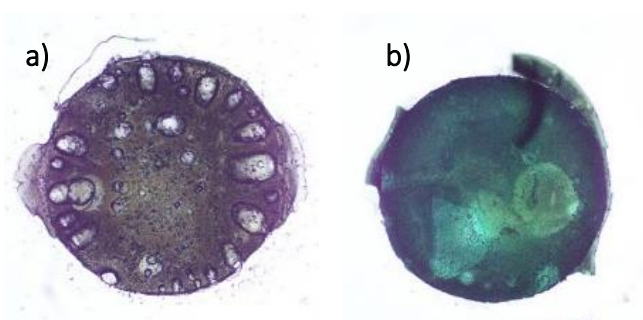


**Figure 107** Elastosil®E43 sensor Spots. a) Photograph of a microscopic view (4x) from a sensor spot dried at room temperature. b) Photograph of a microscopic view (4x) from a sensor spot dried at 4°C.

Polystyrene-containing chips were prepared by using a solution of polystyrene and **PtTPTBPF** in chloroform. This solution was applied to each spot twice and the spots were allowed to dry at room temperature (**Figure 108**). The resulting thin green polystyrene spots stuck to the Kapton and therefore detached from the bottom layer upon removal of the kapton. No conditions could be identified that allowed creating spots that adhered to the glass.

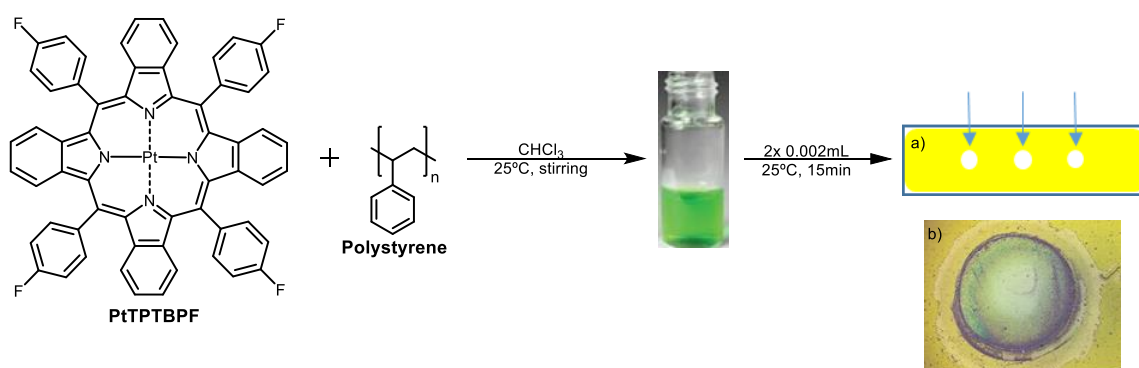


**Figure 108** First attempt to prepare polystyrene-containing sensor spots. a) The sensor solution was applied to a glass bottom layer with Kapton tape stencil glued to it, dried at  $25^\circ\text{C}$ , followed by removal of the Kapton. b) Photograph of a microscopic image (4x) of a **PtTPTBPF**/polystyrene spot stuck to the Kapton.

This issue was addressed by using Norland Optical Adhesive 61 (**NOA 61**), a clear, colourless, liquid photopolymer that cured when exposed to ultraviolet light to improve the adhesion of the polystyrene film on the glass layer. Accordingly, a solution of **NOA 61** was first applied to the glass, followed by two additions of the polystyrene/**PtTPTBPF** solution in chloroform. The solvent was allowed to evaporate at room temperature and the spots were exposed for 90 s to UV light ( $\lambda = 254\text{ nm}$ ) (**Figure 109**).

Unfortunately, bubble formation occurred in some cases during the exposure to UV light (**Figure 109c**), independently of the exposure time, the amount of glue used, or the amount of polystyrene in the second solution. Nevertheless, the sensor spots remained glued to the bottom layers after removal of the Kapton and were responsive when the oxygen content of the medium changed, so the gasket could be dispensed.

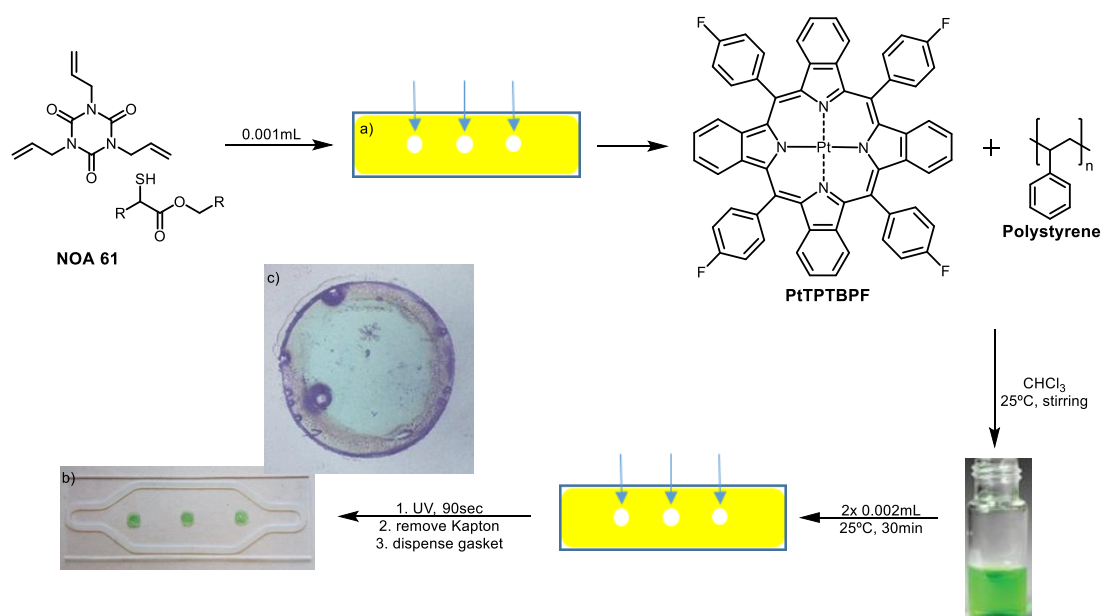


**Figure 109** Second attempt of the preparation of polystyrene chips. a) NOA61 was first applied to a glass bottom layer with Kapton tape stencil glued to it followed by the addition of the sensor solution. The spots were dried at 25°C, submitted to UV light ( $\lambda = 254 \text{ nm}$ ), the Kapton was removed, and the gasket added. b) Photograph of a bottom layer of the three-layer microfluidic chip with three **PtTPTBPF**/polystyrene sensor spots. c) Photograph of a microscopic image (4x) of a **PtTPTBPF**/polystyrene sensor spot.

At this point, three types of chips containing **PtTPTBPF** incorporated in a polymeric matrix in addition to a chip containing Pt(II) complex immobilized within OXNANO nanoparticles were available. Of each type, six chips had been prepared. All of these chips produced high signal intensities, displayed a considerable drop in the detected emission signal when the sensor was submitted to a nitrogen rich medium, and featured thin and homogeneous sensor spots.

### 3.3.4 Validation of the Microfluidic Devices

Oxygen sensing studies were performed with the different chips to evaluate their responsiveness to the presence of oxygen in the medium, to ensure the replicability of results obtained for different chips, and to determine which type of chip would be best for cell studies. Experiments were executed using the setup depicted in **Figure 110**. Contactless sensing was achieved by using a fibre optics system to excite ( $\lambda = 620 \text{ nm}$ ) the Pt(II) complex in the spots and collect the emitted light ( $\lambda = 760 \text{ nm}$ ) through the glass top layer. The

phase-shift of the excitation and emission wavelengths was measured by the oxygen meter and converted by using the Stern-Vollmer relationship.

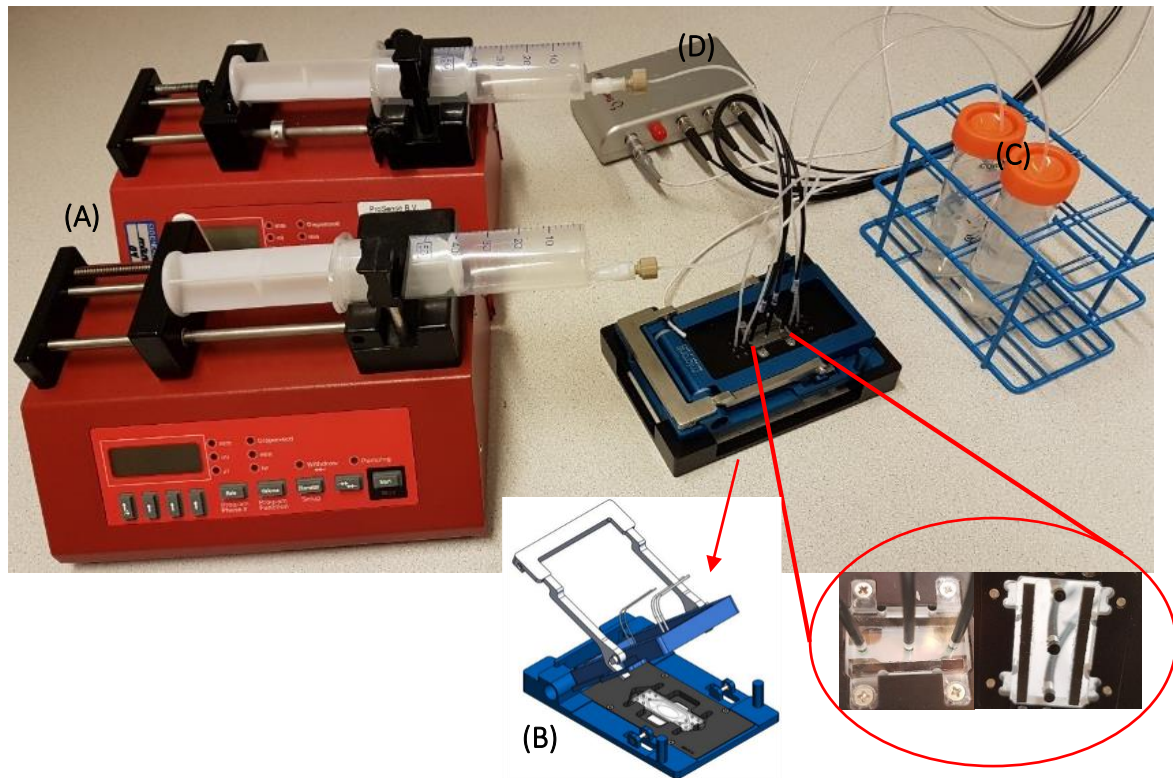


**Figure 110** Experimental setup for the Microfluidic device. Pumps (A) ensure proper liquid flow rates from the syringes through the chip (B) until the falcon tubes (C). Connected to the FireStingO2 oxygen meter (D) there are fibre optics (black cables) for contactless sensing and a temperature sensor (white cable).

The results obtained directly from the oxygen meter were depicted as hypothetical oxygen measurements (raw value) *versus* time (t/s) graphs (**Figure 111** top). In order to obtain reliable quantitative readings, a calibration of the chips was required, after which the thus obtained results were depicted as oxygen partial pressure ( $pO_2$ /hPa) *versus* time (t/s) graphs (**Figure 111** bottom).

Each chip was calibrated by performing a two-point calibration for both  $O_2$  saturated ( $dphi_{100}$ ) and anoxic ( $dphi_0$ ) conditions. In this context, care was taken that the calibration was comparable for sensor spots in the same chip and for chips of the same type. If a chip exhibited substantial variations in the phase shift values of the sensor spots, or if the average  $dphi$  value was considerably different from the values of other chips of the same type, the readings obtained with this chip were considered unreliable.



**Figure 111** Example of the graphs obtained from the oxygen meter readings before (top) and after (bottom) calibration.

The calibration was made by using a three-layer microfluidic chip setup with a glass cover slip instead of a porous membrane as a middle layer to ensure that no oxygen transfer between the two channels occurred. Air saturated water was pumped through the lower channel to determine the  $dphi_{100}$  values of each sensor spot while pure gaseous nitrogen was used for the  $dphi_0$  values. The average phase shift values for each chip type are depicted in **Table 1**. Considering that increasing oxygen levels correspond to decreasing  $dphi$  values and that, according to the results of previous experiments, anoxic conditions give a  $dphi_0$  of around 53 whereby ambient conditions give a  $dphi_{100}$  of about 20, the obtained values were well in accordance with the expected ones.

**Table 1** Average Phase Shift Values for Oxygen Saturated ( $dphi_{100}$ ) and Anoxic ( $dphi_0$ ) Conditions of the Different Sensor Chip Types.

	<i>OXNANO chip</i>	<i>PDMS chip</i>	<i>E43 chip</i>	<i>Polystyrene chip</i>
$dphi_{100}$	$24.3 \pm 0.2$	$23.5 \pm 0.2$	$23.2 \pm 0.2$	$22.4 \pm 0.3$
$dphi_0$	$52.3 \pm 0.2$	$53.3 \pm 0.2$	$53.6 \pm 0.2$	$53.4 \pm 0.2$
<i>Valid chips</i>	6/6	4/6	4/6	5/6

Some of the chips with **PtTPTBPF** incorporated into a polymeric matrix had to be discarded because their sensor spots afforded phase shift values widely different from the expected ones. The respective chips mainly featured sensor spots with a large number of visible holes due to bubble formation during the preparation.

The validation of the calibration of the remaining chips was then performed by flowing a mix of air-saturated water (100% O<sub>2</sub> saturation) and de-oxygenated water (0% O<sub>2</sub> saturation) through the lower channel of the three-layer microfluidic chip to afford five oxygen content standards (0%, 25%, 50%, 75% and 100% O<sub>2</sub> saturation) according to the flow rate of the two solutions. The response of the sensor spots in the chips to the increasing amount of oxygen was recorded and the oxygen content of the solution was only increased once a constant value of the signal was achieved (**Figure 112a**, blue and green graphs). The obtained pO<sub>2</sub> values were averaged for the three sensor spots in each chip and the results plotted against the O<sub>2</sub> content of the solution (**Figure 112b**).

This step was important to confirm that the  $dphi$  values found for each sensor spot of a certain chip during the calibration were the correct ones, thus allowing for reliable oxygen content measurements by the oxygen meter. If the relationship between the obtained pO<sub>2</sub> values for a certain sensor spot and the O<sub>2</sub> content in solution was not linear (**Figure 112a**, red spectrum), a new calibration of the chip was performed followed by a new validation. If a linear relationship could not be achieved, the chip in question was discarded. All the chips considered valid in **Table 1** were confirmed to be properly calibrated according to the validation.

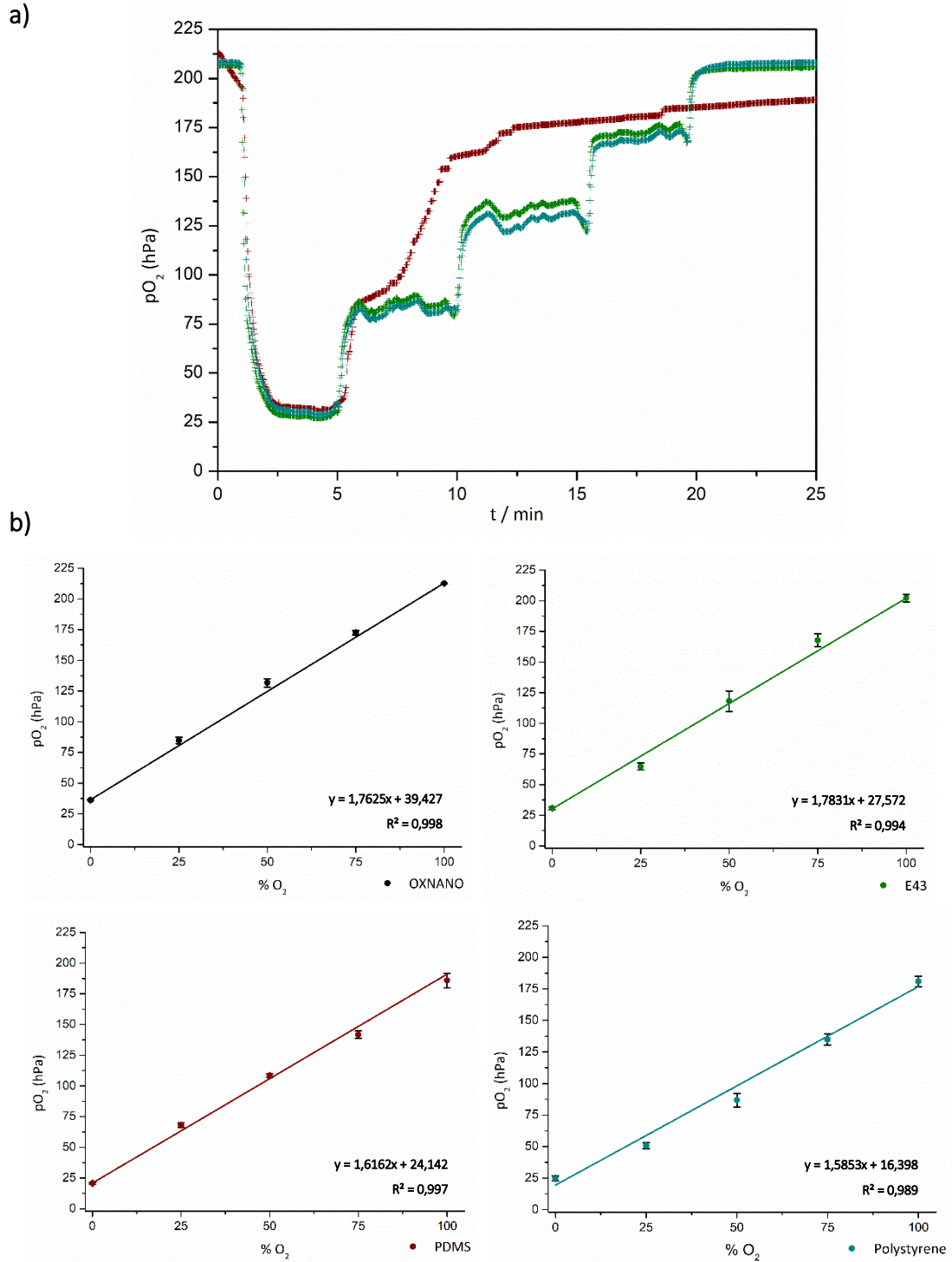


**Figure 112** Validation of Calibration. a) Evolution of the  $pO_2$  values of an OXNANO-containing chip with sensor spots that allowed proper calibration (blue and green graphs) and with spots that afforded unsuitable readings (red graph) when using different oxygen standards. 0% air saturation (from 0-5 min): flow of de-oxygenated water; air saturations of 25% (5-10 min), 50% (10-15 min), 75% (15-20 min): mixture of flows of de-oxygenated water and air saturated water; 100% (20-25 min) air saturation: flow of air saturated water. b) Plot of the averaged  $pO_2$  values obtained for the three spots of the four chip types against  $O_2$  content of the solution.

As can be observed in **Figure 112b**, all chip types were responsive to the increase of oxygen in a linear manner, indicating that the chips could be used as functional oxygen sensors. The positive  $pO_2$  values at 0%  $O_2$  saturation likely indicates that the 0% oxygen standard was not completely de-oxygenated or/and some re-oxygenation occurred while the water flowed through the chip. Although all chip types thus allowed for  $O_2$  quantification, the time required to reach a constant signal in the  $pO_2$  measurements was considerably different between the different types of chips.

When the  $O_2$  saturated water flowing through the lower channel of the chips was replaced by de-oxygenated water, the OXNANO-containing sensor spots responded to the drop of  $O_2$  within 2 minutes whilst the PDMS and the polystyrene-containing chips required fifteen minutes to reach a steady state and the E43-containing chips even twenty-five minutes (**Figure 113**).

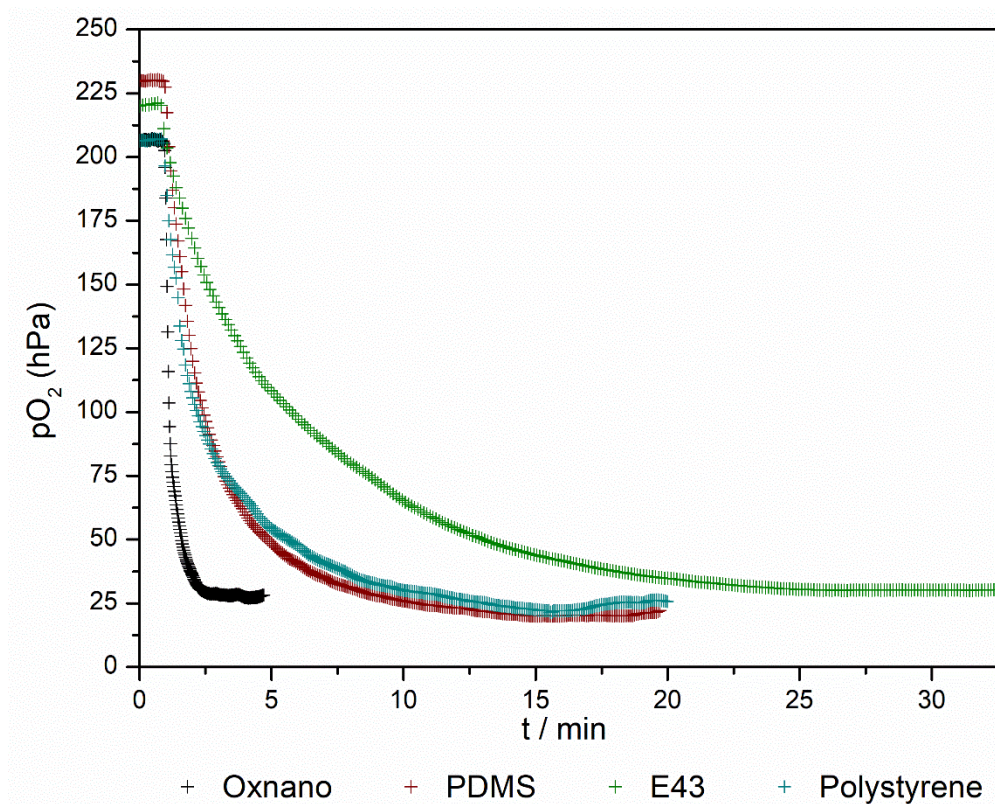


**Figure 113** Time-dependent changes of the  $pO_2$  values of the four different chip types after reducing the  $O_2$  content of the water from 100% to 0%  $O_2$ .



Based on the obtained results, the OXNANO-containing chips were considered the most suitable oxygen sensors, not only because of their fast and linear response to changes in the O<sub>2</sub> content of the water, but also because of their facile preparation. Therefore, the chips containing PtTPTBPF incorporated in a polymeric matrix were not considered further and the following experiments focused on the OXNANO-containing chips.

### 3.3.5 Oxygen Sensing Studies Using Microfluidic Chip Devices Containing OXNANO

Experiments to assess the efficiency of the OXNANO-containing chips as oxygen sensors were carried out in the same microfluidic device as before, but by now using a three-layer setup with a porous membrane in the middle layer that allowed for gas exchange between the two channels (**Figure 114**). Considering the direction of the flow inside the chip, the pO<sub>2</sub> values measured for each sensor spot now varied. The readings from the first spot (inlet) provided information about the oxygen content of the initial solution, the ones from the second spot, at the membrane level, reflected the effect of the medium in the upper channel on the O<sub>2</sub> content of the solution in the lower channel, and the results obtained for the third spot (outlet) showed the final outcome of this effect (**Figure 114**).

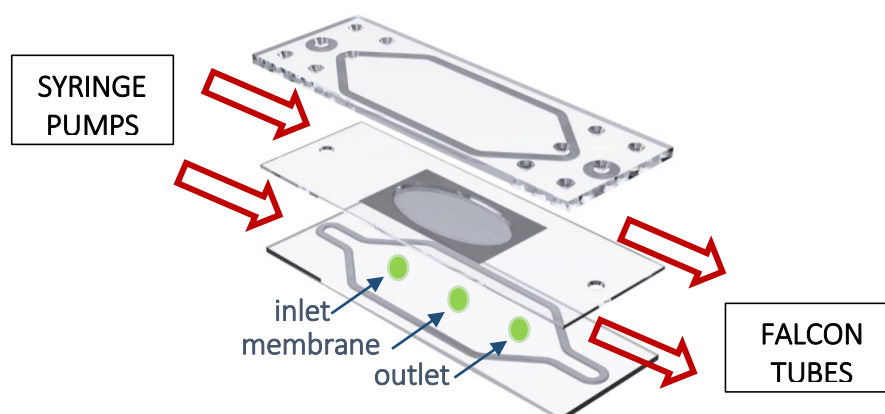


**Figure 114** Representation of the flow direction in the microfluidic device from the syringe pumps to the inlet, the spots, the outlets, and further to the falcon tubes.

Two methods were used to evaluate the  $O_2/N_2$  exchange through the porous membrane in the middle layer. The first one involved passing  $O_2$  saturated water through the lower channel of the chip and gaseous nitrogen through the upper one. The passage of oxygen across the membrane into the upper channel was expected to cause a decrease of the  $pO_2$  values at the second sensor spot and an even more pronounced effect at the third one.

As depicted in **Figure 115**, these results were indeed observed, with a constant  $pO_2$  value at the inlet, a significant drop at the second sensor spot, and an even larger drop of the  $pO_2$  value at the third spot.

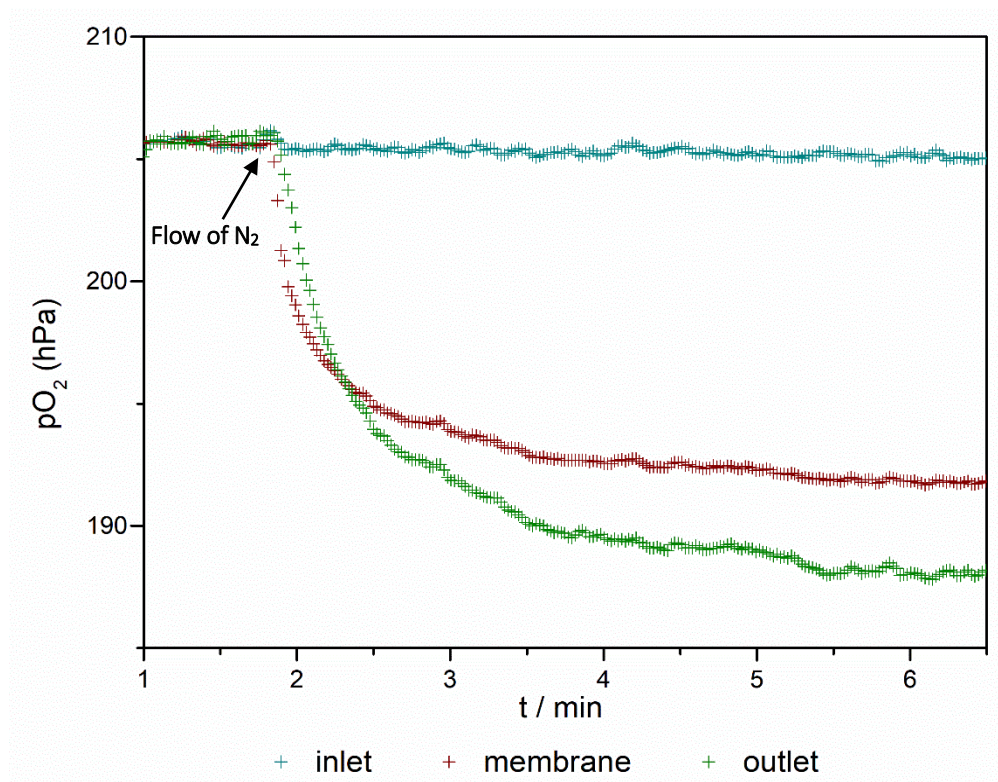


**Figure 115**  $pO_2$  values at the three sensor spots when air saturated water was flowing at  $200 \mu L/min$  through the lower channel and gaseous nitrogen through the upper one.

In the second type of experiment, the oxygenation of de-oxygenated water was studied by passing de-oxygenated water through the lower channel and atmospheric air through the top channel. In this case, an increase of  $pO_2$  values at the middle and outlet spots was expected.

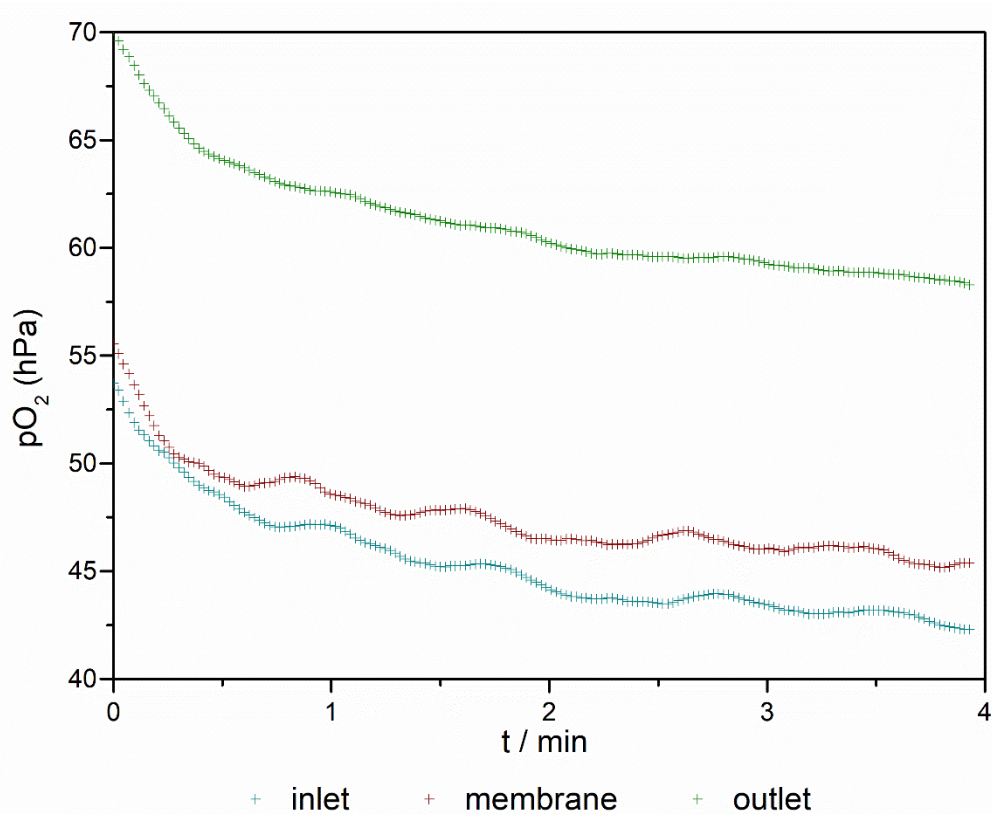


**Figure 116**  $pO_2$  values at the three sensor spots when de-oxygenated water was flowing at a rate of  $200 \mu\text{L}/\text{min}$  through the lower channel while the upper channel was exposed to air.

Unexpectedly, even though the measured  $pO_2$  values at the outlet were indeed around 20 hPa higher than the ones at the inlet, the  $pO_2$  values at the second sensor spot were not that different from the ones at the inlet (**Figure 116**).

To try understand this phenomenon, the experiment was performed at different flow rates. The charts in **Figure 117** summarize the  $pO_2$  values measured at the three sensor spots for different flow rates once the respective signals were stable (steady-state).

An overall decrease of the  $pO_2$  values with increasing flow rate was observed. The difference between the readings at the inlet and the membrane furthermore increased with the decrease of the flow rate. Also, for lower flow rates, the difference of the  $pO_2$  values between the three sensor spots was much more noticeable, with the  $pO_2$  values at the outlet and the membrane being a lot higher than the ones at the inlet (**Figure 117**).

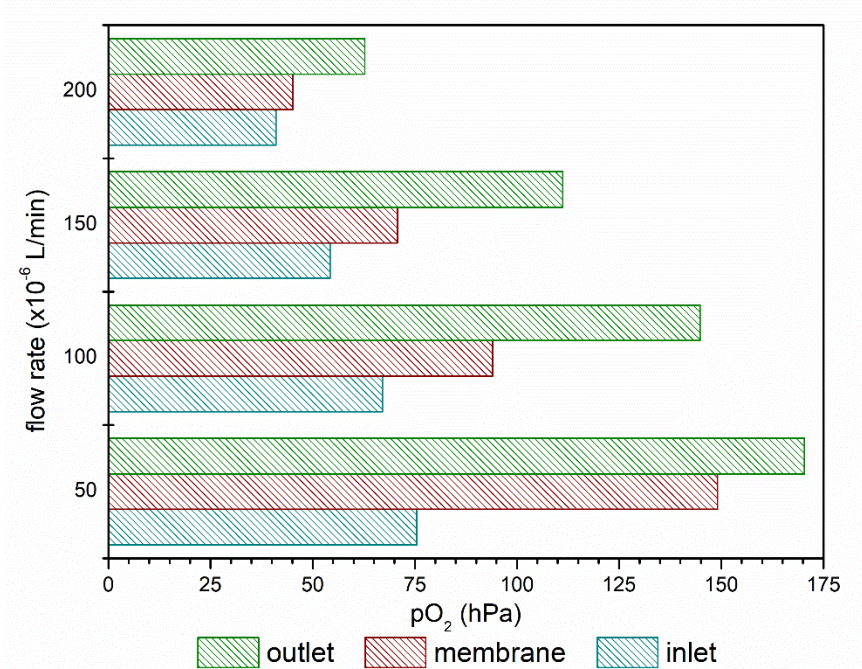


**Figure 117**  $pO_2$  values from the three sensor spots when de-oxygenate water flowed at different rates through the lower channel.

This result was consistent with the idea that when the flow rate was increased, the de-oxygenated water was exposed to atmospheric air for a shorter period of time, leaving less time for the oxygen to diffuse into the solution so that the  $pO_2$  value at the inlet is low. However, a too high flow rate also diminishes the time available for the oxygen to exchange at the membrane, leading to small  $pO_2$  values at the two other spots. The larger  $pO_2$  values obtained at these spots for lower flow rates reflect the more efficient  $O_2$  exchange at the membrane.

These  $O_2/N_2$  exchange experiments were conducted with the six available OXNANO chips, and all of them afforded similar results. The good reproducibility and sensitivity of these chips therefore allowed evaluating their performance in biological assays.

### 3.3.6 Measurement of the Oxygen Consumption of Cells by Using Microfluidic Chip Devices Containing OXNANO

Due to their promising oxygen sensing abilities, the OXNANO-containing chips were used in biological assays to detect the oxygen consumption of cells in their biological environment. Before the cell experiments, the chips were calibrated at 37 °C in an incubator. A polystyrene cover slip was used in this case instead of a porous membrane to prevent the oxygen transfer through the middle layer. Validation of the calibration was also made at 37 °C in an incubator.

The oxygen consumption experiments were conducted by using the setup depicted in **Figure 118** and by using a three-layer chip in which HUVEC cells were seeded in the membrane of the middle layer facing the lower channel. The cell medium was passed through the lower channel and PBS through the upper channel. The experiments were performed by using membranes seeded with 100'000 and 200'000 cells/cm<sup>2</sup>. Unfortunately, no reliable results were obtained from the experiments with 100'000 cells/cm<sup>2</sup>, which is why only the results obtained for the other cell concentration will be discussed below.

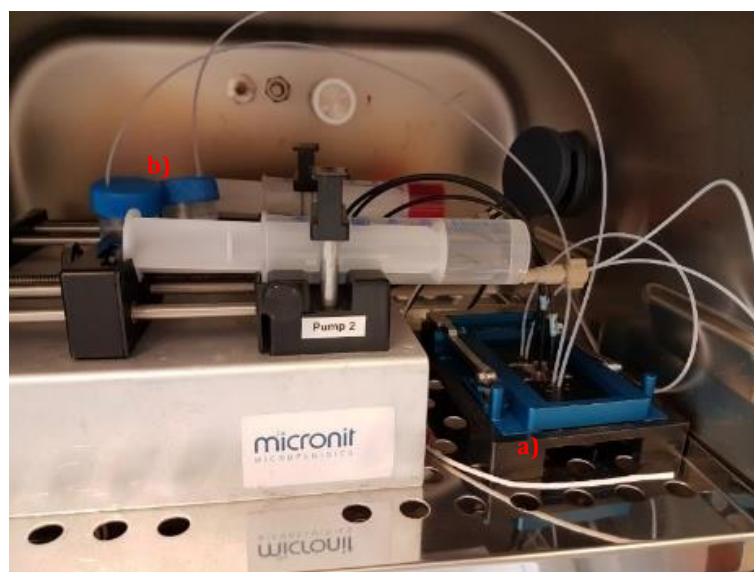


**Figure 118** Experimental setup for the microfluidic device for the cell experiments. The device was assembled in an incubator thermostatted to 37 °C. Pumps ensured a constant flow rate from the syringes to the chip in the holder (a) until the falcon tubes (b). A FireStingO2 device connected to the chip via fibre optics (black cables) allowed the contactless O<sub>2</sub> sensing. A temperature sensor (white cable) was used to monitor the temperature.

During the experiment, the flow of both PBS and cell medium were kept at a rate of  $13 \mu\text{L}/\text{min}$  until the measured  $p\text{O}_2$  values reached constant values. Once this steady state was reached, the flow was stopped. While the flow was on, there was constant replacement of the medium in the chip but once the flow stopped, the medium was not renewed anymore and so the cells were expected to drain the oxygen from the medium present in the lower channel. Accordingly, the  $p\text{O}_2$  values measured at the centre sensor spot should drop.

**Figure 119** shows that, as expected, the oxygen partial pressure decreased substantially after the flow was stopped. Moreover, turning on the flow caused the  $p\text{O}_2$  values to increase again, demonstrating that the cells remained viable and the results reproducible throughout the experiment.

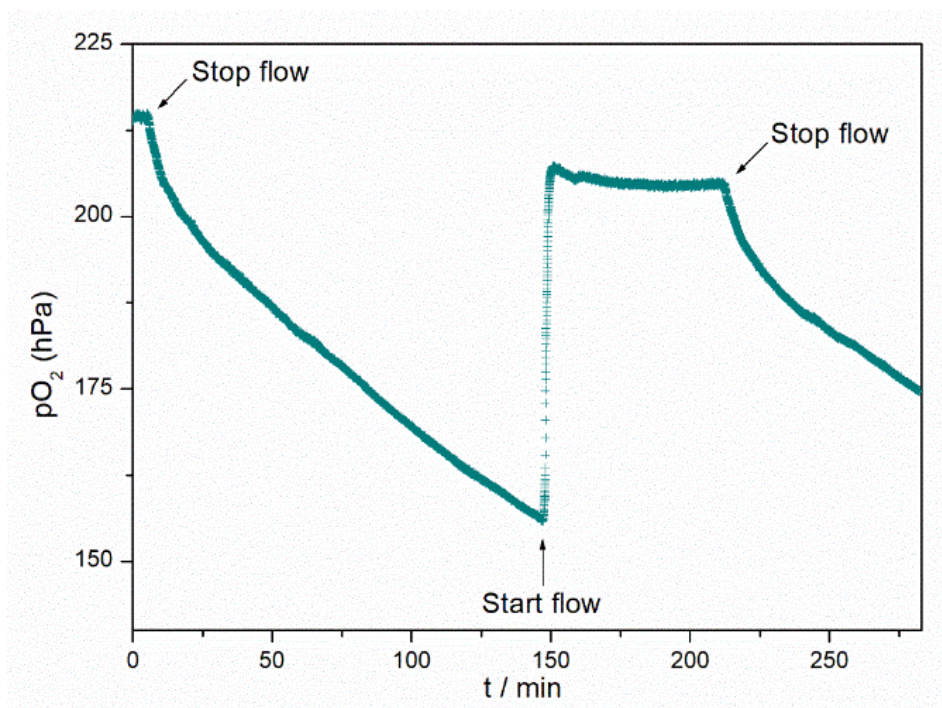


**Figure 119**  $p\text{O}_2$  values measured at the centre sensor spot of the microfluidic chip device. When cell medium flowed at  $13 \mu\text{L}/\text{min}$  the  $p\text{O}_2$  values were constant. After stopping the flow, the values dropped due to the consumption of  $\text{O}_2$  by the HUVEC cells. Restarting the flow caused the  $p\text{O}_2$  level to increase to its original value.

To confirm that the observed decrease of the  $p\text{O}_2$  values was indeed due to oxygen consumption by the cells, the same experiment was performed with no cells present in the

membrane. In this case, no significant changes of the determined  $pO_2$  value were observed, indicating that stopping and restarting the flow had no effect on the readout and that the 60 hPa drop of the  $pO_2$  value when cells were present was indeed caused by their oxygen consumption (Figure 120).

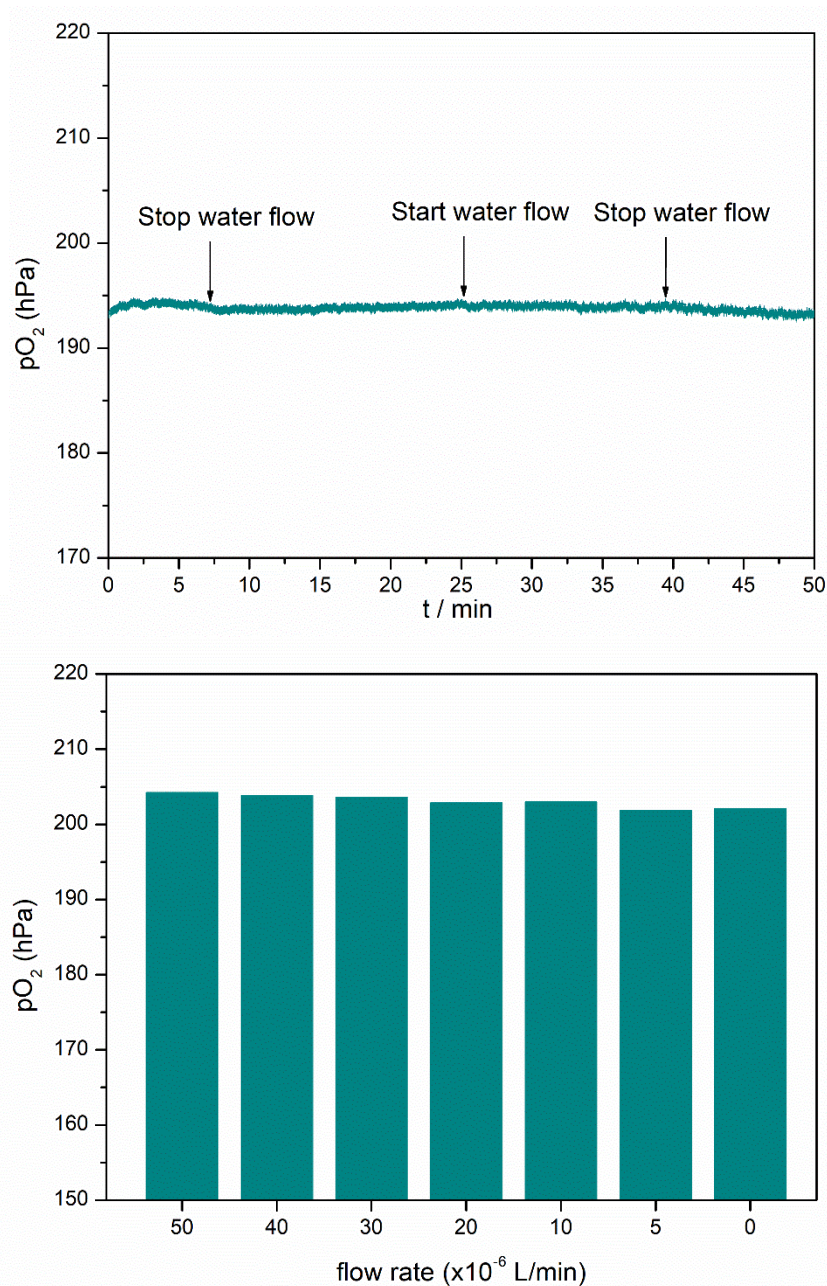


**Figure 120** Top:  $pO_2$  values at the centre sensor spot of the microfluidic chip device when air saturated water flowed at  $13 \mu\text{L}/\text{min}$  in both channels. After stopping the flow, the  $pO_2$  values at the membrane were stable. Bottom:  $pO_2$  values at the centre sensor spot at different flow rates. The  $pO_2$  values were obtained by averaging the values when the signal was stable (in steady state).

### 3.4. CONCLUDING REMARKS

The tetrabenzoporphyrin-derived Pt(II) complex **PtTPTBPF** was successfully synthesized and characterized. Microfluidic devices were prepared containing **PtTPTBPF** incorporated in different matrices and their oxygen sensing capabilities evaluated.

The obtained chips were substantially better than the ones previously developed at Micronit because of the homogeneous distribution of the Pt(II) complex within the sensor spots. Of the polymeric matrices tested, OXNANO nanoparticles proved to be the best. The respective chips were easy to fabricate, had thin sensor spots, and exhibited high oxygen sensitivity. The reproducibility of the measurements was satisfactory and different chips afforded comparable results.

These chips could be used in a biological assay to measure the oxygen consumption of HUVEC cells. A sensitive and fast response to the drop of the oxygen level in the cell medium was observed when the cells were present, confirming that the developed microfluidic chips can be viewed as a new “biosensor-on-a-chip” device.



## **4. Conclusion and Outlook**



In one project of this thesis, cyclopeptide derived hollow coordination compounds were obtained through Pd(II)-directed self-assembly. Specifically, the treatment of the pyridine containing cyclopeptides **CP1** and **CP2** with  $[\text{Pd}(\text{en})(\text{NO}_3)_2]$  afforded the metallamacrocycle **CP1<sub>2</sub>Pd<sub>2</sub>** and the cage **CP2<sub>2</sub>Pd<sub>3</sub>**. These products were characterized by means of NMR spectroscopy and mass spectrometry. The reaction between **CP1** and  $[\text{Pd}(\text{CH}_3\text{CN})_4](\text{BF}_4)_2$  afforded, according to ESI-MS and NMR measurements, a complex with the composition **CP1<sub>6</sub>Pd<sub>3</sub>** and the smaller cage **CP1<sub>4</sub>Pd<sub>2</sub>**. The calculated structures of the three coordination complexes are shown in **Figure 121**.

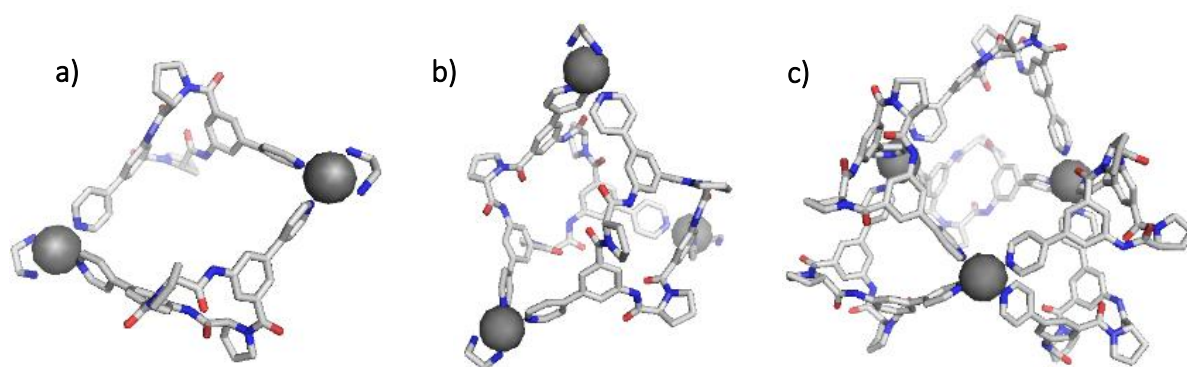


**Figure 121** a) Calculated structure of **CP1<sub>2</sub>Pd<sub>2</sub>** (a), **CP2<sub>2</sub>Pd<sub>3</sub>** (b), and **CP1<sub>6</sub>Pd<sub>3</sub>** (c). All calculations were performed at the semi-empirical PM6 level as implemented in Spartan 18, Wavefunction Inc. Hydrogen atoms are omitted for clarity.

Binding studies indicated that **CP1<sub>2</sub>Pd<sub>2</sub>** incorporated different dicarboxylates, sodium 1,3-benzenedisulfonate (**BDS**), and sodium 2,6-naphthalenedisulfonate (**NDS**) into its cavity. In the case of **BDS** a 1:1 complex was formed that had a  $\log K_a$  of  $4.8 \pm 0.2$  in  $\text{D}_2\text{O}/\text{CD}_3\text{OD}$ , 1:1 (v/v). In the case of **NDS**, binding was slow on the NMR time-scale and involved the binding of two guest molecules as confirmed by a crystal structure of the complex.

Based on these first examples of Pd(II)-containing cyclopeptide-derived coordination compounds, future work should focus on the design of molecular architectures that can, for example, be used as receptors for biorelevant guests.

In the second project, efforts were made at creating luminescent cyclopeptide-derived Pt(II) complexes by coordinating **CP1** or **CP2** to suitable Pt(II)-containing precursors. The coordination of both peptides to a known Pt(II) complex afforded insoluble products that could not be characterized further. To circumvent these solubility issues, the synthesis of the analogous cyclopeptide complexes containing more polar ligands was attempted.

Although mass spectrometry provided evidence for the formation of the target complexes **PtDeg-CP1** and **PtDeg-CP2** (Figure 122) in the crude reaction mixtures, the products could not be isolated in pure form. The impure samples of **PtDeg-CP1** and **PtDeg-CP2** both exhibited orange emission.

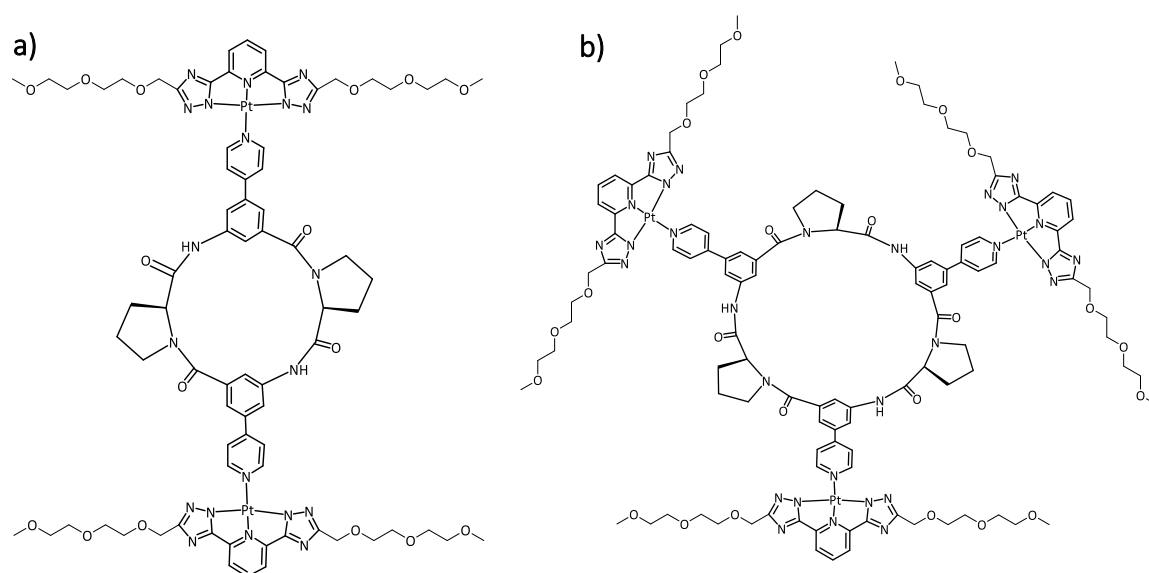


**Figure 122** Structures of the target complexes **PtDeg-CP1** (a) and **PtDeg-CP2** (b).

Further work is necessary to improve the preparation of such complexes. Only then can the characterization of their photophysical properties and self-assembling behavior be addressed.

In the third project of this thesis, microfluidic devices containing the Pt(II) complex **PtTPTBPF** incorporated in different polymeric matrices were prepared and their oxygen sensing abilities characterized. It was shown that chips containing the Pt(II) complex incorporated into OXNANO nanoparticles were highly sensitive to oxygen, easy to fabricate, and allowed reliable oxygen quantification. Chips made by using other polymeric matrices such as PDMS, Elastosil®E43 or polystyrene were less suitable for the measurements. The OXNANO-containing chips furthermore allowed measuring the oxygen consumption of HUVEC cells in a biological assay even in repeated measurements. Future studies should now involve using these chips for monitoring in real time small scale biological processes.

## **5. Experimental Procedures**



## 5.1. Metal Directed Self-Assembly of Cyclopeptide-Containing Macrocycles and Cages

### 5.1.1 Synthetic Procedures

**General details.** All chemicals used in the synthesis, purification, and product analyses were commercially available and used without further purification except for 6N HCl in 1,4-dioxane. To afford this solution, HCl was bubbled through dry 1,4-dioxane under stirring and cooling with an ice bath. The concentration of the solution was then checked by titration with 1M aqueous NaOH and phenolphthalein as an indicator. Reaction control was conducted by using thin layer chromatography: Kieselgel 60 F254/Kieselgel 60G Merck TLC plates. Analyses were carried out as follows: NMR: Bruker AVANCE III 400, Bruker AVANCE 600, peak assignments were confirmed by using H,H-COSY, H,H-NOESY, HMQC and HMBC spectra; spectra were referenced to the residual solvent signals (acetonitrile- $d_3$ :  $\delta^H = 1.94$  ppm,  $\delta^C = 118.26$  ppm, chloroform- $d_1$ :  $\delta^H = 7.26$  ppm,  $\delta^C = 77.16$  ppm, DMSO- $d_6$ :  $\delta^H = 2.50$  ppm,  $\delta^C = 39.5$  ppm, DMF- $d_7$ :  $\delta^H = 8.03$  ppm,  $\delta^C = 163.15$  ppm, Methanol- $d_4$ :  $\delta^H = 3.31$  ppm,  $\delta^C = 49.00$  ppm)<sup>207</sup>; MALDI-TOF-MS: BrukerUltraflex TOF/TOF; ESI-MS: AmaZonETD, Bruker Daltonics and Orbitrap XL, Thermo Fisher Scientific; elemental analysis: Elementar vario Micro Tube. The following abbreviations are used: ABA, 3-aminobenzoic acid; BDS, 1,3-benzenedisulfonate; NDS, 2,6-naphthalenedisulfonate; Pro, L-proline; Py, pyridyl; Bu, *n*-butyl; Bn, benzyl; Ph, phenyl.

**DOSY NMR Spectroscopy.** The DOSY NMR measurements were performed by using a Bruker Avance III HD 400 spectrometer with a superconducting magnet (Bruker Ascend 400) and a magnetic field strength of 9.4 T, corresponding to a proton Larmor frequency of 400.25 MHz. The spectrometer was equipped with a probe head with cryogenically cooled electronics (CryoProbe Prodigy, Bruker Biospin, Germany). The temperature control was calibrated with a platinum resistance thermometer (Pt-100, uncertainty estimated to be  $\pm 0.15$  K) which itself was previously calibrated using a certified standard. Measurements were conducted at a constant temperature of 298 K. The used pulse sequence consisted

of a stimulated echo with bipolar gradients and one spoil gradient as implemented in the spectrometer's software (Bruker TopSpin 3.2, pulse sequence: stebpgp1s). The diffusion measurements were calibrated by using water. The parameters of the measurements (gradient pulse length  $\delta$ , number of scans, diffusion transients) were varied in order to fit the respective sample and to produce similar signal-to-noise ratios. The diffusion time  $\Delta$  was kept at 50.0 ms. The DOSY NMR spectra were processed with DOSY Toolbox, University of Manchester.<sup>208</sup> The diffusion coefficients were calculated by using the Stokes-Einstein equation  $D = k T / 6 \pi \eta r_H$ , where  $k$  is the Boltzmann constant,  $T$  the temperature (298 K),  $\eta$  the viscosity of the solvent,  $D$  the diffusion coefficient, and  $r_H$  the hydrodynamic radius, assuming a hard spherical shape and infinite dilution. The hydrodynamic diameter  $d_H$  is thus  $2 r_H$ . The viscosity  $\eta$  of CD<sub>3</sub>OD/D<sub>2</sub>O, 1:1 (v/v) was estimated to amount to 0.00173 N s m<sup>-2</sup> by using a procedure described in the literature.<sup>209,210</sup> For DMSO-*d*<sub>6</sub>, a viscosity of 0.00219 N s m<sup>-2</sup> was used.<sup>211</sup> Note that the structures measured may deviate considerably from the spherical shape that was assumed in the estimation of the hydrodynamic diameter.<sup>212</sup>

**General Procedure for the cleavage of Boc groups.** A solution of the carbamate in 1,4-dioxane (20 mL/mmol) was cooled with an ice bath and a 6 N solution of HCl in 1,4-dioxane (40 mL/mmol) was added dropwise. The reaction mixture was stirred for 2 h at 25 °C, followed by evaporation of the solvent in vacuum. The sticky resin was triturated with diethyl ether (40 mL/mmol), the resulting suspension was stirred for additional 2.5 h, and the product was filtered off and dried in vacuum.

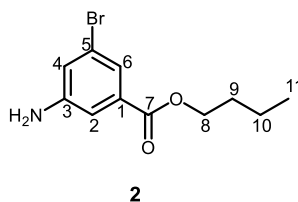
**General Procedure for the cleavage of butyl esters.** The ester was dissolved in 1,4-dioxane (20 mL/mmol). Water (20 mL/mmol) and a 1 M solution of sodium hydroxide in water (5 mL/mmol) were added and the reaction mixture was stirred for 2.5 h at 25 °C. After evaporation of the 1,4-dioxane, the pH value of the aqueous layer was adjusted with saturated aqueous potassium bisulfate to pH 6.4 and the resulting solution was extracted three times with chloroform. The combined organic layers were washed with water and dried over MgSO<sub>4</sub>. After evaporation of the solvent, the residue was dried in vacuum.

**General procedure for the hydrogenation of benzyl esters.** To a solution of the ester in 1,4-dioxane/water, 9:1 (v/v) (60 mL/mmol), 10% Pd/C (15 mass%, suspended in 2 mL of

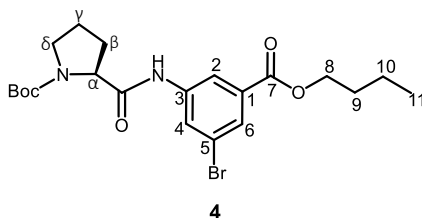


water) was added. The reaction mixture was hydrogenated at atmospheric pressure for 6 d at 25 °C. Subsequently, the catalyst was filtered off through a layer of Celite and washed with 1,4-dioxane/water, 9:1 (v/v). The solvent was evaporated and the sticky residue was treated with ethyl acetate. After evaporation of the solvent, the product was dried in vacuum.

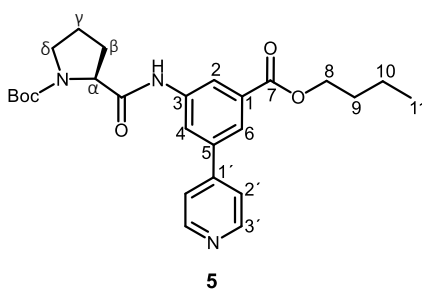
**Synthesis of the cyclopeptides.** The synthetic procedures described were based on previous work executed in the Kubik group.<sup>102,109</sup> Alterations were made in the cyclization reaction conditions and the work-up of the cyclized products to obtain higher yields. All intermediate products were characterized by NMR spectroscopy and/or MALDI-TOF-MS by comparison with the published results. The final products were fully characterized to confirm structure and purity.



**Butyl-3-amino-5-bromobenzoate (2).** Concentrated H<sub>2</sub>SO<sub>4</sub> (6 mL) was added dropwise to a suspension of 3-amino-5-bromobenzoic acid (10 g, 46.3 mmol) in *n*-butanol (60 mL) at room temperature. The mixture was stirred for 3 days and then filtered. A saturated solution of sodium bicarbonate was added to the filtrate until the pH of the solution reached 8. Afterward, the resulting solution was extracted three times with CH<sub>2</sub>Cl<sub>2</sub>. The combined organic layers were dried over MgSO<sub>4</sub>, filtered, the solvent was evaporated and the resulting product was dried under vacuum. Yield: 9.35 g (34,4 mmol, 74%). <sup>1</sup>H NMR (400 MHz, CDCl<sub>3</sub>): δ=7.51 (t, 1H, <sup>4</sup>J=1.6 Hz, H6), 7.26-7.25 (m, 1H, H2), 6.98 (t, 1H, <sup>4</sup>J=2.0 Hz, H4), 4.28 (t, 2H, <sup>3</sup>J=6.6 Hz, BuH(8)), 3.87 (bs, 2H, NH<sub>2</sub>), 1.76-1.69 (m, 2H, BuH(9)), 1.50-1.41 (m, 2H, BuH(10)), 0.97 (t, 3H, <sup>3</sup>J=7.4 Hz, BuCH<sub>3</sub>) ppm. <sup>13</sup>C NMR (101 MHz, CDCl<sub>3</sub>): δ= 165.73 (C7), 147.90 (C3), 133.12 (C1), 122.99 (C5), 122.35(C6), 121.69(C4), 114.70 (C2), 65.30 (C8), 30.84 (C9), 19.37 (C10), 13.89 (C11) ppm.

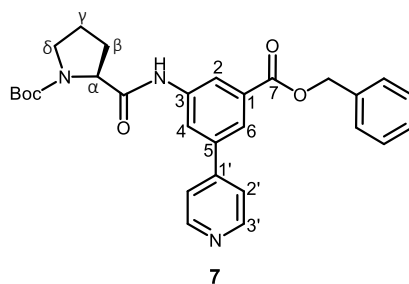


**Boc-Pro-(5-Br-ABA)-OBu (4).** Boc-L-Proline (6.81 g, 31.7 mmol) and butyl-3-amino-5-bromobenzoate (7.18 g, 26.4 mmol) were dissolved in CH<sub>2</sub>Cl<sub>2</sub> (507 mL). DIPEA (12.62 g, 97.7 mmol) and PyCloP (11.4 g, 26.4 mmol) were added at room temperature and the reaction mixture was stirred for 24 hours. Afterwards, the solvent was evaporated, and the residue was purified by column chromatography on silica gel (eluent: EtOAc/*n*-hexane, 1:1 (v/v)) to afford a sticky resin. The resin was triturated with *n*-hexane and the solid thus formed was filtered off and dried in vacuum. Yield: 11.2 g (24.3 mmol, 92%). <sup>1</sup>H NMR (400 MHz, CDCl<sub>3</sub>): δ=9.82 (bs, 1H, NH), 8.16 (s, 2H, (ABAH(2)+ABAH(6))), 7.85 (s, 1H, ABAH(4)), 4.49-4.44 (m, 1H, ProH(α)), 4.31 (t, 2H, <sup>3</sup>J=6.2 Hz, BuH(8)), 3.43-3.35 (m, 2H, ProH(δ)), 2.56-2.46 (m, 1H, ProH(β)), 1.98-1.88 (m, 2H, ProH(β)+ProH(γ)), 1.77-1.70 (m, 1H, ProH(γ)), 1.62-1.59 (m, 2H, BuH(9)), 1.50 (s, 9H, BocCH<sub>3</sub>), 1.48-1.43 (m, 2H, BuH(10)), 0.97 (t, 3H, <sup>3</sup>J=7.6 Hz, BuCH<sub>3</sub>) ppm. **MS (MALDI-TOF):** *m/z* (%)=369.0 [M-Boc+H]<sup>+</sup>, 491.1 [M+Na]<sup>+</sup>, 507.1 [M+K]<sup>+</sup>.



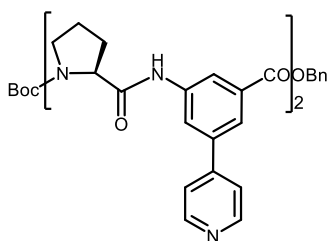
**Boc-Pro-(5-(Pyr-4-yl)-ABA)-OBu (5).** A flask containing Boc-Pro-(5-Br-ABA)-OBu (11.2 g, 24.05 mmol), Pd<sub>2</sub>(dba)<sub>3</sub> (0.22 g, 0.239 mmol), X-Phos (0.45 g, 0.943 mmol), pyridin-4-ylboronic acid (4.64 g, 37.75 mmol), and K<sub>3</sub>PO<sub>4</sub> (10.22 g, 48.00 mmol) was evacuated and back-filled with nitrogen gas three times. Degassed *n*-butanol was added, and the reaction mixture was stirred for 24 hours at 80 °C. The suspension was filtered, and the filter cake was washed with CH<sub>2</sub>Cl<sub>2</sub>. The filtrate was evaporated, and the remaining residue was

purified chromatographically on silica gel (eluent: EtOAc). The sticky resin collected after evaporation of the product fractions was triturated with diethyl ether/*n*-hexane, 1:1 (v/v). Afterwards, the solvent was evaporated, and product was dried under vacuum. Yield: 7.91 g (16.92 mmol, 70%).  $^1\text{H NMR}$  (400 MHz,  $\text{CDCl}_3$ ):  $\delta$ =9.94 (bs, 1H, NH), 8.69-8.68 (m, 2H, (PyH(3')), 8.25 (s, 1H, ABAH(2)), 8.02 (s, 1H, ABAH(6)), 7.97 (s, 1H, ABAH(4)), 7.54-7.53 (m, 2H, PyH(2')), 4.57-4.53 (m, 1H, ProH( $\alpha$ )), 4.35 (t, 2H,  $^3J$ =6.7 Hz, BuH(8)), 3.52-3.42 (m, 2H, ProH( $\delta$ )), 2.55-2.48 (m, 1H, ProH( $\beta$ )), 2.09-1.96 (m, 2H, ProH( $\beta$ )+ProH( $\gamma$ )), 1.80-1.74 (m, 3H, ProH( $\gamma$ )+BuH(9)), 1.54 (s, 9H, BocCH<sub>3</sub>), 1.52-1.44 (m, 2H, BuH(10)), 1.00 (t, 3H,  $^3J$ =7.6 Hz, BuCH<sub>3</sub>) ppm.  $^{13}\text{C NMR}$  (101 MHz,  $\text{CDCl}_3$ ):  $\delta$ = 176.82 (HNC=O), 165.94 (C7), 157.73 (BocC=O), 150.44 (PyC(3')), 147.21 (PyC(1')), 139.63 (C3), 139.10 (C5), 135.38 (C1), 132.09 (C4/6), 121.78 (PyC(2')), 120.78 (C2), 81.29 (BocOC(CH<sub>3</sub>)<sub>3</sub>), 77.36 (C $\alpha$ ), 65.38 (C8), 47.47 (C $\delta$ ), 31.73 (C9), 30.86 (C $\beta$ ), 28.56 (Boc(CH<sub>3</sub>)<sub>3</sub>), 19.39 (C $\delta$ ), 14.27 (C10), 13.93 (C11) ppm. **MS (MALDI-TOF)**:  $m/z$  (%)=368.1 [M-Boc+H]<sup>+</sup>, 468.2 [M+H]<sup>+</sup>, 490.2 [M+Na]<sup>+</sup>.



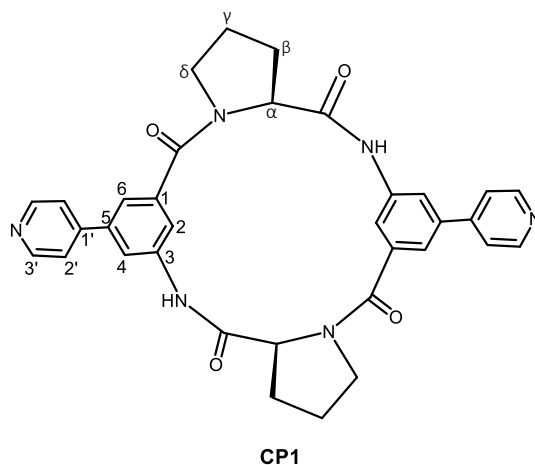
**Boc-Pro-(5-Pyr-4-yl)-ABA-OBn (7)**. Boc-Pro-(5-Pyr-4-yl)-ABA-OBu was saponified at the carboxylic acid group according to the general procedure. To a suspension of the thus obtained acid (3.3 g, 8 mmol) in  $\text{CH}_2\text{Cl}_2$  (165 mL), benzyl alcohol (2.75 mL, 26.4 mmol), DIPEA (4.65g, 36 mmol), and TBTU (3.85 g, 12 mmol) were added, and the reaction mixture was stirred for 2 days at room temperature. Afterwards, the solvent was evaporated, the residue dissolved in EtOAc (200 mL), and the solution was washed with 5% aqueous  $\text{Na}_2\text{CO}_3$  and water. The organic layer was dried over  $\text{MgSO}_4$  and concentrated under reduced pressure. The purification of the residue by column chromatography (eluent: EtOAc) afforded the product as a sticky resin that was subsequently triturated with diethyl ether/hexane, 1:1 (v/v). After evaporation of the solvent and drying of the residue in

vacuum, a colourless powdery solid was obtained. Yield: 3.01 g (6.00 mmol, 75%). <sup>1</sup>H NMR (400 MHz, CDCl<sub>3</sub>): δ=10.11 (s, 1H, NH), 8.69-8.68 (m, 2H, PyH(3')), 8.31 (s, 1H, ABAH(2)), 8.11 (s, 1H, ABAH(6)), 7.95 (s, 1H, ABAH(4)), 7.86-7.85 (m, 2H, PyH(2')), 7.45-7.35 (m, 5H, BnH(Ph)), 5.39-5.30 (m, 2H, BnCH<sub>2</sub>), 4.56-4.52 (m, 1H, ProH(α)), 3.54-3.38 (m, 2H, ProH(δ)), 2.46-2.41 (m, 1H, ProH(β)), 2.04-1.95 (m, 3H, ProH(β)+ProH(γ)), 1.48 (s, 9H, BocCH<sub>3</sub>) ppm. **MS (MALDI-TOF):** *m/z* (%)=502.3 [M+H]<sup>+</sup>, 524.3 [M+Na]<sup>+</sup>, 540.3 [M+K]<sup>+</sup>.

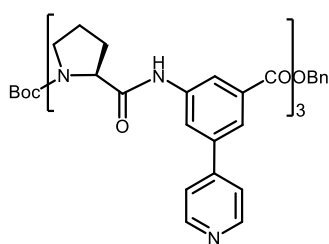


9

**Boc-[Pro-(5-Pyr-4-yl)-ABA]2-OBn (9).** Boc-Pro-(5-Pyr-4-yl)-ABA-OBu was deprotected at the carboxylic acid group according to the general procedure. An equivalent amount of Boc-Pro-(5-Pyr-4-yl)-ABA-OBn was deprotected at the amino group according to the general procedure. Boc-Pro-(5-Pyr-4-yl)-ABA-OH (1,65 g, 4 mmol) and H-Pro-(5-Pyr-4-yl)-ABA-OBn · 2HCl (1,92 g, 4 mmol) were suspended in CH<sub>2</sub>Cl<sub>2</sub> (200 mL). DIPEA (2,32 g, 18 mmol) and PyCloP (2,24 g, 0,52 mmol) were added at room temperature and the reaction mixture was stirred for 24 hours. Afterwards, the solvent was evaporated, the residue was purified by column chromatography (eluent: CH<sub>2</sub>Cl<sub>2</sub>/MeOH 10:1 (v/v)) and the solvent was evaporated. Next, the residue was triturated with *n*-hexane, the solvent was evaporated, and the product was dried in vacuum. Yield: 2.73 g (3.40 mmol, 85%). **MS (MALDI-TOF):** *m/z* (%)=695.4 [M-Boc+H]<sup>+</sup>, 795.4 [M+H]<sup>+</sup>, 817.4 [M+Na]<sup>+</sup>.

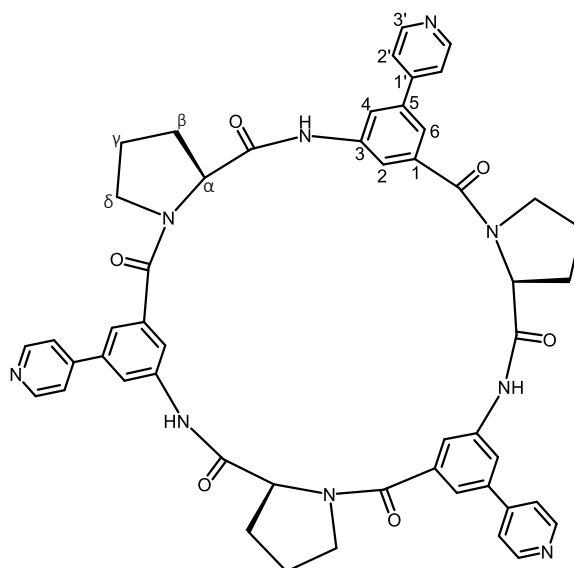


**cyclo[Pro-(5-Pyr-4-yl)-ABA]<sub>2</sub> (CP1).** Boc-[Pro-(5-Pyr-4-yl)-ABA]<sub>2</sub>-OBn was first hydrogenated and then deprotected at the amino group according to the general procedures. The fully deprotected tetrapeptide H-[Pro-(5-Pyr-4-yl)-ABA]<sub>2</sub>-OH (0.71 g, 1.00 mmol) was dissolved in DMF (280 mL) and DIPEA (2.23 mL, 13.00 mmol). This solution was added to a solution of TBTU (1.6 g, 5 mmol) and DIPEA (1.54 mL, 9 mmol) in DMF (120 mL) over the course of 4 hours at 80 °C. If necessary, the pH of the mixture was adjusted to 9 by adding more DIPEA. After the addition was complete, the reaction was left stirring for 2h at 80 °C. The solvent was then evaporated, and the residue purified by flash chromatography (eluent: CH<sub>2</sub>Cl<sub>2</sub>/MeOH 10:1, 5:1, 1:1 (v/v)). The residue collected after evaporation of the product fractions was triturated with hot EtOH (5 mL). The crude product was filtered off and washed with EtOH and diethyl ether. Pure product was obtained as a white solid by crystallization from DMF at room temperature and dried in vacuum at 80 °C. Yield: 0.12 g (0.20 mmol, 20%). **<sup>1</sup>H NMR** (400 MHz, DMSO-*d*<sub>6</sub>): δ 9.55 (s, 2H, NH), 8.65-8.64 (m, 4H, PyH(3')), 8.12 (s, 2H, ABAH(2)), 7.64-7.62 (m, 4H, PyH(2')), 7.49 (t, 2H, <sup>4</sup>J=1.4Hz, ABAH(6)), 7.15 (s, 2H, ABAH(4)), 4.05 (dd, 2H, <sup>3</sup>J<sub>ax,eq</sub> = 2.5 Hz, <sup>3</sup>J<sub>ax,ax</sub> = 8.4 Hz, ProH(α)), 3.66-3.63 (m, 4H, ProH(δ)), 2.25-2.17 (m, 2H, ProH(β)), 2.01-1.92 (m, 6H, ProH(β)+H(γ)) ppm. **<sup>13</sup>C NMR** (101 MHz, DMSO-*d*<sub>6</sub>) δ 171.9 (ProCO), 168.8 (ABACO), 150.4 (PyC(3')), 146.0 (PyC(1')), 139.3 (ABAC(1/3)), 139.0 (ABAC(1/3)), 138.1 (ABAC(5)), 121.1 (PyC(2')), 119.2 (ABAC(6)), 117.7 (ABAC(2)), 117.4 (ABAC(4)), 62.0 (ProC(α)), 46.9 (ProC(δ)), 31.2 (ProC(β)), 22.8 (ProC(γ)) ppm. **MS (MALDI-TOF):** *m/z* (%)=587.4 [M+H]<sup>+</sup>, 609.4 [M+Na]<sup>+</sup>, 625.4 [M+K]<sup>+</sup>. **ELEMENTAL ANALYSIS:** CHN calculated for C<sub>34</sub>H<sub>30</sub>N<sub>6</sub>O<sub>4</sub>·H<sub>2</sub>O: C, 67.54; H, 5.33; N, 13.90; found: C, 67.49; H, 5.29; N, 13.93.



12

**Boc-[Pro-(5-Pyr-4-yl)-ABA]3-OBn (12).** Boc-Pro-(5-Pyr-4-yl)-ABA-OBu was deprotected at the carboxylic acid group according to the general procedure. An equivalent amount of Boc-[Pro-(5-Pyr-4-yl)-ABA]<sub>2</sub>-OBn was deprotected at the amino group according to the general procedure. To a mixture of Boc-Pro-(5-Pyr-4-yl)-ABA-OH (1.24 g, 3.30 mmol), H-[Pro-(5-Pyr-4-yl)-ABA]<sub>2</sub>-OBn · 3HCl (2.64 g, 3.30 mmol) and TBTU in DMF (70 mL), DIPEA (1.32 g, 10.20 mmol) was added dropwise under stirring. The reaction was stirred for 2 days at room temperature. Afterwards, it was poured into water (400 mL) under stirring. The pH of the suspension was adjusted to 4 with 1N HCl and the mixture was stirred for 10 minutes. The precipitate was filtered off, washed with water and dried under vacuum. The crude product was purified by column chromatography (eluent: CH<sub>2</sub>Cl<sub>2</sub>/MeOH 8:1 (v/v)) to afford the product as a powder. Yield: 1.88 g (1.70 mmol, 52%).  
**MS (MALDI-TOF):** *m/z* (%)=989.1 [M-Boc+H]<sup>+</sup>, 1089.2 [M+H]<sup>+</sup>, 1127.4 [M+K]<sup>+</sup>.

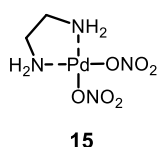


CP2

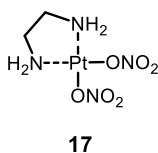
**cyclo[Pro-(5-Pyr-4-yl)-ABA]<sub>3</sub> (CP2).** Boc-[Pro-(5-Pyr-4-yl)-ABA]<sub>3</sub>-OBn was first hydrogenated and then deprotected at the amino group according to the general procedures. The fully deprotected hexapeptide H-[Pro-(5-Pyr-4-yl)-ABA]<sub>3</sub>-OH (0.44 g, 0.42 mmol) was dissolved in DMF (20 mL) and DIPEA (0.70 mL, 3.80 mmol). This solution was added to a solution of TBTU (0.70 g, 2.10 mmol) and DIPEA (1 mL, 5.5 mmol) in DMF (120 mL) over the course of 4 hours at room temperature. If necessary, the pH was adjusted to 9 by adding more DIPEA. After the addition was complete, the reaction was left stirring for 6h at 80 °C. The solvent was then evaporated, and the residue purified by flash chromatography (eluent: CH<sub>2</sub>Cl<sub>2</sub>/MeOH 10:1, 5:1, 1:1 (v/v) and 100% MeOH). All fractions containing the product were combined and evaporated. Acetone was added and a white precipitate was formed. The suspension was centrifuged, and the solvent separated from the solid. The solvent was evaporated, and methanol was added. Again, a white precipitate was formed that was centrifuged. Several cycles of washing, precipitating and centrifuging with acetone or methanol were made until the final compound was pure. Yield: 0.16 g (0.18 mmol, 43%). <sup>1</sup>H NMR (400 MHz, DMSO-*d*<sub>6</sub>): δ 10.52 (s, 3H, NH), 8.69 (d, 6H, <sup>2</sup>J=5.9 Hz, PyH(3')), 8.48 (s, 3H, ABAH(2)), 7.72 (d, 6H, <sup>2</sup>J=5.9 Hz, PyH(2')), 7.62 (s, 3H, ABAH(4)), 7.56 (s, 3H, ABAH(6)), 4.72 (dd, 3H, <sup>3</sup>J<sub>ax,eq</sub> = 4.1 Hz, <sup>3</sup>J<sub>ax,ax</sub> = 8.3 Hz, ProH(α)), 3.50 (t, 6H, <sup>4</sup>J=6.7 Hz, ProH(δ)), 2.36-2.31 (m, 3H, ProH(β)), 2.10-2.03 (m, 3H, ProH(β)), 2.01-1.87 (m, 6H, ProH(γ)) ppm. <sup>13</sup>C NMR (101 MHz, DMSO-*d*<sub>6</sub>) δ 170.5 (ProCO), 168.4 (ABACO), 150.4

(PyC(3')), 146.3 (PyC(1')), 139.9 (ABAC(1/3)), 139.3 (ABAC(1/3)), 137.8 (ABAC(5)), 121.3 (PyC(2')), 119.0 (ABAC(2/6)), 118.9 (ABAC(2/6)), 118.0 (ABAC(4)), 60.1 (ProC( $\alpha$ )), 49.4 (ProC( $\delta$ )), 29.6 (ProC( $\beta$ )), 24.6 (ProC( $\gamma$ )) ppm. **MS (MALDI-TOF):**  $m/z$  (%) = 880.3 [M+H]<sup>+</sup>, 901.3 [M+Na]<sup>+</sup>, 919.4 [M+K]<sup>+</sup>. **ELEMENTAL ANALYSIS:** CHN calculated for C<sub>51</sub>H<sub>45</sub>N<sub>9</sub>O<sub>6</sub>·0.5H<sub>2</sub>O: C, 68.91; H, 5.22; N, 14.18; found: C, 68.88; H, 5.25; N, 14.15.

### 5.1.2 Synthesis of the coordination complexes.

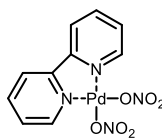


**[Pd(NO<sub>3</sub>)<sub>2</sub>(en)] (15).**<sup>215</sup> [PdCl<sub>2</sub>(en)] (0.2 g, 0.84 mmol) was suspended in water (280 mL) at room temperature. AgNO<sub>3</sub> (0.28 g, 1.68 mmol) was added and the mixture was left stirring for 2 hours. The white solid (AgCl) was then filtered off and the filtrate evaporated in vacuum to yield a pale-yellow solid. Yield: 0.16 g (0.56 mmol, 67%). **ELEMENTAL ANALYSIS:** CHN calculated for C<sub>2</sub>H<sub>8</sub>N<sub>4</sub>O<sub>6</sub>Pd: C, 8.27; H, 2.78; N, 19.30. Found: C, 8.25; H, 2.80; N, 19.66.



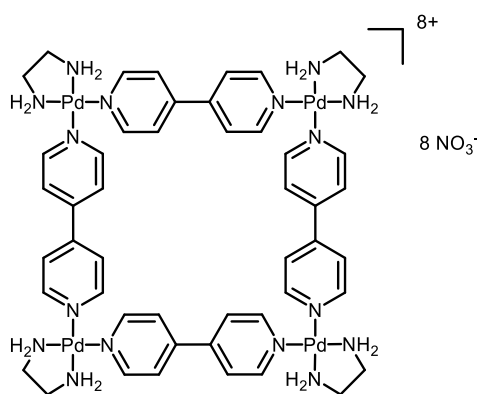
**[Pt(NO<sub>3</sub>)<sub>2</sub>(en)] (17).**<sup>213</sup> [PtCl<sub>2</sub>(en)] (50 mg, 0.15 mmol) was suspended in water (9 mL) at room temperature under stirring. AgNO<sub>3</sub> (51 mg, 0.30 mmol) was added and the mixture was left stirring overnight at room temperature in the dark. The white solid (AgCl) was then filtered off and the filtrate evaporated in vacuum to yield a pale-yellow solid. Yield: 28 mg (0.075 mmol, 50%). **ELEMENTAL ANALYSIS:** CHN calculated for H<sub>8</sub>C<sub>2</sub>N<sub>4</sub>O<sub>6</sub>Pt·2H<sub>2</sub>O: C, 5.79; H, 2.91; N, 13.49. Found: C, 5.75; H, 2.97; N, 13.32.





19

**[Pd(NO<sub>3</sub>)<sub>2</sub>(2,2'-Bipy)] (19).**<sup>214</sup> (2,2'-Bipyridine)dichloropalladium(II) (70 mg, 0.21 mmol) was suspended in water (140 mL). AgNO<sub>3</sub> (0.071 g, 0.42 mmol) was added and the mixture was left stirring for 24 h at 55 °C in the dark. The white solid (AgCl) was then filtered off and the filtrate slowly evaporated at 50 °C to yield a pale-yellow solid. Yield: 50 mg (0.13 mmol, 62%). **ELEMENTAL ANALYSIS:** CHN calculated for C<sub>10</sub>H<sub>8</sub>N<sub>4</sub>O<sub>6</sub>Pd·H<sub>2</sub>O: C, 29.68; H, 2.49; N, 13.85. Found: C, 29.80; H, 2.52; N, 13.88.



21

**Fujita's square (21).**<sup>68</sup> A solution of 4,4'-bipyridine (15.6 mg, 0.1 mmol) in ethanol (800 μL) was added to a solution of [Pd(NO<sub>3</sub>)<sub>2</sub>(en)] (29.0 mg, 0.1 mmol) in water/ethanol (800 μL (1:1 (v/v))). The reaction was left stirring for 30 minutes at room temperature. Afterwards, ethanol (800 μL) was added, and a yellow powder precipitated. The powder was filtered off and characterized. Yield: 33 mg (0.0185 mmol, 74%). <sup>1</sup>H NMR (400 MHz, DMSO-*d*<sub>6</sub>): δ=8.95-9.08 (d, 16H, (PyH(2)+PyH(2')), 8.05-8.22 (d, 16H, (PyH(3)+PyH(3')), 5.50-5.74 (s, 16H, NH<sub>2</sub>), 2.62-2.74 (s, 16H, CH<sub>2</sub>) ppm. **ELEMENTAL ANALYSIS:** CHN calculated for C<sub>48</sub>H<sub>64</sub>N<sub>24</sub>O<sub>24</sub>Pd<sub>4</sub>·9H<sub>2</sub>O: C, 29.58; H, 4.24; N, 17.25. Found: C, 29.69; H, 4.05; N, 17.26.

**Synthesis of CP<sub>12</sub>Pd<sub>2</sub>.** Pd(en)(NO<sub>3</sub>)<sub>2</sub> (3.2 mg, 0.011 mmol) was dissolved in CD<sub>3</sub>OD/D<sub>2</sub>O, 1:1 (v/v) (5 mL) and this solution was added to solid CP1 (5.9 mg, 0.01 mmol) to achieve a final concentration calculated on the basis of the resulting 2:2 complex of 1 mM. The suspension was allowed to react at room temperature in an ultrasound bath until it became

clear (typically between 15 and 60 min). For the ESI-TOF mass spectrum, the sample was diluted with H<sub>2</sub>O prior to the measurement. The <sup>1</sup>H NMR spectrum indicated that this procedure led to the exclusive (>90%) formation of the respective metallamacrocycle. <sup>1</sup>H NMR (400 MHz, CD<sub>3</sub>OD/D<sub>2</sub>O 1:1 (v/v)) δ 8.78 (d, 8H, H(3')), 8.26 (s, 4H, H(2)), 7.83 (d, 8H, H(2')), 7.56 (s, 4H, H(6)), 7.22 (s, 4H, H(4)), 4.10-4.07 (m, 4H, H(α)), 3.86-3.73 (m, 8H, H(δ)), 2.90 (s, 8H, Pd(en)), 2.37-2.32 (m, 4H, H(β)), 2.16-2.06 (m, 12H, H(β)+H(γ)) ppm. <sup>13</sup>C NMR (101 MHz, CD<sub>3</sub>OD/D<sub>2</sub>O 1:1 (v/v)) δ 174.2 (ProCO), 172.0 (ABACO), 152.6 (PyC(3')), 151.5 (PyC(1')), 139.8 (ABAC(1/3)), 139.3 (ABAC(1/3)), 138.5 (ABAC(5)), 125.4 (PyC(2')), 121.5 (ABAC(6)), 119.8 (ABAC(2)), 117.4 (ABAC(4)), 64.3 (ProC(α)), 49.6 (CH<sub>2</sub>CH<sub>2</sub>(en)), 47.8 (ProC(δ)), 32.3 (ProC(β)), 24.0 (ProC(γ)) ppm. MS (ESI-TOF) *m/z* (%) = 376.1 [CP1Pd]<sup>2+</sup>, 587.2 [CP1+H]<sup>+</sup>, 669.2 [CP1<sub>2</sub>Pd]<sup>2+</sup>, 815.1 (100) [CP1<sub>2</sub>Pd<sub>2</sub>+2 NO<sub>3</sub>]<sup>2+</sup>.

**Synthesis of CP1<sub>6</sub>Pd<sub>3</sub>.** Pd(CH<sub>3</sub>CN)<sub>4</sub>(BF<sub>4</sub>)<sub>2</sub> (1.2 mg, 0.0027 mmol) was dissolved in DMSO-*d*<sub>6</sub> (200 μL) and this solution was added to a solution of CP1 (3.0 mg, 0.0051 mmol) in DMSO-*d*<sub>6</sub> (500 μL) to achieve a final concentration of CP1<sub>6</sub>Pd<sub>3</sub> of 1.2 mM. The solution was stirred for 4h at 60 °C. <sup>1</sup>H NMR (400 MHz, DMSO-*d*<sub>6</sub>) δ= 9.82, 9.72, 9.40, 9.29, 9.09, 8.09, 7.97, 7.71, 7.53, 7.35, 7.29, 7.18, 6.36, 4.06, 3.96, 3.83, 3.62, 3.52, 2.16, 2.03, 1.88, 1.74 ppm. MS (ESI-Orbitrap) *m/z* (%) = 587.23 [CP1+H]<sup>+</sup>, 864.57 [CP1<sub>4</sub>Pd<sub>2</sub>+Cl]<sup>3+</sup>, 996.77 [CP1<sub>6</sub>Pd<sub>3</sub>.(BF<sub>4</sub>).NO<sub>3</sub>]<sup>4+</sup>, 1003.03 [CP1<sub>6</sub>Pd<sub>3</sub>.(BF<sub>4</sub>)<sub>2</sub>]<sup>4+</sup>, 1358.04 [CP1<sub>6</sub>Pd<sub>3</sub>.(BF<sub>4</sub>)<sub>2</sub>.NO<sub>3</sub>]<sup>3+</sup>, 1366.38 [CP1<sub>6</sub>Pd<sub>3</sub>.(BF<sub>4</sub>)<sub>3</sub>]<sup>3+</sup>.

Only the chemical shifts of the largest peaks in the <sup>1</sup>H NMR spectrum are listed that belong to CP1<sub>6</sub>Pd<sub>3</sub> according to the DOSY NMR spectrum. Because of the complexity of the resulting <sup>1</sup>H NMR spectrum, the exact amount of CP1<sub>6</sub>Pd<sub>3</sub> in solution could not be quantified. A satisfactory <sup>13</sup>C NMR spectrum could not be obtained, even after extended measuring times, likely because of the complexity of the underlying equilibrium as also reflected in the <sup>1</sup>H NMR spectrum. The MS spectrum contains three additional signals of substantial intensity at *m/z* 693.28, 963.91, and 971.91. The one at 693.28 corresponds to a singly charged ion that does not contain palladium and presumably represents an unspecific adduct of the ligand. The other two signals denote triply charged ions containing palladium whose composition could, however, not be assigned to molecular formulae with matching isotope patterns.

**Synthesis of CP<sub>2</sub>Pd<sub>3</sub>.** Pd(en)(NO<sub>3</sub>)<sub>2</sub> (4.4 mg, 0.015 mmol) was dissolved in 2.5 mL of D<sub>2</sub>O, and this solution was added to a suspension of CP<sub>2</sub> (8.8 mg, 0.01 mmol) in 2.5 mL of CD<sub>3</sub>CN to achieve a final concentration calculated on the basis of the expected 2:3 complex of 1 mM (final volume of 5 mL in CD<sub>3</sub>CN/ D<sub>2</sub>O 1:1 (v/v)). The suspension was allowed to react under stirring at room temperature until it became clear (typically instantaneously to 30 min). For the ESI-TOF mass spectrum, the sample was diluted with H<sub>2</sub>O prior to the measurement. The <sup>1</sup>H NMR spectrum indicated that this procedure led to the exclusive (>90%) formation of the respective complex. <sup>1</sup>H NMR (400 MHz, CD<sub>3</sub>CN/D<sub>2</sub>O 1:1 (v/v)) δ 8.55 (d, 12H, H(3')), 8.31 (s, 6H, H(4)), 8.24 (s, 6H, H(2)), 7.73 (d, 12H, H(2')), 7.56 (s, 6H, H(6)), 4.50 (t, 6H, H(α)), 4.07-4.03 (m, 6H, H(δ)), 3.49 (t, 6H, H(δ)), 2.79 (s, 12H, Pd(en)), 2.44-2.40 (m, 6H, H(β)), 2.01-1.99 (m, 12H, H(β)+H(γ)), 1.87-1.83 (m, 6H, H(γ)) ppm. <sup>13</sup>C NMR (101 MHz, CD<sub>3</sub>CN/D<sub>2</sub>O 1:1 (v/v)) δ 172.4 (ProCO), 170.2 (ABACO), 151.4 (PyC(3')), 149.7 (PyC(1')), 138.5 (ABAC(1/3)), 136.9 (ABAC(1/3)), 135.8 (ABAC(5)), 123.6 (PyC(2')), 121.9 (ABAC(6)), 120.9 (ABAC(2)), 119.5 (ABAC(4)), 62.6 (ProC(α)), 50.8 (ProC(δ)), 46.4 (CH<sub>2</sub>CH<sub>2</sub>(en)), 29.5 (ProC(β)), 25.3 (ProC(γ)) ppm. MS (ESI-TOF) *m/z* (%) = 376.9 [CP<sub>2</sub>Pd<sub>3</sub>]<sup>6+</sup>, 464.3 [CP<sub>2</sub>Pd<sub>3</sub> + 1 NO<sub>3</sub>]<sup>5+</sup>, 522.6 [CP<sub>2</sub>Pd]<sup>2+</sup>.

### 5.1.3 Binding Studies with CP<sub>1</sub>Pd<sub>2</sub>

**Dicarboxylate Binding.** A 1 mM solution of CP<sub>1</sub>Pd<sub>2</sub> was prepared by adding a solution of Pd(en)(NO<sub>3</sub>)<sub>2</sub> (1.6 mg, 5.5 mmol) in CD<sub>3</sub>OD/D<sub>2</sub>O, 1:1 (v/v) (2.5 mL) to solid CP<sub>1</sub> (2.9 mg, 5.0 mmol) (host solution). The solvent for the guest solutions was prepared by dissolving Na<sub>2</sub>CO<sub>3</sub> (1.1 mg, 10.4 mmol) in CD<sub>3</sub>OD/D<sub>2</sub>O, 1:1 (v/v) (10.4 mL). The guest solutions were prepared by dissolving a dicarboxylic acid (1 mmol) in this solvent (1 mL) to obtain a 1 mM guest concentration. The following dicarboxylic acids were used: 2,6-naphthalenedicarboxylic acid (a), isophthalic acid (b), terephthalic acid (c), diphenic acid (d), adipic acid (e), glutaric acid (f). The solutions for the <sup>1</sup>H NMR spectroscopic measurements were prepared from these stock solutions. Solutions of the binding partners alone were prepared by mixing the respective stock solution (250 μL) with CD<sub>3</sub>OD/D<sub>2</sub>O, 1:1 (v/v) (250 μL). For the mixtures, the host solution (250 μL) was added to a guest solution (250 μL). The concentrations of the binding partners thus amounted to 0.5 mM in the final

solutions. The NMR tubes were placed in an ultrasound bath for 15 min at room temperature, followed by measurement of the  $^1\text{H}$  NMR spectra.

**Carbonate/bicarbonate buffer solution (pH 9.2).** 0.02 M solutions of  $\text{Na}_2\text{CO}_3$  (solution A) and  $\text{NaHCO}_3$  (solution B) were prepared in  $\text{D}_2\text{O}$ . 2 mL of solution A and 8 mL of solution B were mixed. The pH 9.2 was confirmed with a pH meter.

**Borate buffer solution (pH 9.2).** A 0.025 M solution of  $\text{Na}_2\text{B}_4\text{O}_7 \cdot 10\text{H}_2\text{O}$  (solution A) and a 0.1 M solution of  $\text{NaOH}$  (solution B) were prepared in  $\text{D}_2\text{O}$ . 5 mL of solution A and 0.36 mL of solution B were mixed and diluted to 10 mL with  $\text{D}_2\text{O}$ . The pH 9.2 was confirmed with a pH meter.

**Addition of terephthalate to buffered solution of  $\text{CP1}_2\text{Pd}_2$ .** A 2.5 mM solution of  $\text{CP1}_2\text{Pd}_2$  was prepared by adding a solution of  $\text{Pd}(\text{en})(\text{NO}_3)_2$  (0.8 mg, 2.7 mmol) in  $\text{CD}_3\text{OD}/\text{D}_2\text{O}$ , 1:1 (v/v) (0.5 mL) to **CP1** (1.5 mg, 2.5 mmol) (solution A). Solution B was prepared by dissolving terephthalic acid (0.42 mg, 0.0025 mmol) in 1 mL of carbonate/bicarbonate buffer solution (pH 9.2) to obtain a concentration of 2.5 mM. A series of NMR tubes were set up, each containing solution A (100  $\mu\text{L}$ ) and different volumes of solution B (0, 50, 100 and 200  $\mu\text{L}$ ). All samples were made up to 500  $\mu\text{L}$  by adding 200  $\mu\text{L}$  of  $\text{CD}_3\text{OD}$  and the required volume of carbonate/bicarbonate buffer solution to afford a 0.5 mM concentration of  $\text{CP1}_2\text{Pd}_2$  in each tube. The tubes were placed in an ultrasound bath for 15 min at room temperature, followed by measuring the  $^1\text{H}$  NMR spectra.

**NMR titration of 1,3-benzenedisulfonate (BDS).** A 2.5 mM solution of  $\text{CP1}_2\text{Pd}_2$  was prepared by adding a solution of  $\text{Pd}(\text{en})(\text{NO}_3)_2$  (2.8 mg, 9.8 mmol) in  $\text{CD}_3\text{OD}/\text{D}_2\text{O}$ , 1:1 (v/v) (1.8 mL) to **CP1** (5.3 mg, 9.0 mmol) (solution A). Solution B was prepared by dissolving sodium 1,3-benzenedisulfonate (80%) (4.4 mg, 12.5 mmol) in  $\text{CD}_3\text{OD}/\text{D}_2\text{O}$ , 1:1 (v/v) (5.0 mL) to obtain a concentration of 2.5 mM. A series of NMR tubes were set up, each containing solution B (100  $\mu\text{L}$ ) and different volumes of solution A (0–200  $\mu\text{L}$  in 20  $\mu\text{L}$  steps). All samples were made up to 500  $\mu\text{L}$  by adding the required volume of  $\text{CD}_3\text{OD}/\text{D}_2\text{O}$ , 1:1 (v/v) to afford a 0.5 mM concentration of 1,3-benzenedisulfonate in each tube. The tubes were placed in an ultrasound bath for 15 min at room temperature, followed by measuring the  $^1\text{H}$  NMR spectra. The chemical shifts of the guest protons were plotted against the host/guest ratio and the stability constant  $K_a$  of the complex was determined by non-linear regression, using

a fitting procedure for 1:1 complex equilibria implemented in HypNMR (Hyperquad Limited).

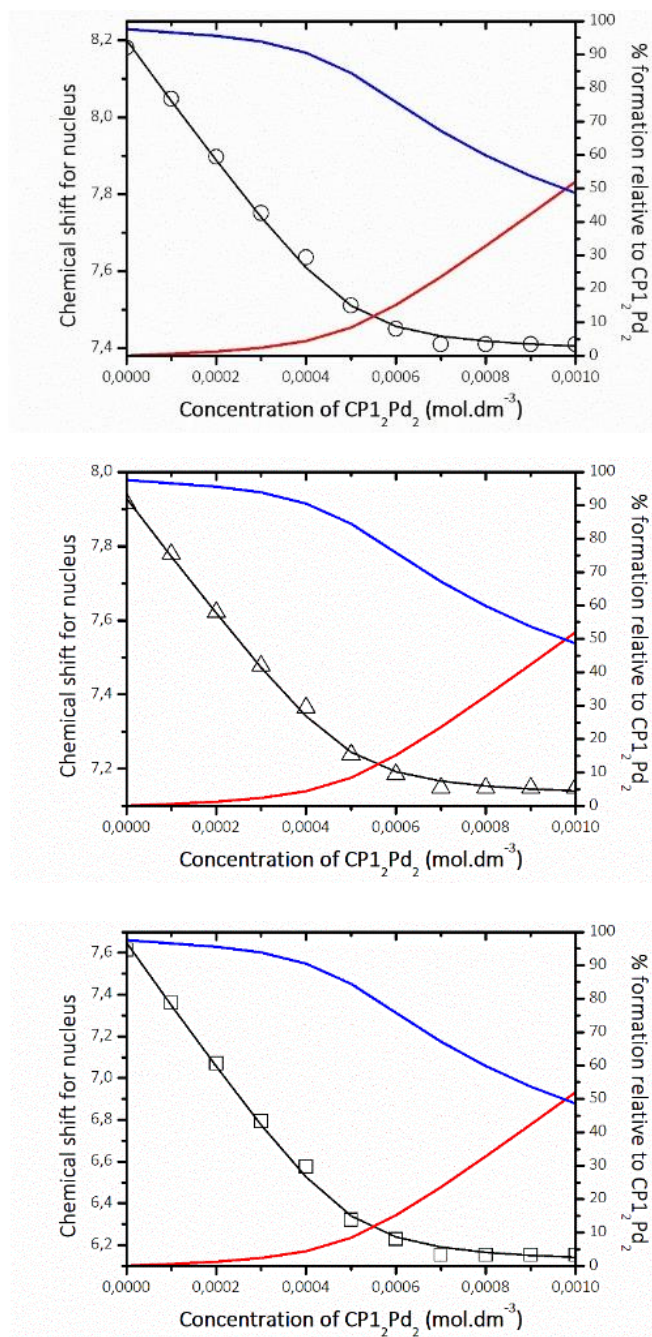
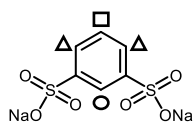


**Figure 123** Binding isotherms obtained in the NMR titration of BDS with  $CP_{12}Pd_2$  by following the shifts of the signals of BDS. The fitting of the isotherms was performed by using HypNMR2008.

**NMR titration with 2,6-naphthalenedisulfonate (NDS).** A 2 mM solution **CP1<sub>2</sub>Pd<sub>2</sub>** was prepared by adding a solution of Pd(en)(NO<sub>3</sub>)<sub>2</sub> (3.8 mg, 13.2 mmol) in CD<sub>3</sub>OD/D<sub>2</sub>O, 1:1 (v/v) (3.0 mL) to **CP1** (7.0 mg, 12.0 mmol) (solution A). Solution B was prepared by dissolving sodium 2,6-naphthalenedisulfonate (97%) (8.6 mg, 25.0 mmol) in CD<sub>3</sub>OD/D<sub>2</sub>O, 1:1 (v/v) (2.0 mL) to obtain a concentration of 12.5 mM. A series of NMR tubes were set up, each containing solution A (250 μL) and different volumes of solution B (0–200 μL in 20 μL steps). All samples were made up to 500 μL by adding the required volume of CD<sub>3</sub>OD/D<sub>2</sub>O, 1:1 (v/v) to afford a concentration of 1.0 mM of **CP1<sub>2</sub>Pd<sub>2</sub>** in each tube. The tubes were placed in an ultrasound bath for 15 min at room temperature, followed by measuring the <sup>1</sup>H NMR spectra.

**Crystallization of CP1<sub>2</sub>Pd<sub>2</sub>·2NDS.** A 2 mM solution **CP1<sub>2</sub>Pd<sub>2</sub>** was prepared by adding a solution of Pd(en)(NO<sub>3</sub>)<sub>2</sub> (1.3 mg, 4.4 mmol) in CD<sub>3</sub>OD/D<sub>2</sub>O, 1:1 (v/v) (1.0 mL) to **CP1** (2.3 mg, 4.0 mmol) (solution A). Solution B was prepared by dissolving sodium 2,6-naphthalenedisulfonate (97%) (8.6 mg, 25.0 mmol) in CD<sub>3</sub>OD/D<sub>2</sub>O, 1:1 (v/v) (2.0 mL) to obtain a concentration of 12.5 mM. A glass vial was set up containing solution A (1.0 mL) and solution B (320 μL). The sample was made up to 2 mL by adding the required volume of CD<sub>3</sub>OD/D<sub>2</sub>O, 1:1 (v/v) to afford a 1.0 mM concentration of **CP1<sub>2</sub>Pd<sub>2</sub>** and 2.0 mM concentration of NDS in the vial. The vial was placed in an ultrasound bath for 15 min at room temperature. Afterward, this vial was placed in a closed flask containing CD<sub>3</sub>CN and placed in the fridge. Crystals were obtained after 2 weeks by slow diffusion of CD<sub>3</sub>CN into the complex solution.

#### 5.1.4 Binding Studies with **CP2<sub>2</sub>Pd<sub>3</sub>**

**Qualitative binding studies with 1,3-benzenedisulfonate (BDS).** A 2.5 mM solution of **CP2<sub>2</sub>Pd<sub>3</sub>** was prepared by adding a solution of Pd(en)(NO<sub>3</sub>)<sub>2</sub> (2.2 mg, 0.0075 mmol) in 0.5 mL of D<sub>2</sub>O to a suspension of **CP2** (4.4 mg, 0.005 mmol) in 0.5 mL of CD<sub>3</sub>CN (final volume of 1.0 mL in CD<sub>3</sub>CN/ D<sub>2</sub>O 1:1 (v/v)). The suspension was allowed to react under stirring at room temperature until it became clear (typically instantaneously to 30 min, Solution A). Solution B was prepared by dissolving BDS (80%) (0.9 mg, 0.0025 mmol) in CD<sub>3</sub>CN/D<sub>2</sub>O, 1:1 (v/v) (1.0 mL) to obtain a concentration of 2.5 mM. A series of NMR tubes were set up, each

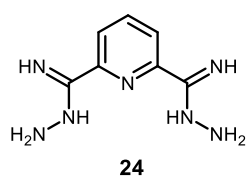
containing solution A (100  $\mu\text{L}$ ) and different volumes of solution B (0–400  $\mu\text{L}$  in 100  $\mu\text{L}$  steps). All samples were made up to 500  $\mu\text{L}$  by adding the required volume of  $\text{CD}_3\text{CN}/\text{D}_2\text{O}$ , 1:1 (v/v) to afford a 0.5 mM concentration of **CP2<sub>2</sub>Pd<sub>3</sub>** in each tube. Precipitation occurred in all samples almost instantaneously after the addition of solution B. The tubes were placed under sonication, but the precipitated never dissolved. Another series of NMR tubes was set up containing solution A (100  $\mu\text{L}$ ) and the required volume of  $\text{CD}_3\text{CN}/\text{D}_2\text{O}$ , 1:1 (v/v) to ultimately afford a 0.5 mM concentration of **CP2<sub>2</sub>Pd<sub>3</sub>** in each tube (final volume of 500  $\mu\text{L}$ ). The samples were stirred at room temperature and different volumes of solution B (0–100  $\mu\text{L}$  in 10  $\mu\text{L}$  steps) were added. Precipitation was observed already at 0.1 equivalents of BDS (10  $\mu\text{L}$ ). The procedure was repeated, but this time solution B was added to the samples under stirring at 50°C and again precipitation occurred. Due to the complex resulting  $^1\text{H}$  NMR spectra it was not possible to evaluate complex formation.

**Qualitative binding studies with 2,6-naphthalenedisulfonate (NDS).** A 2.5 mM solution of **CP2<sub>2</sub>Pd<sub>3</sub>** was prepared by adding a solution of  $\text{Pd}(\text{en})(\text{NO}_3)_2$  (2.2 mg, 0.0075 mmol) in 0.5 mL of  $\text{D}_2\text{O}$  to a suspension of **CP2** (4.4 mg, 0.005 mmol) in 0.5 mL of  $\text{CD}_3\text{CN}$  (final volume of 1.0 mL in  $\text{CD}_3\text{CN}/\text{D}_2\text{O}$  1:1 (v/v)). The suspension was allowed to react under stirring at room temperature until it became clear (typically instantaneously to 30 min, Solution A). Solution B was prepared by dissolving NDS (97%) (0.9 mg, 0.0025 mmol) in  $\text{CD}_3\text{CN}/\text{D}_2\text{O}$ , 1:1 (v/v) (1.0 mL) to obtain a concentration of 2.5 mM. A series of NMR tubes were set up, each containing solution A (100  $\mu\text{L}$ ) and different volumes of solution B (0–400  $\mu\text{L}$  in 100  $\mu\text{L}$  steps). All samples were made up to 500  $\mu\text{L}$  by adding the required volume of  $\text{CD}_3\text{CN}/\text{D}_2\text{O}$ , 1:1 (v/v) to afford a 0.5 mM concentration of **CP2<sub>2</sub>Pd<sub>3</sub>** in each tube. Precipitation occurred in all samples almost instantaneously after the addition of solution B. The tubes were sonicated, but the precipitate did not dissolve. Another series of NMR tubes was set up containing solution A (100  $\mu\text{L}$ ) and the required volume of  $\text{CD}_3\text{CN}/\text{D}_2\text{O}$ , 1:1 (v/v) to ultimately afford a 0.5 mM concentration of **CP2<sub>2</sub>Pd<sub>3</sub>** in each tube (final volume of 500  $\mu\text{L}$ ). The samples were stirred at room temperature and different volumes of solution B (0–100  $\mu\text{L}$  in 10  $\mu\text{L}$  steps) were added. Precipitation was observed already at 0.1 equivalents of BDS (10  $\mu\text{L}$ ). The procedure was repeated, but this time solution B was added to the samples under stirring at 50°C and again precipitation occurred. Due to the complex resulting  $^1\text{H}$  NMR spectra it was not possible to evaluate complex formation.

## 5.2. Synthesis and Characterization of Luminescent Neutral Pt(II) Complexes Tethered to Cyclopeptides.

### 5.2.1 Synthetic Procedures

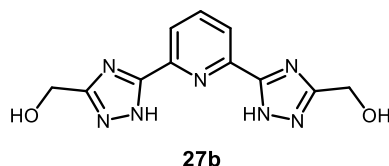
**General details.** All chemicals used in synthesis, purification, and product analyses were commercially available and used without further purification. 2,6-Bis(3-(trifluoromethyl)-1*H*-1,2,4-triazol-5-yl)pyridine (**27a**) was provided by the De Cola group. Product formation was checked by using thin layer chromatography: Kieselgel 60 F254/Kieselgel 60G Merck TLC plates. Analyses were carried out as follows: NMR: Bruker AVANCE III 400, Bruker AVANCE 600 digital NMR, peak assignments were confirmed by using H,H-COSY, H,H-NOESY, HMQC and HMBC spectra, spectra were referenced to the residual solvent signals (DMSO-*d*<sub>6</sub>:  $\delta^H = 2.50\text{ppm}$ ,  $\delta^C = 39.5\text{ppm}$ ); MALDI-TOF-MS: BrukerUltraflex TOF/TOF; ESI-MS: AmaZonETD, Bruker Daltonics; elemental analysis: Elementar vario Micro Tube. The following abbreviations are used: Py, pyridyl; tz, triazole; Deg, 2-(2-methoxyethoxy)ethoxy)methyl. The synthetic procedures were performed according to the ones described in the literature.<sup>142,215,216</sup>



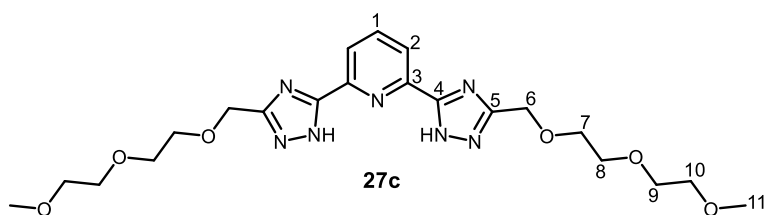
**Pyridine-2,6-bis(carboximidhydrazide) (24).**<sup>215</sup> Pyridine-2,6-dicarbonitrile (2 g, 15.6 mmol) was dissolved in EtOH (100 mL) and treated with hydrazine monohydrate (15.1 mL, 310 mmol), which led to immediate precipitate formation. The reaction mixture was stirred overnight at room temperature. Subsequently, the precipitate was filtered off and washed with cold EtOH to obtain a pale yellow solid. Yield: 1.51 g (7.8 mmol, 50%). <sup>1</sup>H NMR (400 MHz, DMSO-*d*<sub>6</sub>):  $\delta$  7.81 (d, 2H, <sup>2</sup>J=7.6 Hz, PyH), 7.65 (t, 1H, <sup>4</sup>J=7.3 Hz, PyH), 6.04 (s, 4H, NH),



5.23 (s, 4H, NH<sub>2</sub>) ppm. <sup>13</sup>C NMR (101 MHz, DMSO-*d*<sub>6</sub>) δ 150.3 (2C, C=NH), 143.6 (2C, PyCN), 136.0 (1C, PyCH), 117.9 (2C, PyCH) ppm. **MS (ESI-TOF)** *m/z* (%) = 194.31 (100%) [M+H]<sup>+</sup>.

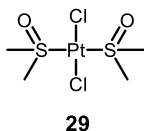


**(Pyridine-2,6-diylbis(1H-1,2,4-triazole-5,3-diyl))dimethanol (27b).** Pyridine-2,6-bis(carboximidhydrazide) (0.1 g, 0.52 mmol) was dissolved in glycolic acid (2 mL). This mixture was heated to 80 °C for 24 h and afterwards concentrated in vacuum. Ethylene glycol (2 mL) was added, and the mixture heated to 140 °C for 2 h. After cooling down to room temperature, water was added to precipitate side products. The solution was evaporated, and acetone was added. Again, a precipitate formed, which was filtered off. The filtrate was again evaporated. The residue was purified by RP8 column chromatography (eluent: H<sub>2</sub>O/MeOH 5:1, 3:1, 1:1 (v/v)). All fractions containing the product were combined and chloroform was added to precipitate the last impurities. The solid was filtrated off and the solution evaporated to obtain a white powder. Yield: 0.05 g (0.18 mmol, 35%). <sup>1</sup>H NMR (400 MHz, DMSO-*d*<sub>6</sub>): δ 14.21 (bs, 2H, NH), 8.17-8.08 (m, 3H, PyH), 5.36 (s, 2H, OH), 4.55 (s, 4H, CH<sub>2</sub>) ppm. <sup>13</sup>C NMR (101 MHz, DMSO-*d*<sub>6</sub>) δ 175.9 (2C, tzC-Py), 158.7 (2C, PyCN), 130.6 (1C, PyCH), 113.1 (2C, PyCH), 54.8 (2C, CH<sub>2</sub>) ppm. **MS (ESI-TOF)** *m/z* (%) = 274.21 [M+H]<sup>+</sup>. **ELEMENTAL ANALYSIS:** CHN calculated for C<sub>11</sub>H<sub>11</sub>N<sub>7</sub>O<sub>2</sub>·0.5CHCl<sub>3</sub>: C, 41.49; H, 3.48; N, 29.45. Found: C, 41.63; H, 3.94; N, 29.79.

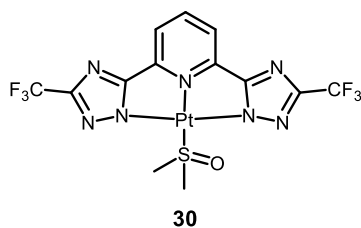


**2,6-Bis(3-((2-(2-methoxyethoxy)ethoxy)methyl)-1H-1,2,4-triazol-5-yl)pyridine (27c).**

Pyridine-2,6-bis(carboximidhydrazone) (0.3 g, 1.6 mmol) was dissolved in 2-(2-(2-methoxyethoxy)ethoxy)acetic acid (4 mL). This mixture was heated to 80 °C for 24 h and afterwards concentrated in vacuum. Ethylene glycol (2 mL) was added, and the mixture heated to 140 °C for 2h. After cooling down to room temperature, acetone was added to precipitate impurities. The precipitate was filtered off and the solution evaporated. The residue was purified by HPLC (eluent: gradient of H<sub>2</sub>O/MeOH mixture from 80:20 (% v/v) to 20:80 (% v/v) during 80 min). All fractions containing the product were combined and evaporated to obtain a yellow oil. Yield: 0.46 g (0.97 mmol, 63%). **<sup>1</sup>H NMR** (400 MHz, D<sub>2</sub>O): δ 7.60 (t, 1H, <sup>4</sup>J=7.8 Hz, PyH(1)), 7.42 (d, 2H, <sup>2</sup>J=7.8 Hz, PyH(2)), 4.52 (s, 4H, TegH(6)), 3.73-3.69 (m, 8H, TegH(7+8 or 9+10)), 3.67-3.64 (m, 4H, TegH(7 or 8 or 9 or 10)), 3.58-3.57 (m, 4H, TegH(7 or 8 or 9 or 10)), 3.33 (s, 6H, TegH(11)) ppm. **<sup>13</sup>C NMR** (101 MHz, D<sub>2</sub>O) δ 157.5 (2C, tzC5), 156.0 (2C, tzC4), 144.9 (2C, PyC3), 138.8 (1C, PyC1), 121.2 (2C, PyC2), 70.9, 69.8, 69.5, 69.4 (8C, TegC7, 8, 9, 10), 64.2 (2C, TegC6), 57.9 (2C, TegC11) ppm. **MS (MALDI-TOF):** *m/z* (%) = 478.21 [M+H]<sup>+</sup>, 500.32 [M+Na]<sup>+</sup>, 516.23 [M+K]<sup>+</sup>. **ELEMENTAL ANALYSIS:** CHN calculated for C<sub>21</sub>H<sub>31</sub>N<sub>7</sub>O<sub>6</sub>·2H<sub>2</sub>O: C, 49.11; H, 6.87; N, 19.09. Found: C, 49.05; H, 6.83; N, 19.96.

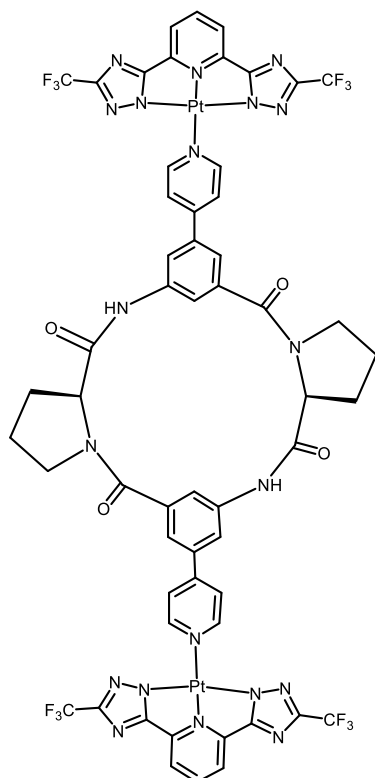


[Pt(DMSO)<sub>2</sub>Cl<sub>2</sub>] (**29**).<sup>216</sup> K<sub>2</sub>PtCl<sub>4</sub> (1.0 g, 2.4 mmol) was dissolved in water (8 mL) and DMSO (4 mL) and the resulting mixture was stirred at room temperature for 2h. The yellow precipitate was filtered off, washed with water, EtOH and diethyl ether and dried. Yield: 1.01 g (2.4 mmol, quantitative). **ELEMENTAL ANALYSIS:** CHN calculated for C<sub>4</sub>H<sub>12</sub>Cl<sub>2</sub>O<sub>2</sub>PtS<sub>2</sub>: C, 11.38; H, 2.86; S, 15.19. Found: C, 11.23; H, 2.98; S, 15.45.



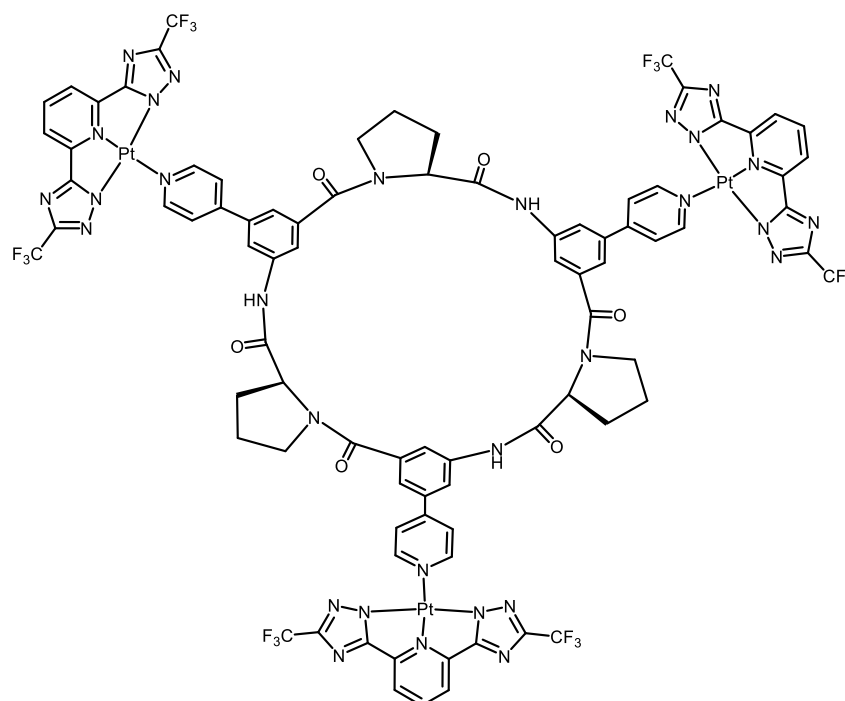
Pt(2,6-bis(3-(trifluoromethyl)-1,2,4-triazol-5-yl)pyridine)(DMSO) (**30**).<sup>142</sup> [PtDMSO<sub>2</sub>Cl<sub>2</sub>] (0.42 g, 0.99 mmol) and 2,6-bis(3-(trifluoromethyl)-1H-1,2,4-triazol-5-yl)pyridine (**27a**) (0.21 g, 0.99 mmol) were dissolved in DMF and the mixture was heated to 75 °C in a round bottom flask equipped with a reflux condenser overnight. The reaction mixture was allowed to cool to room temperature and the solvent removed in vacuum. DCM was added, the resulting suspension was sonicated and afterwards centrifuged. The supernatant was removed and the residue suspended in DCM. After centrifugation of the suspension, the solid was suspended in MeOH, sonicated and the solution was centrifuged again to obtain the pure product as a red solid. Yield: 0.39 g (0.63 mmol, 64 %). **<sup>1</sup>H NMR** (400 MHz, MeOD) δ 8.26 (s, 1H), 7.89 (d, *J*=7.9 Hz, 2H), 2.71 (s, 6H). **<sup>19</sup>F NMR** (377 MHz, MeOD) δ -65.66 (s). **MS (ESI-TOF)** *m/z* (%): 643.01 [M+Na]<sup>+</sup>.

## 5.2.2 Synthesis of the coordination compounds



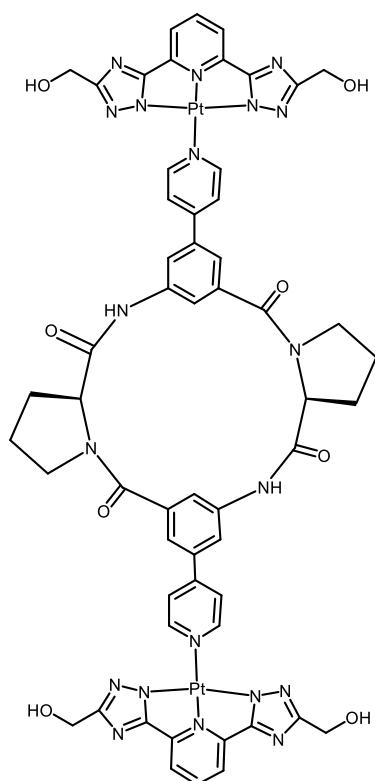
**PtCF<sub>3</sub>-CP1.** Method 1: Compound **30** (10.5 mg, 0.017 mmol) was dissolved in MeCN (5 mL) and this solution was added to solid **CP1** (3.0 mg, 0.005 mmol). The suspension was left stirring at room temperature until all the solvent had evaporated (typically overnight). 1 mL of acetonitrile was then added, the suspension was centrifuged, and the supernatant discarded. This process was repeated four times with acetonitrile (1 mL each), twice with methanol (1 mL each) and once with dichloromethane (1 mL). The resulting precipitate was analysed by NMR spectroscopy and ESI-MS spectrometry. **<sup>1</sup>H NMR** (400 MHz, DMF-*d*<sub>7</sub>): complex spectrum, no peak assignment possible. **MS (ESI-TOF)** *m/z* (%) = 350.2 [**27a**+H]<sup>+</sup>, 587.3 [**CP1**+H]<sup>+</sup>, 643.3 [**30**+Na]<sup>+</sup>. Method 2: Compound **30** (10.5 mg, 0.017 mmol) was dissolved in DMF (5 mL) and this solution was added to solid **CP1** (3.0 mg, 0.005 mmol). The solution was left stirring for 2 days at room temperature. Water was added to the reaction mixture until a precipitate was formed. The suspension was centrifuged and the supernatant discarded. Acetonitrile (1 mL) was then added to the precipitate, the suspension was again centrifuged and the supernatant discarded. This process was

repeated four times with acetonitrile (1 mL each), twice with methanol (1 mL each) and once with dichloromethane (1 mL). The resulting precipitate was analysed by NMR spectroscopy and ESI-MS spectrometry. **NMR analysis:** not possible since the precipitate was not soluble in deuterated solvents. **MS (HR-ESI)  $m/z$  (%) = 1129.2 [Pt(27a-2H)CP1+H]<sup>+</sup>.**

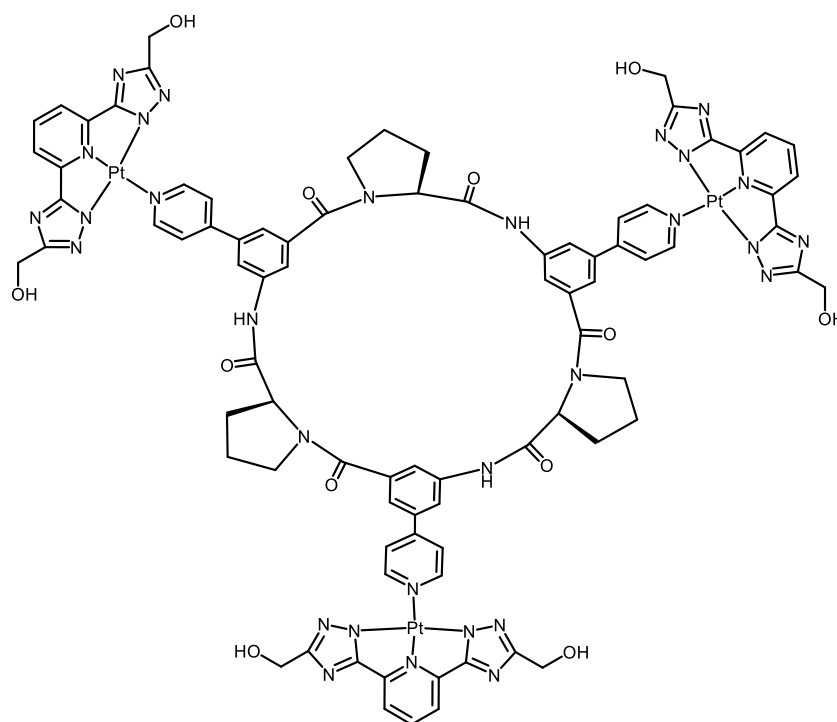


**PtCF<sub>3</sub>-CP2. Method 1:** Compound **30** (15.5 mg, 0.025 mmol) was dissolved in MeCN (8 mL) and this solution was added to solid **CP2** (4.4 mg, 0.005 mmol). The suspension was left stirring at room temperature until all the solvent had evaporated (typically overnight). 1 mL of acetonitrile was then added, the suspension was centrifuged and the supernatant discarded. This process was repeated four times with acetonitrile (1 mL each), twice with methanol (1 mL each) and once with dichloromethane (1 mL). The resulting precipitate was analysed by NMR spectroscopy and ESI-MS spectrometry. **<sup>1</sup>H NMR** (400 MHz, DMF-*d*<sub>7</sub>): complex spectrum, no peak assignment possible. **MS (ESI-TOF)  $m/z$  (%) = 350.1 [27a+H]<sup>+</sup>, 879.9 [CP2+H]<sup>+</sup>, 643.1 [30+Na]<sup>+</sup>.** **Method 2:** Compound **30** (15.5 mg, 0.025 mmol) was dissolved in DMF (8 mL) and this solution was added to solid **CP2** (4.4 mg, 0.005 mmol). The solution was left stirring for 2 days at room temperature. Water was added to the reaction mixture until a precipitate was formed. The suspension was centrifuged and the

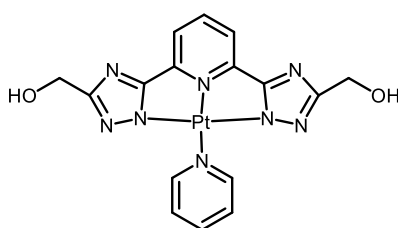
supernatant discarded. Acetonitrile (1 mL) was then added to the precipitate, the suspension was again centrifuged and the supernatant discarded. This process was repeated four times with acetonitrile (1 mL each), twice with methanol (1 mL each) and once with dichloromethane (1 mL). The resulting precipitate was analysed by NMR spectroscopy and ESI-MS spectrometry. **NMR analysis:** not possible since precipitate was not soluble in deuterated solvents. **MS (ESI-TOF)  $m/z$  (%) = 880.4 [CP2+H]<sup>+</sup>, 1422.4 [Pt(27a-2H)CP2+H]<sup>+</sup>, 1965.4 [Pt(27a-2H)<sub>2</sub>CP2+H]<sup>+</sup>, 2506.4 [PtCF<sub>3</sub>-CP2+H]<sup>+</sup>.**



**PtCH<sub>2</sub>OH-CP1.** [Pt(DMSO)<sub>2</sub>Cl<sub>2</sub>] (6.4 mg, 0.017 mmol) and **27b** (4.6 mg, 0.017 mmol) were dissolved in DMF (8 mL). Subsequently, DIPEA (6.4  $\mu$ L, 0.037 mmol) was added and the reaction mixture heated to 80 °C. Afterwards, **CP1** (3.0 mg, 0.005 mmol) was added and the reaction mixture held at 80 °C for 24 h. The formation of the product was not observed.

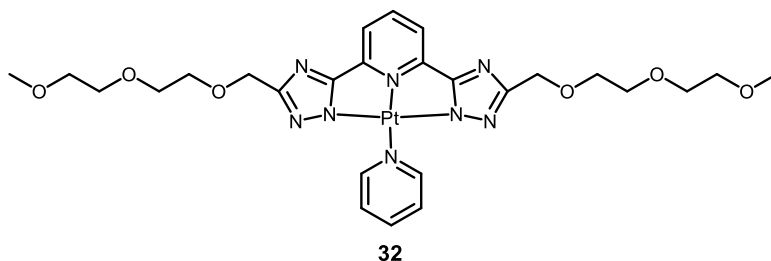


**PtCH<sub>2</sub>OH-CP2.** [Pt(DMSO)<sub>2</sub>Cl<sub>2</sub>] (9.7 mg, 0.025 mmol) and **27b** (6.8 mg, 0.025 mmol) were dissolved in DMF (10 mL). Subsequently, DIPEA (9.6 μL, 0.055 mmol) was added and the reaction mixture heated to 80 °C. Afterwards, **CP2** (4.4 mg, 0.005 mmol) was added and the reaction mixture was held at 80 °C for 24 h. The formation of the product was not observed.

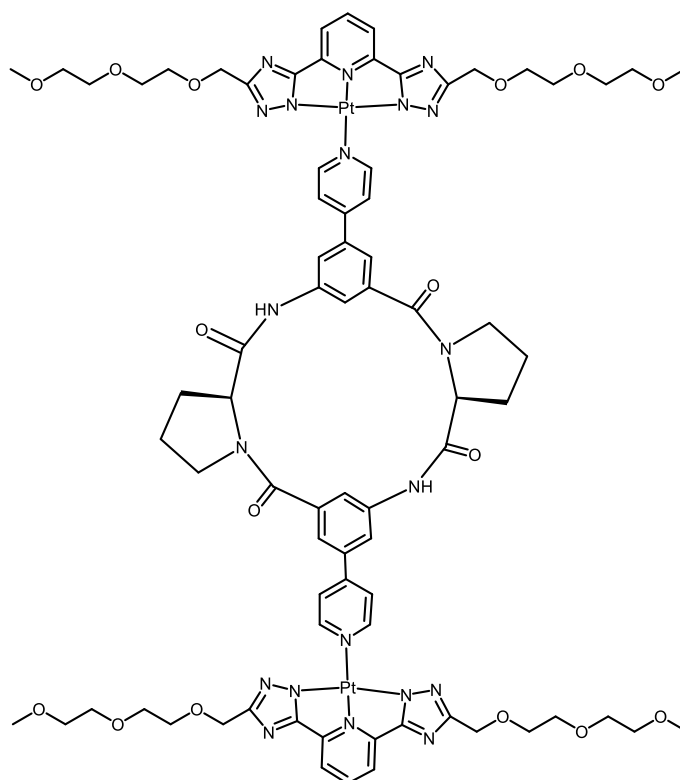


**31**

**Compound 31.** [Pt(DMSO)<sub>2</sub>Cl<sub>2</sub>] (8.2 mg, 0.021 mmol) and **27b** (5.69 mg, 0.021 mmol) were dissolved in DMF (5 mL). Subsequently, DIPEA (4.7 μL, 0.027 mmol) was added and the reaction mixture heated to 80 °C. Afterwards, pyridine (1.0 mg, 0.013 mmol) was added and the reaction mixture was held at 80 °C for 24 h. The formation of the product was not observed.



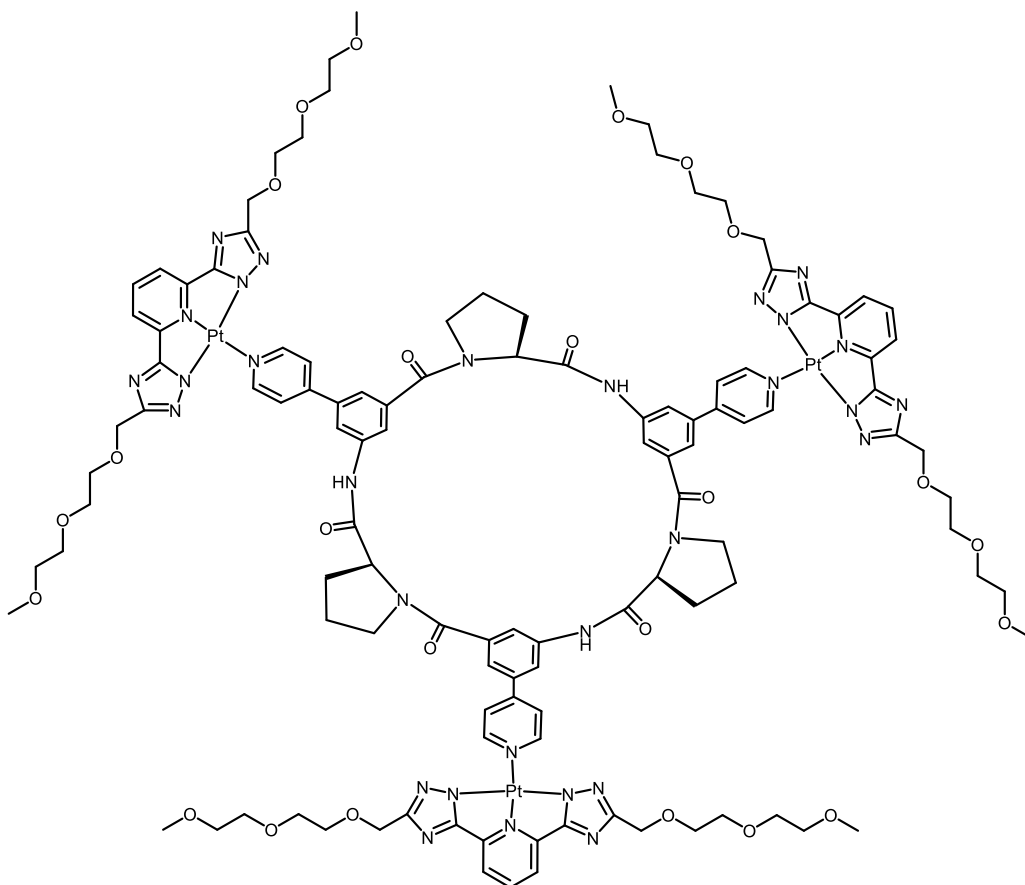
**Compound 32.** [Pt(DMSO)<sub>2</sub>Cl<sub>2</sub>] (8.2 mg, 0.021 mmol) and **27c** (10.05 mg, 0.021 mmol) were dissolved in DMF (10 mL). Subsequently, DIPEA (4.7 μL, 0.027 mmol) was added and the reaction mixture heated to 80 °C. Afterwards, pyridine (1.0 mg, 0.013 mmol) was added and the reaction mixture was held at 80 °C for 24 h. A sample was collected from the reaction mixture and analysed by ESI-TOF MS spectrometry. **MS (ESI-TOF) *m/z* (%) = 750.6 [32+H]<sup>+</sup>**. No further work-up was performed.



**PtDeg-CP1.** [Pt(DMSO)<sub>2</sub>Cl<sub>2</sub>] (6.4 mg, 0.017 mmol) and **27c** (7.9 mg, 0.017 mmol) were dissolved in DMF (8 mL). Subsequently, DIPEA (6.4 μL, 0.037 mmol) was added and the reaction mixture heated to 80 °C. Afterwards, **CP1** (3.0 mg, 0.005 mmol) was added and the reaction mixture was held at 80 °C for 24 h. The reaction mixture was allowed to cool



to room temperature. Various purification techniques were investigated but a pure product could not be isolated. An emissive product (0.8 mg) was isolated by HPLC and analysed by mass spectrometry. **MS (MALDI-TOF)  $m/z$  (%) = 1257.4 [Pt(27c-2H)CP1+H]<sup>+</sup>, 1927.6 [Pt<sub>2</sub>(27c-2H)<sub>2</sub>CP1+H]<sup>+</sup> = [PtDeg-CP1+H]<sup>+</sup>.**

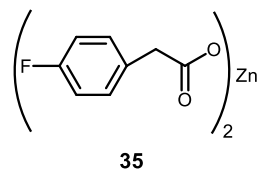


**PtDeg-CP2.** [Pt(DMSO)<sub>2</sub>Cl<sub>2</sub>] (9.7 mg, 0.025 mmol) and **27c** (11.9 mg, 0.025 mmol) were dissolved in DMF (10 mL). Subsequently, DIPEA (9.6 μL, 0.055 mmol) was added and the reaction mixture heated to 80 °C. Afterwards, **CP2** (4.4 mg, 0.005 mmol) was added and the reaction mixture was held at 80 °C for 24 h. The reaction mixture was allowed to cool to room temperature. Various purification techniques were investigated, but a pure product could not be isolated. An emissive product (1.1 mg) was isolated by HPLC and analysed by mass spectrometry. **MS (MALDI-TOF)  $m/z$  (%) = 902.4 [CP2+Na]<sup>+</sup>, 1572.5 [Pt(27c-2H)CP2+Na]<sup>+</sup>, 2242.6 [Pt<sub>2</sub>(27c-2H)<sub>2</sub>CP2+Na]<sup>+</sup>, 2912.8 [Pt<sub>3</sub>(27c-2H)<sub>3</sub>CP2+Na]<sup>+</sup> = [PtTeg-CP2+Na]<sup>+</sup>.**

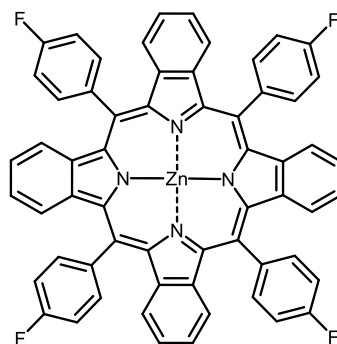
## 5.3. Luminescent Pt(II) Porphyrin Complexes as Oxygen Sensors for Microfluidic Devices

### 5.3.1 Synthetic Procedures

**General details.** All chemicals used in synthesis, purification, and product analyses were commercially available and used without further purification. Reaction control was conducted by using thin layer chromatography. MALDI-TOF-MS spectra were acquired by using a Bruker Ultraflex TOF/TOF spectrometer and UV-Vis spectra were recorded on a Varian CARY 100 spectrometer. The synthesis was performed according to the literature procedure.<sup>217</sup>

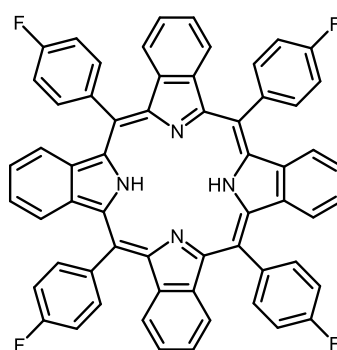


**Zinc(II)fluorophenylacetate (35).** Zinc acetate (3.0 g, 0.016 mol) and fluorophenylacetic acid (7.6 g, 0.049 mol) were dissolved in MeOH (500mL). The mixture was stirred overnight at room temperature. The precipitate was filtered off and washed several times with MeOH, affording a white powder. Yield: 3.2 g (0.0086 mol, 53%). **ELEMENTAL ANALYSIS:** CHN calculated for  $C_{16}H_{12}F_2O_4Zn$ : C, 51.71; H, 3.25. Found: C, 51.68; H, 3.20.



37

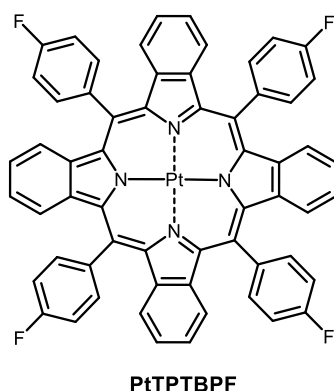
**Zinc(II)meso-tetra(4-fluorophenyl)tetrabenzoporphyrin (37).** Phthalimide (5.0 g, 0.034 mmol), fluorophenylacetic acid (6.8 g, 0.044 mol) and zinc(II) fluorophenylacetate **35** (3.2 g, 0.008 mol) were ground in a mortar and transferred into a 25mL round-bottom flask. The mixture was melted and stirred for 2h at 360 °C until the colour turned dark green. The melt was cooled, dissolved in acetone, and precipitated with water. The product was dissolved in toluene and purified on an Al<sub>2</sub>O<sub>3</sub> column. The column was eluted with toluene:hexane, 2:1 (v/v) to remove the yellow fraction and with toluene to remove the red fractions. Finally, 1.5 vol% THF in DCM was used to elute the product that was obtained as a dark-green powder after evaporation of the solvent. Yield: 0.6 g (0.6 mmol, 7.4%). **MS (MALDI-TOF):**  $m/z$  (%) = [M<sup>+</sup>] calc. 948.185, found 948.421. **UV-Vis** (CH<sub>2</sub>Cl<sub>2</sub>): 423, 453, 602, 650 nm.



38

**Meso-tetra(4-fluorophenyl)tetrabenzoporphyrin (38).** Zn(II) complex **37** (0.59 g, 0.6 mmol) was dissolved in THF (11 mL). Methanesulfonic acid (2mL) was added and the solution was stirred for 20 min. The product was precipitated by adding water. It was filtered off, washed and dried, yielding a dark-green powder. Yield: 0.44 g (0.5 mmol, 80%).

**MS (MALDI-TOF):**  $m/z$  (%) =  $[M^+]$  calc. 886.272, found 886.456. **UV-Vis** ( $\text{CH}_2\text{Cl}_2$ ): 462, 497, 589, 636, 695 nm.



**Platinum(II)meso-tetra(4-fluorophenyl)tetrabenzoporphyrin (PtTPTBPF).**  $\text{PtCl}_2$  (0.26 g, 0.001 mol) was dissolved in benzonitrile (2 mL). The hot solution was added into a 50 mL flask containing compound **38** (0.44 g, 0.5 mmol) in diphenyl ether (23 mL). The solution was stirred at 190 °C for 3h. The progress of the reaction was monitored by UV-Vis spectroscopy. Heating was continued until the absorption of the ligand had disappeared completely. The solution was cooled, diluted with hexane (40 mL) and subjected to a column packed with  $\text{Al}_2\text{O}_3$  in hexane. The column was washed with hexane and hexane:toluene, 1:1 (v/v) to remove the diphenyl ether and benzonitrile. The complex was eluted with dichloromethane and the solvent removed under reduced pressure to yield a dark-green powder. Yield: 0.10 g (0.09 mmol, 18%). **MS (MALDI-TOF):**  $m/z$  (%) =  $[M^+]$  calc. 1080.02, found 1080.516. **UV-Vis** ( $\text{CH}_2\text{Cl}_2$ ): 465, 496, 589, 645, 700 nm.

## 5.3.2 Oxygen detection studies

### 5.3.2.1 Oxygen Meter

Oxygen measurements were performed on a FireStingO2 meter (PyroScience, Germany, see **Figure 124**). This device was PC-controlled (USB) and contained four channels to which optical fibres were connected to allow contactless sensing. The phase-shift between the excitation and emission wavelengths was measured in the oxygen meter and converted internally by using the Stern-Vollmer equation. The excitation wavelength was 620 nm (orange-red), whereas emission was measured at 760 nm (NIR). A precision temperature sensor connected to the temperature port and integrated sensors for atmospheric pressure (mbar) and relative humidity (%RH) allowed automatic real-time compensation of the oxygen measurements.

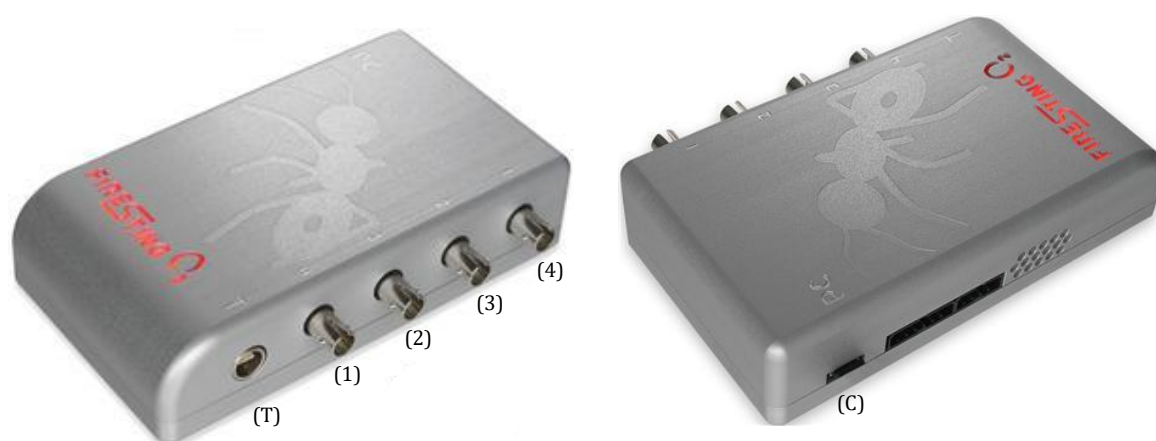


**Figure 124** FireStingO2 meter. Channels (1) to (4) connect to fibre optics, port (T) connects to the temperature sensor and port (C) connects via USB to a computer.

The measurements were acquired by using the Pyro Oxygen Logger software from Pyroscience. After starting the program, the window in **Figure 125** appeared. The four panels Channel 1-4 corresponded to the channels 1-4 of the FireStingO2. In the panel Overview, the measurements from the 4 channels and the temperature sensor were seen simultaneously. Before starting the measurements, the experimental conditions were chosen in the option “Settings” by activating the channel, setting the units to hPa (mbar), which was the fundamental oxygen unit measured by the FirestingO2, changing the sensor

code to **PD7-540-250**, and selecting water (DO), external temperature sensor and internal pressure sensor. These settings were copied to all channels.

The sensor readings of each channel were displayed in its corresponding panel in a numeric display (A) and a chart recorder (B). The Signal Intensity (C) of the oxygen sensor was shown as a horizontal indicator bar just underneath the numeric display (A). A reasonable oxygen sensor showed signal intensities between 50 and 500. If the signal intensity dropped below 50, this indicator bar turned gradually from grey to red, indicating that the sensor was about to get degraded soon. The actual Compensation Temperature was shown in the temperature display (D) in degree Celsius (°C). Quantitative measurements could only be obtained when the sensor was calibrated. The calibration procedure is explained in page 180. The button Save Setup was used to save the current settings and calibration data of all channels. They could be reloaded anytime by pressing the button Load Setup. This allowed switching between different laboratory setups with a single FireStingO2 and using several oxygen sensors repeatedly.

To start measuring, the button "start" (E) and the option *continuous* of Measurement were selected and data saving was activated by clicking on the red "start" button (F) of Log to File. The saved data files were simple text-files with the file extension ".txt" that could be easily imported into common spreadsheet programs.

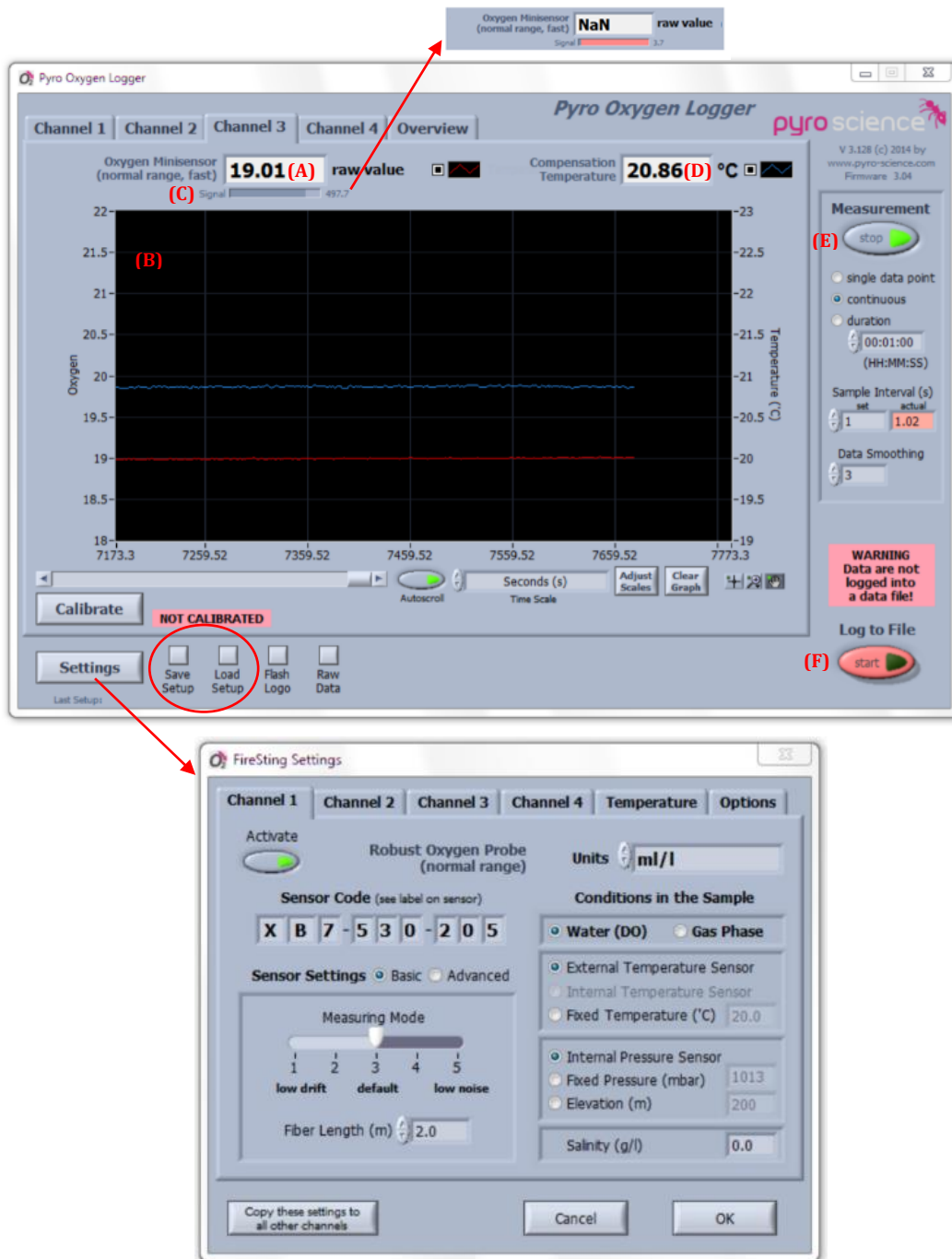


**Figure 125** Pyro Oxygen Logger Software. On the top, the main window with numeric (A) and chart (B) oxygen measurements is shown. The settings window, where the experiment conditions are chosen, is shown below.

### 5.3.2.2 Microfluidic device

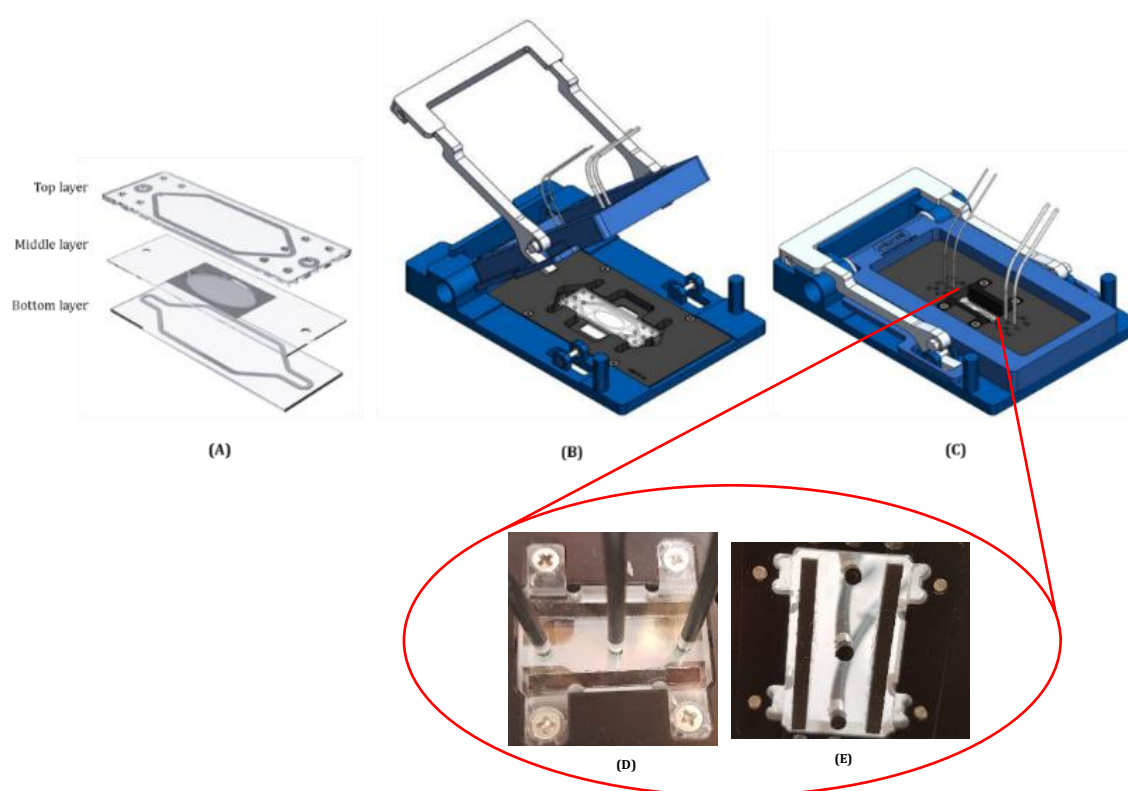


**Figure 126** Setup of the microfluidic chip and the Fluidic Connect Pro (FCP) chip holder. The three-layer chip (A) is stacked and placed in the FCP (B), which is closed in order to compress the chip layers together, creating a tight environment (C). The optical fibres are placed into the insert ((D) and (E)) for sensing.

The microfluidic device was manufactured by Micronit Microtechnologies (Enschede, The Netherlands). It consisted of a microfluidic chip and a Fluidic Connect Pro (FCP) chip holder. Each chip contained three 15x45 mm layers, a 0.7 mm thick glass bottom layer where the sensor spots were applied, a 0.4mm thick middle layer (made either from glass or polystyrene), containing a porous polyethylene terephthalate (PET) membrane (hydrophilic, 0.45  $\mu\text{m}$  pore size, 12  $\mu\text{m}$  thickness,  $1.6 \times 10^6$  pore density, and  $1 \text{ cm}^2$  surface area) or a polyvinylidene fluoride (PVDF) membrane (hydrophobic, Millipore Durapore PVDF type GVHP, 125  $\mu\text{m}$  thickness, 0.22  $\mu\text{m}$  pore size), and a 1.1 mm thick glass top layer (Figure 126 A). The three layers were assembled together within the FCP (Figure 126 B), which had previously been connected to the two tubings of the inlet (inner diameter of 254  $\mu\text{m}$ ) and the two other tubings of the outlet (inner diameter of 500  $\mu\text{m}$ ). The tubings



were held in the FCP by rubber ferrules, ensuring proper sealing between the chip and the tubes (**Figure 127**).

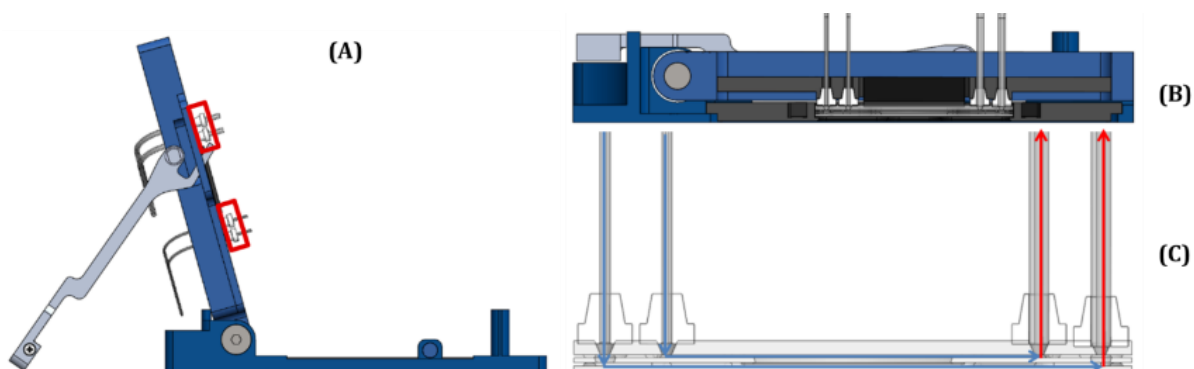


**Figure 127** Section of the FCP and schematic overview of the flow generated within the assembled chip. Tubings are held by ferrules (in the red rectangles) (A) that ensure a tight seal between the FCP and the chip when the clamp is closed (B). The direction of the flow is from the inlet tubings into the chip (blue arrows) and then to the outlets (red arrows) (C).

Different gasket designs (350  $\mu\text{m}$  thick) on the top and bottom layers (**Figure 126 A**) allowed for the creation of bottom and top chambers. The flow in the two chambers depends on the configuration of the layers: the top layer contained two inlets and two outlets to let liquid flow through the top and bottom chambers, while the middle layer contained only one inlet and one outlet to let the liquid go to the lower chamber of the chip. The volume of the bottom chamber was 100 $\mu\text{L}$  and that of the top chamber was 150 $\mu\text{L}$ .

The inlet tubings were connected to liquid-filled syringes via Luer-lock connectors, which were attached to syringe pumps. The pumps applied pressure on the plunger, thus generating a liquid flow from the syringe to the tubing and subsequently to the chip. The applied pressure was controlled to set the desired flow rate (**Figure 128**).

A modified insert for the FCP (**Figure 126 D and E**) was designed to keep the optical fibres aligned and at a constant distance from the top glass of the chip. The design was drawn using SolidWorks and SolidCAM (Dassault Systèmes, France). Inserts were fabricated by micro-milling a polycarbonate substrate.

In the final design, three sensor spots could be monitored from the top layer by optical fibres located at a distance of approximately 2.2 mm from the sensors (1.1 mm glass thickness from the top layer, 0.4 mm thickness from the middle layer and 2x 350  $\mu\text{m}$  from the gaskets in the top and bottom layers). Two 1.1 mm thick rubber bands were added in the bottom of the insert to compress the chip when the FCP was closed.

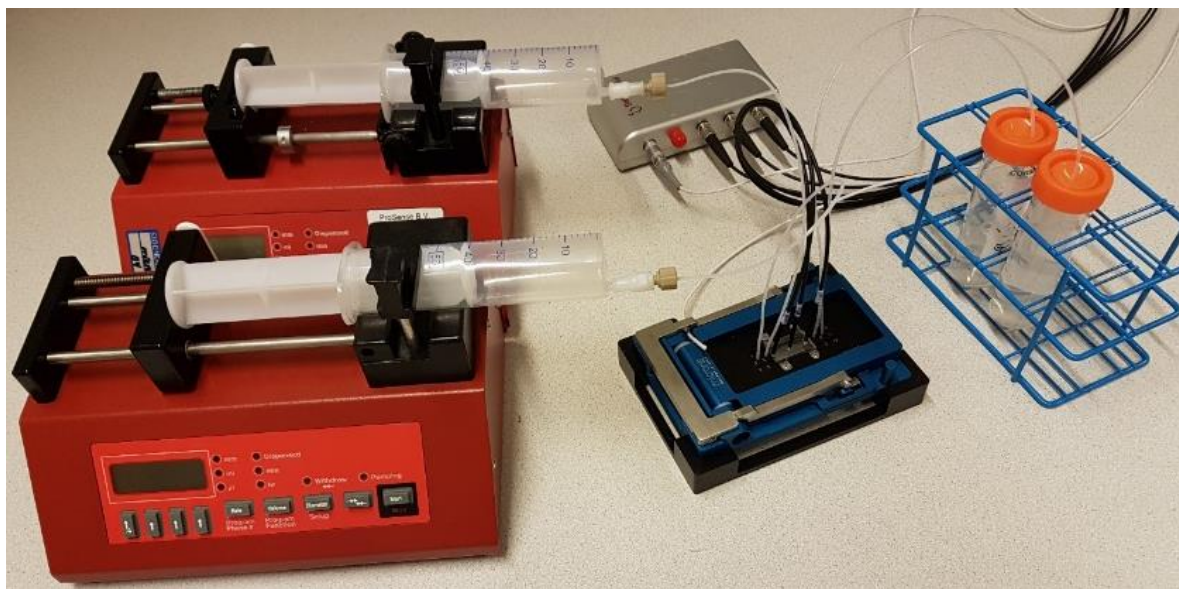


**Figure 128** Experimental setup for the microfluidic device. Pumps ensure a proper liquid flow rate from the syringes through the chip to the falcon tubes. Connected to the FireStingO2 device there are fibre optics (black cables) for contactless sensing and a temperature sensor (white cable).

### 5.3.2.3 Preparation of Oxygen Sensors

The geometry of the sensors was controlled by placing Kapton tape stencil on gasket free bottom layers. The Kapton was initially cut according to the dimensions of the bottom layer (15x45 mm). Three spherical holes, each with a diameter of 2 mm were added that served to create the sensor spots (**Figure 129**).

The layers containing the Kapton tape were then submitted to an oxygen plasma activation treatment (5min) at 50% power with an Atto plasma laboratory unit (Diener electronic GmbH + Co. KG, Ebhausen, Germany), after which aliquots of the sensor solution were added to the holes in sufficient amount to ultimately create a signal intensity higher than 50. In some cases, blade-coating of the sensor spots with a curing agent was required to immobilize them on the glass surface. PDMS (Sylgard 184, Dow Corning, USA, with a 10:1 (w/w) base/curing agent ratio) was chosen for its high oxygen permeability and easy handling. Prior to use, the PDMS was degassed for 30 min by using a desiccator and a vacuum pump. After application, curing was performed by placing the sensor layers in the oven at 70 °C overnight. The Kapton was removed and the perfluorinated gasket was dispensed on the glass and cured on a hot plate for 10 min at 150 °C. At least five chips per oxygen sensor solution were made.

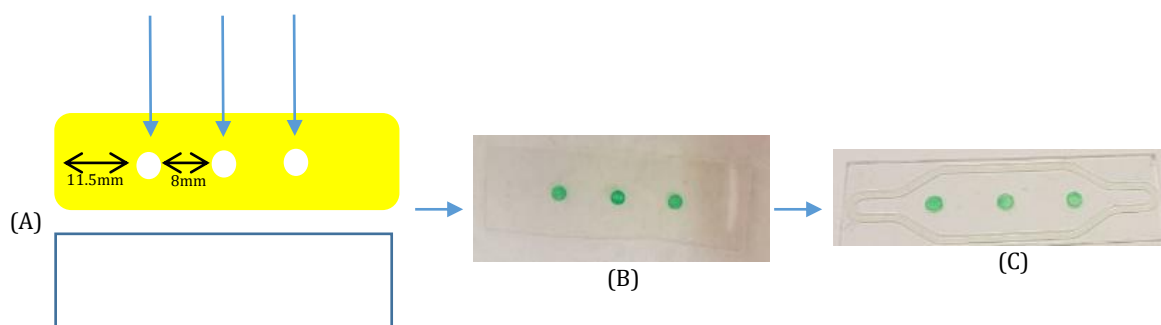


**Figure 129** Preparation of the oxygen sensors. The sensor solution was applied to the glass bottom layer containing an attached Kapton tape stencil (schematic (A)). After sensor preparation, the Kapton was removed (B) and the gasket was added (C).

#### 5.3.2.4 Preparation of Oxygen Standards

De-oxygenated water was obtained by bubbling nitrogen through a centrifuge tube filled with MilliQ water for at least 30 min. Air saturated water was obtained by using an aquarium pump to bubble air through a half-filled centrifuge tube with MilliQ water. Pure gaseous nitrogen was also used directly from the bottle.

### 5.3.2.5 Signal Intensity and N<sub>2</sub> Sensitivity

Prior to the application of the gasket on the bottom layers, the sensing ability of the spots was tested to ensure that the chips were indeed functional. To this end, the optical fibre was applied to the spot through the bottom of the layer to confirm the signal intensity was between 50 and 500. Afterwards, gaseous nitrogen was pumped through a tube directly on the spot. If the measured pO<sub>2</sub> value decreased substantially after initiating the nitrogen flow, the sensor was considered to be functional.

### 5.3.2.6 Oxygen Sensors Calibration

The sensors were calibrated by using microfluidic chips with non-porous glass or polystyrene middle layers, depending on the setup of the following experiments.

The two-point calibration involved flowing air-saturated water at a rate of 200 µL/min through the lower channel (between the bottom and the middle layers) for the 21% O<sub>2</sub> point and pumping gaseous nitrogen through a PEEK tube in the same channel for the 0% O<sub>2</sub> point.

The sensor calibration was accomplished by selecting the Calibrate button in the main window of the Pyro Oxygen Logger software (**Figure 130 A**). In the new window (**Figure 130 B**) 2-Point in Water or Humid Air was selected. In the panel Adjust Calibration Conditions, External Temperature Sensor was selected (100% Humidity and 0% Calibration). At this point, the oxygen sensor readings from the air-saturated water appeared on the graph in the panel. Once the values remained constant and reached the expected range of the connected sensor type, the button Set Air turned white. Clicking on it saved the actual oxygen reading for the calibration. After clicking the finish button, this process was repeated for all other channels. Afterwards, the air-saturated water was changed to gaseous nitrogen and the calibrations was repeated as described before for all channels. This time, however, the set 0% button was selected. After these measurements, the calibration conditions were saved in the main window (Save Setup) so that they can always be uploaded when the sensor was used.

In the calibration window under the buttons Set Air and Set 0%, the phase shifts (dphi) were shown. These values helped to assess if the calibration was valid or not since, as a rule of thumb, anoxic conditions gave a value of around 53, whereby ambient gave a value of ca. 20.

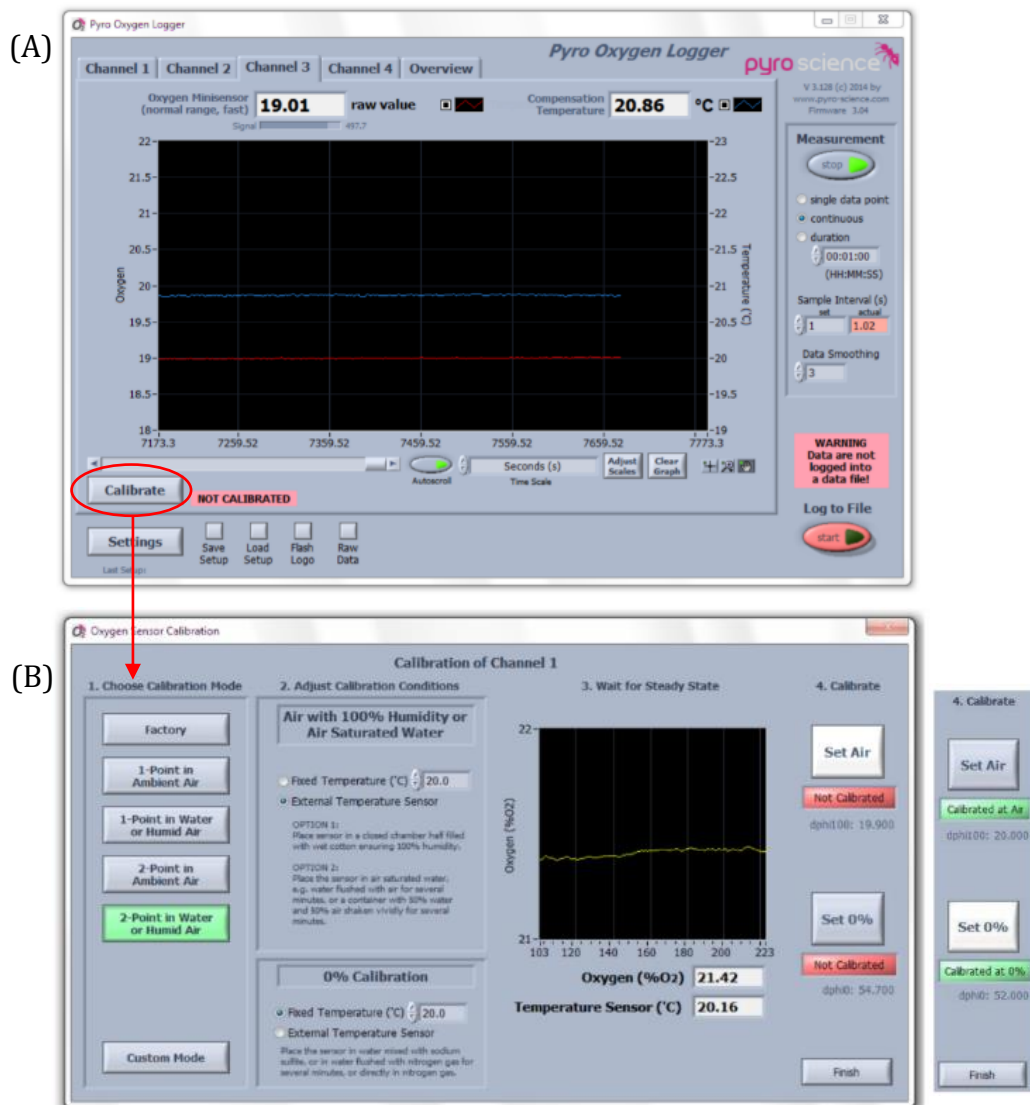


**Figure 130** Window display from Pyro Oxygen Logger for the Oxygen sensors calibration. In the main window (A) clicking on Calibrate opened the Calibration window (B) where different conditions could be chosen. When readings reached a steady state, the corresponding buttons turned white so that the calibration value could be set.

### 5.3.2.7 Validation of the Calibration

The calibration of the sensors (**Figure 131**) was validated by flowing a mix of air-saturated water and de-oxygenated water through the lower channel (between the bottom and middle layers) of a chip device with a non-porous glass or polystyrene middle layer. The liquids were mixed by connecting the chip to a T-connector attached to two different syringe pumps. All connections comprised PEEK tubings (length: approximately 8 cm, ID: 0.02"). Five oxygen contents were realized by the flow rates of the two solutions according to Table 2. The total flow rate was kept at 200  $\mu\text{L}/\text{min}$ .

**Table 2** Composition of the different Oxygen Standards for Calibration Validation

<i>Standard</i> (% of air saturation)	Flow rate air-saturated water ( $\mu\text{L}/\text{min}$ )	Flow rate de-oxygenated water ( $\mu\text{L}/\text{min}$ )
0	0	200
25	50	150
50	100	100
75	150	50
100	200	0

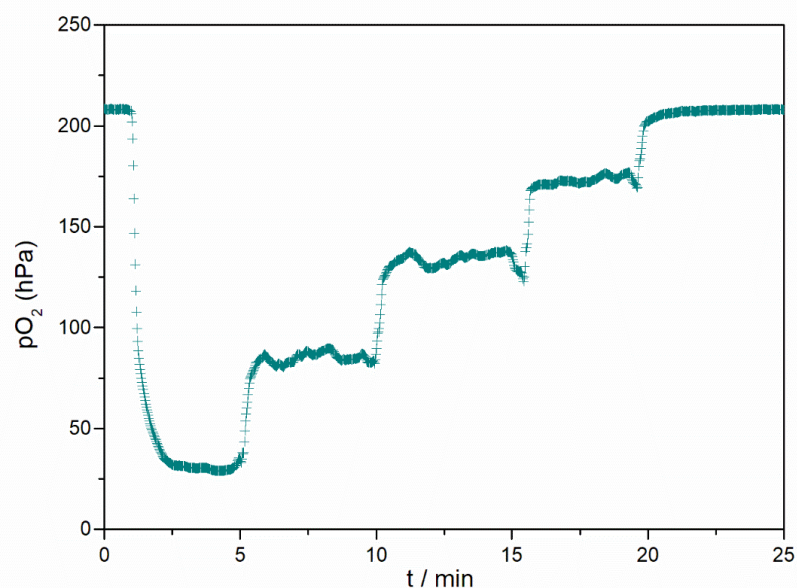


**Figure 131** Evolution of the  $p\text{O}_2$  of a microfluidic chip when using different oxygen standards. The  $p\text{O}_2$  values were averages of the values obtained for the three channels. 0% air saturation (from 0-5min): flow of de-oxygenated water; air saturations of 25% (5-10min), 50% (10-15min), 75% (15-20min): mixture of flows of de-oxygenated water and air saturated water; 100% (20-25min) air saturation: flow of air saturated water.

### 5.3.2.8 $N_2/O_2$ exchange through the Hydrophobic Membrane

**De-oxygenation of water.** De-oxygenation of  $O_2$  saturated water was studied using chips with a glass middle layer containing a PVDF membrane. The hydrophobicity of PVDF allowed flowing air-saturated water at a rate of 200  $\mu\text{L}/\text{min}$  in the lower channel (between the bottom and middle layer), whereas gaseous nitrogen was pumped through the upper channel (between the middle layer and top layer). The flow of nitrogen was only started when the  $pO_2$  values were constant and similar between the three different channels (inlet, membrane and outlet). Only PEEK tubings were used to reduce the oxygen transfer from ambient air through the walls of the tubes. Oxygen detection was carried out with the FireStingO2 device and data recording was performed by using the Pyro Oxygen Logger program.

**Oxygenation of Water.** Oxygenation of de-oxygenated water was studied by chips with a glass middle layer containing a PVDF membrane. The hydrophobicity of PVDF allowed flowing water at a rate of 200  $\mu\text{L}/\text{min}$  in the lower channel (between the bottom and middle layer), whereas atmospheric air was pumped through the upper channel (between the middle layer and top layer). Two different syringe pumps were connected to the lower channel through a T-connector. One of the syringes contained air-saturated water and the other de-oxygenated water. The chip was left under a flow of air-saturated water until the  $pO_2$  values were constant and similar between the three channels (inlet, membrane and outlet). At this point, a flow of de-oxygenated water was started and the one for the air-saturated water stopped. Oxygen detection was carried out with the FireStingO2 device and data recording was performed by using the Pyro Oxygen Logger program. Only PEEK tubings were used to reduce the oxygen transfer from the ambient air through the walls of the tubes. The effect of the flow rate on the oxygenation of the water was also studied, by performing the same experiment at flow rates of 50  $\mu\text{L}/\text{min}$ , 100  $\mu\text{L}/\text{min}$  and 150  $\mu\text{L}/\text{min}$ .

### 5.3.3 Oxygen Consumption Studies

#### 5.3.3.1 Cell Experiments

Biological experiments were performed at the University of Twente (BIOS Laboratories). Human Umbilical Vein Endothelial Cells (HUVECs) (ATCC, Virginia, USA) were incubated at 37°C and 5% CO<sub>2</sub> in Endothelial Cell Growth Medium (ECGM) (Cell Applications Inc., San Diego, USA) and passaged twice a week at 80% confluency. All material used in these experiments (chips, FCP, pumps, tubings, ferrules) was previously sterilized with 70 vol% ethanol. Before use, EtOH was flushed out from the tubings with PBS. Ferrules and connectors were also washed once with PBS.

**Thawing HUVECs.** Huvecs were stored in a liquid nitrogen tank at the BIOS lab. A frozen vial (10<sup>6</sup> cells) was taken from the tank and the lid was opened to remove the liquid nitrogen residues. ECGM (1 mL, from 9 mL previously prepared in a 10 mL tube) was added to the vial and resuspended until the ice was completely melted. The procedure was repeated a few times by using 1 mL of medium, placing it into the vial, resuspending it, taking 1 mL from the vial, putting it into the 10 mL tube, taking again 1 mL and placing it into the vial etc. Finally, everything was added to the 10 mL tube affording 10 mL of the cell suspension. This suspension was centrifuged, the supernatant discarded, and the pellet was resuspended in medium (1 mL). This suspension was added to a collagen-coated T75 flask (Sigma-Aldrich, St. Louis, USA) previously filled with ECGM (11 mL) and incubated at 37 °C and 5% CO<sub>2</sub> for at least 2 h. Afterwards, the medium was refreshed to remove the DMSO used in the freezing medium. The cells were then passaged on the next day.

**Passaging Cells.** ECGM and a solution of trypsin in ethylenediaminetetraacetic acid (0.5%, Trypsin-EDTA, Gibco®, ThermoFischer Scientific, Grand Island, New York (USA)) were pre-heated in a water bath. The medium present on the T75 flask incubated with the cells was discarded and the flask washed with a phosphate-buffered saline solution (PBS (10x), pH 7.4, Gibco®, ThermoFischer Scientific, Grand Island, New York (USA)) (10 mL). The trypsin solution (2 mL) was added to the flask and incubated for 5 min. After the flask was checked under the microscope to confirm if the cells had detached, RPMI-1640 inactivating medium (Roswell Park Memorial Institute (RPMI) 1640 Medium, ThermoFischer Scientific, Grand



Island, New York (USA)) (8 mL) was added. This suspension was transferred to a 10 mL tube. A sample (100  $\mu$ L) was taken to a vial and mixed with a trypan blue solution (0.4%, Trypan Blue Solution, Gibco®, ThermoFischer Scientific, Grand Island, New York (USA)) (100  $\mu$ L). This mixture was used for the cell counter. The suspension in the 10 mL tube was centrifuged, the supernatant discarded, and the pellet resuspended in warm medium. The amount of medium was resuspended depending on the targeted number of flasks. For three flasks, for example, 3 mL were resuspended of which 1 mL was placed in each flask (the flasks already contained ECGM (11 mL) by the time of the addition).

**Cell Seeding of the Middle Layers.** The middle layers in the chips used for the cell experiments were made of polystyrene and contained a porous PET membrane. The PET membrane was cell-seeded with HUVECs on the bottom side, causing the cells in the experiments to face the lower channel (between the bottom layer and middle layer) of the chip. Before cell seeding, the bottom part of the membranes was coated with fibronectin (Sigma-Aldrich, St. Louis, USA) to produce a thin coating for cell attachment. The fibronectin solution (150  $\mu$ L, 40  $\mu$ g/mL in PBS) was pipetted onto the membranes, which were left inside the flow hood for 2 h. The remaining fibronectin solution was then discarded, and the membranes washed once with PBS (150  $\mu$ L). The coated middle layers were either immediately used or stored at 4 °C for later use in a parafilm-sealed Petri dish. Middle layers containing a cell seeding density of 200'000 and 100'000 cells/cm<sup>2</sup> were produced. To this end, the cells were treated as described in 5.2.7.2 but after cell counting, the pellet was resuspended in an amount of medium that would allow taking an aliquot of 150  $\mu$ L containing the desired cell concentration. This aliquot was then added to the previously fibronectin-coated membranes. The middle layers were then incubated overnight at 37 °C and 5% CO<sub>2</sub>.

**Setup of the Microfluidic Device.** Two sterile 50 mL Luer syringes (Sigma-Aldrich, St. Louis, USA) were used, one filled with PBS and the other with pre-heated cell medium (37 °C). All efforts were made to ensure that no air bubbles were present in the syringes. Two Tefzel tubings with an inner diameter of 254  $\mu$ m were used to connect each syringe via a Luer-lock connector to the inlets chip holder. Two Tefzel tubings with an inner diameter of 500  $\mu$ m were used to connect the outlets' hole of the FCP to waste bins. To make sure that the inlet tubings were completely filled with liquid before closing the FCP

and starting the experiment, the syringe plunger was pressed until a continuous liquid flow could be observed at the end side of each inlet tubing. The outlet tubings were previously filled with PBS. When all tubings, connectors, and ferrules were in place, the chip device was assembled by placing all three layers in a PBS-filled Petri dish and stacking them on top of each other with the help of sterile surgical tweezers. All bubbles on the chip layers were previously removed with the aid of a pipette. The assembled chip was then placed in the dedicated space of the FCP chip holder by using surgical tweezers. The FCP was quickly closed and the whole set-up was transported to the incubator (37 °C), where the pumps, fibre optics and temperature sensor (connected to the FireStingO2 device) had already been placed. The fully assembled system is shown in **Figure 132**.

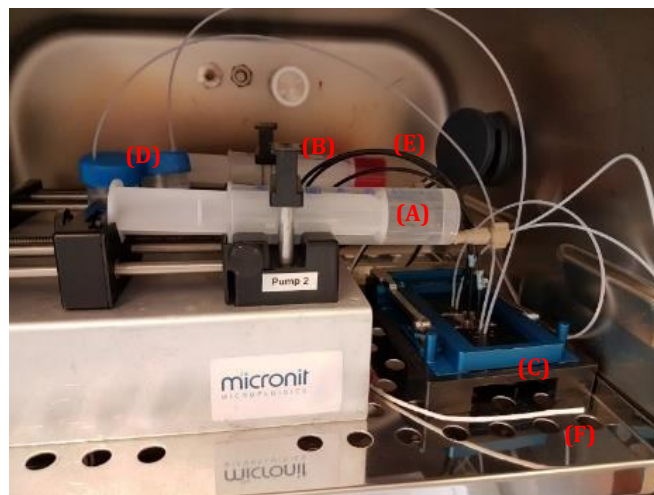


**Figure 132** Experimental setup for the microfluidic device for the cell experiments. The whole system was assembled in an incubator at 37 °C. Pumps ensured the proper liquid flow rate from the syringes to the chip in the FCP (C) and further to the falcon tubes (D). PBS (syringe (A)) was pumped through the upper channel of the chip while cell medium (syringe (B)) was pumped through the lower channel. Connected to the FireStingO2 device there were fibre optics (black cables (E)) for contactless sensing and a temperature sensor (white cable (F)).

**Oxygen Consumption.** The consumption of oxygen from the cell medium by HUVECS was studied by using the setup shown in **Figure 132**. Cell medium was pumped through the lower channel of the chip since the cells were on the bottom part of the membrane. PBS was pumped through the upper channel. The flow rate of the pumps was set at 13  $\mu\text{L}/\text{min}$ . Oxygen detection was carried out with the FireStingO2 device and data recording was performed by using the Pyro Oxygen Logger program. Continuous flow occurred until

oxygen sensor readings reached a steady-state (approximately 1 h). At that point, the flow was stopped for 2 h. Afterwards, the flow was reinstated for another hour and again stopped for 2 h.

### *5.3.3.2 Flow effect on the sensor*

A set-up similar to the one on **Figure 132**, where both syringes contained air-saturated water was used to study the effect of the flow rate on the sensor. The setup was assembled in a laboratory oven at 37 °C. In a first experiment, air-saturated water was pumped at 13  $\mu\text{L}/\text{min}$  through both channels until the oxygen sensor readings presented a steady-state. At this moment, the flow was stopped. In the second experiment, a gradient of flows (50, 40, 30, 20, 10, 5  $\mu\text{L}/\text{min}$ ) was tested by using the same set-up before the flow was stopped. These experiments were carried out with chips containing polystyrene as middle layers with a porous PET membrane.



## References



- 1 E. C. Constable and C. E. Housecroft, *Chem. Soc. Rev.*, 2013, **42**, 1429–1439.
- 2 J. W. Buchler, *Angew. Chem. Int. Ed. Engl.*, 1978, **17**, 407–423.
- 3 M. Senge, A. Ryan, K. Letchford, S. MacGowan and T. Mielke, *Symmetry*, 2014, **6**, 781–843.
- 4 L. Randaccio, S. Geremia, N. Demitri and J. Wuerges, *Molecules*, 2010, **15**, 3228–3259.
- 5 K. E. van Holde, K. I. Miller and H. Decker, *J. Biol. Chem.*, 2001, **276**, 15563–15566.
- 6 I. Bertini, H. B. Gray, J. Valentine and S. Lippard, *Bioinorganic Chemistry, University Science Books*, 1994.
- 7 C. Chen and K. S. Suslick, *Coord. Chem. Rev.* 1993, **128**, 293–322.
- 8 M. Fujita, Y. J. Kwon, S. Washizu and K. Ogura, *J. Am. Chem. Soc.*, 1994, **116**, 1151–1152.
- 9 B. F. Hoskins and R. Robson, *J. Am. Chem. Soc.*, 1990, **112**, 1546–1554.
- 10 E. C. Constable, S. M. Elder, J. Healy, M. D. Ward and D. A. Tocher, *J. Am. Chem. Soc.*, 1990, **112**, 4590–4592.
- 11 M. Aoyagi, S. Tashiro, M. Tominaga, K. Biradha and M. Fujita, *Chem. Commun.*, 2002, 2036–2037.
- 12 M. Fujita, F. Ibukuro, K. Yamaguchi and K. Ogura, *J. Am. Chem. Soc.*, 1995, **117**, 4175–4176.
- 13 M. Yoshizawa, K. Ono, K. Kumazawa, T. Kato and M. Fujita, *J. Am. Chem. Soc.*, 2005, **127**, 10800–10801.
- 14 M. Mauro, A. Aliprandi, C. Cebrián, D. Wang, C. Kübel and L. De Cola, *Chem. Commun.*, 2014, **50**, 7269–7272.
- 15 S. M. Borisov, G. Zenkl and I. Klimant, *ACS Appl. Mater. Interfaces*, 2010, **2**, 366–374.
- 16 J.-M. Lehn, *Supramolecular Chemistry: Concepts and Perspectives*, Wiley-VCH, 1995, 1–9.
- 17 J.-M. Lehn, *Angew. Chem. Int. Ed. Engl.*, 1988, **27**, 89–112.
- 18 J.-M. Lehn, *Angew. Chem. Int. Ed. Engl.*, 1990, **29**, 1304–1319.
- 19 J.-M. Lehn, J. L. Atwood, F. Vogtle, D. D. Macnicol and J. E. D. Davies, *Comprehensive Supramolecular Chemistry, Volume 9: Templating, Self-Assembly and Self-Organization*, Pergamon, 1996.
- 20 M. Albrecht, *Naturwissenschaften*, 2007, **94**, 951–966.
- 21 G. Whitesides, J. Mathias and C. Seto, *Science*, 1991, **254**, 1312–1319.
- 22 R. G. Chapman and J. C. Sherman, *J. Am. Chem. Soc.*, 1995, **117**, 9081–9082.
- 23 H. Kitagawa, Y. Kobori, M. Yamanaka, K. Yoza and K. Kobayashi, *Proc. Natl. Acad. Sci. U.S.A.*, 2009, **106**, 10444–10448.
- 24 M. Fujita, K. Umemoto, M. Yoshizawa, N. Fujita, T. Kusukawa and K. Biradha, *Chem. Commun.*, 2001, 509–518.
- 25 H. Jude, D. J. Sinclair, N. Das, M. S. Sherburn and P. J. Stang, *J. Org. Chem.*, 2006, **71**, 4155–4163.
- 26 L. Fabbrizzi and A. Poggi, Eds., *Transition Metals in Supramolecular Chemistry*, Springer Netherlands, Dordrecht, 1994.
- 27 J.-P. Sauvage, *Transition Metals in Supramolecular Chemistry*, Chichester, England; New York: Wiley, 1999.
- 28 J.-P. Sauvage and C. Dietrich-Buchecker, *Molecular Catenanes, Rotaxanes and Knots: A Journey Through the World of Molecular Topology*, Wiley-VCH, 1999.
- 29 V. Balzani, A. Credi, F. M. Raymo and J. F. Stoddart, *Angew. Chem. Int. Ed.*, 2000, **39**, 3348–3391.
- 30 V. Balzani, A. Credi, S. Silvi and M. Venturi, *Chem. Soc. Rev.*, 2006, **35**, 1135–1149.

- 31 A. Credi and H. Tian, *Adv. Funct. Mater.*, 2007, **17**, 679–682.
- 32 B. Olenyuk, A. Fechtenkötter and P. J. Stang, *J. Chem. Soc., Dalton Trans.*, 1998, 1707–1728.
- 33 S. Sato, Y. Ishido and M. Fujita, *J. Am. Chem. Soc.*, 2009, **131**, 6064–6065.
- 34 N. M. Kostić and L.-M. Dutcă, in *Comprehensive Coordination Chemistry II*, Elsevier, 2003, 555–672.
- 35 R. W. Hay and M. P. Pujari, *Inorg. Chim. Acta*, 1986, **123**, 47–51.
- 36 P. J. Steel, *Molecules*, 2004, **9**, 440–448.
- 37 M. Fujita, *Chem. Soc. Rev.*, 1998, **27**, 417.
- 38 A. Ikeda, M. Yoshimura, H. Udzu, C. Fukuhara and S. Shinkai, *J. Am. Chem. Soc.*, 1999, **121**, 4296–4297.
- 39 S. B. Lee, S. Hwang, D. S. Chung, H. Yun and J.-I. Hong, *Tetrahedron Lett.*, 1998, **39**, 873–876.
- 40 M. Fujita, O. Sasaki, T. Mitsuhashi, T. Fujita, J. Yazaki, K. Yamaguchi and K. Ogura, *Chem. Commun.*, 1996, 1535–1536.
- 41 D. J. Tranchemontagne, Z. Ni, M. O’Keeffe and O. M. Yaghi, *Angew. Chem. Int. Ed.*, 2008, **47**, 5136–5147.
- 42 M. M. Conn and J. Rebek, *Chem. Rev.*, 1997, **97**, 1647–1668.
- 43 M. Fujita, M. Tominaga, A. Hori and B. Therrien, *Acc. Chem. Res.*, 2005, **38**, 369–378.
- 44 R. Custelcean, *Chem. Soc. Rev.*, 2014, **43**, 1813–1824.
- 45 S. Turega, M. Whitehead, B. R. Hall, M. F. Haddow, C. A. Hunter and M. D. Ward, *Chem. Commun.*, 2012, **48**, 2752.
- 46 W. Meng, B. Breiner, K. Rissanen, J. D. Thoburn, J. K. Clegg and J. R. Nitschke, *Angew. Chem. Int. Ed.*, 2011, **50**, 3479–3483.
- 47 P. Mal, B. Breiner, K. Rissanen and J. R. Nitschke, *Science*, 2009, **324**, 1697–1699.
- 48 M. M. J. Smulders and J. R. Nitschke, *Chem. Sci.*, 2012, **3**, 785–788.
- 49 C. J. Hastings, M. D. Pluth, R. G. Bergman and K. N. Raymond, *J. Am. Chem. Soc.*, 2010, **132**, 6938–6940.
- 50 M. Fujita, *Coord. Chem. Rev.*, 1996, **148**, 249–264.
- 51 M. Fujita and K. Ogura, *Bull. Chem. Soc. Jpn.*, 1996, **69**, 1471–1482.
- 52 D. M. Vriezema, M. Comellas Aragonès, J. A. A. W. Elemans, J. J. L. M. Cornelissen, A. E. Rowan and R. J. M. Nolte, *Chem. Rev.*, 2005, **105**, 1445–1490.
- 53 T. Murase, H. Takezawa and M. Fujita, *Chem. Commun.*, 2011, **47**, 10960–10962.
- 54 I. A. Riddell, M. M. J. Smulders, J. K. Clegg and J. R. Nitschke, *Chem. Commun.*, 2011, **47**, 457–459.
- 55 Y. R. Hristova, M. M. J. Smulders, J. K. Clegg, B. Breiner and J. R. Nitschke, *Chem. Sci.*, 2011, **2**, 638–641.
- 56 J. Han, A. F. B. Räder, F. Reichart, B. Aikman, M. N. Wenzel, B. Woods, M. Weinmüller, B. S. Ludwig, S. Stürup, G. M. M. Groothuis, H. P. Permentier, R. Bischoff, H. Kessler, P. Horvatovich and A. Casini, *Bioconjug. Chem.*, 2018, **29**, 3856–3865.
- 57 T. R. Schulte, M. Krick, C. I. Asche, S. Freye and G. H. Clever, *RSC Adv.*, 2014, **4**, 29724–29728.
- 58 A. J. Pryde, B. L. Shaw and B. Weeks, *J. Chem. Soc., Chem. Commun.*, 1973, 947.
- 59 A. W. Maverick and F. E. Klavetter, *Inorg. Chem.*, 1984, **23**, 4129–4130.
- 60 A. W. Schwabacher, J. Lee and H. Lei, *J. Am. Chem. Soc.*, 1992, **114**, 7597–7598.
- 61 M. Fujita, J. Yazaki, T. Kuramochi and K. Ogura, *Bull. Chem. Soc. Jpn.*, 1993, **66**, 1837–1839.



- 62 C. A. Hunter and L. D. Sarson, *Angew. Chem. Int. Ed.*, 1994, **33**, 2313–2316.
- 63 B. Hasenknopf, J.-M. Lehn, N. Boumediene, A. Dupont-Gervais, A. Van Dorselaer, B. Kneisel and D. Fenske, *J. Am. Chem. Soc.*, 1997, **119**, 10956–10962.
- 64 R. Chakrabarty, P. S. Mukherjee and P. J. Stang, *Chem. Rev.*, 2011, **111**, 6810–6918.
- 65 M. Fujita, J. Yazaki and K. Ogura, *J. Am. Chem. Soc.*, 1990, **112**, 5645–5647.
- 66 M. Fujita, J. Yazaki and K. Ogura, *Tetrahedron Lett.*, 1991, **32**, 5589–5592.
- 67 M. Fujita, J. Yazaki and K. Ogura, *Chem. Lett.*, 1991, **20**, 1031–1032.
- 68 M. Fujita, O. Sasaki, T. Mitsunashi, T. Fujita, J. Yazaki, K. Yamaguchi and K. Ogura, *Chem. Commun.*, 1996, 1535–1536.
- 69 M. Fujita, F. Ibukuro, K. Yamaguchi and K. Ogura, *J. Am. Chem. Soc.*, 1995, **117**, 4175–4176.
- 70 M. Fujita, S. Nagao and K. Ogura, *J. Am. Chem. Soc.*, 1995, **117**, 1649–1650.
- 71 S. Anderson, H. L. Anderson and J. K. M. Sanders, *Acc. Chem. Res.*, 1993, **26**, 469–475.
- 72 M. Lofthagen, R. Chadha and J. S. Siegel, *J. Am. Chem. Soc.*, 1991, **113**, 8785–8790.
- 73 M. Fujita, K. Umemoto, M. Yoshizawa, N. Fujita, T. Kusukawa and K. Biradha, *Chem. Commun.*, 2001, 509–518.
- 74 T. Kusukawa and M. Fujita, *J. Am. Chem. Soc.*, 1999, **121**, 1397–1398.
- 75 T. Kusukawa and M. Fujita, *Angew. Chem. Int. Ed.*, 1998, **37**, 3142–3144.
- 76 S.-Y. Yu, T. Kusukawa, K. Biradha and M. Fujita, *J. Am. Chem. Soc.*, 2000, **122**, 2665–2666.
- 77 M. Yoshizawa, T. Kusukawa, M. Fujita and K. Yamaguchi, *J. Am. Chem. Soc.*, 2000, **122**, 6311–6312.
- 78 H. Ito, T. Kusukawa and M. Fujita, *Chem. Lett.*, 2000, **29**, 598–599.
- 79 M. Fujita, D. Oguro, M. Miyazawa, H. Oka, K. Yamaguchi and K. Ogura, *Nature*, 1995, **378**, 469–471.
- 80 M. Han, D. M. Engelhard and G. H. Clever, *Chem. Soc. Rev.*, 2014, **43**, 1848–1860.
- 81 S. Saha, I. Regeni and G. H. Clever, *Coord. Chem. Rev.*, 2018, **374**, 1–14.
- 82 K. Harris, D. Fujita and M. Fujita, *Chem. Commun.*, 2013, **49**, 6703–6712.
- 83 D. A. McMorran and P. J. Steel, *Angew. Chem. Int. Ed. Engl.*, 1998, **37**, 3295–3297.
- 84 J. Anhäuser, R. Puttreddy, Y. Lorenz, A. Schneider, M. Engeser, K. Rissanen and A. Lützen, *Org. Chem. Front.*, 2019, **6**, 1226–1235.
- 85 C. Klein, C. Gütz, M. Bogner, F. Topić, K. Rissanen and A. Lützen, *Angew. Chem. Int. Ed.*, 2014, **53**, 3739–3742.
- 86 K. Suzuki, M. Kawano and M. Fujita, *Angew. Chem. Int. Ed.*, 2007, **46**, 2819–2822.
- 87 Q.-F. Sun, J. Iwasa, D. Ogawa, Y. Ishido, S. Sato, T. Ozeki, Y. Sei, K. Yamaguchi and M. Fujita, *Science*, 2010, **328**, 1144–1147.
- 88 J. C. Lewis, *ACS Catalysis*, 2013, **3**, 2954–2975.
- 89 M. Albrecht and P. Stortz, *Chem. Soc. Rev.*, 2005, **34**, 496–506.
- 90 S. Zhang, *Nat. Biotechnol.*, 2003, **21**, 1171–1178.
- 91 D. E. Przybyla and J. Chmielewski, *Biochemistry*, 2010, **49**, 4411–4419.
- 92 M. Panciera, M. Amorín and J. R. Granja, *Chem. Eur. J.*, 2014, **20**, 10260–10265.
- 93 S.-Y. Qin, H.-F. Jiang, X.-J. Liu, Y. Pei, H. Cheng, Y.-X. Sun and X.-Z. Zhang, *Soft Matter*, 2014, **10**, 947–951.
- 94 S. Lou, X. Wang, Z. Yu and L. Shi, *Adv. Sci.*, 2019, **6**, 1802043.
- 95 J. Y. Rho, H. Cox, E. D. H. Mansfield, S. H. Ellacott, R. Peltier, J. C. Brendel, M. Hartlieb, T. A. Waigh and S. Perrier, *Nat. Commun.*, 2019, **10**, 1–9.

- 96 S.-Y. Qin, Y.-F. Chu, L. Tao, S.-S. Xu, Z.-Y. Li, R.-X. Zhuo and X.-Z. Zhang, *Soft Matter*, 2011, **7**, 8635.
- 97 H. Tan, W. Qu and G. Chen, *Int. J. Quantum Chem.*, 2005, **102**, 1106–1115.
- 98 R. J. Brea, C. Reiriz and J. R. Granja, *Chem. Soc. Rev.*, 2010, **39**, 1448–1456.
- 99 M. R. Silk, B. Mohanty, J. B. Sampson, M. J. Scanlon, P. E. Thompson and D. K. Chalmers, *Angew. Chem. Int. Ed.*, 2019, **58**, 596–601.
- 100 E. Bartolami, J. Knoops, Y. Bessin, M. Fossépré, J. Chamieh, P. Dumy, M. Surin and S. Ulrich, *Chem. Eur. J.*, 2017, **23**, 14323–14331.
- 101 R. Zou, Q. Wang, J. Wu, J. Wu, C. Schmuck and H. Tian, *Chem. Soc. Rev.*, 2015, **44**, 5200–5219.
- 102 A. Ganß, C. Xu, A. Guenet, H. Kelm, N. Kyritsakas, J.-M. Planeix, S. Kubik and M. W. Hosseini, *CrystEngComm*, 2016, **18**, 7685–7689.
- 103 F. Fujimura and S. Kimura, *Org. Lett.*, 2007, **9**, 793–796.
- 104 Y. Dong, D. T. J. Loong, A. K. L. Yuen, R. J. Black, S. O'Malley, J. K. Clegg, L. F. Lindoy and K. A. Jolliffe, *Supramol. Chem.*, 2012, **24**, 508–519.
- 105 S. Chakraborty, P. Tyagi, D.-F. Tai, G.-H. Lee and S.-M. Peng, *Molecules*, 2013, **18**, 4972–4985.
- 106 P. Wipf and C. Wang, *Org. Lett.*, 2006, **8**, 2381–2384.
- 107 M. Panciera, M. Amorín, L. Castedo and J. R. Granja, *Chem. Eur. J.*, 2013, **19**, 4826–4834.
- 108 S. Kubik and R. Goddard, *J. Org. Chem.*, 1999, **64**, 9475–9486.
- 109 A. Ganß, Dissertation: Neuartige supramolekulare Koordinationsverbindungen mit Cyclen- oder Cyclopeptiduntereinheiten, TU Kaiserslautern, 2016.
- 110 S. Kubik, *J. Am. Chem. Soc.*, 1999, **121**, 5846–5855.
- 111 L. Zhu, M. Lu, D. Qu, Q. Wang and H. Tian, *Org. Biomol. Chem.*, 2011, **9**, 4226–4233.
- 112 S. H. A. M. Leenders, R. Becker, T. Kumpulainen, B. de Bruin, T. Sawada, T. Kato, M. Fujita and J. N. H. Reek, *Chem. Eur. J.*, 2016, **22**, 15468–15474.
- 113 R. A. Adrian, S. Zhu, K. K. Klausmeyer and J. A. Walmsley, *Inorg. Chem. Commun.*, 2007, **10**, 1527–1530.
- 114 T. Sawada, M. Yoshizawa, S. Sato and M. Fujita, *Nat. Chem.*, 2009, **1**, 53–56.
- 115 S. Pohl, R. Goddard and S. Kubik, *Tetrahedron Lett.*, 2001, **42**, 7555–7558.
- 116 C. Gütz, R. Hovorka, G. Schnakenburg and A. Lützen, *Chem. Eur. J.*, 2013, **19**, 10890–10894.
- 117 C. Gütz, R. Hovorka, C. Klein, Q.-Q. Jiang, C. Bannwarth, M. Engeser, C. Schmuck, W. Assenmacher, W. Mader, F. Topić, K. Rissanen, S. Grimme and A. Lützen, *Angew. Chem. Int. Ed.*, 2014, **53**, 1693–1698.
- 118 M. Fujita, *Chem. Soc. Rev.*, 1998, **27**, 417.
- 119 V. Balzani, G. Bergamini, S. Campagna and F. Puntoriero, in *Photochemistry and Photophysics of Coordination Compounds I*, eds. V. Balzani and S. Campagna, Springer Berlin Heidelberg, Berlin, Heidelberg, 2007, 1–36.
- 120 J. Mei, N. L. C. Leung, R. T. K. Kwok, J. W. Y. Lam and B. Z. Tang, *Chem. Rev.*, 2015, **115**, 11718–11940.
- 121 C. M. Strabler, S. Sinn, R. Pehn, J. Pann, J. Dutzler, W. Viertel, J. Prock, K. Ehrmann, A. Weninger, H. Kopacka, L. De Cola and P. Brüggegger, *Faraday Discuss.*, 2017, **198**, 211–233.
- 122 D. Gust, T. A. Moore and A. L. Moore, *Acc. Chem. Res.*, 2009, **42**, 1890–1898.

- 123 A. Hagfeldt, G. Boschloo, L. Sun, L. Kloo and H. Pettersson, *Chem. Rev.*, 2010, **110**, 6595–6663.
- 124 H. Yersin, *Highly Efficient OLEDs with Phosphorescent Materials*, Wiley-VCH, 2008.
- 125 P.-T. Chou and Y. Chi, *Chem. Eur. J.*, 2007, **13**, 380–395.
- 126 M. M. Richter, *Chem. Rev.*, 2004, **104**, 3003–3036.
- 127 S. D. Bella, *Chem. Soc. Rev.*, 2001, **30**, 355–366.
- 128 J. Wang, H.-B. Liu, Z. Tong and C.-S. Ha, *Coord. Chem. Rev.*, 2015, **303**, 139–184.
- 129 D. Septiadi, A. Aliprandi, M. Mauro and L. D. Cola, *RSC Adv.*, 2014, **4**, 25709–25718.
- 130 O. Laporte and W. F. Meggers, *J. Opt. Soc. Am.*, 1925, **11**, 459–463.
- 131 M. Mauro, A. Aliprandi, D. Septiadi, N. S. Kehr and L. D. Cola, *Chem. Soc. Rev.*, 2014, **43**, 4144–4166.
- 132 A. Galstyan, A. R. Naziruddin, C. Cebrián, A. Iordache, C. G. Daniliuc, L. D. Cola and C. A. Strassert, *Eur. J. Inorg. Chem.*, 2015, **2015**, 5822–5831.
- 133 J. Sanning, P. R. Ewen, L. Stegemann, J. Schmidt, C. G. Daniliuc, T. Koch, N. L. Doltsinis, D. Wegner and C. A. Strassert, *Angew. Chem. Int. Ed.*, 2015, **54**, 786–791.
- 134 K. Li, G. S. M. Tong, Q. Wan, G. Cheng, W.-Y. Tong, W.-H. Ang, W.-L. Kwong and C.-M. Che, *Chem. Sci.*, 2016, **7**, 1653–1673.
- 135 C. A. Strassert, C.-H. Chien, M. D. Galvez Lopez, D. Kourkoulos, D. Hertel, K. Meerholz and L. De Cola, *Angew. Chem. Int. Ed.*, 2011, **50**, 946–950.
- 136 N. K. Allampally, M. Bredol, C. A. Strassert and L. De Cola, *Chem. Eur. J.*, 2014, **20**, 16863–16868.
- 137 C. Cebrián, M. Mauro, D. Kourkoulos, P. Mercandelli, D. Hertel, K. Meerholz, C. A. Strassert and L. D. Cola, *Adv. Mater.*, 2013, **25**, 437–442.
- 138 M. Mydlak, M. Mauro, F. Polo, M. Felicetti, J. Leonhardt, G. Diener, L. De Cola and C. A. Strassert, *Chem. Mater.*, 2011, **23**, 3659–3667.
- 139 M. Mauro, A. Aliprandi, D. Septiadi, N. S. Kehr and L. D. Cola, *Chem. Soc. Rev.*, 2014, **43**, 4144–4166.
- 140 D. Septiadi, A. Aliprandi, M. Mauro and L. D. Cola, *RSC Adv.*, 2014, **4**, 25709–25718.
- 141 D. Genovese, A. Aliprandi, E. A. Prasetyanto, M. Mauro, M. Hirtz, H. Fuchs, Y. Fujita, H. Uji-I, S. Lebedkin, M. Kappes and L. D. Cola, *Adv. Funct. Mater.*, 2016, **26**, 5271–5278.
- 142 S. Sinn, F. Biedermann, M. Vishe, A. Aliprandi, C. Besnard, J. Lacour and L. De Cola, *ChemPhysChem*, 2016, **17**, 1829–1834.
- 143 J. C. Biffinger, H. W. Kim and S. G. DiMugno, *ChemBioChem*, 2004, **5**, 622–627.
- 144 S. Sinn, F. Biedermann and L. De Cola, *Chem. Eur. J.*, 2017, **23**, 1965–1971.
- 145 M. Mauro, A. Aliprandi, C. Cebrián, D. Wang, C. Kübel and L. De Cola, *Chem. Commun.*, 2014, **50**, 7269–7272.
- 146 J. W. Scannell, A. Blanckley, H. Boldon and B. Warrington, *Nat. Rev. Drug Discovery*, 2012, **11**, 191–200.
- 147 G. Caponigro and W. R. Sellers, *Nat. Rev. Drug Discovery*, 2011, **10**, 179–187.
- 148 J. Bowes, A. J. Brown, J. Hamon, W. Jarolimek, A. Sridhar, G. Waldron and S. Whitebread, *Nat. Rev. Drug Discovery*, 2012, **11**, 909–922.
- 149 D. Huh, G. A. Hamilton and D. E. Ingber, *Trends Cell Biol.*, 2011, **21**, 745–754.
- 150 K. Yum, S. G. Hong, K. E. Healy and L. P. Lee, *Biotechnol. J.*, 2014, **9**, 16–27.
- 151 D. Huh, B. D. Matthews, A. Mammoto, M. Montoya-Zavala, H. Y. Hsin and D. E. Ingber, *Science*, 2010, **328**, 1662–1668.
- 152 N. K. Inamdar and J. T. Borenstein, *Curr. Opin. Biotechnol.*, 2011, **22**, 681–689.

- 153 D. Huh, D. C. Leslie, B. D. Matthews, J. P. Fraser, S. Jurek, G. A. Hamilton, K. S. Thorneloe, M. A. McAlexander and D. E. Ingber, *Sci. Transl. Med.*, 2012, **4**, 159ra147-159ra147.
- 154 S. R. Khetani and S. N. Bhatia, *Nat. Biotechnol.*, 2008, **26**, 120–126.
- 155 S. N. Bhatia, U. J. Balis, M. L. Yarmush and M. Toner, *FASEB J.*, 1999, **13**, 1883–1900.
- 156 D. Huh, Y. Torisawa, G. A. Hamilton, H. J. Kim and D. E. Ingber, *Lab Chip*, 2012, **12**, 2156.
- 157 A. M. Ghaemmaghami, M. J. Hancock, H. Harrington, H. Kaji and A. Khademhosseini, *Drug Discov. Today*, 2012, **17**, 173–181.
- 158 A. D. van der Meer and A. van den Berg, *Integr. Biol.*, 2012, **4**, 461.
- 159 F. Li, Z. Yin, G. Jin, H. Zhao and S. T. C. Wong, *PLoS Comput Biol*, 2013, **9**, e1003043.
- 160 A. Williamson, S. Singh, U. Fernekorn and A. Schober, *Lab Chip*, 2013, **13**, 3471.
- 161 P. D. I. Fletcher, S. J. Haswell, E. Pombo-Villar, B. H. Warrington, P. Watts, S. Y. F. Wong and X. Zhang, *Tetrahedron*, 2002, **58**, 4735–4757.
- 162 D. S. Peterson, T. Rohr, F. Svec and J. M. J. Fréchet, *Anal. Chem.*, 2002, **74**, 4081–4088.
- 163 G. H. Seong, J. Heo and R. M. Crooks, *Anal. Chem.*, 2003, **75**, 3161–3167.
- 164 H. L. T. Lee, P. Boccazzi, R. J. Ram and A. J. Sinskey, *Lab Chip*, 2006, **6**, 1229–1235.
- 165 K. S. Lee, P. Boccazzi, A. J. Sinskey and R. J. Ram, *Lab Chip*, 2011, **11**, 1730–1739.
- 166 S. A. Pfeiffer and S. Nagl, *Methods Appl. Fluoresc.*, 2015, **3**, 034003.
- 167 S. M. Grist, L. Chrostowski and K. C. Cheung, *Sensors*, 2010, **10**, 9286–9316.
- 168 A. Sin, K. C. Chin, M. F. Jamil, Y. Kostov, G. Rao and M. L. Shuler, *Biotechnol. Prog.*, 2004, **20**, 338–345.
- 169 A. P. Vollmer, R. F. Probst, R. Gilbert and T. Thorsen, *Lab Chip*, 2005, **5**, 1059–1066.
- 170 R. H. W. Lam, M.-C. Kim and T. Thorsen, *Anal. Chem.*, 2009, **81**, 5918–5924.
- 171 J. R. Etzkorn, W.-C. Wu, Z. Tian, P. Kim, S.-H. Jang, D. R. Meldrum, A. K.-Y. Jen and B. A. Parviz, *J. Micromech. Microeng.*, 2010, **20**, 095017.
- 172 A. Zanzotto, N. Szita, P. Boccazzi, P. Lessard, A. J. Sinskey and K. F. Jensen, *Biotechnol. Bioeng.*, 2004, **87**, 243–254.
- 173 A. Zanzotto, P. Boccazzi, N. Gorret, T. K. V. Dyk, A. J. Sinskey and K. F. Jensen, *Biotechnol. Bioeng.*, 2006, **93**, 40–47.
- 174 J. E. Rogers, K. A. Nguyen, D. C. Hufnagle, D. G. McLean, W. Su, K. M. Gossett, A. R. Burke, S. A. Vinogradov, R. Pachter and P. A. Fleitz, *J. Phys. Chem. A*, 2003, **107**, 11331–11339.
- 175 O. S. Finikova, A. V. Cheprakov and S. A. Vinogradov, *J. Org. Chem.*, 2005, **70**, 9562–9572.
- 176 V. V. Rozhkov, M. Khajehpour and S. A. Vinogradov, *Inorg. Chem.*, 2003, **42**, 4253–4255.
- 177 S. M. Borisov, G. Nuss, W. Haas, R. Saf, M. Schmuck and I. Klimant, *J. Photochem. Photobiol. A*, 2009, **201**, 128–135.
- 178 Y. Cao, Y.-E. Lee Koo and R. Kopelman, *Analyst*, 2004, **129**, 745.
- 179 C. S. Burke, O. McGaughey, J.-M. Sabattié, H. Barry, A. K. McEvoy, C. McDonagh and B. D. MacCraith, *Analyst*, 2005, **130**, 41–45.
- 180 D. A. Chang-Yen and B. K. Gale, *Lab Chip*, 2003, **3**, 297.
- 181 M.-C. Bélanger and Y. Marois, *J. Biomed. Mater. Res.*, 2001, **58**, 467–477.
- 182 P. C. Thomas, S. R. Raghavan and S. P. Forry, *Anal. Chem.*, 2011, **83**, 8821–8824.
- 183 L. Wang, W. Liu, Y. Wang, J. Wang, Q. Tu, R. Liu and J. Wang, *Lab Chip*, 2013, **13**, 695–705.

- 184 M. Viefhues, S. Sun, D. Valikhani, B. Nidetzky, E. X. Vrouwe, T. Mayr and J. M. Bolivar, *J. Micromech. Microeng.*, 2017, **27**, 065012.
- 185 P. C. Thomas, M. Halter, A. Tona, S. R. Raghavan, A. L. Plant and S. P. Forry, *Anal. Chem.*, 2009, **81**, 9239–9246.
- 186 B. Ungerböck, V. Charwat, P. Ertl and T. Mayr, *Lab Chip*, 2013, **13**, 1593.
- 187 D. B. Papkovsky, J. Olah, I. V. Troyanovsky, N. A. Sadovsky, V. D. Romyantseva, A. F. Mironov, A. I. Yaropolov and A. P. Savitsky, *Biosens. Bioelect.*, 1992, **7**, 199–206.
- 188 I. Klimant, M. Kühl, R. N. Glud and G. Holst, *Sens. Actuators B Chem.*, 1997, **38**, 29–37.
- 189 S.-K. Lee and I. Okura, *Analyst*, 1997, **122**, 81–84.
- 190 S.-K. Lee and I. Okura, *Anal. Chim. Acta*, 1997, **342**, 181–188.
- 191 P. Douglas and K. Eaton, *Sens. Actuators B Chem.*, 2002, **82**, 200–208.
- 192 Y. Amao, K. Asai, I. Okura, H. Shinohara and H. Nishide, *Analyst*, 2000, **125**, 1911–1914.
- 193 S. M. Borisov, T. Mayr, G. Mistlberger, K. Waich, K. Koren, P. Chojnacki and I. Klimant, *Talanta*, 2009, **79**, 1322–1330.
- 194 S. M. Borisov, G. Nuss and I. Klimant, *Anal. Chem.*, 2008, **80**, 9435–9442.
- 195 E. Schmäzlin, J. T. van Dongen, I. Klimant, B. Marmodée, M. Steup, J. Fisahn, P. Geigenberger and H.-G. Löhmannsröben, *Biophys. J.*, 2005, **89**, 1339–1345.
- 196 E. Schmäzlin, B. Walz, I. Klimant, B. Schewe and H.-G. Löhmannsröben, *Sens. Actuators B Chem.*, 2006, **119**, 251–254.
- 197 S. M. Borisov, T. Mayr and I. Klimant, *Anal. Chem.*, 2008, **80**, 573–582.
- 198 T. Femmer, M. L. Eggersdorfer, A. J. C. Kuehne and M. Wessling, *Lab Chip*, 2015, **15**, 3132–3137.
- 199 Y. Gao, J. Li, H. C. Shum and H. Chen, *Langmuir*, 2016, **32**, 4815–4819.
- 200 T. Ladner, D. Flitsch, T. Schlepütz and J. Büchs, *Microb. Cell Fact.*, 2015, **14**, 161–175.
- 201 D. Flitsch, T. Ladner, M. Lukacs and J. Büchs, *Microb. Cell Fact.*, 2016, **15**, 45–56.
- 202 E. Dupuis, 2016. *Personal communication*.
- 203 S. M. Borisov and I. Klimant, *Dyes Pigm.*, 2009, **83**, 312–316.
- 204 A. P. Vollmer, R. F. Probst, R. Gilbert and T. Thorsen, *Lab Chip*, 2005, **5**, 1059–1066.
- 205 R. H. W. Lam, M.-C. Kim and T. Thorsen, *Anal. Chem.*, 2009, **81**, 5918–5924.
- 206 J. Ehgartner, P. Sulzer, T. Burger, A. Kasjanow, D. Bouwes, U. Krühne, I. Klimant and T. Mayr, *Sens. Actuators B Chem.*, 2016, **228**, 748–757.
- 207 H. E. Gottlieb, V. Kotlyar and A. Nudelman, *J. Org. Chem.*, 1997, **62**, 7512–7515.
- 208 M. Nilsson, *J. Magn. Reson.*, 2009, **200**, 296–302.
- 209 R. Evans, Z. Deng, A. K. Rogerson, A. S. McLachlan, J. J. Richards, M. Nilsson and G. A. Morris, *Angew. Chem. Int. Ed.*, 2013, **52**, 3199–3202.
- 210 J. W. Thompson, T. J. Kaiser and J. W. Jorgenson, *J. Chromatogr. A*, 2006, **1134**, 201–209.
- 211 R. Evans, Z. Deng, A. K. Rogerson, A. S. McLachlan, J. J. Richards, M. Nilsson and G. A. Morris, *Angew. Chem. Int. Ed.*, 2013, **52**, 3199–3202.
- 212 A. Macchioni, G. Ciancaleoni, C. Zuccaccia and D. Zuccaccia, *Chem. Soc. Rev.*, 2008, **37**, 479–489.
- 213 S. H. A. M. Leenders, R. Becker, T. Kumpulainen, B. de Bruin, T. Sawada, T. Kato, M. Fujita and J. N. H. Reek, *Chem. Eur. J.*, 2016, **22**, 15468–15474.
- 214 R. A. Adrian, S. Zhu, K. K. Klausmeyer and J. A. Walmsley, *Inorg. Chem. Commun.*, 2007, **10**, 1527–1530.
- 215 M. Mydlak, M. Mauro, F. Polo, M. Felicetti, J. Leonhardt, G. Diener, L. De Cola and C. A. Strassert, *Chem. Mater.*, 2011, **23**, 3659–3667.

- 216 J. H. Price, A. N. Williamson, R. F. Schramm and B. B. Wayland, *Inorg. Chem.*, 1972, **11**, 1280–1284.
- 217 S. M. Borisov and I. Klimant, *Dyes Pigm.*, 2009, **83**, 312–316.

## **Appendix I: Additional Images**





## Additional Spectra

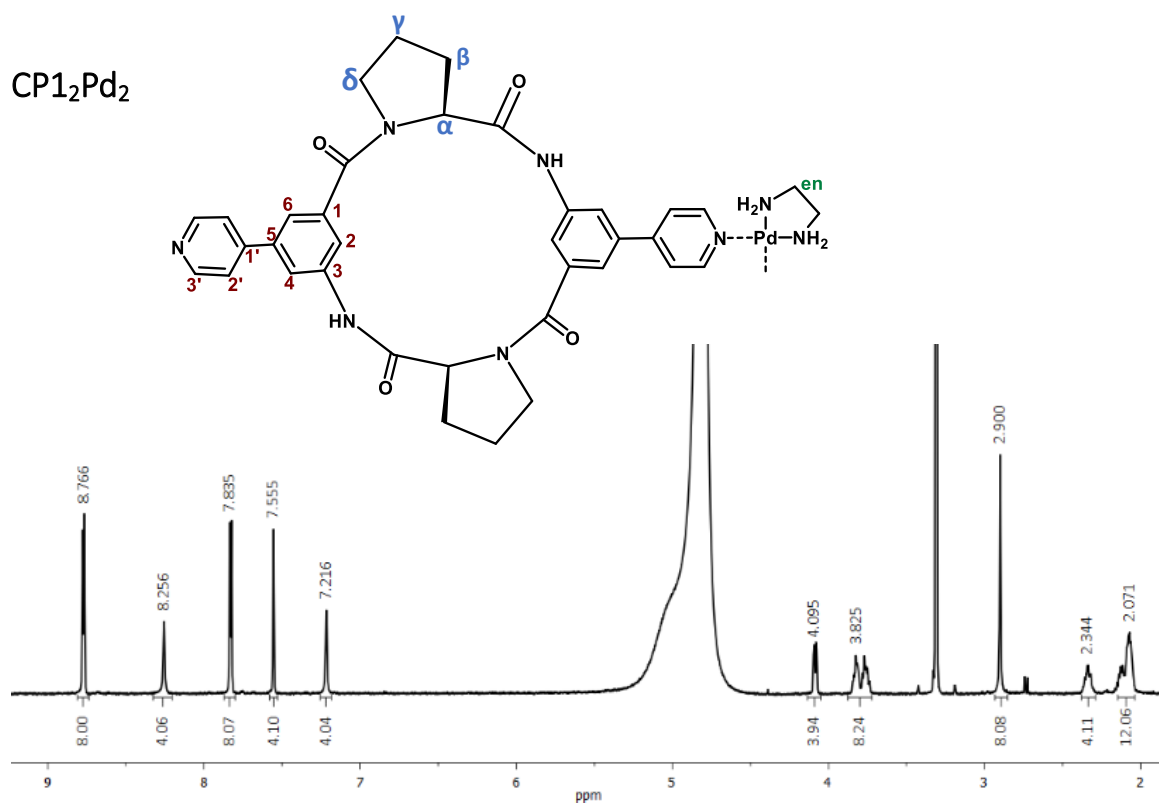


Figure 133 <sup>1</sup>H NMR spectrum of CP<sub>1</sub><sub>2</sub>Pd<sub>2</sub> (1mM) in CD<sub>3</sub>OD/D<sub>2</sub>O, 1:1 (v/v).

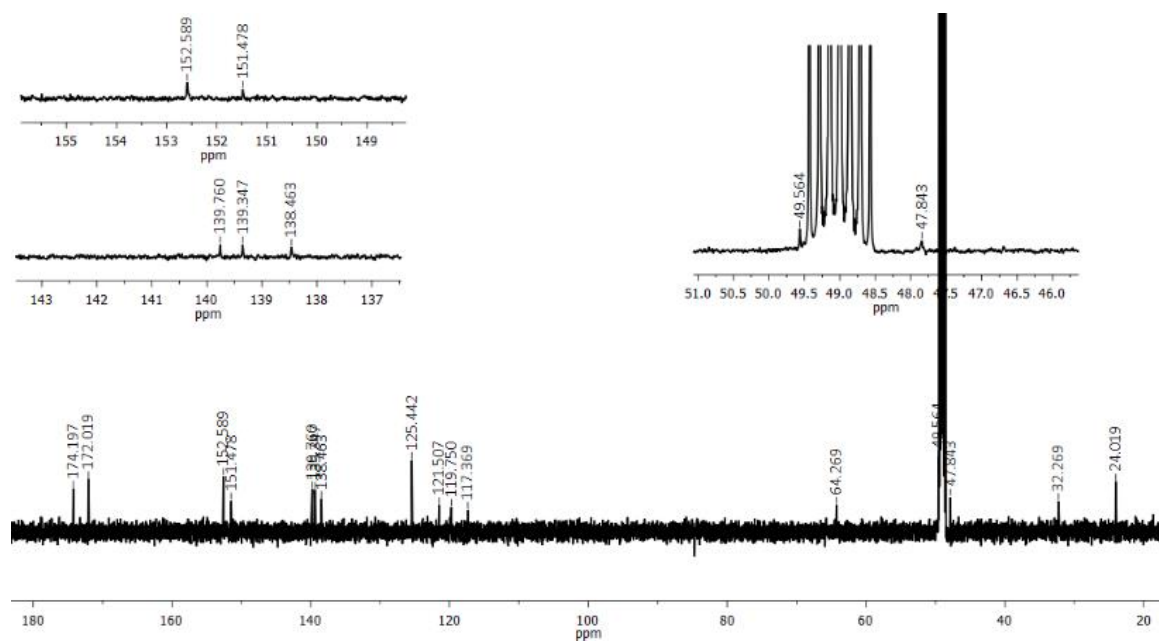


Figure 134 <sup>13</sup>C NMR spectrum of CP<sub>1</sub><sub>2</sub>Pd<sub>2</sub> (1mM) in CD<sub>3</sub>OD/D<sub>2</sub>O, 1:1 (v/v).

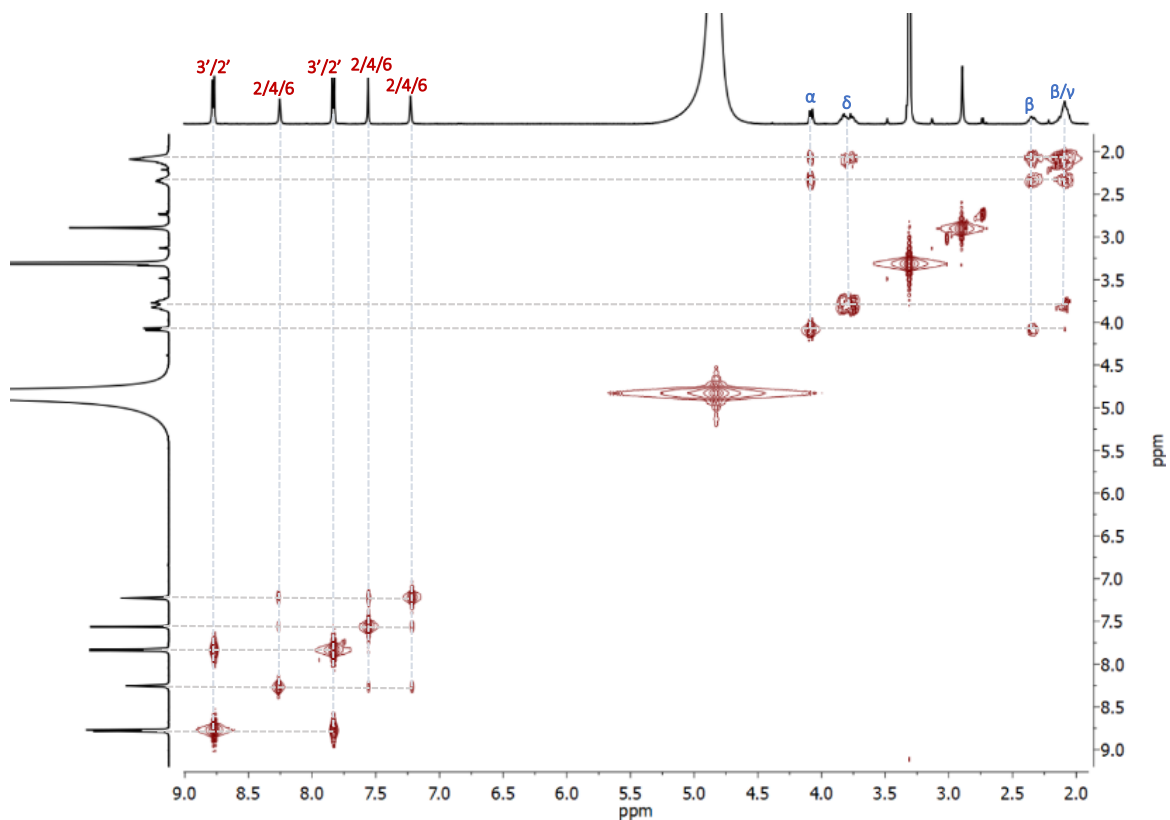


Figure 135 COSY NMR spectrum of  $CP1_2Pd_2$  (1mM) in  $CD_3OD/D_2O$ , 1:1 (v/v).

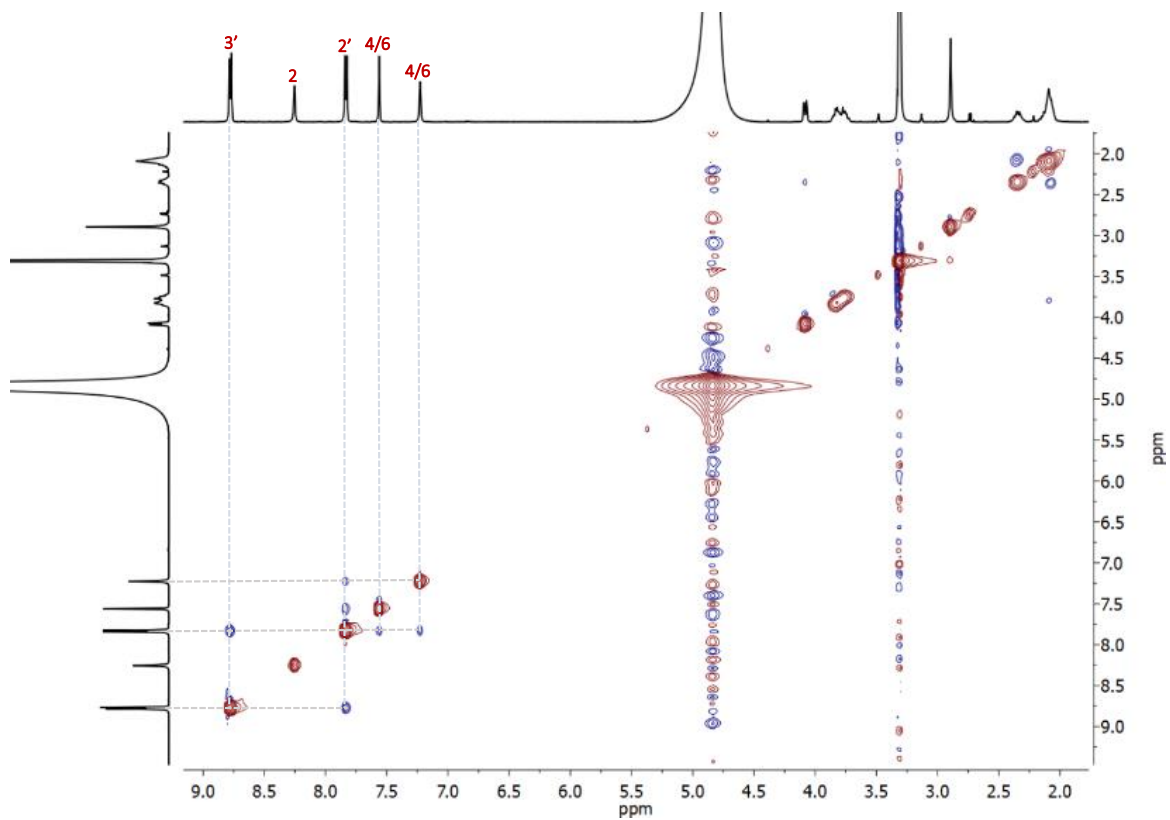


Figure 136 ROESY NMR spectrum of  $CP1_2Pd_2$  (1mM) in  $CD_3OD/D_2O$ , 1:1 (v/v).

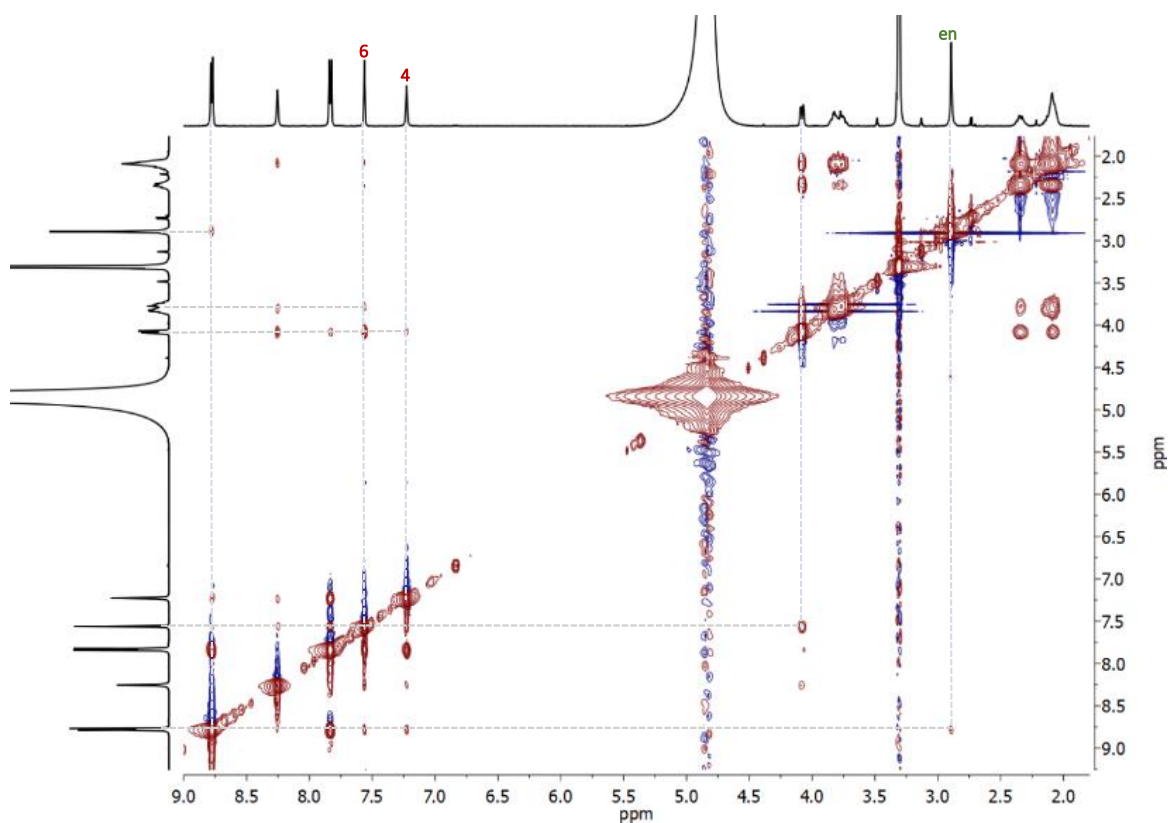
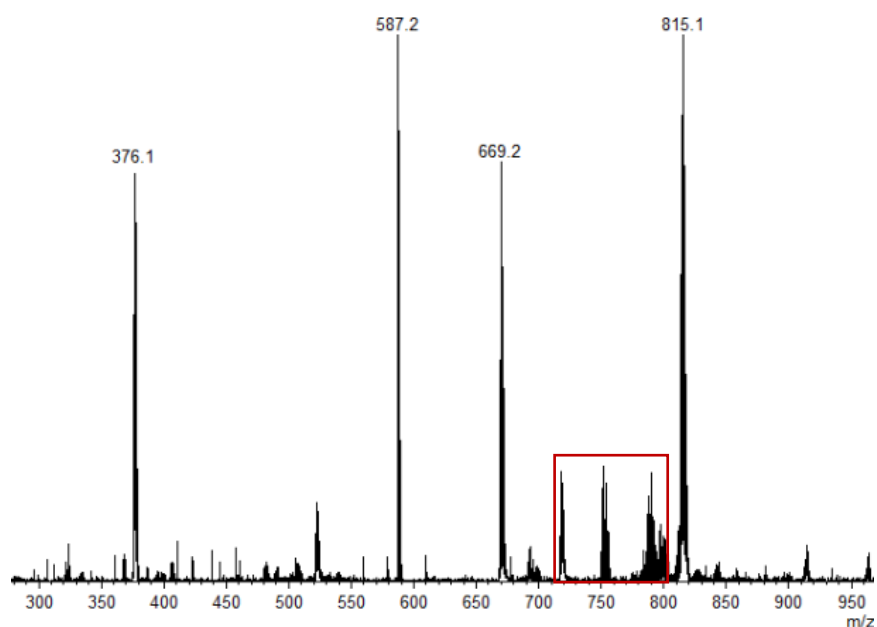


Figure 137 NOESY NMR spectrum of  $CP1_2Pd_2$  (1mM) in  $CD_3OD/D_2O$ , 1:1 (v/v).



		<i>m/z calcd.</i>	<i>m/z exp.</i>
$[CP1+Pd(en)]^{2+}$	$2 C_{34}H_{30}N_6O_4 + C_2H_8N_2Pd^{2+}$	376.1	376.1
$[CP1+H]^+$	$C_{34}H_{30}N_6O_4 + H^+$	587.2	587.2
$[CP1_2+Pd(en)]^{2+}$	$2 C_{34}H_{30}N_6O_4 + C_2H_8N_2Pd^{2+}$	669.2	669.2
$[CP1_2Pd_2+2 NO_3]^{2+}$	$C_{72}H_{76}N_{16}O_8Pd_2^{4+} + 2 NO_3^-$	815.2	815.1

Figure 138 ESI-TOF MS spectrum (positive mode) of the metallamacrocycle  $CP1_2Pd_2$ . The peaks inside the red square are due to fragmentation of the ions with  $m/z=815.1$ .

CP2<sub>2</sub>Pd<sub>3</sub>

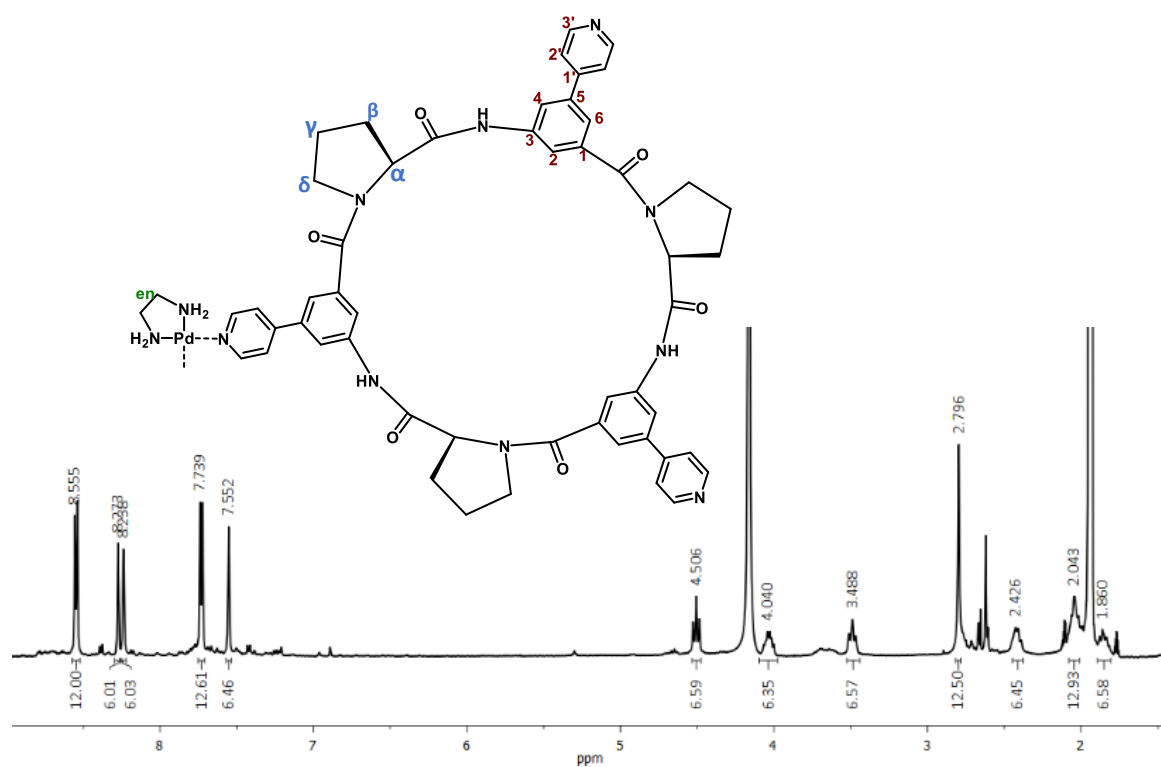


Figure 139 <sup>1</sup>H NMR spectrum of CP2<sub>2</sub>Pd<sub>3</sub> (1mM) in CD<sub>3</sub>CN/D<sub>2</sub>O, 1:1 (v/v).

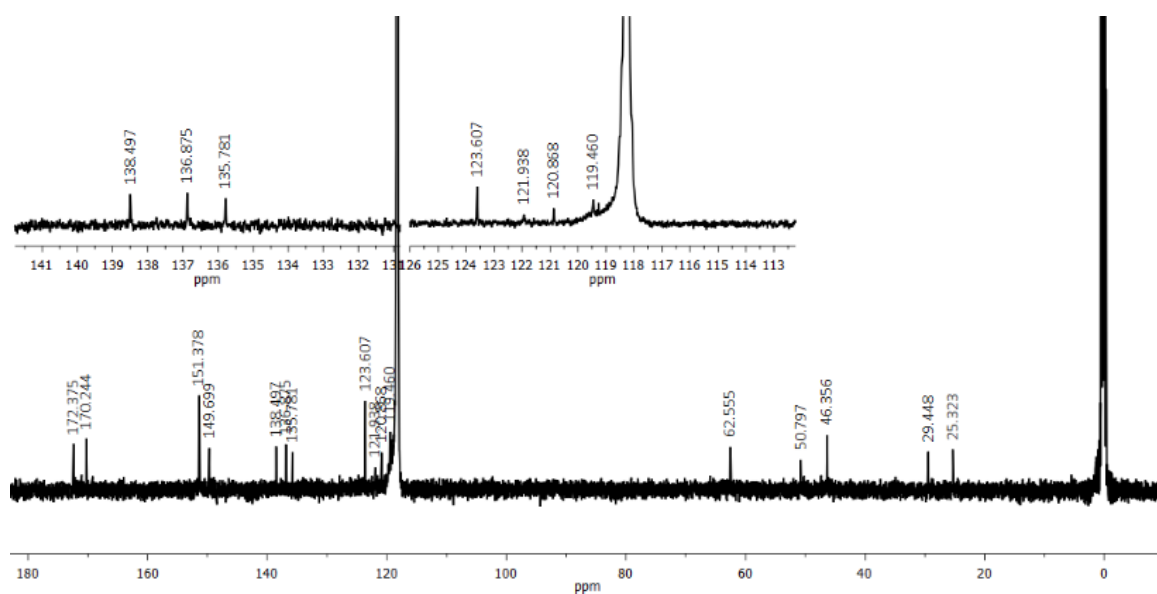


Figure 140 <sup>13</sup>C NMR spectrum of CP2<sub>2</sub>Pd<sub>3</sub> (1mM) in CD<sub>3</sub>CN/D<sub>2</sub>O, 1:1 (v/v).

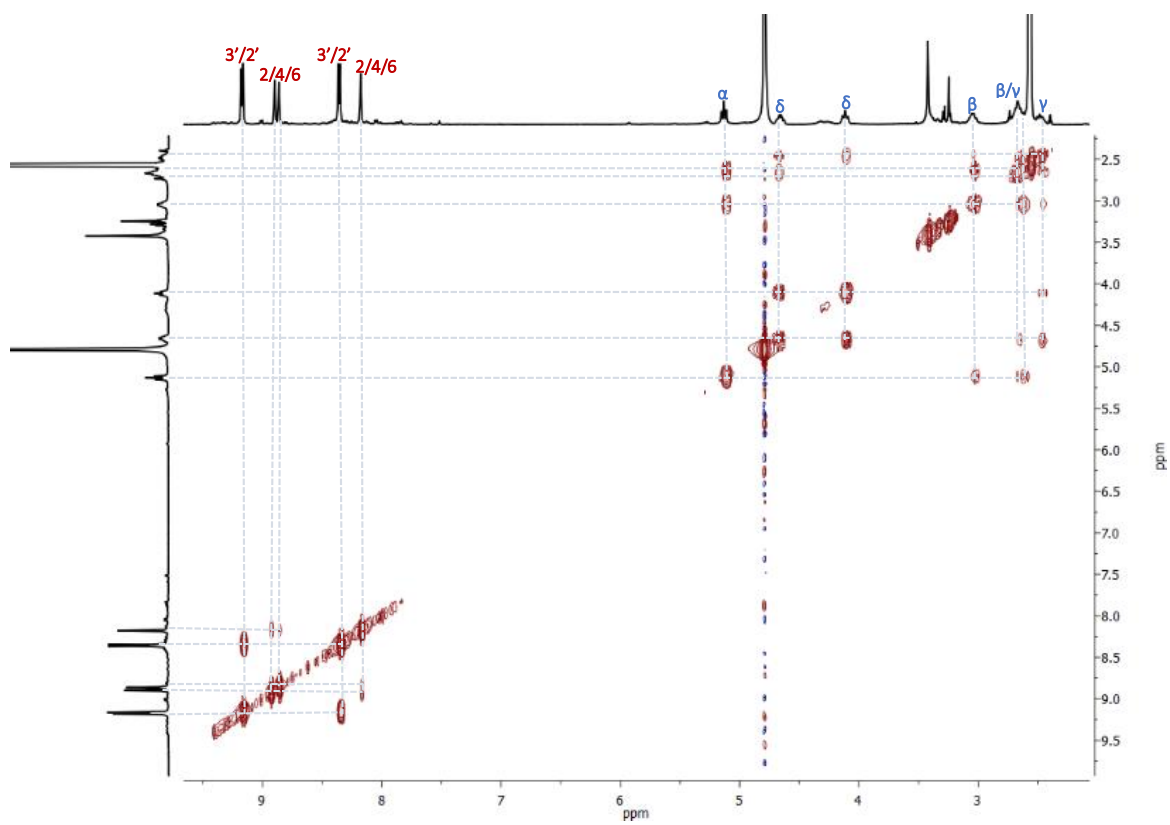


Figure 141 COSY NMR spectrum of  $CP2_2Pd_3$  (1mM) in  $CD_3CN/D_2O$ , 1:1 (v/v).

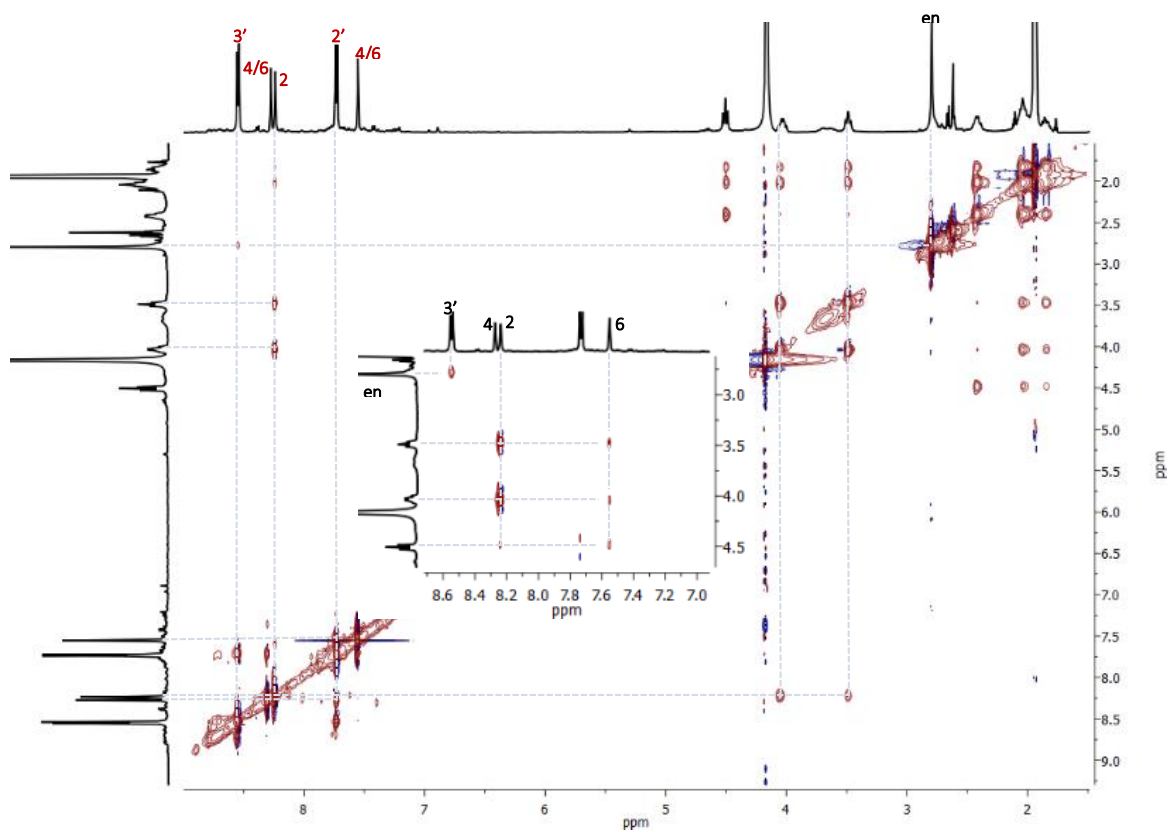
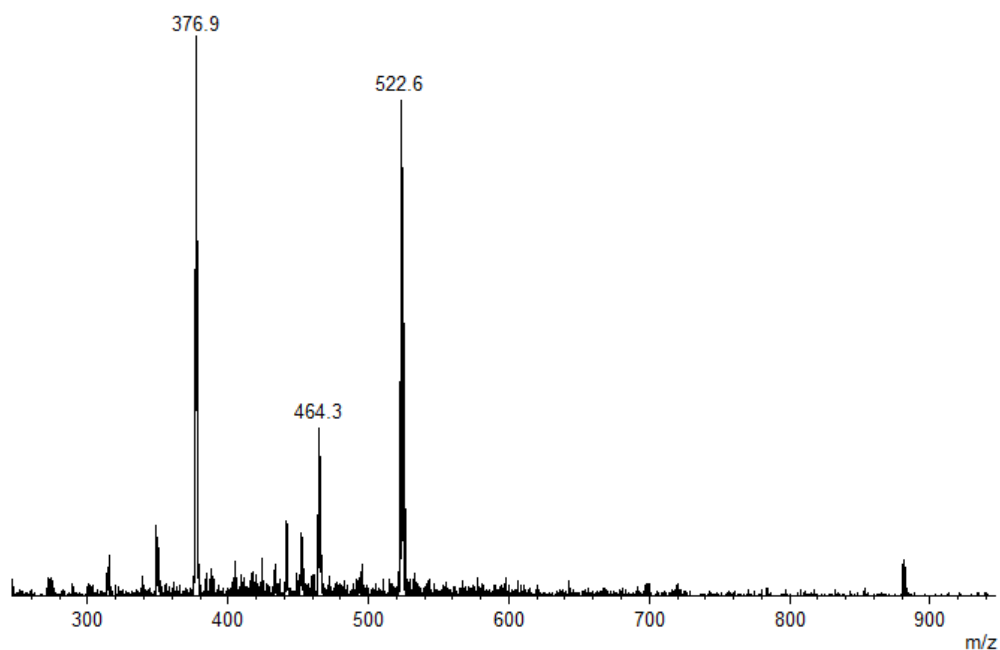


Figure 142 NOESY NMR spectrum of  $CP2_2Pd_3$  (1mM) in  $CD_3CN/D_2O$ , 1:1 (v/v).



		<i>m/z calcd.</i>	<i>m/z exp.</i>
[CP <sub>2</sub> Pd <sub>3</sub> ] <sup>6+</sup>	C <sub>108</sub> H <sub>114</sub> N <sub>24</sub> O <sub>12</sub> Pd <sub>3</sub> <sup>6+</sup>	376.4	376.9
[CP <sub>2</sub> Pd <sub>3</sub> + NO <sub>3</sub> ] <sup>5+</sup>	C <sub>108</sub> H <sub>114</sub> N <sub>24</sub> O <sub>12</sub> Pd <sub>3</sub> <sup>6+</sup> + NO <sub>3</sub> <sup>-</sup>	464.1	464.3
[CP <sub>2</sub> +Pd(en)] <sup>2+</sup>	C <sub>51</sub> H <sub>45</sub> N <sub>9</sub> O <sub>6</sub> + C <sub>2</sub> H <sub>8</sub> N <sub>2</sub> Pd <sup>2+</sup>	522.6	522.6

Figure 143 ESI-TOF MS spectrum (positive mode) of the cage CP<sub>2</sub>Pd<sub>2</sub>.

### CP<sub>1</sub><sub>6</sub>Pd<sub>3</sub>

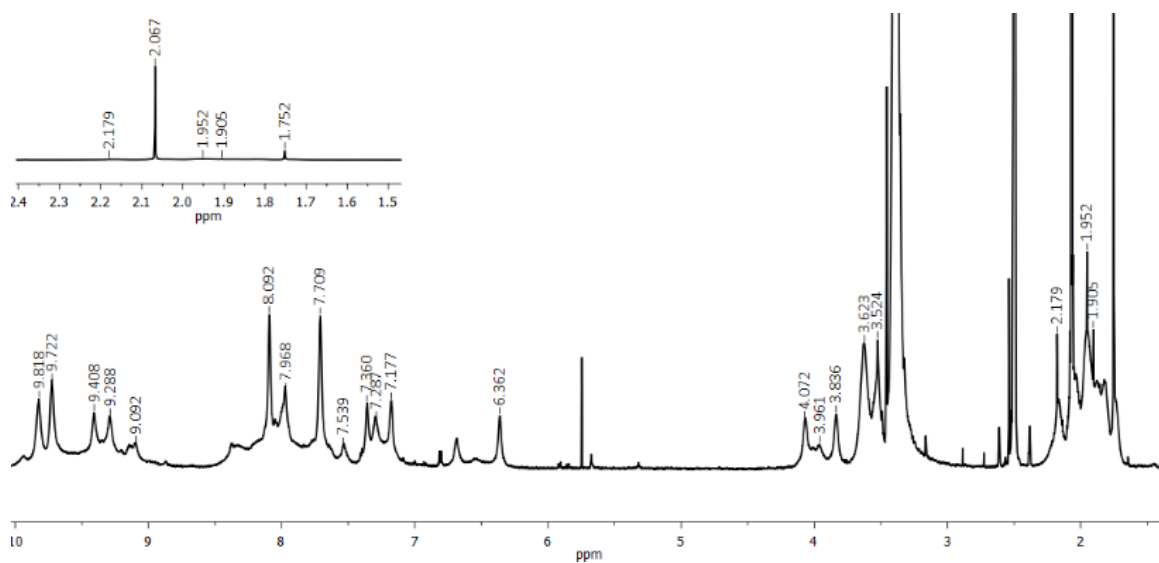
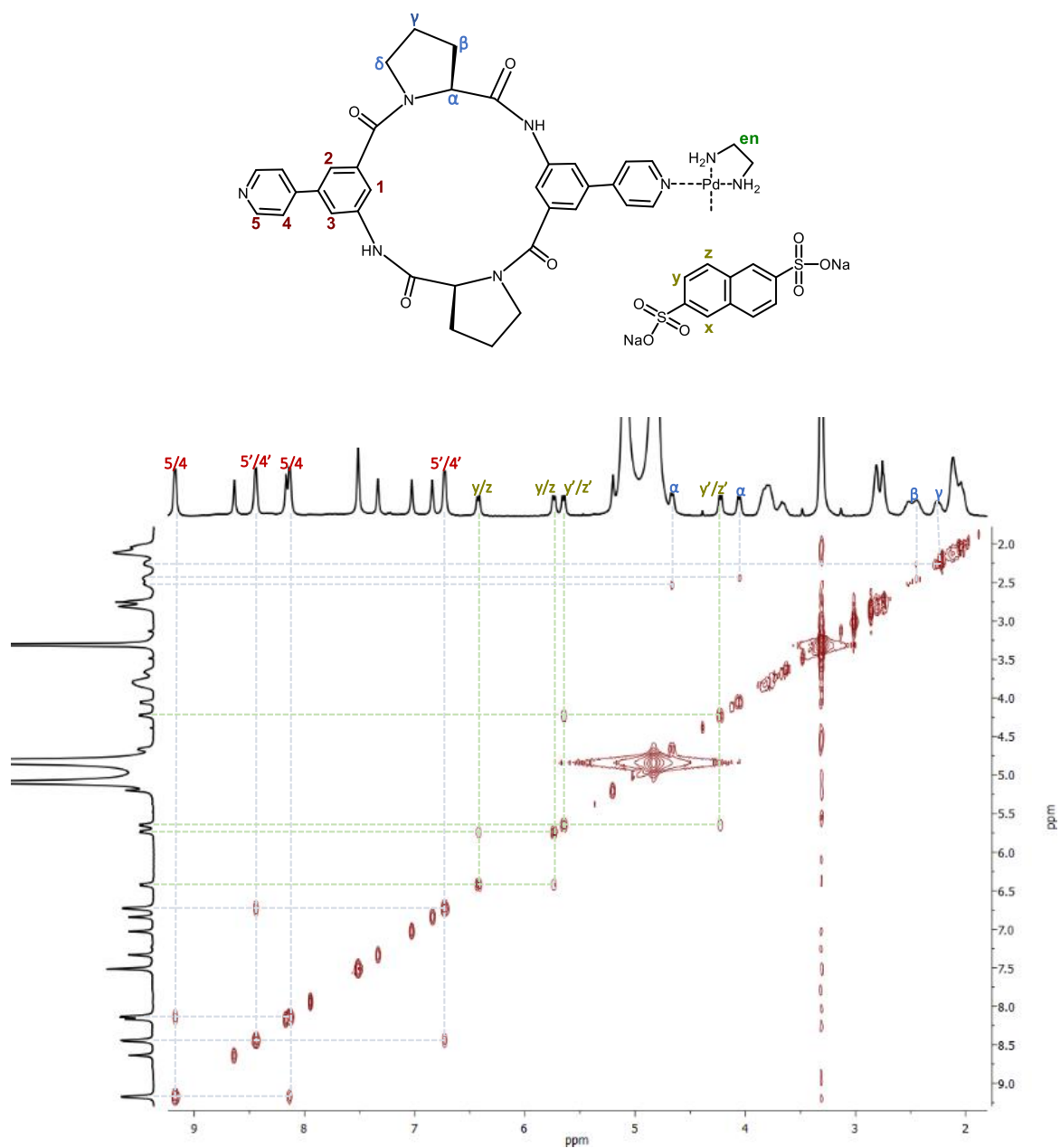
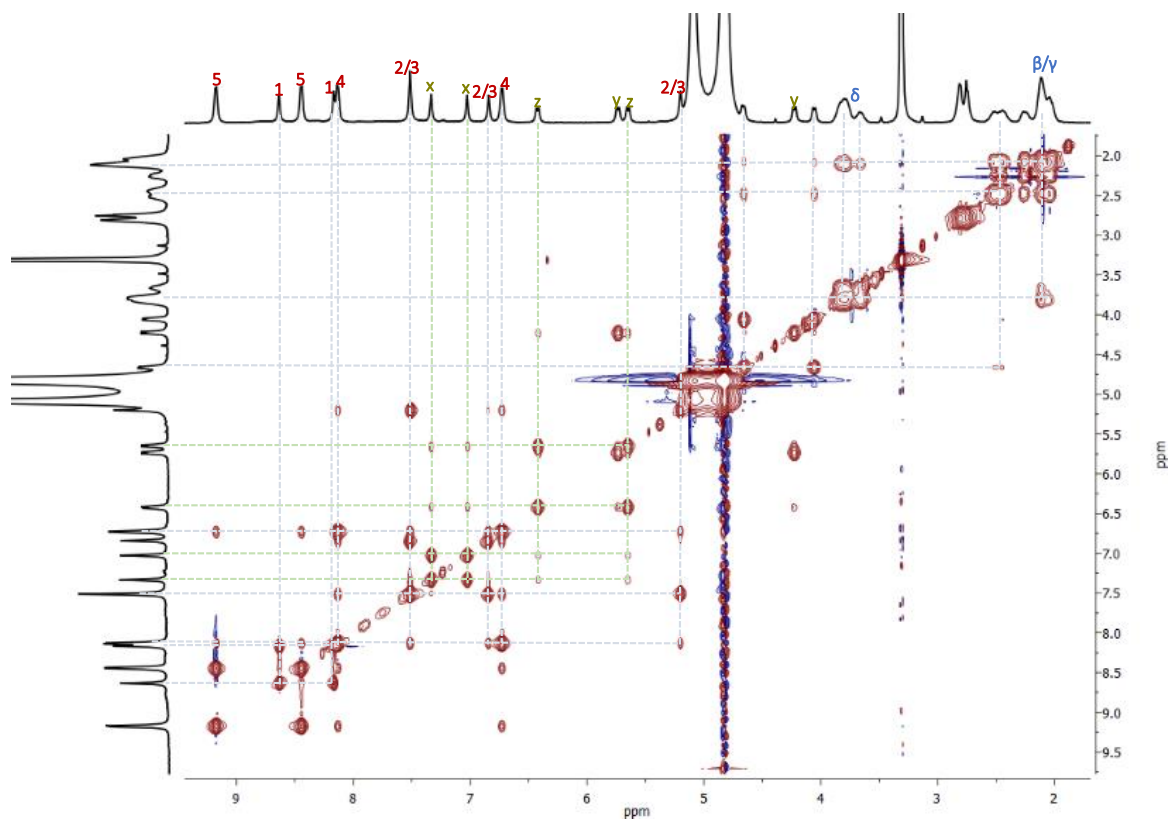


Figure 144 <sup>1</sup>H NMR spectrum of CP<sub>1</sub><sub>6</sub>Pd<sub>3</sub> (1mM) in DMSO-*d*<sub>6</sub>.

CP1<sub>2</sub>Pd<sub>2</sub>·2NDS



**Figure 145** COSY NMR spectrum of a mixture of CP1<sub>2</sub>Pd<sub>2</sub> (1 mM) and NDS (2 mM) in CD<sub>3</sub>OD/D<sub>2</sub>O, 1:1 (v/v). Grey lines mark crosspeaks between signals of the metallamacrocycle and the green lines the crosspeaks between the anion signals.



**Figure 146** NOESY NMR spectrum of a mixture of  $CP1_2Pd_2$  (1mM) and  $NDS$  (2 mM) in  $CD_3OD/D_2O$ , 1:1 (v/v). Grey lines mark crosspeaks between signals of the metallamacrocycle and the green lines the crosspeaks between the anion signals.



## Mean planes (angles and torsions)

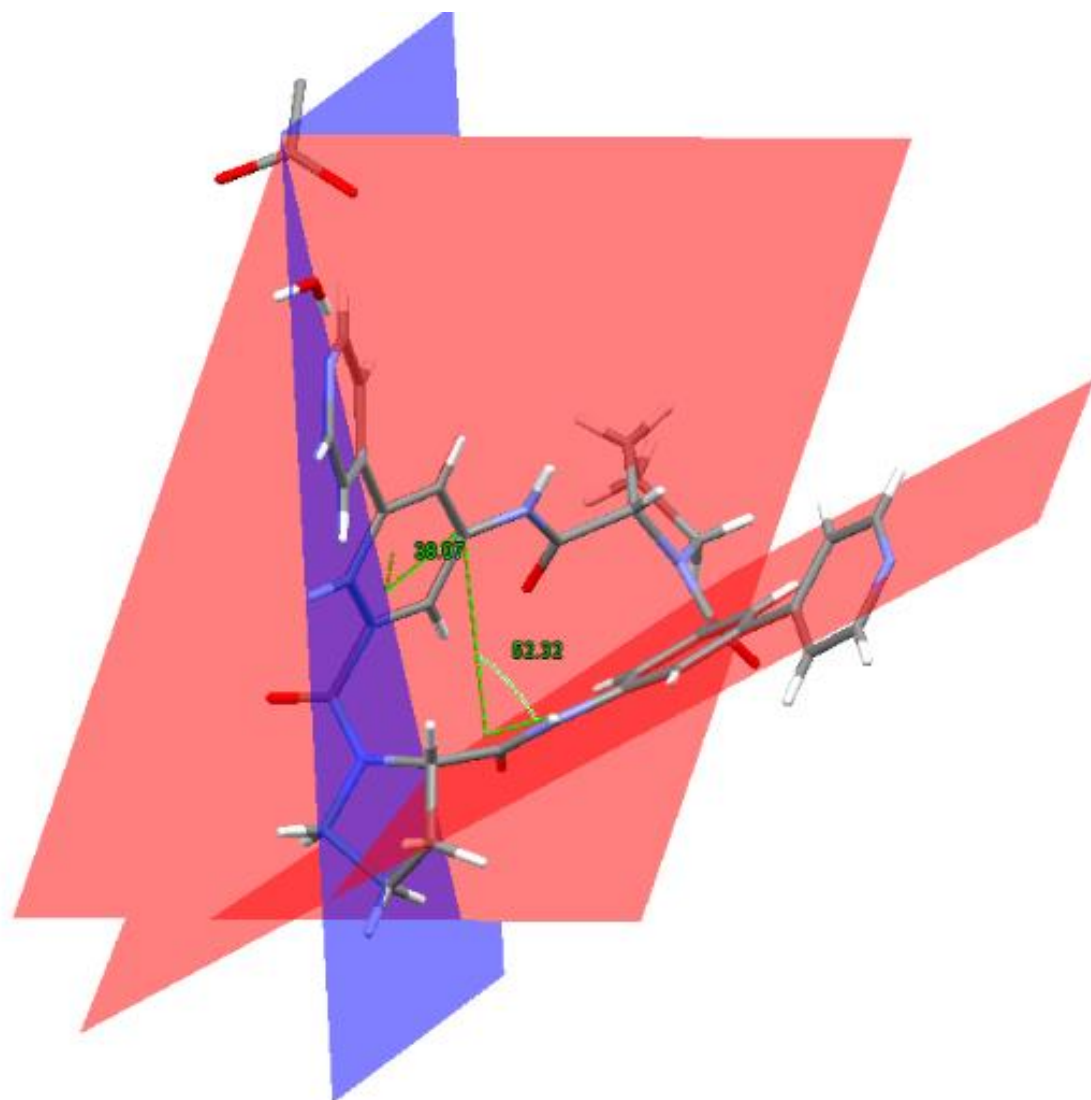


**Figure 147** Crystal structure of **CP1**. The mean planes created by the phenyl rings are shown in red and those created by the pyridine ring in blue. The angle between the mean planes of the phenyl rings is  $52.32^\circ$  and the torsion of the pyridyl subunit in relation to the phenyl ring  $38.07^\circ$ .

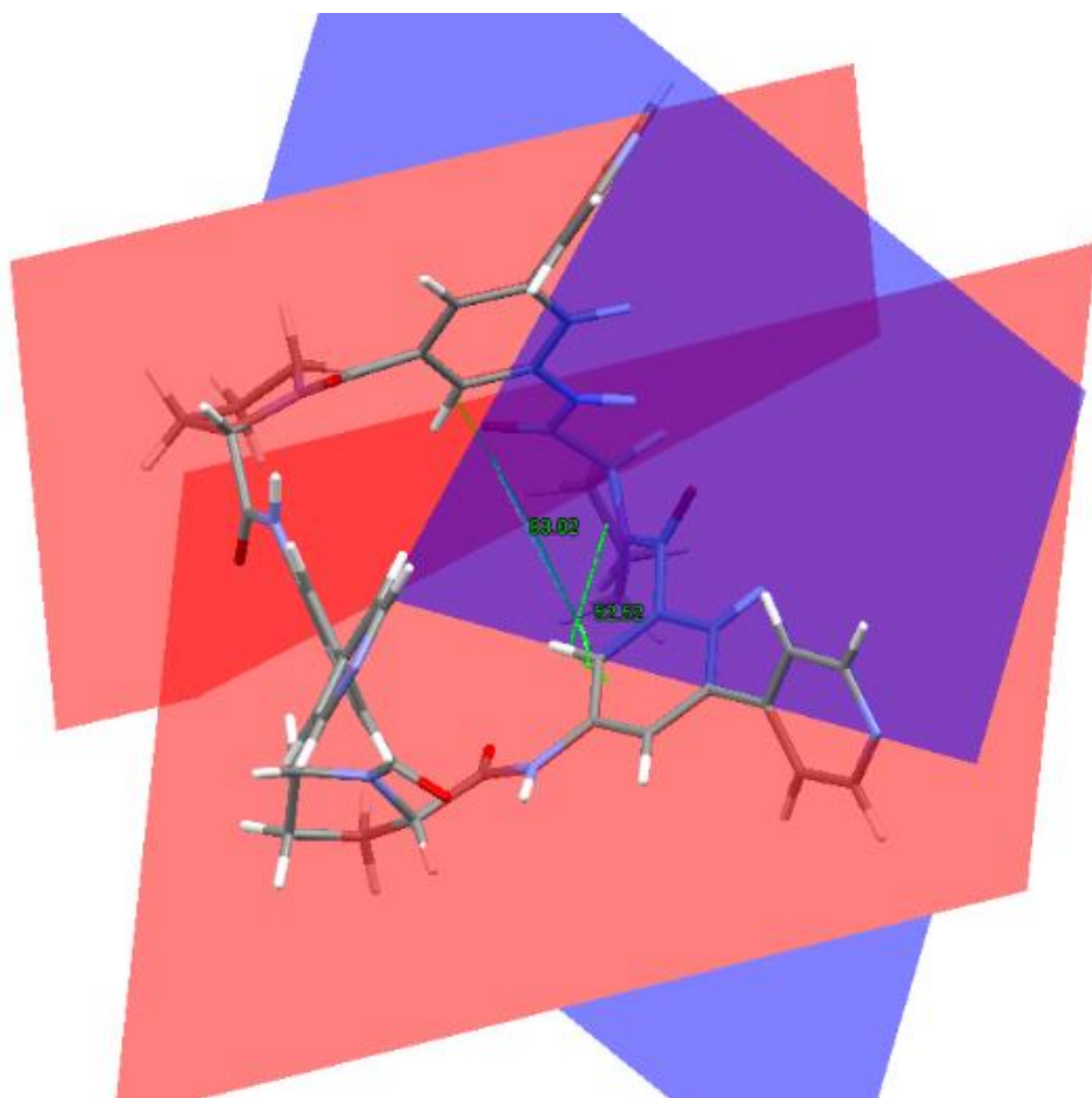


**Figure 148** Calculated structure of CP2. The mean planes created by the phenyl rings are shown in red and those created by the pyridine ring in blue. The angle between the mean planes of the phenyl rings is 83.02° and the torsion of the pyridyl subunit in relation to the phenyl ring 52.52°.

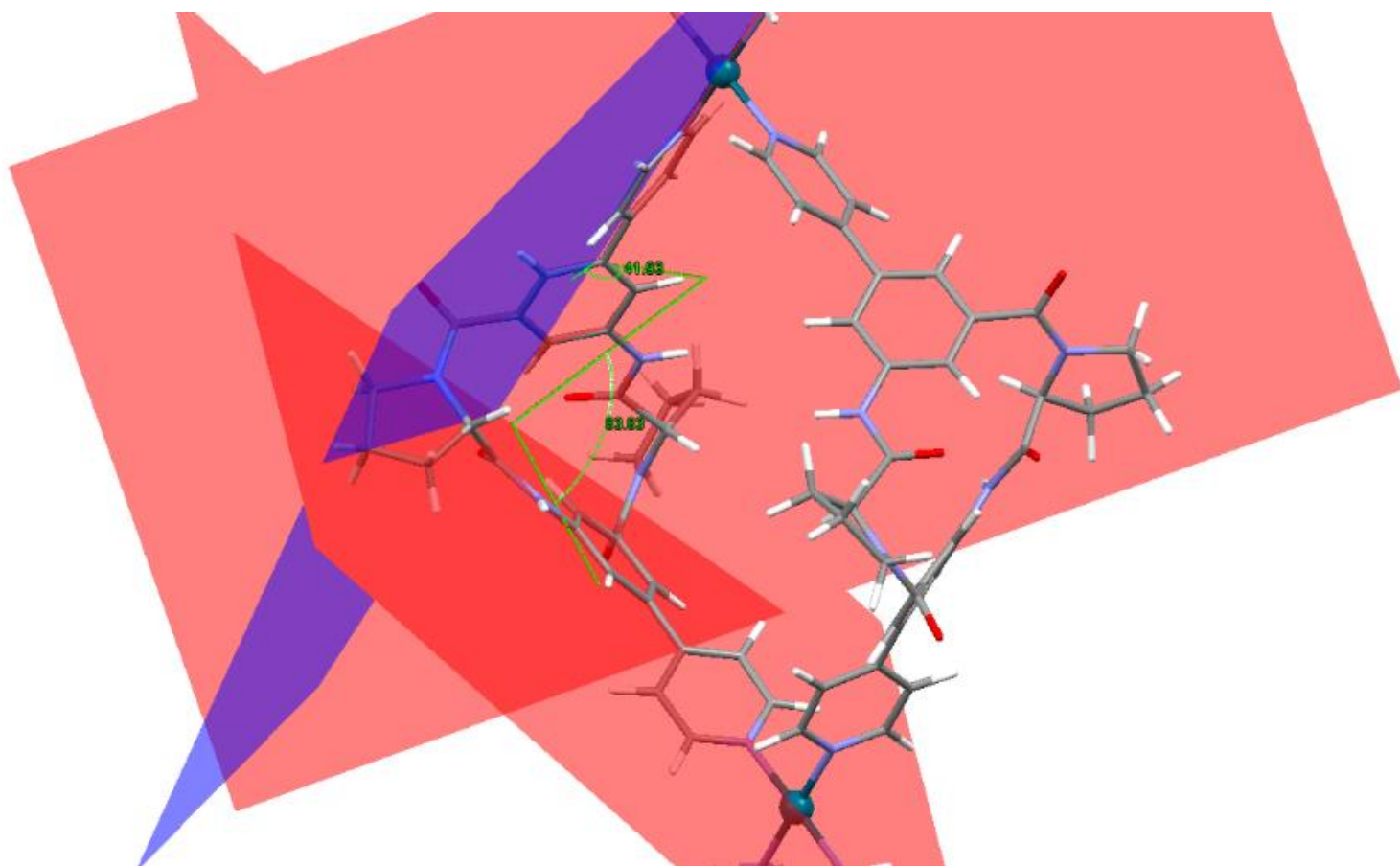


**Figure 149** Calculated structure of  $CP1_2Pd_2$ . The mean planes created by the phenyl rings are shown in red and those created by the pyridine ring in blue. The angle between the mean planes of the phenyl rings is  $83.83^\circ$  and the torsion of the pyridyl subunit in relation to the phenyl ring  $41.93^\circ$ .

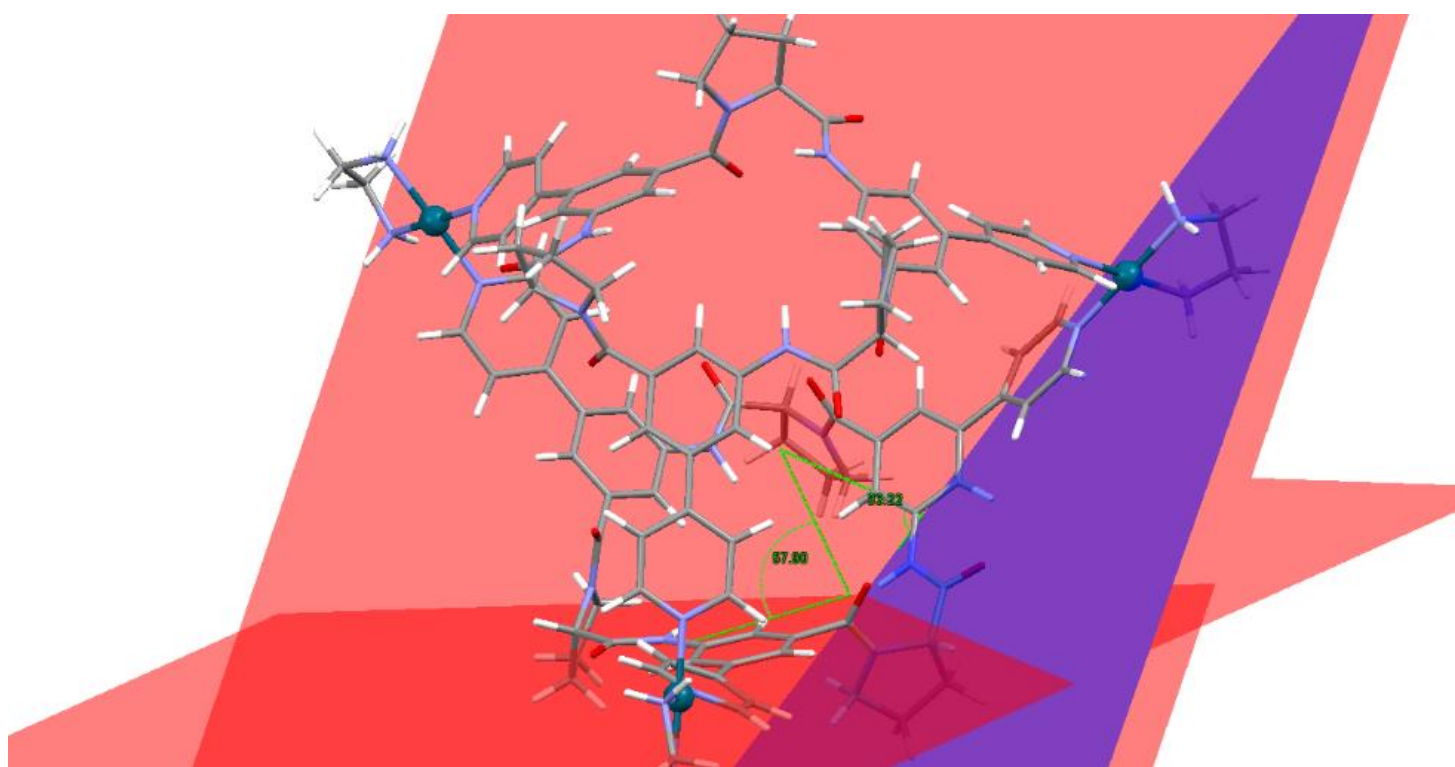


**Figure 150** Calculated structure of  $\text{CP}_2\text{Pd}_3$ . The mean planes created by the phenyl rings are shown in red and those created by the pyridine ring in blue. The angle between the mean planes of the phenyl rings is  $57.90^\circ$  and the torsion of the pyridyl subunit in relation to the phenyl ring  $33.22^\circ$ .

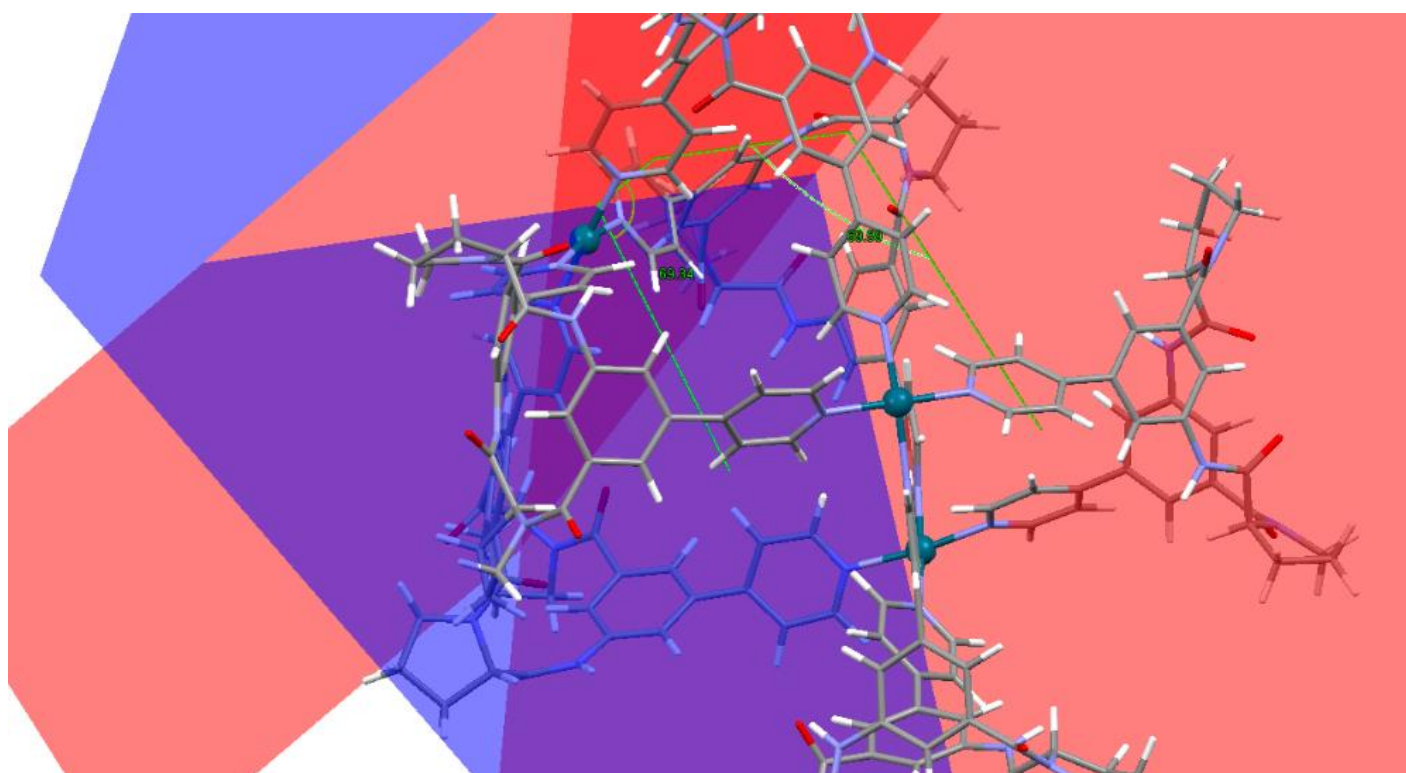


**Figure 151** Calculated structure of  $\text{CP16Pd}_3$ . The mean planes created by the phenyl rings are shown in red and those created by the pyridine ring in blue. The angle between the mean planes of the phenyl rings is  $69.59^\circ$  and the torsion of the pyridyl subunit in relation to the phenyl ring  $69.34^\circ$ .

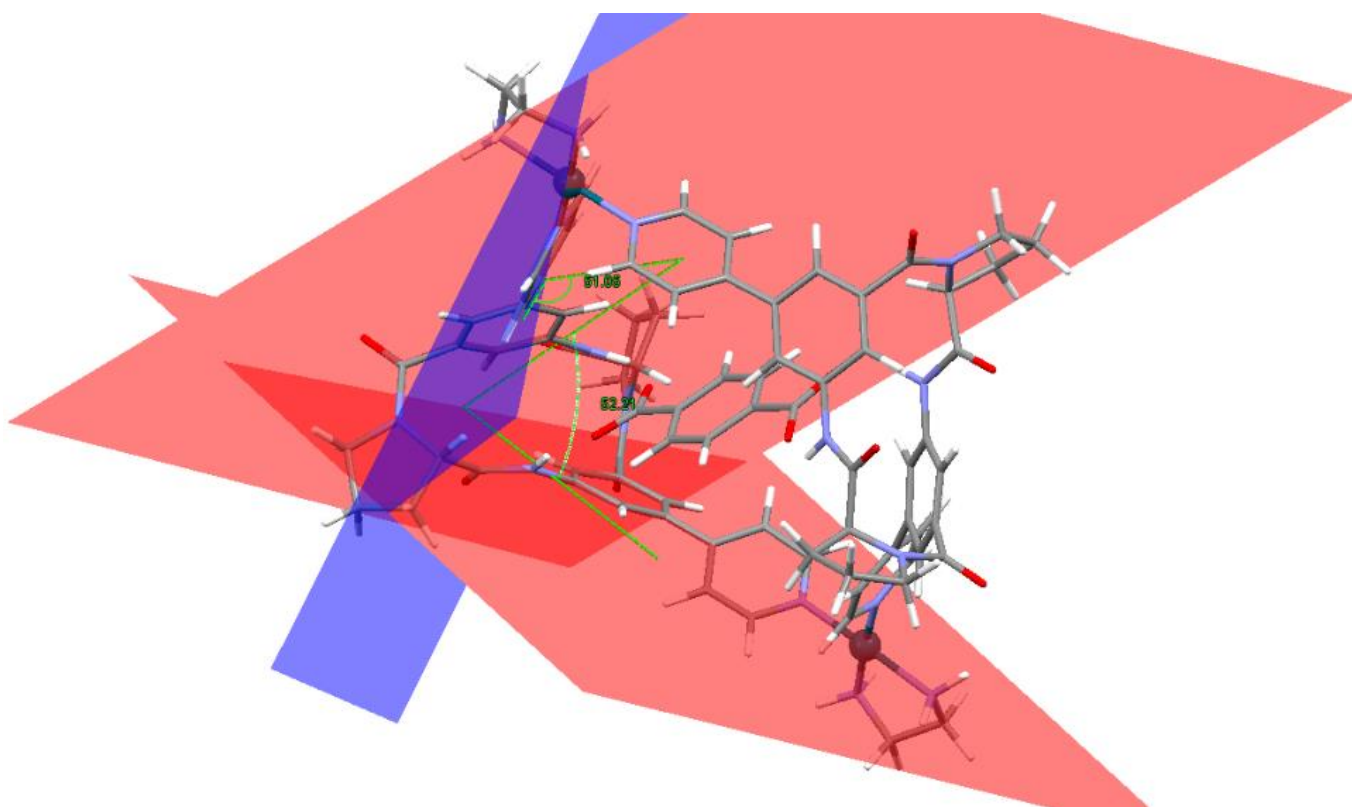


**Figure 152** Calculated structure of  $CP12Pd_2$  + terephthalate. The mean planes created by the phenyl rings are shown in red and those created by the pyridine ring in blue. The angle between the mean planes of the phenyl rings is  $52.21^\circ$  and the torsion of the pyridyl subunit in relation to the phenyl ring  $51.05^\circ$ .

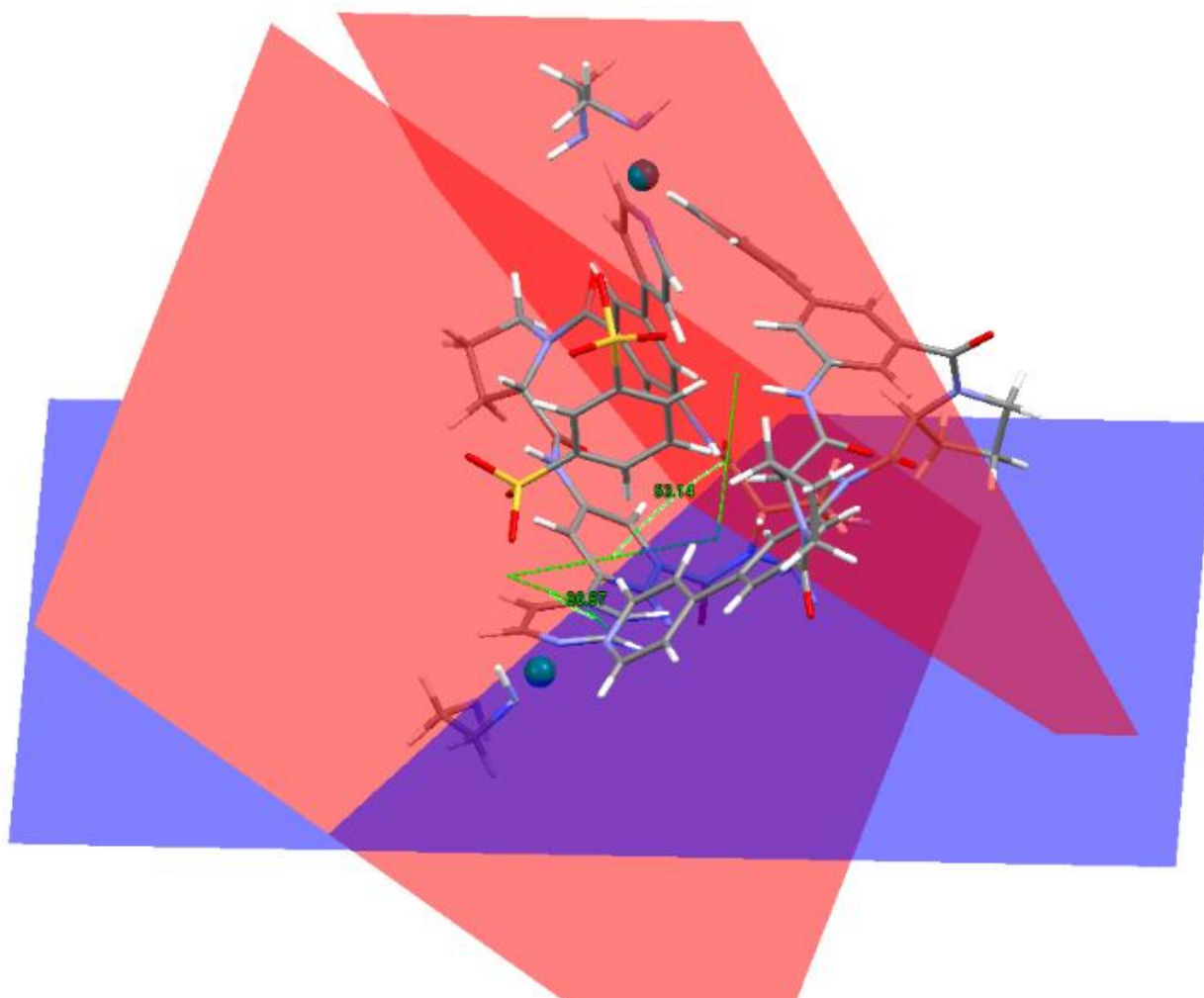


**Figure 153** Calculated structure of  $CP12Pd_2 \cdot BDS$ . The mean planes created by the phenyl rings are shown in red and those created by the pyridine ring in blue. The angle between the mean planes of the phenyl rings is  $53.14^\circ$  and the torsion of the pyridyl subunit in relation to the phenyl ring  $36.87^\circ$ .

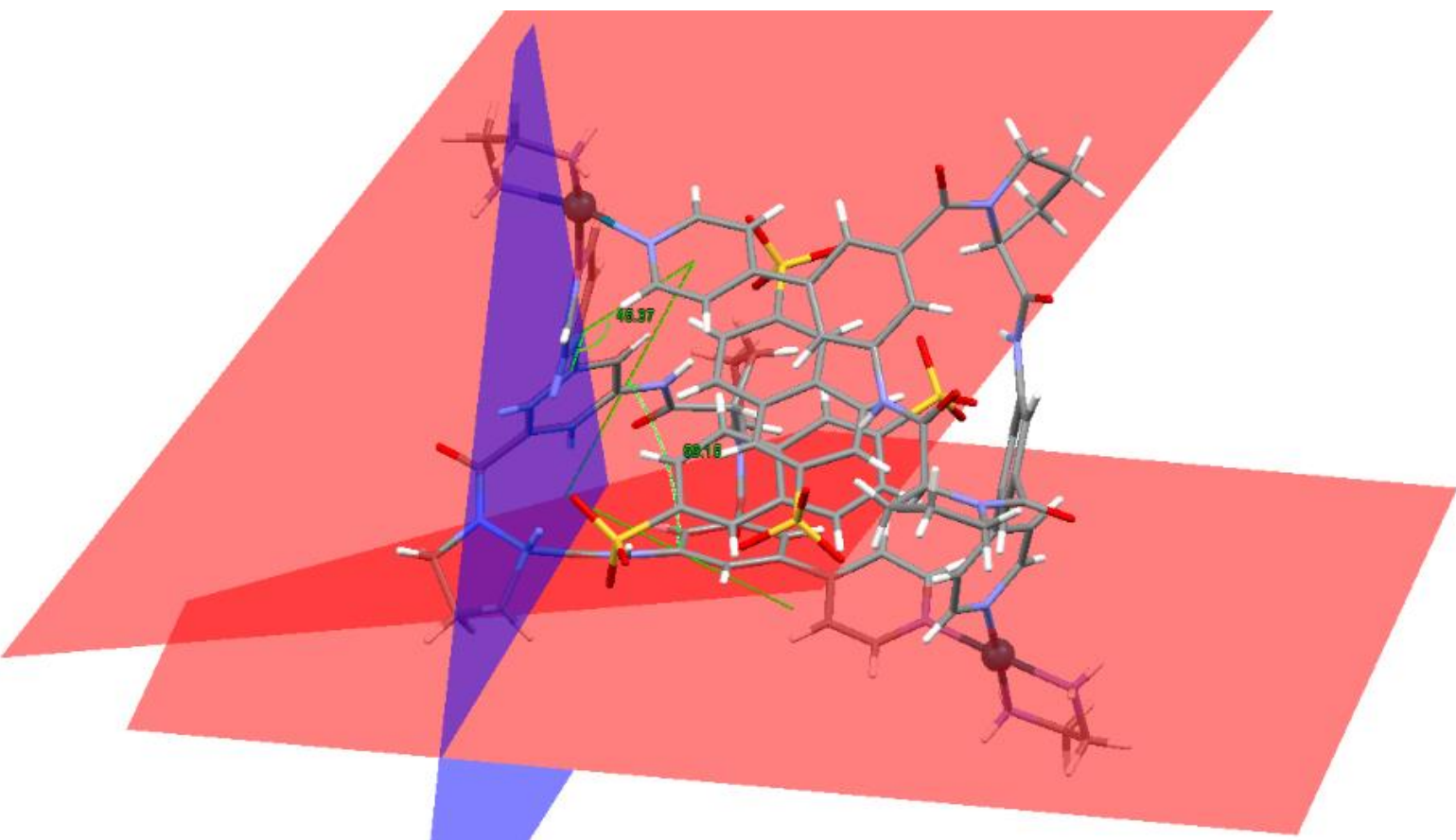


**Figure 154** Calculated structure of  $CP1_2Pd_2 \cdot 2NDS$ . The mean planes created by the phenyl rings are shown in red and those created by the pyridine ring in blue. The angle between the mean planes of the phenyl rings is  $59.12^\circ$  and the torsion of the pyridyl subunit in relation to the phenyl ring  $45.37^\circ$ .



## **Appendix II: Publication and SI**





## Palladium(II)-Mediated Assembly of a $M_2L_2$ Macrocycle and $M_3L_6$ Cage from a Cyclopeptide-Derived Ligand

Lígia M. Mesquita,<sup>†</sup> Jana Anhäuser,<sup>‡</sup> Daniel Bellaire,<sup>§</sup> Sabine Becker,<sup>⊥</sup> Arne Lützen,<sup>‡</sup> and Stefan Kubik<sup>\*,†</sup>

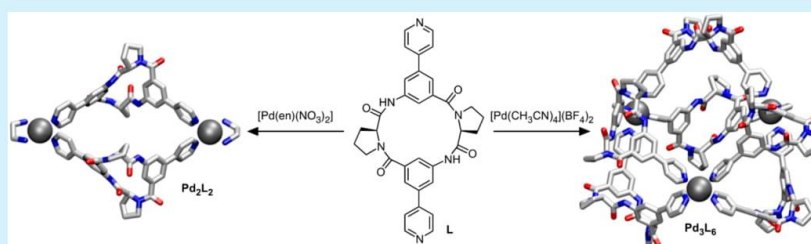
<sup>†</sup>Fachbereich Chemie - Organische Chemie, Technische Universität Kaiserslautern, Erwin-Schrödinger-Straße, 67663 Kaiserslautern, Germany

<sup>‡</sup>Kekulé-Institut für Organische Chemie und Biochemie, Rheinische Friedrich-Wilhelms-Universität Bonn, Gerhard-Domagk-Straße 1, 53121 Bonn, Germany

<sup>§</sup>Fachbereich Maschinenbau und Verfahrenstechnik - Lehrstuhl für Thermodynamik, Technische Universität Kaiserslautern, Erwin-Schrödinger-Straße, 67663 Kaiserslautern, Germany

<sup>⊥</sup>Fachbereich Chemie - Anorganische Chemie, Technische Universität Kaiserslautern, Erwin-Schrödinger-Straße, 67663 Kaiserslautern, Germany

### Supporting Information

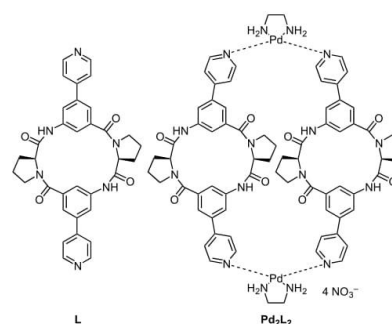


**ABSTRACT:** A cyclic tetrapeptide **L** comprising two *L*-proline and two 3-amino-5-(pyridin-4-yl)benzoic acid subunits assembles into a dimetallic metallamacrocycle  $Pd_2L_2$  and a trimetallic coordination cage  $Pd_3L_6$  in the presence of suitable palladium(II) precursors.  $Pd_2L_2$  recognizes organic anions in aqueous media, forming a particularly stable complex with sodium 2,6-naphthalenedisulfonate, in which two dianionic guest molecules reside in the cavity surrounded by the cyclopeptide ligands.

The self-assembly of appropriate ligands mediated by metal–ligand interactions allows accessing a wide variety of hollow coordination compounds with structures ranging from simple rings to complex polyhedra or other architectures.<sup>1</sup> The appeal of this approach is that the structure and composition of the products can rather reliably be predicted on the basis of a set of rules, which mainly consider the preferred coordination number and geometry of the transition metals and the number and arrangement of the Lewis basic sites in the ligands. The corresponding coordination compounds can serve as receptors,<sup>2</sup> catalysts,<sup>3</sup> or reaction chambers<sup>4</sup> or stabilize reactive species<sup>5</sup> or peptide conformations.<sup>6</sup> They are typically constructed from polyfunctional, rigid, and often aromatic ligands, although ligands derived from natural compounds have also been used.<sup>7</sup> The latter have the advantage of permitting the assembly of complexes that share structural features with natural systems, but they sometimes suffer from conformational flexibility, rendering their self-assembly less predictable than that of abiotic ligands.

We recently described the cyclic tetrapeptide **L** (Scheme 1) with two diverging pyridyl units and showed that this peptide forms two coordination polymers with  $CdCl_2$  and  $HgCl_2$ .<sup>8</sup> In these

Scheme 1



polymers, the metal ions serve as V-shaped nodes, connecting similarly V-shaped cyclopeptide rings.<sup>9</sup> The almost 90° angle between the aromatic cyclopeptide subunits is slightly larger

Received: July 6, 2019

Published: August 6, 2019

than that found in the crystal structure of the free peptide,<sup>8</sup> indicating that **L** can act as a hinge by adapting its conformation to the requirements of metal coordination. Here, we show that **L** can also serve to obtain discrete hollow coordination complexes, some of which exhibit a pronounced affinity for suitable anionic substrates in aqueous solvents.<sup>10</sup>

First, we tested the coordination of **L** to metal centers predisposed to arrange two ligands at a 90° angle. To this end, cyclopeptide **L**, prepared as described previously,<sup>8</sup> was reacted with Fujita's palladium(II) complex [Pd(en)(NO<sub>3</sub>)<sub>2</sub>].<sup>1d</sup> The reaction was performed by adding 1.1 equiv of [Pd(en)(NO<sub>3</sub>)<sub>2</sub>] in D<sub>2</sub>O/CD<sub>3</sub>OD, 1:1 (v/v), to solid **L** and treating the suspension in an ultrasound bath at 25 °C until it was clear. Because **L** is insoluble in this solvent, its dissolution in the presence of [Pd(en)(NO<sub>3</sub>)<sub>2</sub>] suggested that interactions with the metal ions occurred. The <sup>1</sup>H NMR spectrum of the resulting solution is depicted in Figure 1.

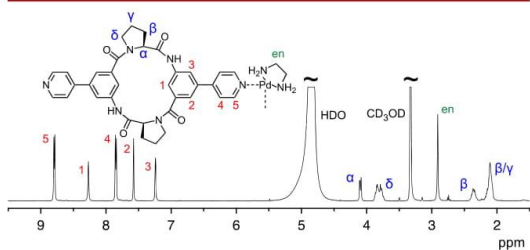


**Figure 1.** <sup>1</sup>H NMR spectrum of a 1 mM solution of **L** in D<sub>2</sub>O/CD<sub>3</sub>OD, 1:1 (v/v), containing 1.1 equiv of [Pd(en)(NO<sub>3</sub>)<sub>2</sub>].

Each set of chemically equivalent protons appears in this spectrum as one signal, indicating the formation of a symmetrical product. Successful metal coordination is usually inferred from the deshielding of the pyridyl protons,<sup>11</sup> but a reliable comparison of the <sup>1</sup>H NMR spectra of **L** prior to and after complex formation could not be made because of the insolubility of **L** in water/methanol. Information about the formation of Pd<sub>2</sub>L<sub>2</sub> could, however, be derived by ESI-TOF MS and DOSY NMR spectroscopy. In the ESI-TOF mass spectrum of the mixture of **L** and [Pd(en)(NO<sub>3</sub>)<sub>2</sub>], a peak was observed at *m/z* = 815.13, which corresponds to the ion {[L<sub>2</sub>·(Pd(en))<sub>2</sub>·(NO<sub>3</sub>)<sub>2</sub>]}<sup>2+</sup>. This peak thus confirmed the presence of Pd<sub>2</sub>L<sub>2</sub> in the solution. Other prominent peaks appeared at *m/z* ratios of 376.05, 587.21, and 669.17 (see the Supporting Information). They were assigned to protonated **L** (*m/z* calcd 587.24) and the monopalladium(II) complexes [L·Pd(en)]<sup>2+</sup> (*m/z* calcd 376.10) and [L<sub>2</sub>·Pd(en)]<sup>2+</sup> (*m/z* calcd 669.22). These ions could have been formed during ionization or the dilution of the sample prior to measuring the mass spectrum, but their presence could also indicate that the interaction between **L** and the metal is not sufficiently effective to cause Pd<sub>2</sub>L<sub>2</sub> to be the only product in the equilibrium.

In the DOSY NMR spectrum of the solution, the cyclopeptide and ethylenediamine signals appeared as a single trace, showing that the components of Pd<sub>2</sub>L<sub>2</sub> diffuse at the same rate and that they therefore belong to the same compound, also ruling out the presence of substantial amounts of mononuclear complexes in solution (see the Supporting Information). The diffusion coefficient (*D* = (1.103 ± 0.019) × 10<sup>-10</sup> m<sup>2</sup> s<sup>-1</sup>) corresponds to a hydrodynamic diameter of 22.9 ± 0.4 Å according to the Stokes–Einstein equation. Unfortunately, attempts to crystallize

Pd<sub>2</sub>L<sub>2</sub> from solutions of **L** and [Pd(en)(NO<sub>3</sub>)<sub>2</sub>] failed, only yielding crystals of the free cyclopeptide that, according to X-ray crystallography, adopts a conformation similar to the one previously reported (see the Supporting Information).<sup>8</sup>

Preliminary information about the structure of Pd<sub>2</sub>L<sub>2</sub> was therefore obtained from calculations, which were based on the crystal structure of **L**. The results are shown in Figure 2.

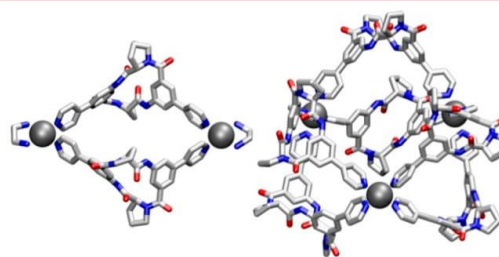


**Figure 2.** Calculated structures of Pd<sub>2</sub>L<sub>2</sub> (left) and Pd<sub>3</sub>L<sub>6</sub> (right). The geometry optimizations were performed at the semiempirical PM6 level as implemented in Spartan 18, Wavefunction Inc. Hydrogen atoms are omitted for clarity.

Figure 2 shows that Pd<sub>2</sub>L<sub>2</sub> is D<sub>2</sub> symmetric, consistent with its simple <sup>1</sup>H NMR spectrum. The main difference between the cyclopeptide conformation in Pd<sub>2</sub>L<sub>2</sub> and in the crystal structure of **L** is the larger angle between the aromatic subunits that amounts to 98.4° instead of 54.5°. **L** is therefore not optimally preorganized for palladium coordination, but the strain in Pd<sub>2</sub>L<sub>2</sub> is likely small as related cyclopeptides have been shown to adopt conformations with varying arrangements of the aromatic subunits.<sup>12</sup> The average diameter of this structure amounts to 25.0 Å when considering the van der Waals radii of hydrogen atoms (see the Supporting Information). Because of the oblong shape of the complex and the fact that its structure was calculated in the gas phase, one cannot expect this diameter to exactly match the one calculated on the basis of the Stokes–Einstein equation, but the agreement is likely reasonable (see the Supporting Information).<sup>13</sup> Taken together, the NMR and mass spectrometric results show that the treatment of **L** with [Pd(en)(NO<sub>3</sub>)<sub>2</sub>] yielded the metallamacrocycle Pd<sub>2</sub>L<sub>2</sub>.

We then investigated whether the cavity of this metallacycle is available for guest binding. As dicarboxylates had previously been shown to interact with some of Fujita's coordination compounds,<sup>2</sup> we initially focused on this substrate class. Complex formation was qualitatively investigated by comparing the NMR spectra of various sodium dicarboxylates in D<sub>2</sub>O/CD<sub>3</sub>OD, 1:1 (v/v), in the absence and in the presence of Pd<sub>2</sub>L<sub>2</sub>. The dicarboxylates were derived from terephthalic acid, isophthalic acid, diphenic acid, 2,6-naphthalene dicarboxylic acid, adipic acid, and glutaric acid. In all spectra, the presence of Pd<sub>2</sub>L<sub>2</sub> caused a pronounced upfield shift of the guest signals (see the Supporting Information), indicating that an interaction took place. The direction of the shifts suggested the incorporation of the dicarboxylates into the Pd<sub>2</sub>L<sub>2</sub> cavity, where they experienced the shielding of the surrounding aromatic rings. Unfortunately, we did not succeed in quantifying the stabilities of these complexes because the buffers used in the respective NMR titrations to ensure constant pH either prevented complex formation (carbonate) or caused the decomposition of Pd<sub>2</sub>L<sub>2</sub> (borate).

We therefore turned our attention to disulfonates as guests, which are fully deprotonated at neutral pH, eliminating the need to use buffers. Figure 3 shows the  $^1\text{H}$  NMR spectra of sodium

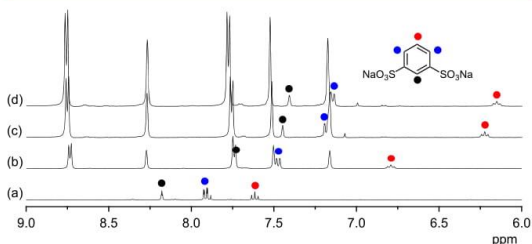


**Figure 3.**  $^1\text{H}$  NMR spectra of BDS (0.5 mM) in  $\text{D}_2\text{O}/\text{CD}_3\text{OD}$ , 1:1 (v/v), in the absence (a) and in the presence of 0.6 (b), 1.2 (c), and 1.8 (d) equiv of  $\text{Pd}_2\text{L}_2$  (the filled circles mark the signals of the guest).

1,3-benzenedisulfonate (BDS) in the presence of 0.6, 1.2, and 1.8 equiv of  $\text{Pd}_2\text{L}_2$  in  $\text{D}_2\text{O}/\text{CD}_3\text{OD}$ , 1:1 (v/v). These spectra show that the presence of  $\text{Pd}_2\text{L}_2$  caused a substantial upfield shift of the guest protons. As only a single set of averaged signals was observed for host and guest, complex formation was fast on the NMR time scale.

The ESI-TOF MS spectrum of an equimolar mixture of  $\text{Pd}_2\text{L}_2$  and BDS contained a single peak at  $m/z = 871.20$  (see the Supporting Information), which corresponds to the doubly charged complex of  $\text{Pd}_2\text{L}_2$  with one BDS molecule ( $m/z$  calcd 871.18), showing that the 1:1 complex was the dominant species (although the formation of an invisible neutral 1:2 complex could not be excluded). We performed an NMR titration during which increasing amounts of  $\text{Pd}_2\text{L}_2$  were added to a solution of BDS, and the shifts of the guest signals were followed. The resulting binding isotherm, evaluated by assuming a 1:1 stoichiometry, afforded a  $\log K_a$  of  $4.8 \pm 0.2$ , showing that the complex had a considerable stability in the aqueous solvent mixture.

When subsequently using sodium 2,6-naphthalenedisulfonate (NDS) as guest, a different picture emerged. The outcome of the NMR spectroscopic binding study during which increasing amounts of NDS were added to a solution of  $\text{Pd}_2\text{L}_2$  is shown in Figure 4. This figure shows that the presence of NDS caused the appearance of a new set of signals in the  $^1\text{H}$  NMR spectrum that progressively became more pronounced as the amount of the disulfonate increased. The signals of  $\text{Pd}_2\text{L}_2$  concomitantly became less intensive until they disappeared at an NDS/ $\text{Pd}_2\text{L}_2$

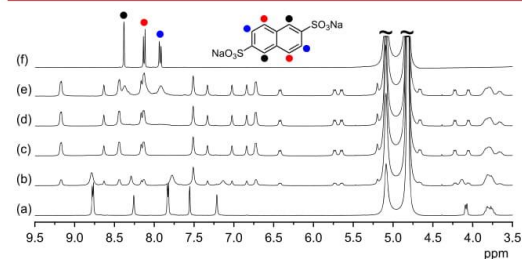


**Figure 4.**  $^1\text{H}$  NMR spectra of  $\text{Pd}_2\text{L}_2$  (1 mM) in  $\text{D}_2\text{O}/\text{CD}_3\text{OD}$ , 1:1 (v/v), in the absence (a) and in the presence of 1.0 (b), 2.0 (c), 3.0 (d), and 5.0 (e) equiv of NDS. Trace (f) shows the NDS spectrum.

ratio of 2:1. Further addition of NDS caused the appearance of the signals of the free guest. The equilibrium of NDS binding was therefore slow on the NMR time scale and likely involved the complexation of two NDS molecules. All signals of  $\text{Pd}_2\text{L}_2$  and NDS moreover split upon complex formation, indicating that the complex had a lower symmetry than  $\text{Pd}_2\text{L}_2$  alone. DOSY NMR spectroscopy demonstrated that the signals derived from  $\text{Pd}_2\text{L}_2$  and those of NDS were part of a single species with a diffusion coefficient  $D$  of  $(1.261 \pm 0.061) \times 10^{-10} \text{ m}^2 \text{ s}^{-1}$  and a corresponding hydrodynamic diameter of  $20.0 \pm 0.9 \text{ \AA}$  (see the Supporting Information). In the ESI-TOF mass spectrum, no signals of a complex species could be observed, likely because the binding of two molecules of NDS to  $\text{Pd}_2\text{L}_2$  afforded a neutral complex.

The signals in the NMR spectrum of the complex could be assigned by using 2D NMR techniques, demonstrating that some of the guest signals experienced pronounced upfield shifts upon complex formation of almost 4 ppm. Unfortunately, mainly exchange peaks were observed in the NOESY and ROESY NMR spectra, but there were no intermolecular cross-peaks between signals of  $\text{Pd}_2\text{L}_2$  and NDS, which would have provided information about the solution structure of the complex (see the Supporting Information). Insight into the structural aspects of NDS complexation could, fortunately, be obtained from the crystal structure of the complex, which is shown in Figure 5.

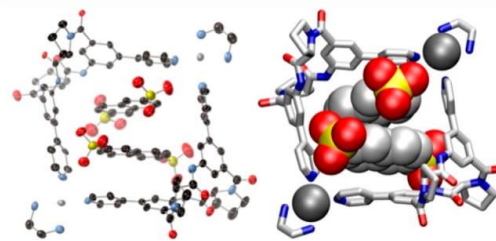


**Figure 5.** Molecular structure of  $\text{Pd}_2\text{L}_2 \cdot 2 \text{ NDS}$ . Hydrogen atoms are omitted for clarity. Thermal ellipsoids on the left structure are set at 50% probability.

This structure confirmed the expected complex composition, involving two molecules of NDS included in the cavity of  $\text{Pd}_2\text{L}_2$ . The structure of the metallamacrocycle alone is similar to the calculated one shown in Figure 2, but the complex is overall  $C_2$  symmetric as a consequence of the arrangement of the two NDS molecules. The pyridyl units facing the edges of the included guests thus have a different environment than those aligned along the faces, explaining the signal splitting in the NMR spectrum. Both guest molecules are arranged in a parallel fashion, with some protons residing within the clefts produced by the aromatic units along the cyclopeptide rings, explaining the considerable shielding in the NMR. The sulfonate groups of the guests are arranged in close proximity, but their Coulomb repulsion is obviously compensated by the sum of the interactions stabilizing the complex, including the attractive electrostatic interactions with the metal centers. NDS binding leads to a slight contraction of  $\text{Pd}_2\text{L}_2$ , with the average diameter amounting to 24.1  $\text{\AA}$  (see the Supporting Information), which could explain the increase of the diffusion coefficient upon complex formation. The structure of this complex is somewhat reminiscent of a previously described dipalladium(II) metal-

lamacrocycle derived from 4,4'-bipyridinium ligands with two included 1,5-dihydroxynaphthalene molecules with the exception that (i) the  $\text{Pd}_2\text{L}_2$  complex is chiral due to the two cyclopeptide units, (ii) the NDS guests are both negatively charged, and (iii) the  $\text{Pd}_2\text{L}_2$  is a tetracation whereas the bipyridinium derived complex has eight positive charges, demonstrating the strong mutual stabilization of the eight components in the NDS complex of  $\text{Pd}_2\text{L}_2$ .<sup>14</sup> Because of this mutual stabilization, the formation of the NDS complex of  $\text{Pd}_2\text{L}_2$  is likely cooperative with the binding constant related to the binding of the second NDS molecule being larger than the one associated with the formation of the 1:1 complex. Moreover, the complex is rather stable as reflected in the fact that the equilibrium is slow on the NMR time scale and that complex formation is complete once the required 2 equiv of the guest is present. The complexity of the binding equilibrium, involving two stability constants, and the high stability of the complex unfortunately prevented the quantitative assessment of complex stability from the NMR titration, which is why we focused in this study on the structural characterization of the complex.

We also tested whether larger coordination cages are accessible by coordination of **L** to other palladium(II) salts.<sup>1f</sup> In this context, **L** was reacted with  $[\text{Pd}(\text{CH}_3\text{CN})_4](\text{BF}_4)_2$  for 4 h at 60 °C in DMSO-*d*<sub>6</sub>. The <sup>1</sup>H NMR spectrum of the resulting solution differed profoundly from the spectrum of **L** in the same solvent prior to the addition of the metal salt, suggesting that metal coordination had taken place (see the Supporting Information), consistent also with the upfield shifts of signals in the aromatic region of the spectrum. The complexity of the resulting spectrum indicated the presence of a mixture of species with a prominent product exhibiting a set of characteristic peaks. DOSY NMR spectroscopy confirmed that this product represented a single species with a diffusion coefficient *D* of  $(0.733 \pm 0.067) \times 10^{-10} \text{ m}^2 \text{ s}^{-1}$ , corresponding to a hydrodynamic diameter of  $27.2 \pm 2.5 \text{ \AA}$  (see the Supporting Information). In the ESI mass spectrum, peaks were visible at *m/z* ratios of 1003.03 and 1366.40 (see the Supporting Information) that could be assigned to the ions of a coordination cage  $\text{Pd}_3\text{L}_6$  with two (*m/z* calcd 1003.03) and three  $\text{BF}_4^-$  counterions (calcd *m/z* 1366.40). The calculated structure of this *D*<sub>3</sub> symmetric cage is depicted in Figure 2. In this structure, pairwise equivalent subunits of **L** have different environments, explaining the complex signal pattern in the <sup>1</sup>H NMR spectrum. The average diameter of  $\text{Pd}_3\text{L}_6$  (see the Supporting Information) was estimated to amount to 28.3 Å, which is in good agreement with the experimental one. Hence, also larger coordination compounds can be generated by using **L**.

Appropriately designed cyclopeptides can therefore serve as ligands for the generation of chiral hollow coordination compounds, the structure and composition of which can be controlled by the nature of the metal nodes. Such complexes feature functional groups along their surfaces that can induce interesting receptor properties. In the example presented here, the Coulomb repulsion between two simultaneously bound dianions was compensated, for example, by a combination of electrostatic, aromatic, and hydrogen bonding interactions between the metallacycle and the guests. We are currently exploring whether this concept could be extended to other molecular architectures by using larger cyclopeptides.

## ■ ASSOCIATED CONTENT

### Supporting Information

The Supporting Information is available free of charge on the ACS Publications website at DOI: 10.1021/acs.orglett.9b02338.

Details about the synthesis and characterization of  $\text{Pd}_2\text{L}_2$  and  $\text{Pd}_3\text{L}_6$ , results of the qualitative and quantitative binding studies (PDF)

### Accession Codes

CCDC 1922090–1922091 contain the supplementary crystallographic data for this paper. These data can be obtained free of charge via [www.ccdc.cam.ac.uk/data\\_request/cif](http://www.ccdc.cam.ac.uk/data_request/cif), or by emailing [data\\_request@ccdc.cam.ac.uk](mailto:data_request@ccdc.cam.ac.uk), or by contacting The Cambridge Crystallographic Data Centre, 12 Union Road, Cambridge CB2 1EZ, UK; fax: +44 1223 336033.

## ■ AUTHOR INFORMATION

### Corresponding Author

\*E-mail: [kubik@chemie.uni-kl.de](mailto:kubik@chemie.uni-kl.de).

### ORCID

Arne Lützen: 0000-0003-4429-0823

Stefan Kubik: 0000-0003-0526-7014

### Notes

The authors declare no competing financial interest.

## ■ ACKNOWLEDGMENTS

The funding of this work from the European Union's Horizon 2020 research and innovation programme under the Marie Skłodowska-Curie Grant Agreement No. 642192 is gratefully acknowledged. We also thank S. Schindler and J. Becker, Justus-Liebig-University, for providing assistance with the crystal measurement, and H. Hasse, University of Kaiserslautern, for providing the NMR equipment for the DOSY NMR measurements.

## ■ REFERENCES

- (1) (a) Stang, P. J.; Olenyuk, B. Self-assembly, symmetry, and molecular architecture: coordination as the motif in the rational design of supramolecular metallacyclic polygons and polyhedra. *Acc. Chem. Res.* **1997**, *30*, 502–518. (b) Leininger, S.; Olenyuk, B.; Stang, P. J. Self-assembly of discrete cyclic nanostructures mediated by transition metals. *Chem. Rev.* **2000**, *100*, 853–908. (c) Seidel, S. R.; Stang, P. J. High-symmetry coordination cages via self-assembly. *Acc. Chem. Res.* **2002**, *35*, 972–983. (d) Fujita, M.; Tominaga, M.; Hori, A.; Therrien, B. Coordination assemblies from a Pd(II)-cornered square complex. *Acc. Chem. Res.* **2005**, *38*, 369–378. (e) Ronson, T. K.; Zarra, S.; Black, S. P.; Nitschke, J. R. Metal–organic container molecules through subcomponent self-assembly. *Chem. Commun.* **2013**, *49*, 2476–2490. (f) Harris, K.; Fujita, D.; Fujita, M. Giant hollow  $M_nL_{2n}$  spherical complexes: structure, functionalisation and applications. *Chem. Commun.* **2013**, *49*, 6703–6712. (g) Han, M.; Engelhard, D. M.; Clever, G. H. Self-assembled coordination cages based on banana-shaped ligands. *Chem. Soc. Rev.* **2014**, *43*, 1848–1860. (h) Cook, T. R.; Stang, P. J. Recent developments in the preparation and chemistry of metallacycles and metallacages via coordination. *Chem. Rev.* **2015**, *115*, 7001–7045. (i) McConnell, A. J.; Wood, C. S.; Neelakandan, P. P.; Nitschke, J. R. Stimuli-responsive metal-ligand assemblies. *Chem. Rev.* **2015**, *115*, 7729–7793. (j) Chen, L.-J.; Yang, B.-H.; Shionoya, M. Chiral metallosupramolecular architectures. *Chem. Soc. Rev.* **2017**, *46*, 2555–2576. (k) Zhang, D.; Ronson, T. K.; Nitschke, J. R. Functional capsules via subcomponent self-assembly. *Acc. Chem. Res.* **2018**, *51*, 2423–2436.

- (2) Fujita, M. Metal-directed self-assembly of two- and three-dimensional synthetic receptors. *Chem. Soc. Rev.* **1998**, *27*, 417–425.
- (3) Pluth, M. D.; Bergman, R. G.; Raymond, K. N. Proton-mediated chemistry and catalysis in a self-assembled supramolecular host. *Acc. Chem. Res.* **2009**, *42*, 1650–1659.
- (4) Yoshizawa, M.; Klosterman, J. K.; Fujita, M. Functional molecular flasks: new properties and reactions within discrete, self-assembled hosts. *Angew. Chem., Int. Ed.* **2009**, *48*, 3418–3438.
- (5) Breiner, B.; Clegg, J. K.; Nitschke, J. R. Reactivity modulation in container molecules. *Chem. Sci.* **2011**, *2*, 51–56.
- (6) Tashiro, S.; Tominaga, M.; Yamaguchi, Y.; Kato, K.; Fujita, M. Folding a de novo designed peptide into an  $\alpha$ -helix through hydrophobic binding by a bowl-shaped host. *Angew. Chem., Int. Ed.* **2006**, *45*, 241–244.
- (7) (a) Albrecht, M.; Stortz, P. Metallacyclopeptides: artificial analogues of naturally occurring peptides. *Chem. Soc. Rev.* **2005**, *34*, 496–506. (b) Kiehne, U.; Lützen, A. Diastereoselective self-assembly of double- and triple-stranded helicates from a D-isomannide derivative. *Org. Lett.* **2007**, *9*, 5333–5336. (c) Zou, R.; Wang, Q.; Wu, J.; Wu, J.; Schmuck, C.; Tian, H. Peptide self-assembly triggered by metal ions. *Chem. Soc. Rev.* **2015**, *44*, 5200–5219.
- (8) Ganß, A.; Xu, C.; Guenet, A.; Kelm, H.; Kyritsakas, N.; Planeix, J.-M.; Kubik, S.; Hosseini, M. W. Molecular tectonics: homochiral coordination polymers based on pyridyl-substituted cyclic tetrapeptides. *CrystEngComm* **2016**, *18*, 7685–7689.
- (9) For another example of a cyclopeptide-derived coordination polymer, see: (a) Chakraborty, S.; Tyagi, P.; Tai, D.-F.; Lee, G.-H.; Peng, S.-M. A lead(II) 3D coordination polymer based on a marine cyclic peptide motif. *Molecules* **2013**, *18*, 4972–4985.
- (10) For examples of cyclopeptide-derived coordination complexes, see: (a) Wipf, P.; Wang, C. Synthesis and Ag(I) complexation studies of tethered westiellamide. *Org. Lett.* **2006**, *8*, 2381–2384. (b) Fujimura, F.; Kimura, S. Columnar assembly formation and metal binding of cyclic tri- $\beta$ -peptides having terpyridine ligands. *Org. Lett.* **2007**, *9*, 793–796. (c) Dong, Y.; Loong, D. T. J.; Yuen, A. K. L.; Black, R. J.; O'Malley, S.; Clegg, J. K.; Lindoy, L. F.; Jolliffe, K. A. Molecular capsules and coordination polymers from a backbone-modified cyclic peptide bearing pyridyl arms. *Supramol. Chem.* **2012**, *24*, 508–519. (d) Panciera, M.; Amorín, M.; Castedo, L.; Granja, J. R. Design of stable  $\beta$ -sheet-based cyclic peptide assemblies assisted by metal coordination: selective homo- and heterodimer formation. *Chem. - Eur. J.* **2013**, *19*, 4826–4834.
- (11) Fujita, M.; Yazaki, J.; Ogura, K. Preparation of a macrocyclic polynuclear complex,  $[(en)Pd(4,4'-bpy)]_4(NO_3)_8$ , which recognizes an organic molecule in aqueous media. *J. Am. Chem. Soc.* **1990**, *112*, 5645–5647.
- (12) Pohl, S.; Goddard, R.; Kubik, S. A new cyclic tetrapeptide composed of L-proline and 3-aminobenzoic acid subunits. *Tetrahedron Lett.* **2001**, *42*, 7555–7558.
- (13) Macchioni, A.; Ciancaleoni, G.; Zuccaccia, C.; Zuccaccia, D. Determining accurate molecular sizes in solution through NMR diffusion spectroscopy. *Chem. Soc. Rev.* **2008**, *37*, 479–489.
- (14) Blanco, V.; Chas, M.; Abella, D.; Pia, E.; Platas-Iglesias, C.; Peinador, C.; Quintela, J. M. Self-Assembly of 1:2 inclusion complexes between a metallocycle host and dihydroxyaromatic guests: a redox controlled complexation process. *Org. Lett.* **2008**, *10*, 409–412.

**Palladium(II)-Mediated Assembly of a  $M_2L_2$  Macrocycle and  $M_3L_6$  Cage from a  
Cyclopeptide-Derived Ligand**

Lígia M. Mesquita,<sup>#</sup> Jana Anhäuser,<sup>†</sup> Daniel Bellaire,<sup>§</sup> Sabine Becker,<sup>‡</sup>

Arne Lützen,<sup>†</sup> Stefan Kubik<sup>\*,#</sup>

<sup>#</sup> *Fachbereich Chemie - Organische Chemie, Technische Universität Kaiserslautern, Erwin-Schrödinger-Straße, 67663 Kaiserslautern, Germany.*

<sup>†</sup> *Rheinische Friedrich-Wilhelms-Universität Bonn, Kekulé-Institut für Organische Chemie und Biochemie, Gerhard-Domagk-Straße 1, 53121 Bonn, Germany.*

<sup>§</sup> *Fachbereich Maschinenbau und Verfahrenstechnik - Lehrstuhl für Thermodynamik, Technische Universität Kaiserslautern, Erwin-Schrödinger-Straße, 67663 Kaiserslautern, Germany.*

<sup>‡</sup> *Fachbereich Chemie - Anorganische Chemie, Technische Universität Kaiserslautern, Erwin-Schrödinger-Straße, 67663 Kaiserslautern, Germany.*

**CONTENT**

Synthetic Procedures.....	S2
NMR and MS Spectra of <b>L</b> .....	S6
NMR and MS Spectra of <b>Pd<sub>2</sub>L<sub>2</sub></b> .....	S9
NMR and MS Spectra of <b>Pd<sub>3</sub>L<sub>6</sub></b> .....	S14
Dicarboxylate Binding to <b>Pd<sub>2</sub>L<sub>2</sub></b> (Qualitative Binding Studies).....	S20
Sodium 1,3-Benzenedisulfonate Binding to <b>Pd<sub>2</sub>L<sub>2</sub></b> .....	S22
Sodium 2,6-Naphthalenedisulfonate Binding to <b>Pd<sub>2</sub>L<sub>2</sub></b> .....	S25
NMR Spectra of the 2,6-Naphthalenedisulfonate Complex of <b>Pd<sub>2</sub>L<sub>2</sub></b> .....	S27
X-Ray Data Collection and Refinement.....	S31
References.....	S37



## Synthetic Procedures

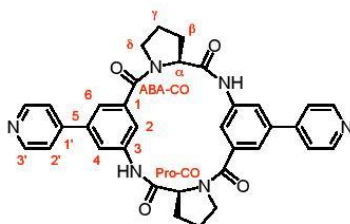
**General details.** Analyses were carried out as follows: melting points, Müller SPM-X 300; NMR, Bruker AVANCE III 400 and 600 (peak assignments were confirmed by using H,H-COSY, HMQC, and HMBC spectra; spectra were referenced to the residual solvent signals (DMSO- $d_6$ :  $\delta^H = 2.50$  ppm,  $\delta^C = 39.52$  ppm; CD<sub>3</sub>OD:  $\delta^H = 3.31$  ppm,  $\delta^C = 49.00$  ppm);<sup>1</sup> MALDI TOF-MS, BrukerUltraflex TOF/TOF; ESI MS, these measurements were performed by using a Paul-type quadrupole ion trap instrument (AmaZonETD, Bruker Daltonics) or an Orbitrap XL (Thermo Fisher Scientific), HR-ESI(+) MS were recorded from DMSO solutions, Res 30000, 7  $\mu$ L DMSO solution injected via autosampler (operated with acetonitrile) using standard ESI conditions; elemental analysis, Elementar vario Micro cube. The following abbreviations are used: ABA, 3-aminobenzoic acid; BDS, 1,3-benzenedisulfonate; NDS, 2,6-naphthalenedisulfonate; Pro, L-proline.

**DOSY NMR Spectroscopy.** The DOSY NMR measurements were performed by using a Bruker Avance III HD 400 spectrometer with a superconducting magnet (Bruker Ascend 400) of magnetic field strength of 9.4 T, corresponding to a proton Larmor frequency of 400.25 MHz. The spectrometer was equipped with a probe head with cryogenically cooled electronics (CryoProbe Prodigy, Bruker Biospin, Germany). The temperature control was calibrated with a platinum resistance thermometer (Pt-100, uncertainty estimated to be  $\pm 0.15$  K) which itself was previously calibrated using a certified standard. Measurements were conducted at a constant temperature of 298 K. The used pulse sequence consisted of a stimulated echo with bipolar gradients and one spoil gradient as implemented in the spectrometer's software (Bruker TopSpin 3.2, pulse sequence: *stebpgp1s*). The diffusion measurements were calibrated on the spectrometer by using water. The parameters of the measurements (gradient pulse length  $\delta$ , number of scans, diffusion transients) were varied in order to fit the respective sample and to produce similar signal-to-noise ratios. The diffusion time big delta ( $\Delta$ ) was kept at 50.0 ms.

The DOSY NMR spectra were processed with DOSY Toolbox, University of Manchester.<sup>2</sup> The diffusion coefficients were calculated by using the Stokes-Einstein equation  $D = k T / 6 \pi \eta r_H$  where  $k$  is the Boltzmann constant,  $T$  is the temperature (298 K),  $\eta$  is the viscosity of the solvent,  $D$  is the

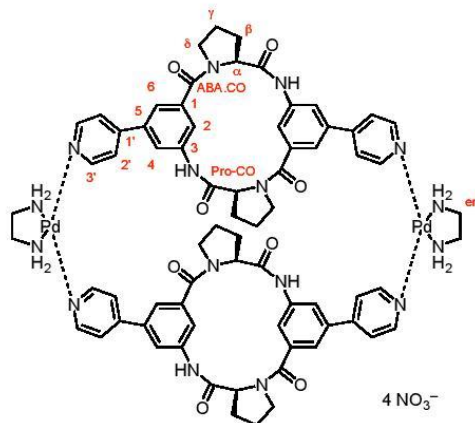
diffusion coefficient, and  $r_H$  is the hydrodynamic radius, assuming a hard spherical shape and infinite dilution. The hydrodynamic diameter  $d_H$  is thus twice  $r_H$ . The viscosity  $\eta$  of CD<sub>3</sub>OD/D<sub>2</sub>O, 1:1 (v/v) was estimated to amount to 0.00173 N s m<sup>-2</sup> by using a procedure described in the literature.<sup>3,4</sup> For DMSO-*d*<sub>6</sub>, a viscosity of 0.00219 N s m<sup>-2</sup> was used.<sup>3</sup> Note that the structure of **PdL<sub>2</sub>** deviates considerably from the spherical shape that was assumed in the estimation of the hydrodynamic diameter.<sup>5</sup>

**Cyclopeptide L.** The ligand **L** was isolated as a colorless solid according to the previously described procedure in typical amounts of 120 mg (0.2 mmol).<sup>6</sup> <sup>1</sup>H NMR (600 MHz, DMSO-*d*<sub>6</sub>, 22 °C)  $\delta$  9.55 (s, 2H, NH), 8.65-8.64 (m, 4H, H(3')), 8.12 (s, 2H, H(2)), 7.64-7.62 (m, 4H, H(2')), 7.49 (t, 2H, <sup>4</sup>J = 1.4 Hz, H(6)), 7.15 (s, 2H, H(4)), 4.05 (dd, 2H, <sup>3</sup>J<sub>ax,eq</sub> = 2.5 Hz, <sup>3</sup>J<sub>ax,ax</sub> = 8.4 Hz, H( $\alpha$ )), 3.66-3.63 (m, 4H, H( $\delta$ )), 2.25-2.17 (m, 2H, H( $\beta$ )), 2.01-1.92 (m, 6H, H( $\beta$ )+H( $\gamma$ )) ppm. <sup>13</sup>C NMR (151 MHz, DMSO-*d*<sub>6</sub>, 22 °C)  $\delta$  171.9 (ProCO), 168.8 (ABACO), 150.4 (C(3')), 146.0 (C(1')), 139.3 (C(1/3)), 139.0 (C(1/3)), 138.1 (C(5)), 121.1 (C(2')), 119.3 (C(6)), 117.7 (C(2)), 117.4 (C(4)), 62.0 (C( $\alpha$ )), 46.9 (C( $\delta$ )), 31.3 (C( $\beta$ )), 22.9 (C( $\gamma$ )) ppm. MS (MALDI-TOF):  $m/z$  (%) = 587.4 (89) [M+H]<sup>+</sup>, 609.4 (100) [M+Na]<sup>+</sup>, 625.4 (35) [M+K]<sup>+</sup>.



**[Pd(en)(NO<sub>3</sub>)<sub>2</sub>].** The palladium(II) complex was synthesized according to the literature.<sup>7</sup> Specifically, [PdCl<sub>2</sub>(en)] (0.2 g, 0.84 mmol) was suspended in water (280 mL) at room temperature. AgNO<sub>3</sub> (0.28 g, 1.68 mmol) was added and the mixture was left stirring for 2 hours. The white precipitate (AgCl) was filtered off and the filtrate evaporated in vacuum to yield a pale-yellow solid. The product was isolated in a yield of 160 mg (0.56 mmol, 67%) as pale-yellow solid and its purity was confirmed by elemental analysis. CHN calculated for C<sub>2</sub>H<sub>8</sub>N<sub>4</sub>O<sub>6</sub>Pd (M.W.: 286.50): C, 8.27; H, 2.78; N, 19.30; found: C, 8.25; H, 2.80; N, 19.66.

**Metallamacrocyclic Pd<sub>2</sub>L<sub>2</sub>.** This complex was prepared on the NMR scale and characterized in solution without isolation. Specifically, [Pd(en)(NO<sub>3</sub>)<sub>2</sub>] (3.2 mg, 0.011 mmol) was dissolved in CD<sub>3</sub>OD/D<sub>2</sub>O, 1:1 (v/v) (5 mL) and this solution was added to solid **L** (5.9 mg, 0.01 mmol) to achieve a final concentration of the 2:2 complex of 1 mM. The suspension was allowed to react at room temperature in an ultrasound bath until it became clear (typically between 15 and 60 min). The <sup>1</sup>H NMR spectrum indicated that this procedure led to the exclusive (>95%) formation of the respective complex. For the ESI-TOF mass spectrum, the sample was diluted with H<sub>2</sub>O prior to the measurement. <sup>1</sup>H NMR (400 MHz, CD<sub>3</sub>OD/D<sub>2</sub>O, 1:1 (v/v), 22 °C) δ 8.78 (m, 8H, H(3')), 8.26 (s, 4H, H(2)), 7.83 (d, 8H, H(2')), 7.56 (s, 4H, H(6)), 7.23 (s, 4H, H(4)), 4.10-4.07 (m, 4H, H(α)), 3.86-3.73 (m, 8H, H(δ)), 2.89 (s, 8H, Pd(en)), 2.37-2.32 (m, 4H, H(β)), 2.16-2.06 (m, 12H, H(β)+H(γ)) ppm. <sup>13</sup>C NMR (101 MHz, CD<sub>3</sub>OD/D<sub>2</sub>O, 1:1 (v/v), 22 °C) δ 174.2 (ProCO), 172.0 (ABACO), 152.6 (C(3')), 151.5 (C(1')), 139.8 (C(1/3)), 139.4 (C(1/3)), 138.5 (C(5)), 125.5 (C(2')), 121.5 (C(6)), 119.8 (C(2)), 117.4 (C(4)), 64.3 (C(α)), 49.6 (C(en)), 47.8 (C(δ)), 32.3 (C(β)), 24.0 (C(γ)) ppm. MS (ESI-TOF) *m/z* (%) = 376.1 (75) [L·Pd(en)]<sup>2+</sup>, 587.2 (99) [L+H]<sup>+</sup>, 669.2 (78) [L<sub>2</sub>·Pd(en)]<sup>2+</sup>, 815.1 (100) [L<sub>2</sub>·(Pd(en))<sub>2</sub>+2 NO<sub>3</sub>]<sup>2+</sup>.



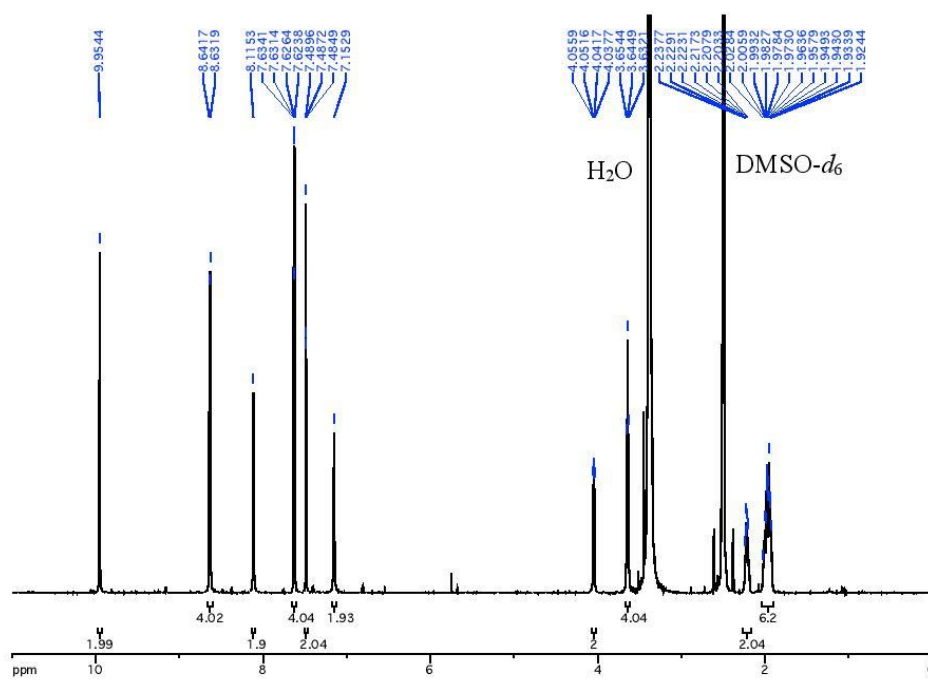
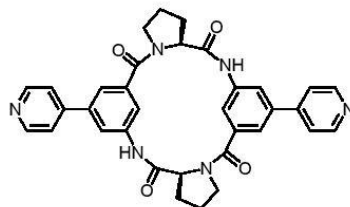
**Coordination Cage Pd<sub>3</sub>L<sub>6</sub>.** This complex was prepared on the NMR scale and characterized in solution without isolation. Specifically, [Pd(CH<sub>3</sub>CN)<sub>4</sub>](BF<sub>4</sub>)<sub>2</sub> (1.2 mg, 2.7 μmol) was dissolved in DMSO-*d*<sub>6</sub> (200 μL) and this solution was added to a solution of **L** (3.0 mg, 5.1 μmol) in DMSO-*d*<sub>6</sub> (500 μL) to achieve a final concentration of **Pd<sub>3</sub>L<sub>6</sub>** complex of 1.2 mM. The solution was stirred for 4 h at 60 °C. Because of the complexity of the resulting <sup>1</sup>H NMR spectrum the exact amount of **Pd<sub>3</sub>L<sub>6</sub>** in solution could not be quantified. Only the chemical shifts of the largest peaks in the <sup>1</sup>H NMR

spectrum are listed that belong to **Pd<sub>3</sub>L<sub>6</sub>** according to the DOSY NMR spectrum. A satisfactory <sup>13</sup>C NMR spectrum could not be obtained, even after extended measuring times, likely because of the complexity of the underlying equilibrium as also reflected in the <sup>1</sup>H NMR spectrum. <sup>1</sup>H NMR (400 MHz, DMSO-*d*<sub>6</sub>, 22 °C) δ 9.82, 9.72, 9.40, 9.29, 9.09, 8.09, 7.97, 7.71, 7.53, 7.35, 7.29, 7.18, 6.36, 4.06, 3.96, 3.83, 3.62, 3.52, 2.16, 2.03, 1.88, 1.82, 1.74 ppm. MS (ESI-Orbitrap) *m/z* (%) = 587.23 (100) [**L+H**]<sup>+</sup>, 864.57 (25) [Pd<sub>2</sub>L<sub>4</sub>+Cl]<sup>3+</sup>, 996.77 (37) [**Pd<sub>3</sub>L<sub>6</sub>+BF<sub>4</sub>+NO<sub>3</sub>**]<sup>4+</sup>, 1003.03 (64) [**Pd<sub>3</sub>L<sub>6</sub>+2BF<sub>4</sub>**]<sup>4+</sup>, 1358.04 (19) [**Pd<sub>3</sub>L<sub>6</sub>+2BF<sub>4</sub>+NO<sub>3</sub>**]<sup>3+</sup>, 1366.38 (20) [**Pd<sub>3</sub>L<sub>6</sub>+3BF<sub>4</sub>**]<sup>3+</sup>.

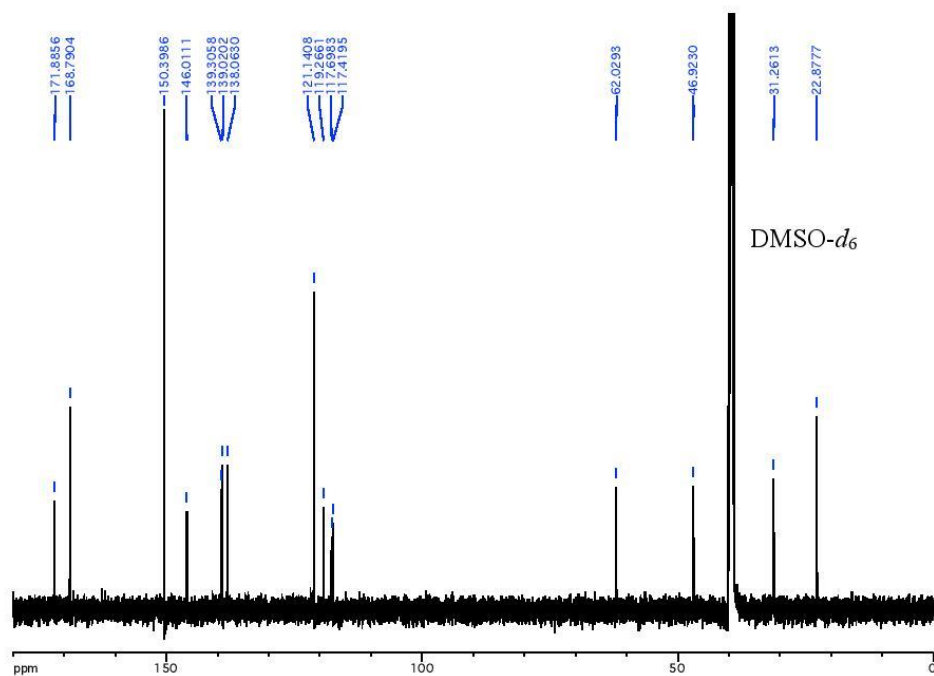
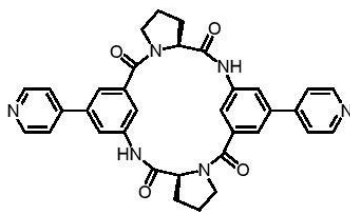
The MS spectrum contains three additional signals of substantial intensity at *m/z* 693.28, 963.91, and 971.91. The one at 693.28 corresponds to a singly charged ion that does not contain palladium and presumably represents an unspecific adduct of the ligand. The other two signals denote triply charged ions containing palladium whose composition could, however, not be assigned to molecular formulae with matching isotope patterns.

## NMR and MS Spectra of L

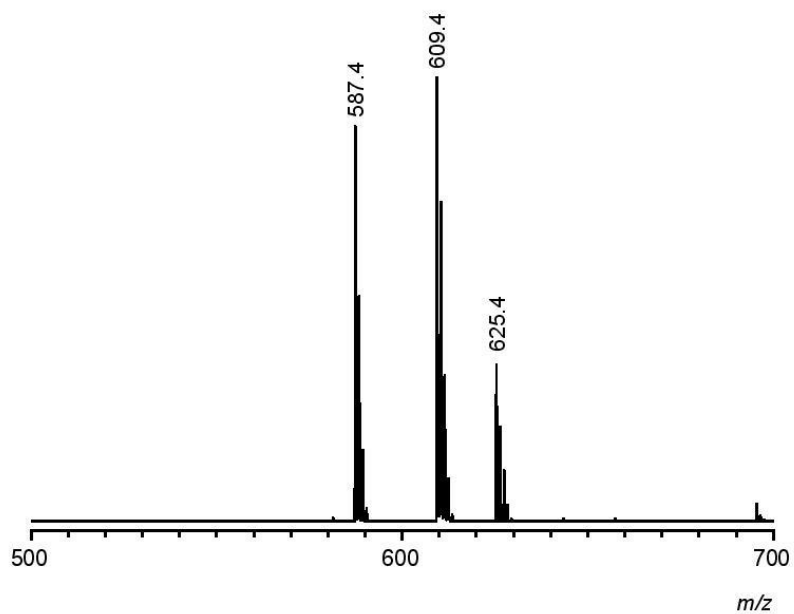
<sup>1</sup>H-NMR: Cyclopeptide L (600 MHz, DMSO-*d*<sub>6</sub>, 22 °C).



<sup>13</sup>C NMR: Cyclopeptide L (151 MHz, DMSO-*d*<sub>6</sub>, 22 °C).



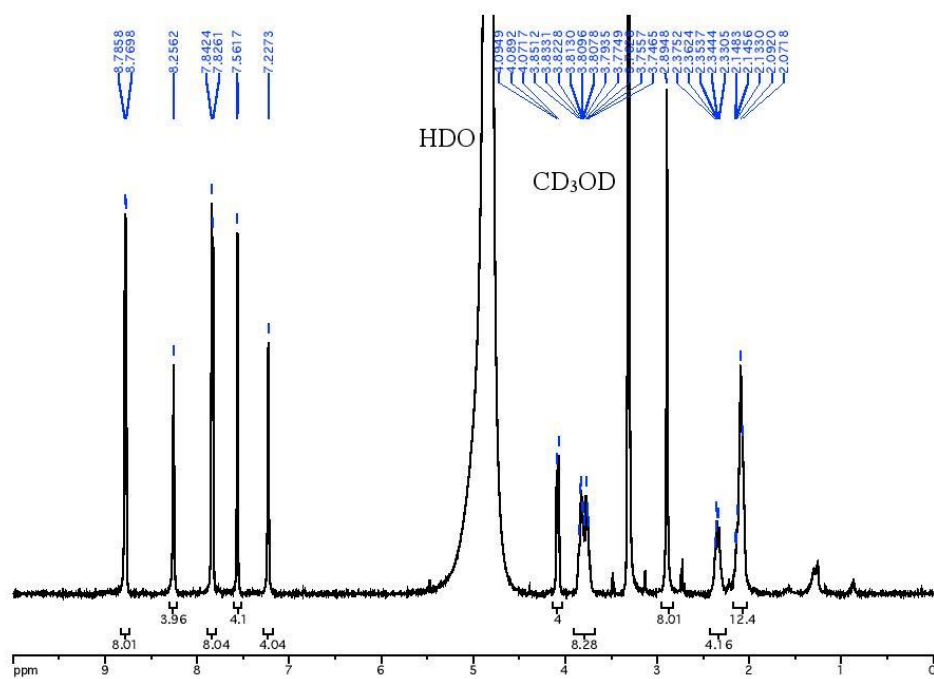
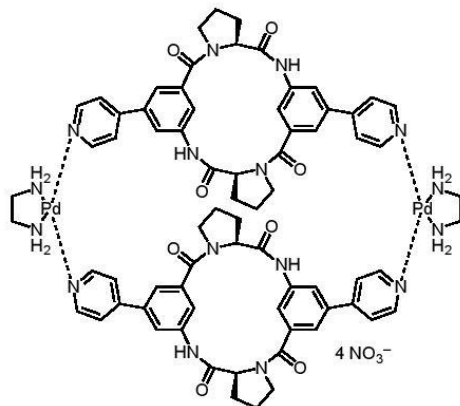
MALDI-TOF MS: Cyclopeptide **L** (positive mode).



		<i>m/z calcd.</i>	<i>m/z exp.</i>
$[\mathbf{L}+\mathbf{H}]^+$	$\text{C}_{34}\text{H}_{30}\text{N}_6\text{O}_4 + \text{H}^+$	587.2	587.4
$[\mathbf{L}+\mathbf{Na}]^+$	$\text{C}_{34}\text{H}_{30}\text{N}_6\text{O}_4 + \text{Na}^+$	609.2	609.4
$[\mathbf{L}+\mathbf{K}]^+$	$\text{C}_{34}\text{H}_{30}\text{N}_6\text{O}_4 + \text{K}^+$	625.2	625.4

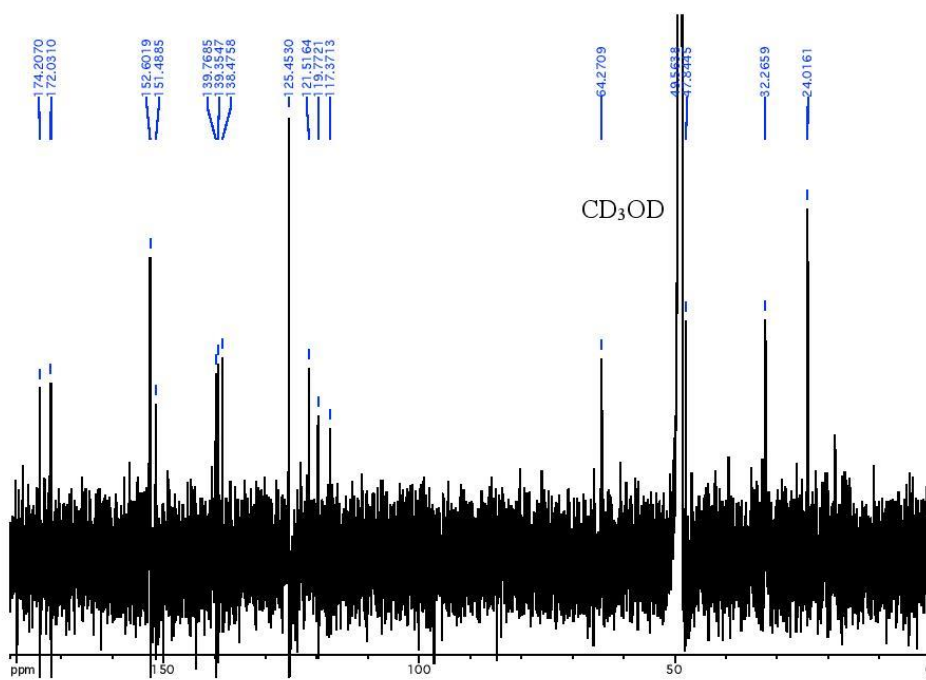
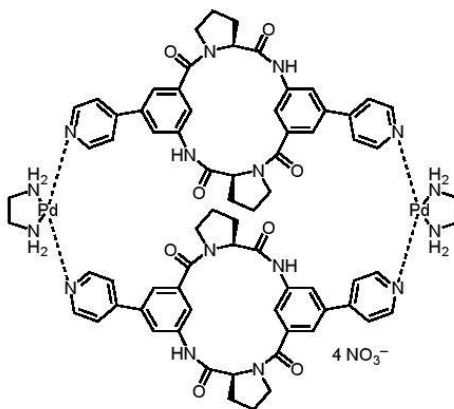
## NMR and MS Spectra of Pd<sub>2</sub>L<sub>2</sub>

<sup>1</sup>H NMR: Pd<sub>2</sub>L<sub>2</sub> (400 MHz, CD<sub>3</sub>OD/D<sub>2</sub>O, 1:1 (v/v), 22 °C).

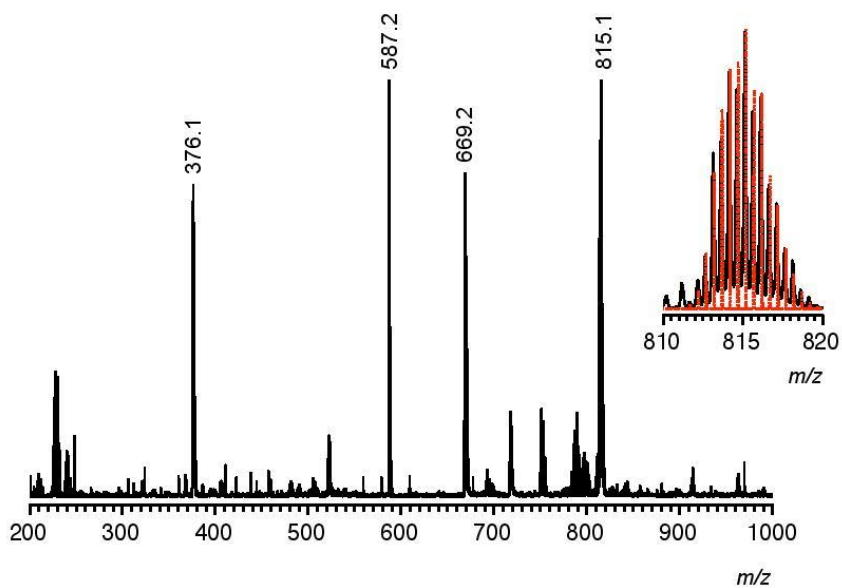




$^{13}\text{C}$  NMR: **Pd<sub>2</sub>L<sub>2</sub>** (101 MHz, CD<sub>3</sub>OD/D<sub>2</sub>O, 1:1 (v/v), 22 °C).



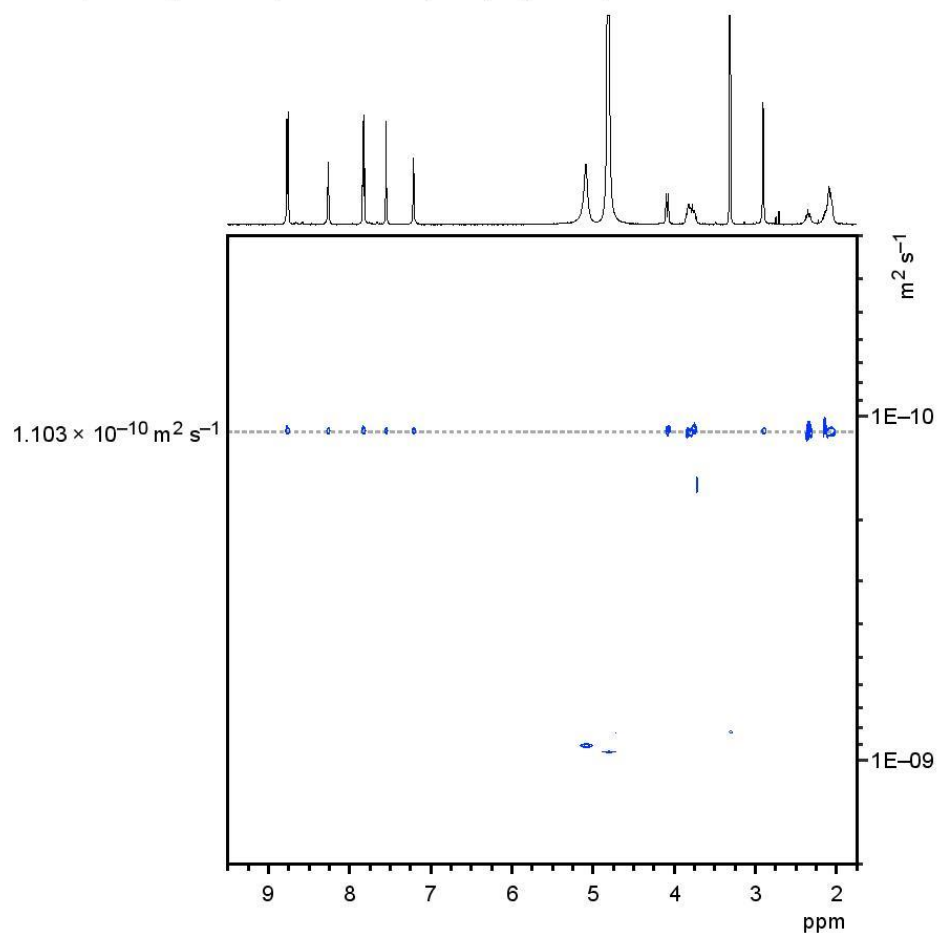
ESI-TOF MS: **Pd<sub>2</sub>L<sub>2</sub>** (positive mode).



		<i>m/z calcd.</i>	<i>m/z exp.</i>
$[\mathbf{L}+\text{Pd}(\text{en})]^{2+}$	$2 \text{ C}_{34}\text{H}_{30}\text{N}_6\text{O}_4 + \text{C}_2\text{H}_8\text{N}_2\text{Pd}^{2+}$	376.1	376.1
$[\mathbf{L}+\text{H}]^+$	$\text{C}_{34}\text{H}_{30}\text{N}_6\text{O}_4 + \text{H}^+$	587.2	587.2
$[\mathbf{L}_2+\text{Pd}(\text{en})]^{2+}$	$2 \text{ C}_{34}\text{H}_{30}\text{N}_6\text{O}_4 + \text{C}_2\text{H}_8\text{N}_2\text{Pd}^{2+}$	669.2	669.2
$[\mathbf{Pd}_2\mathbf{L}_2+2 \text{ NO}_3]^{2+}$	$\text{C}_{72}\text{H}_{76}\text{N}_{16}\text{O}_8\text{Pd}_2^{4+} + 2 \text{ NO}_3^-$	815.2	815.1

(The inset shows the calculated isotope pattern for  $[\mathbf{Pd}_2\mathbf{L}_2+2 \text{ NO}_3]^{2+}$  in red)

DOSY NMR: **Pd<sub>2</sub>L<sub>2</sub>** (400 MHz, CD<sub>3</sub>OD/D<sub>2</sub>O, 1:1 (v/v), 25 °C).



Diffusion coefficient  $D$  derived from this experiment:

$$D = (1.103 \pm 0.019) \times 10^{-10} \text{ m}^2 \text{ s}^{-1}$$

Calculated hydrodynamic diameter  $d_H$  derived from the Stokes-Einstein equation:

$$d_H = 22.9 \pm 0.4 \text{ \AA}$$

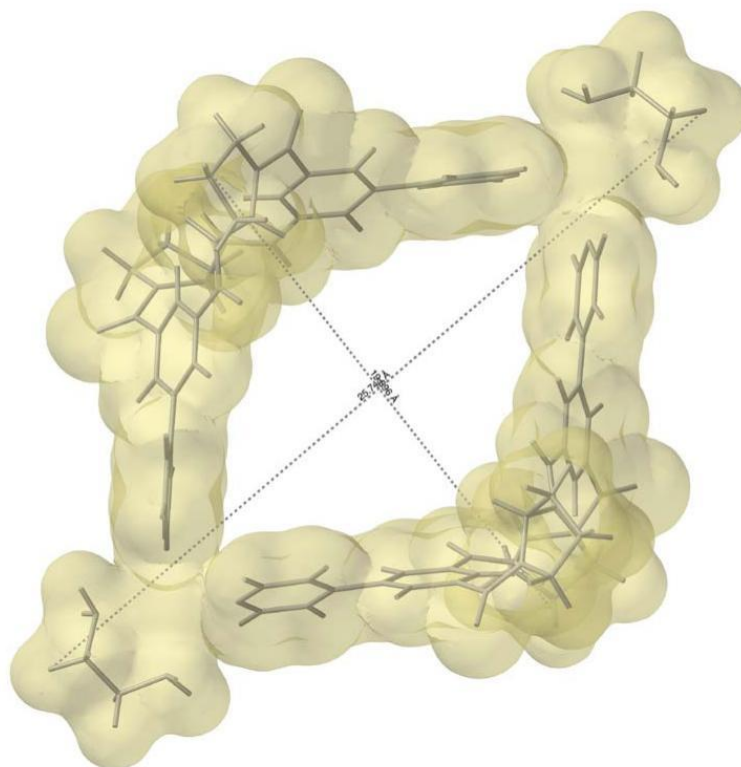
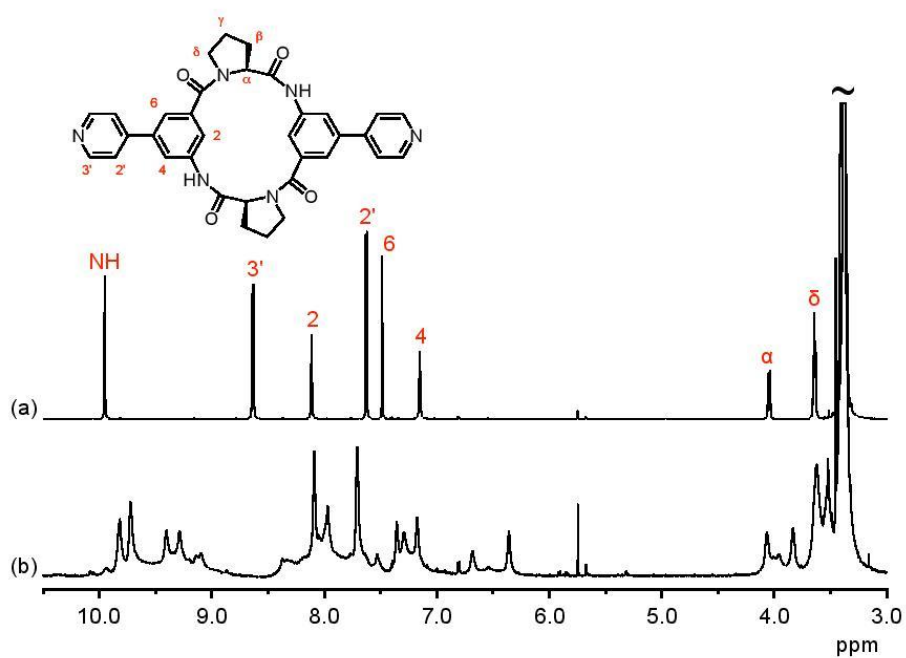


Figure S1: Estimated molecular dimensions of **Pd<sub>2</sub>L<sub>2</sub>** from the structure calculated at the semi-empirical PM6 level as implemented in Spartan 18, Wavefunction Inc. From the marked distances of hydrogen atoms, an average diameter of 25.0 Å can be estimated when considering the van-der-Waals radii of hydrogen atoms (1.1 Å).

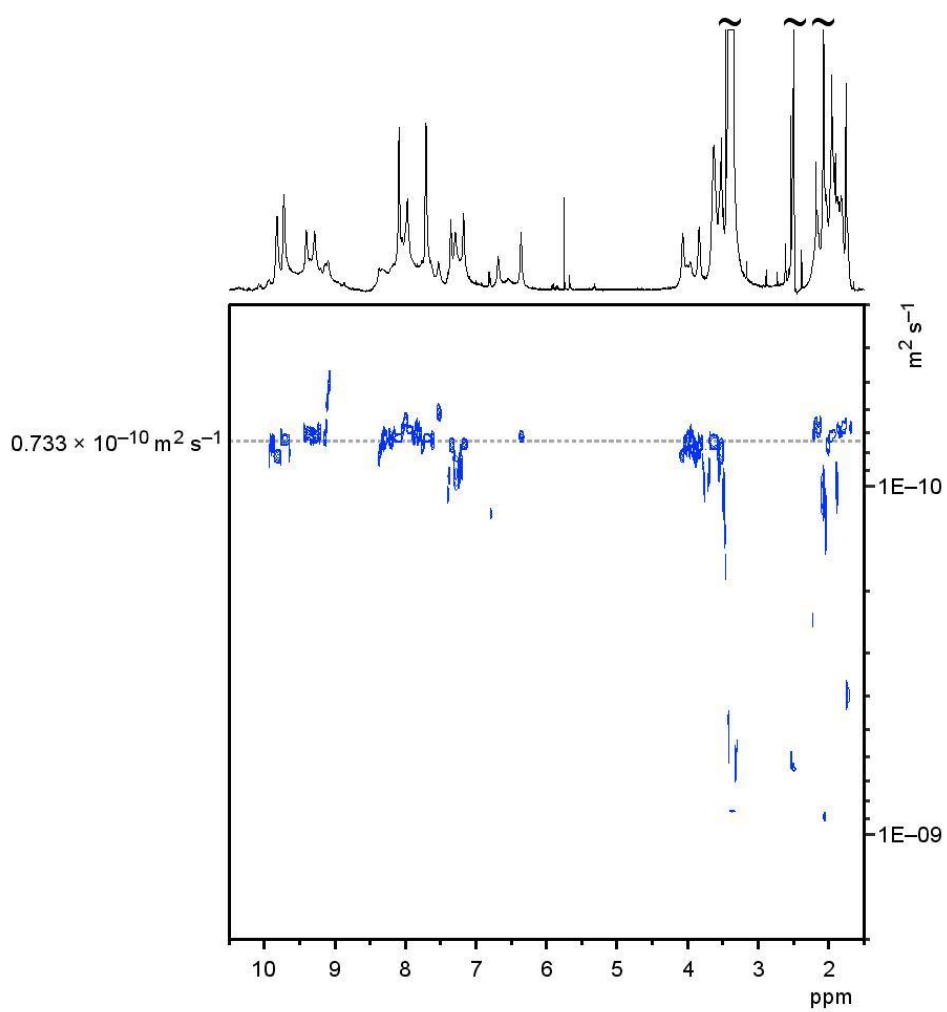
### NMR and MS Spectra of Pd<sub>3</sub>L<sub>6</sub>

<sup>1</sup>H NMR: Pd<sub>3</sub>L<sub>6</sub> (600 MHz, DMSO-*d*<sub>6</sub>, 22 °C).

Trace (a) shows the <sup>1</sup>H NMR spectrum of **L** in DMSO-*d*<sub>6</sub> and trace (b) the spectrum resulting when treating **L** in DMSO-*d*<sub>6</sub> with 0.5 equiv of [Pd(CH<sub>3</sub>CN)<sub>4</sub>](BF<sub>4</sub>)<sub>2</sub> for 4 h at 60 °C. The NH signal in the spectrum of **L** at 9.55 ppm is not visible in the spectrum of the cage because of H/D exchange.



DOSY NMR: **Pd<sub>3</sub>L<sub>6</sub>** (400 MHz, DMSO-*d*<sub>6</sub>, 25 °C).



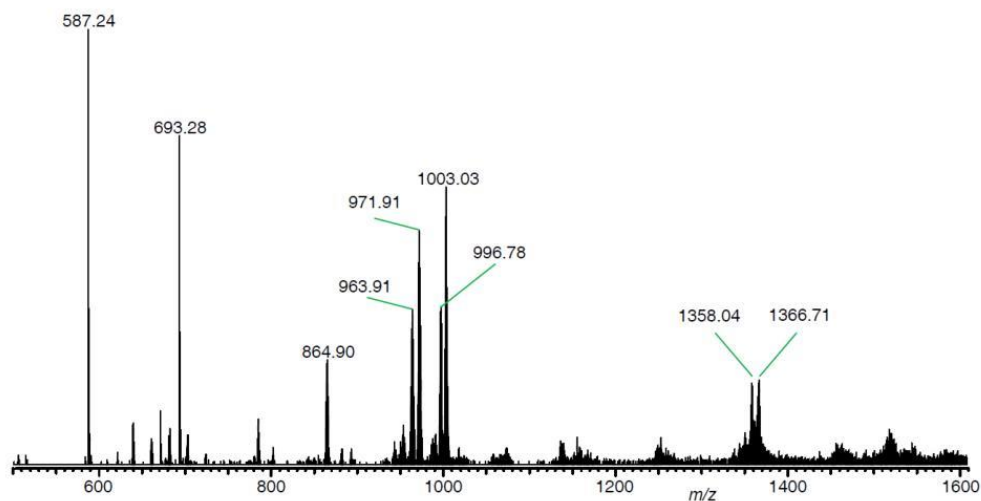
Diffusion coefficient  $D$  derived from this experiment:

$$D = (0.733 \pm 0.067) \times 10^{-10} \text{ m}^2 \text{ s}^{-1}$$

Calculated hydrodynamic diameter  $d_H$  derived from the Stokes-Einstein equation:

$$d_H = 27.2 \pm 2.5 \text{ \AA}$$

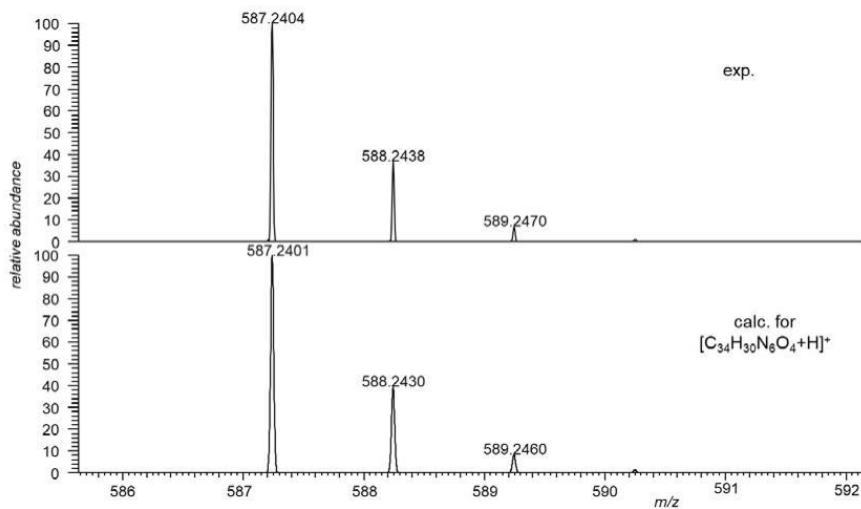
ESI HR-MS: **Pd<sub>3</sub>L<sub>6</sub>** (Orbitrap XL, positive mode).



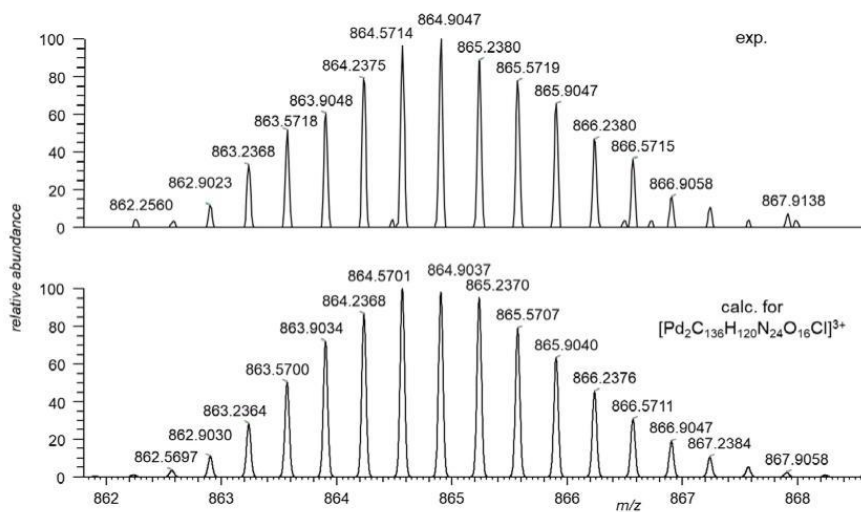
		<i>m/z calcd.</i>	<i>m/z exp.</i>
[L+H] <sup>+</sup>	C <sub>34</sub> H <sub>30</sub> N <sub>6</sub> O <sub>4</sub> + H <sup>+</sup>	587.24	587.24
[Pd <sub>2</sub> L <sub>4</sub> +Cl] <sup>3+</sup>	{[Pd <sub>2</sub> (C <sub>34</sub> H <sub>30</sub> N <sub>6</sub> O <sub>4</sub> ) <sub>4</sub> ]Cl} <sup>3+</sup>	864.90	864.90
[Pd <sub>3</sub> L <sub>6</sub> +BF <sub>4</sub> +NO <sub>3</sub> ] <sup>4+</sup>	{[Pd <sub>3</sub> (C <sub>34</sub> H <sub>30</sub> N <sub>6</sub> O <sub>4</sub> ) <sub>6</sub> ](BF <sub>4</sub> )(NO <sub>3</sub> ) <sup>4+</sup>	996.78	996.78
[Pd <sub>3</sub> L <sub>6</sub> +2BF <sub>4</sub> ] <sup>4+</sup>	{[Pd <sub>3</sub> (C <sub>34</sub> H <sub>30</sub> N <sub>6</sub> O <sub>4</sub> ) <sub>6</sub> ](BF <sub>4</sub> ) <sub>2</sub> ] <sup>4+</sup>	1003.03	1003.03
[Pd <sub>3</sub> L <sub>6</sub> +2BF <sub>4</sub> +NO <sub>3</sub> ] <sup>3+</sup>	{[Pd <sub>3</sub> (C <sub>34</sub> H <sub>30</sub> N <sub>6</sub> O <sub>4</sub> ) <sub>6</sub> ](BF <sub>4</sub> ) <sub>2</sub> (NO <sub>3</sub> ) <sup>3+</sup>	1358.04	1358.04
[Pd <sub>3</sub> L <sub>6</sub> +3BF <sub>4</sub> ] <sup>3+</sup>	{[Pd <sub>3</sub> (C <sub>34</sub> H <sub>30</sub> N <sub>6</sub> O <sub>4</sub> ) <sub>6</sub> ](BF <sub>4</sub> ) <sub>3</sub> ] <sup>3+</sup>	1366.38	1366.38

The additional signals in this spectrum at *m/z* 693.28, 963.91, and 971.91 correspond to a singly charged ion that does not contain palladium and presumably represents an unspecific adduct of the ligand (693.28) and triply charged ions containing palladium (963.91 and 971.91) whose composition could, however, not be assigned to molecular formulae with matching isotope patterns. Note, that the ions containing chloride and nitrate result from anion exchange processes of the weakly coordinating tetrafluoroborate anions against these strongly coordinating anions in the ESI source of our Orbitrap mass spectrometer as these abundant ions cannot be removed completely even after extended purging.

Comparison of the experimental and calculated isotope pattern of the signals at  $m/z$  587.24 that can be assigned to  $C_{34}H_{30}N_6O_4 + H^+$ :

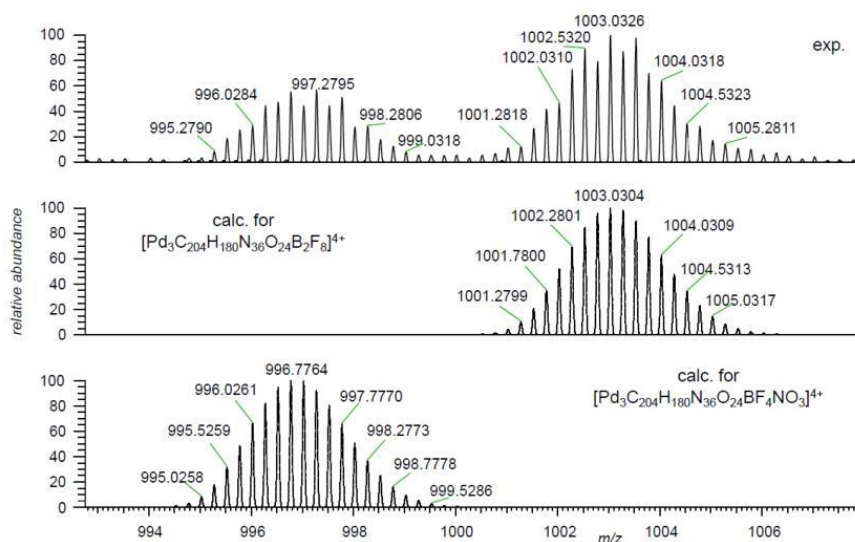


Comparison of the experimental and calculated isotope pattern of the signal at  $m/z$  864.90 that can be assigned to  $\{[Pd_2(C_{34}H_{30}N_6O_4)_4]Cl\}^{3+}$ :

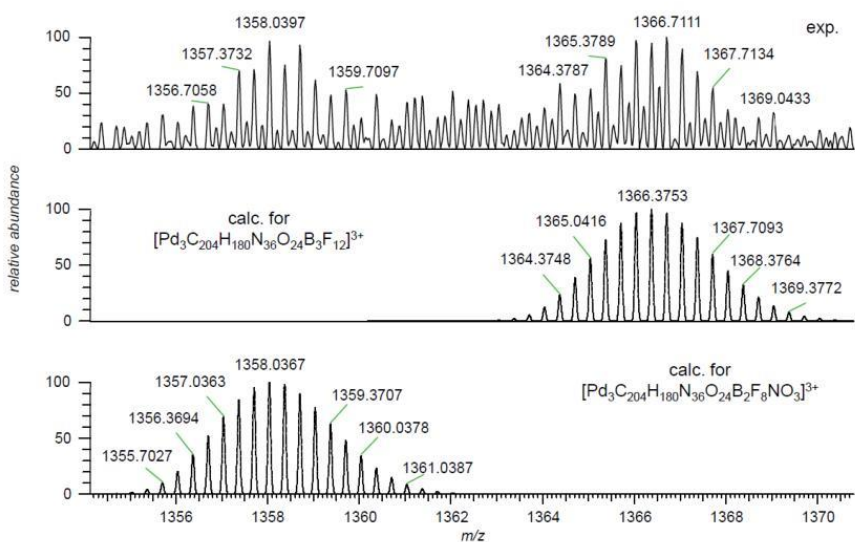




Comparison of the experimental and calculated isotope patterns of the signals at  $m/z$  996.78 and 1003.03 that can be assigned to  $\{[\text{Pd}_3(\text{C}_{34}\text{H}_{30}\text{N}_6\text{O}_4)_6](\text{BF}_4)(\text{NO}_3)\}^{4+}$  and  $\{[\text{Pd}_3(\text{C}_{34}\text{H}_{30}\text{N}_6\text{O}_4)_6](\text{BF}_4)_2\}^{4+}$ , respectively:



Comparison of the experimental and calculated isotope patterns of the signals at  $m/z$  1358.04 and 1366.37 that can be assigned to  $\{[\text{Pd}_3(\text{C}_{34}\text{H}_{30}\text{N}_6\text{O}_4)_6](\text{BF}_4)_2(\text{NO}_3)\}^{3+}$  and  $\{[\text{Pd}_3(\text{C}_{34}\text{H}_{30}\text{N}_6\text{O}_4)_6](\text{BF}_4)_3\}^{3+}$ , respectively:



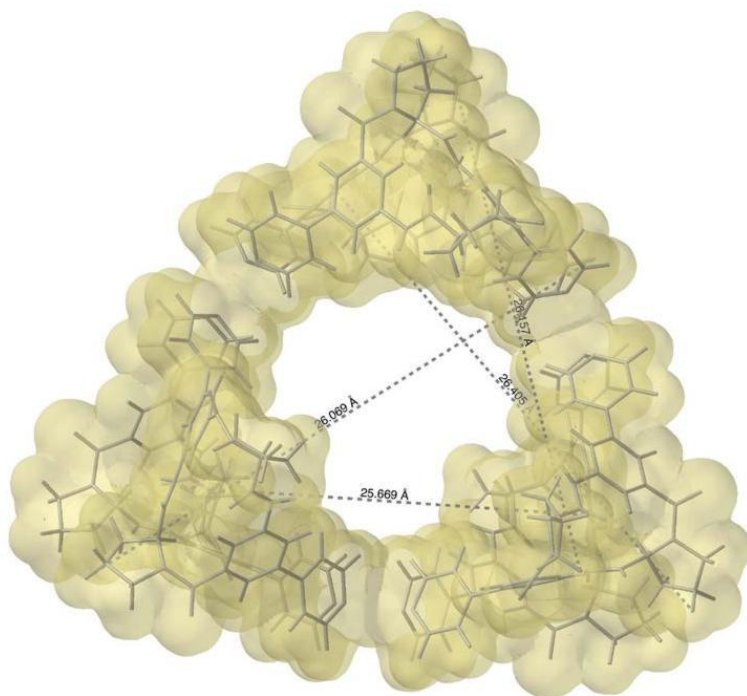


Figure S2: Estimated molecular dimensions of **Pd<sub>3</sub>L<sub>6</sub>** from the structure calculated at the semi-empirical PM6 level as implemented in Spartan 18, Wavefunction Inc. From the marked distances of hydrogen atoms, an average diameter of 28.3 Å can be estimated when considering the van-der-Waals radii of hydrogen atoms (1.1 Å).

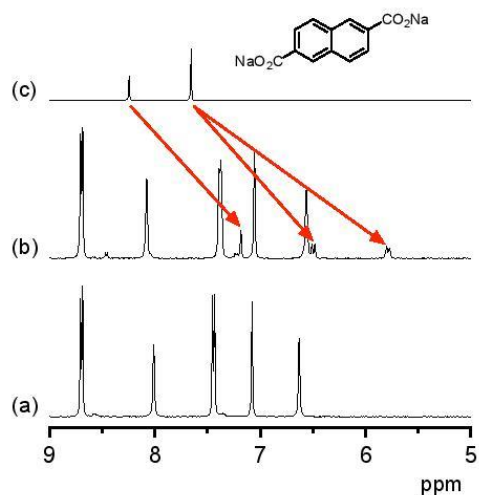
### Dicarboxylate Binding to Pd<sub>2</sub>L<sub>2</sub> (Qualitative Binding Studies)

A 1 mM solution of **Pd<sub>2</sub>L<sub>2</sub>** was prepared by adding a solution of [Pd(en)(NO<sub>3</sub>)<sub>2</sub>] (1.6 mg, 5.5 mmol) in CD<sub>3</sub>OD/D<sub>2</sub>O, 1:1 (v/v) (2.5 mL) to solid **L** (2.9 mg, 5.0 mmol) (host solution) at room temperature. The solvent for the guest solutions was prepared by dissolving Na<sub>2</sub>CO<sub>3</sub> (1.1 mg, 10.4 mmol) in CD<sub>3</sub>OD/D<sub>2</sub>O, 1:1 (v/v) (10.4 mL). The guest solutions were prepared by dissolving a dicarboxylic acid (1 mmol) in this solvent (1 mL) to obtain a 1 mM guest concentration. The following dicarboxylic acids were used: 2,6-naphthalenedicarboxylic acid (a), isophthalic acid (b), terephthalic acid (c), diphenic acid (d), adipic acid (e), glutaric acid (f).

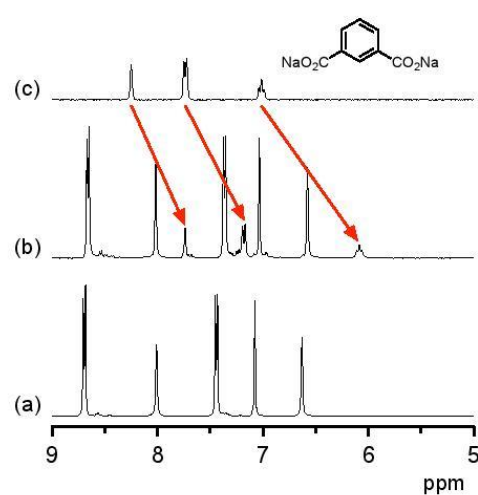
The solutions for the <sup>1</sup>H NMR spectroscopic measurements were prepared from these stock solutions. Solutions of the binding partners alone were prepared by mixing the respective stock solution (250 μL) with CD<sub>3</sub>OD/D<sub>2</sub>O, 1:1 (v/v) (250 μL). For the mixtures, the host solution (250 μL) was added to a guest solution (250 μL). The concentrations of the binding partners thus amounted to 0.5 mM in the final solutions.

The NMR tubes were placed in an ultrasound bath for 15 min at room temperature, followed by measurement of the <sup>1</sup>H NMR spectra. The spectra obtained are depicted below. All spectra show that the guest signals shift upfield in the presence of **Pd<sub>2</sub>L<sub>2</sub>**, indicating that the dicarboxylic acids form complexes with the metallacycle in which they are likely incorporated into the cavity of the ring.

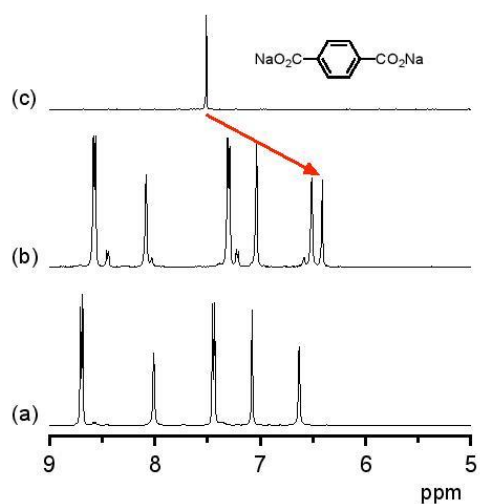
(a) 2,6-naphthalenedicarboxylate



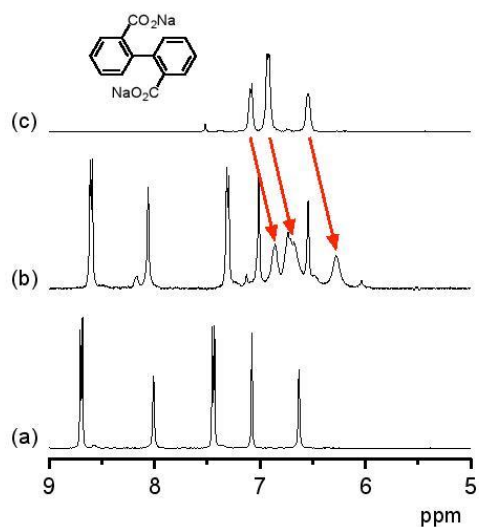
(b) isophthalate



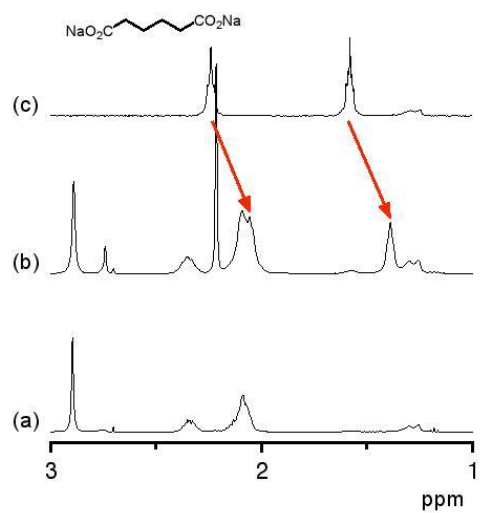
(c) terephthalate



(d) diphenate



(e) adipate



(f) glutarate

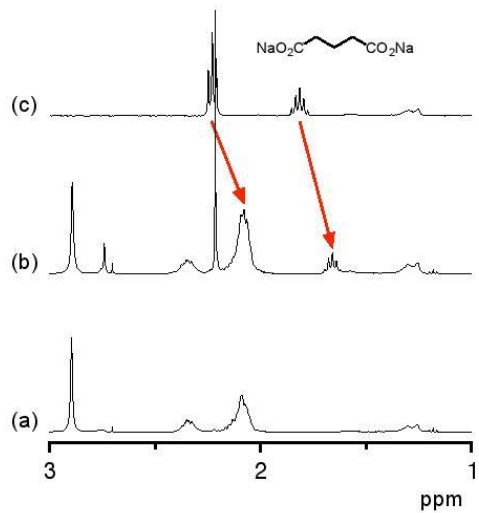
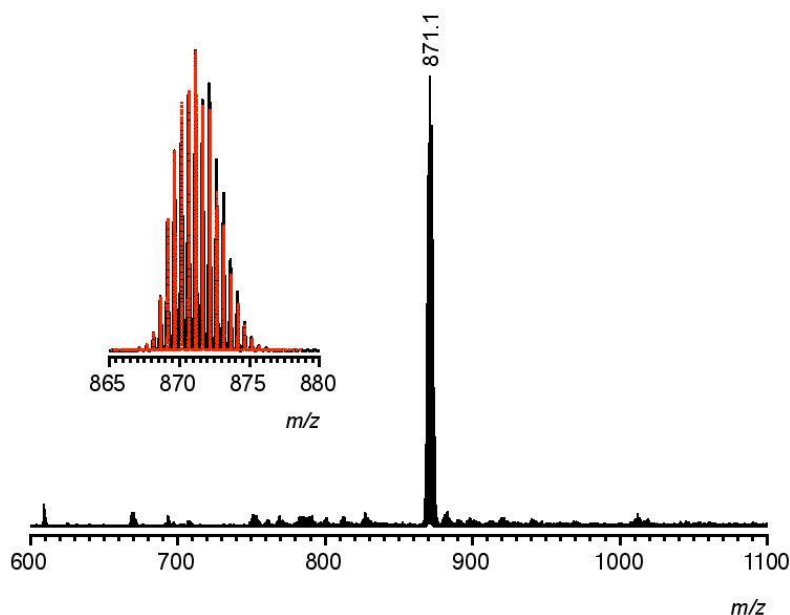


Figure S3:  $^1\text{H}$  NMR spectra of **Pd<sub>2</sub>L<sub>2</sub>** (0.5 mM) (a), of a dicarboxylic acid (0.5 mM) (c), and of equimolar mixtures of **Pd<sub>2</sub>L<sub>2</sub>** and a dicarboxylic acid (each 0.5 mM) (b) in a solution of  $\text{Na}_2\text{CO}_3$  (0.5 mM) in  $\text{CD}_3\text{OD}/\text{D}_2\text{O}$ , 1:1 (v/v).

### Sodium 1,3-Benzenedisulfonate Binding to Pd<sub>2</sub>L<sub>2</sub>

ESI-TOF MS: Pd<sub>2</sub>L<sub>2</sub> + 1 equiv of sodium 1,3-benzenedisulfonate (positive mode).



		<i>m/z</i> <i>calcd.</i>	<i>m/z</i> <i>exp.</i>
[Pd <sub>2</sub> L <sub>2</sub> +BDS] <sup>2+</sup>	C <sub>72</sub> H <sub>76</sub> N <sub>16</sub> O <sub>8</sub> Pd <sub>2</sub> <sup>4+</sup> + C <sub>6</sub> H <sub>4</sub> O <sub>6</sub> S <sub>2</sub> <sup>2-</sup>	871.2	871.1

(The inset shows the calculated isotope pattern for [Pd<sub>2</sub>L<sub>2</sub>+BDS]<sup>2+</sup> in red)

**NMR titration of 1,3-Benzenedisulfonate with Pd<sub>2</sub>L<sub>2</sub>.** A 2.5 mM solution of Pd<sub>2</sub>L<sub>2</sub> was prepared by adding a solution of [Pd(en)(NO<sub>3</sub>)<sub>2</sub>] (2.8 mg, 9.8 mmol) in CD<sub>3</sub>OD/D<sub>2</sub>O, 1:1 (v/v) (1.8 mL) to **L** (5.3 mg, 9.0 mM) (solution A). Solution B was prepared by dissolving sodium 1,3-benzenedisulfonate (80%) (4.4 mg, 12.5 mmol) in CD<sub>3</sub>OD/D<sub>2</sub>O, 1:1 (v/v) (5.0 mL) to obtain a concentration of 2.5 mM. A series of NMR tubes was set up each containing solution B (100 μL) and different volumes of solution A (0–200 μL in 20 μL steps). All samples were made up to 500 μL by adding the required volume of CD<sub>3</sub>OD/D<sub>2</sub>O, 1:1 (v/v) to afford a 0.5 mM concentration of 1,3-benzenedisulfonate in each tube. The tubes were placed in an ultrasound bath for 15 min at room temperature, followed by measuring the <sup>1</sup>H NMR spectra (22 °C). The chemical shifts of the guest protons were plotted against the host/guest ratio and the stability constant *K*<sub>a</sub> of the complex was determined by non-linear regression and using a fitting procedure for a 1:1 complex implemented in proFit (Quantum Soft).

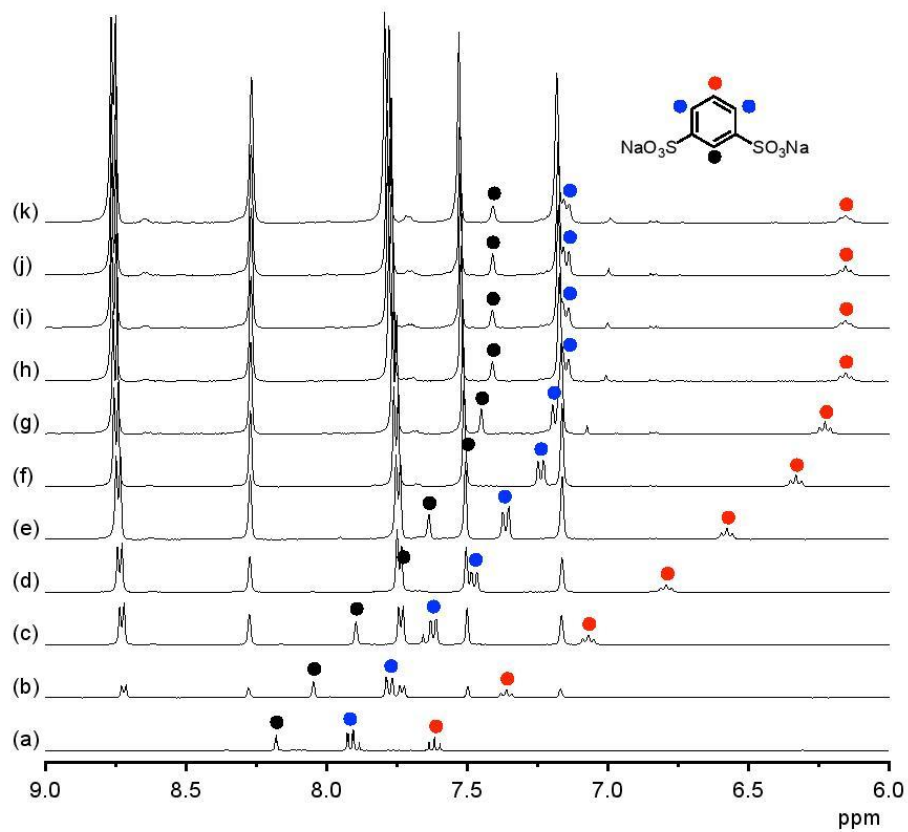


Figure S4: <sup>1</sup>H NMR spectra of the NMR titration of sodium 1,3-benzenedisulfonate (0.5 mM) in CD<sub>3</sub>OD/D<sub>2</sub>O, 1:1 (v/v) at 22 °C with increasing amounts of Pd<sub>2</sub>L<sub>2</sub> ((a) 0 equiv, (b) 0.2 equiv (c) 0.4 equiv (d) 0.6 equiv (e) 0.8 equiv (f) 1.0 equiv (g) 1.2 equiv (h) 1.4 equiv (i) 1.6 equiv (j) 1.8 equiv (k) 2.0 equiv). The signals of the guest are marked with colored dots.

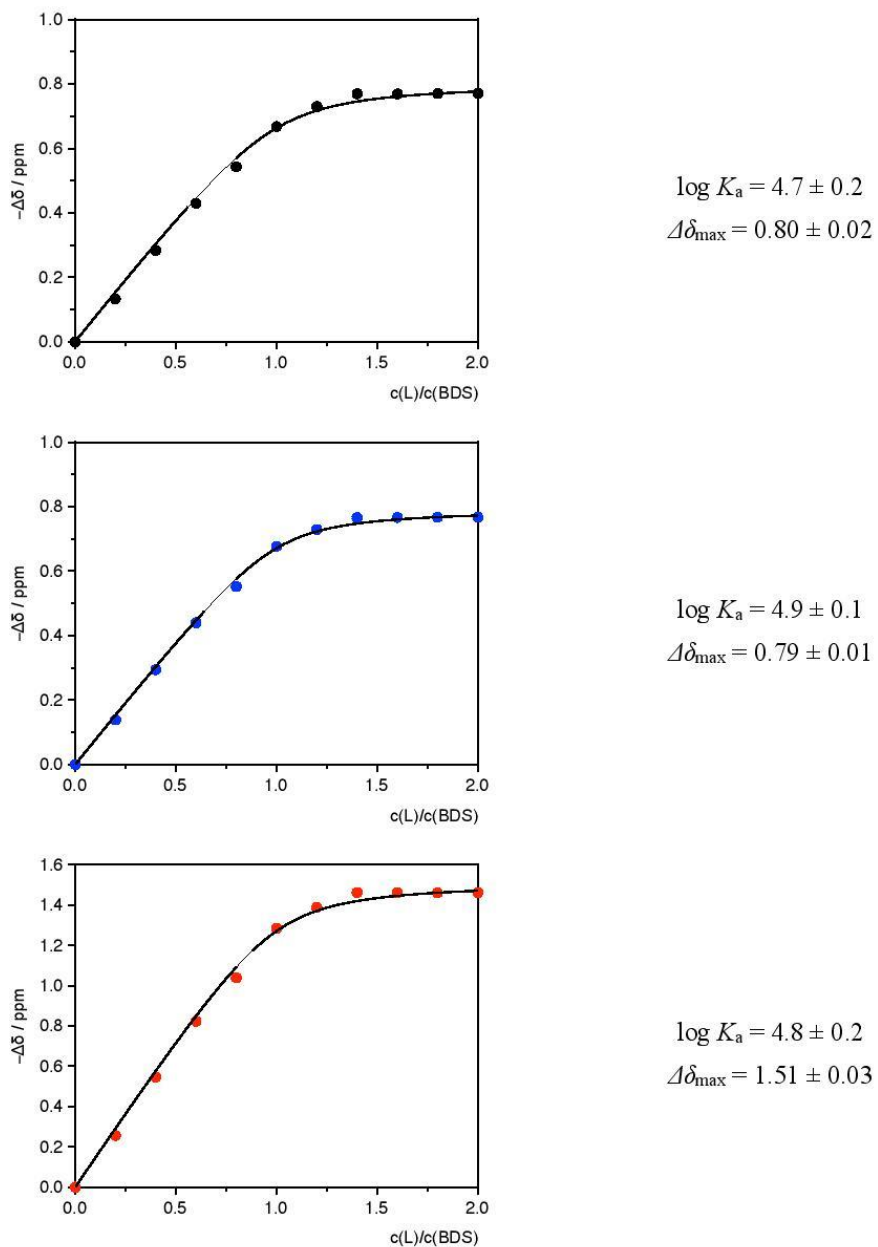


Figure S5: Binding isotherms constructed from the NMR titration. The circles denote the experimental signal shifts and the lines the calculated binding isotherm. The colors of the circles in the three diagrams correlate with those used in Figure S4. The stability constants  $\log K_a$  and maximum chemical shifts  $\Delta\delta_{\max}$  resulting from each isotherm are also specified.

### Sodium 2,6-Naphthalenedisulfonate Binding to Pd<sub>2</sub>L<sub>2</sub>

**NMR titration of Pd<sub>2</sub>L<sub>2</sub> with 2,6-Naphthalenedisulfonate.** A 2 mM solution of Pd<sub>2</sub>L<sub>2</sub> was prepared by adding a solution of [Pd(en)(NO<sub>3</sub>)<sub>2</sub>] (3.8 mg, 13.2 mmol) in CD<sub>3</sub>OD/D<sub>2</sub>O, 1:1 (v/v) (3.0 mL) to L (7.0 mg, 12.0 mM) (solution A). Solution B was prepared by dissolving sodium 2,6-naphthalenedisulfonate (97%) (8.6 mg, 25.0 mmol) in CD<sub>3</sub>OD/D<sub>2</sub>O, 1:1 (v/v) (2.0 mL) to obtain a concentration of 12.5 mM. A series of NMR tubes was set up each containing solution A (250 μL) and different volumes of solution B (0–200 μL in 40 μL steps). All samples were made up to 500 μL by adding the required volume of CD<sub>3</sub>OD/D<sub>2</sub>O, 1:1 (v/v) to afford a concentration of 1.0 mM concentration of Pd<sub>2</sub>L<sub>2</sub> in each tube. The tubes were placed in an ultrasound bath for 15 min at room temperature, followed by measuring the <sup>1</sup>H NMR spectra (22 °C).

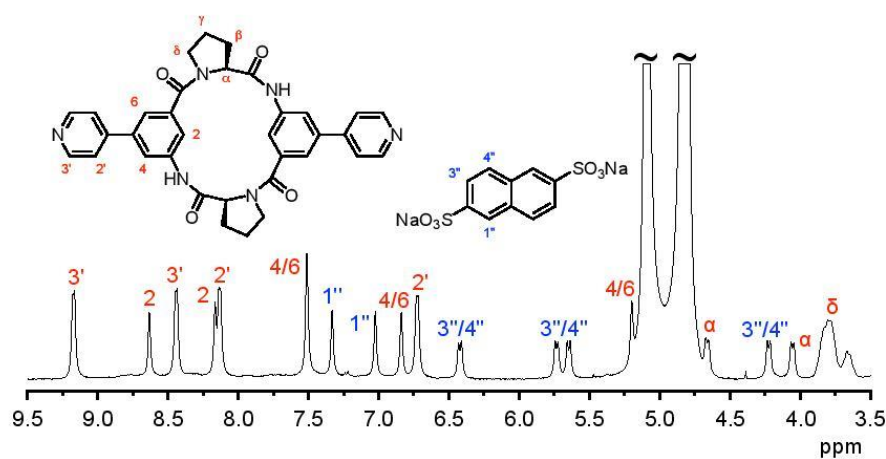


Figure S6: <sup>1</sup>H NMR spectrum of Pd<sub>2</sub>L<sub>2</sub> (1.0 mM) in CD<sub>3</sub>OD/D<sub>2</sub>O, 1:1 (v/v) containing 2 equiv of 2,6-naphthalenedisulfonate with the peaks assigned to the respective protons in the two components of the complex (22 °C).



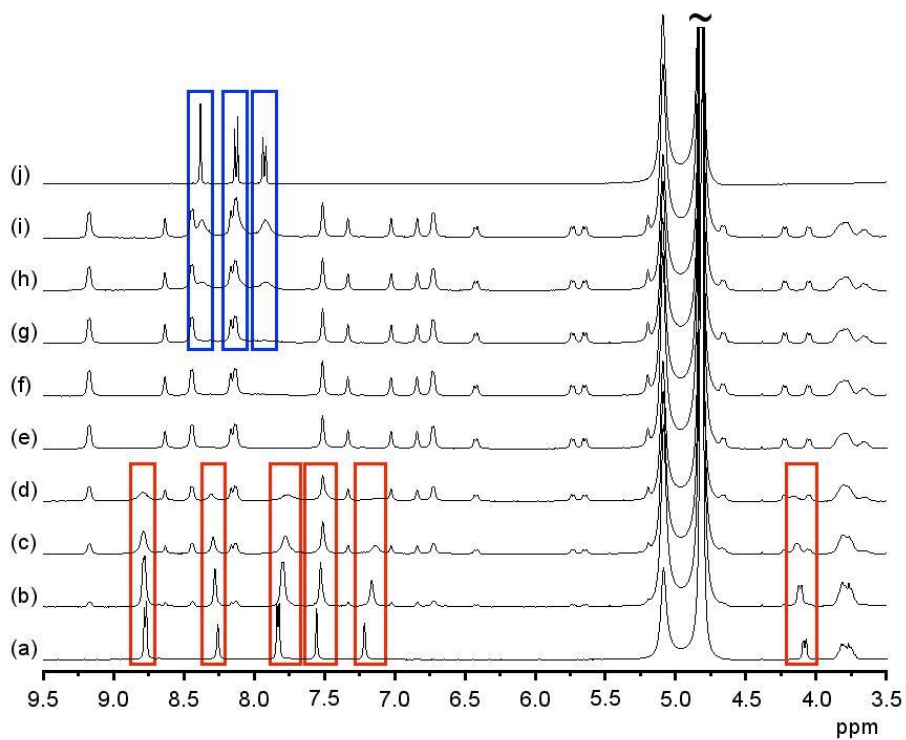
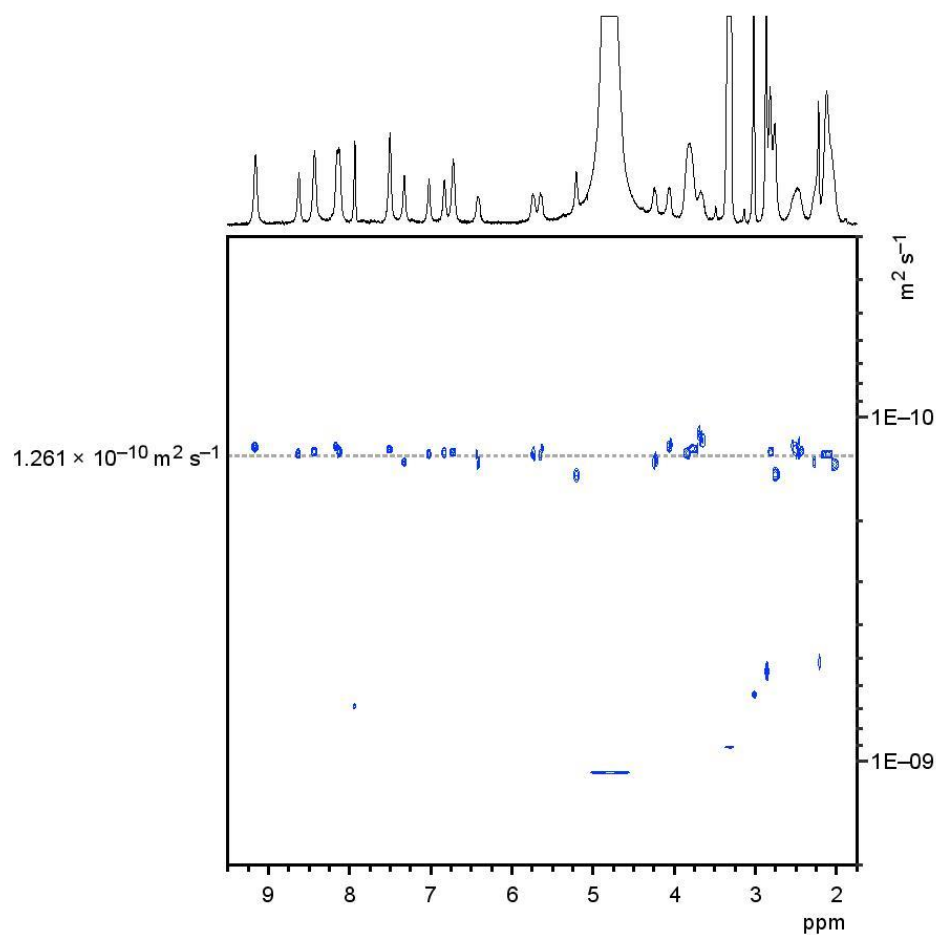


Figure S7: <sup>1</sup>H NMR spectra of the NMR titration of **Pd<sub>2</sub>L<sub>2</sub>** (1.0 mM) in CD<sub>3</sub>OD/D<sub>2</sub>O, 1:1 (v/v) with increasing amounts of 2,6-naphthalenedisulfonate ((a) 0 equiv, (b) 0.5 equiv (c) 1.0 equiv (d) 1.5 equiv (e) 2.0 equiv (f) 2.5 equiv (g) 3.0 equiv (h) 4.0 equiv (i) 5.0 equiv) (22 °C). The spectrum of 2,6-naphthalenedisulfonate is shown in (j). The signals of disappearing **Pd<sub>2</sub>L<sub>2</sub>** and those of appearing free 2,6-naphthalenedisulfonate are marked with red and blue boxes, respectively.

DOSY NMR: **Pd<sub>2</sub>L<sub>2</sub>** + 2.0 equiv of 2,6-naphthalenedisulfonate (400 MHz, CD<sub>3</sub>OD/D<sub>2</sub>O, 1:1 (v/v), 25 °C).



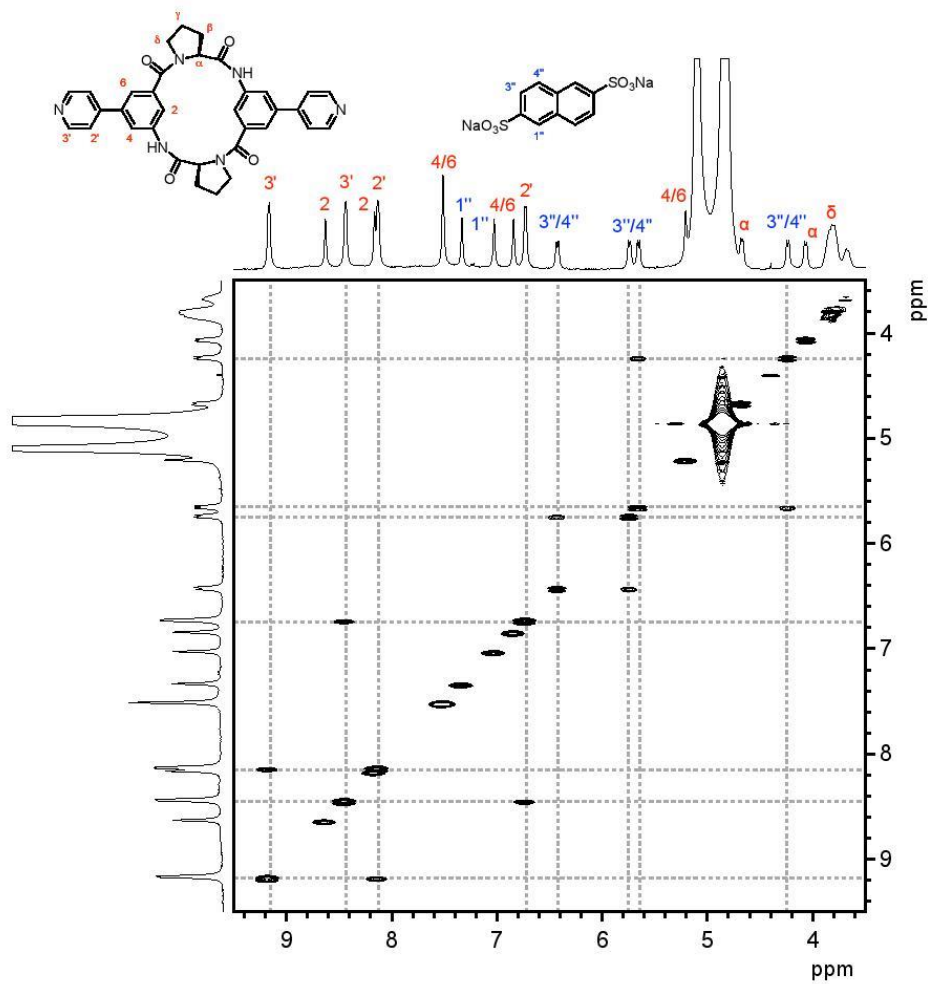
Diffusion coefficient *D* derived from this experiment:

$$D = (1.261 \pm 0.061) \times 10^{-10} \text{ m}^2 \text{ s}^{-1}$$

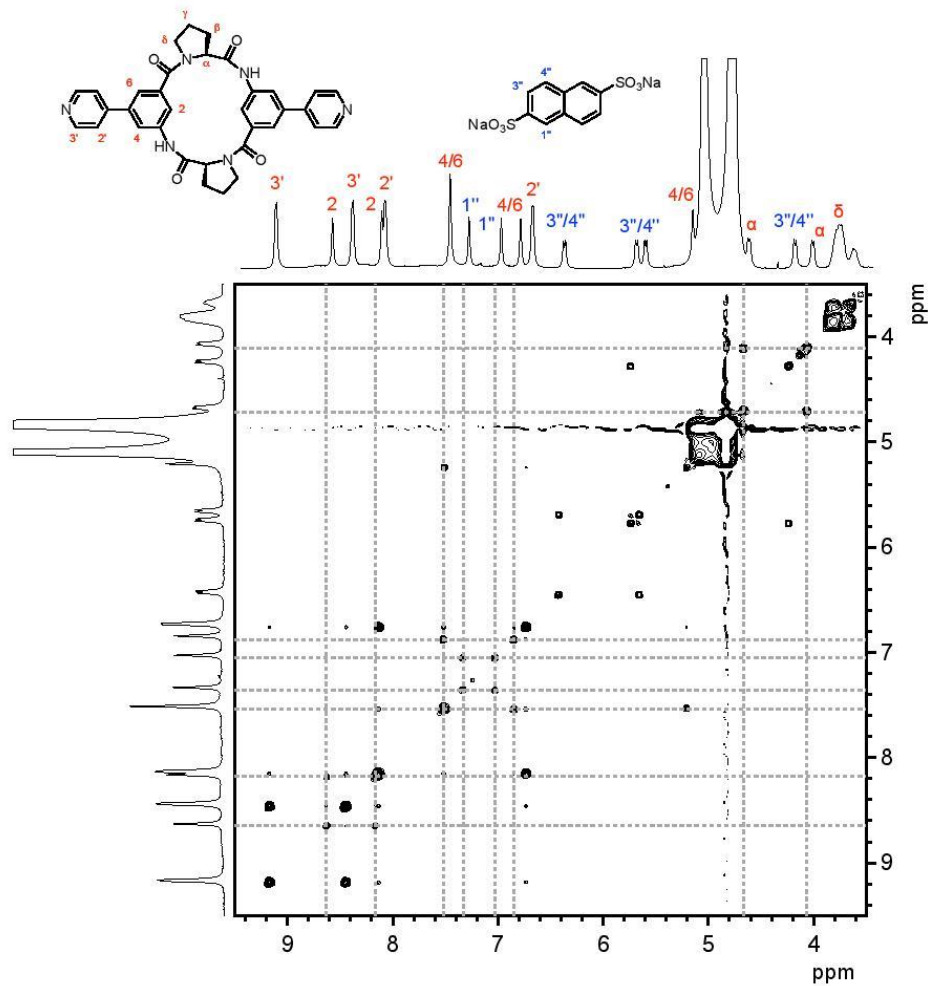
Calculated hydrodynamic diameter *d<sub>H</sub>* derived from the Stokes-Einstein equation:

$$d_H = 20.0 \pm 0.9 \text{ \AA}$$

COSY NMR: **Pd<sub>2</sub>L<sub>2</sub>** + 2.0 equiv of 2,6-naphthalenedisulfonate (400 MHz, CD<sub>3</sub>OD/D<sub>2</sub>O, 1:1 (v/v), 22 °C).

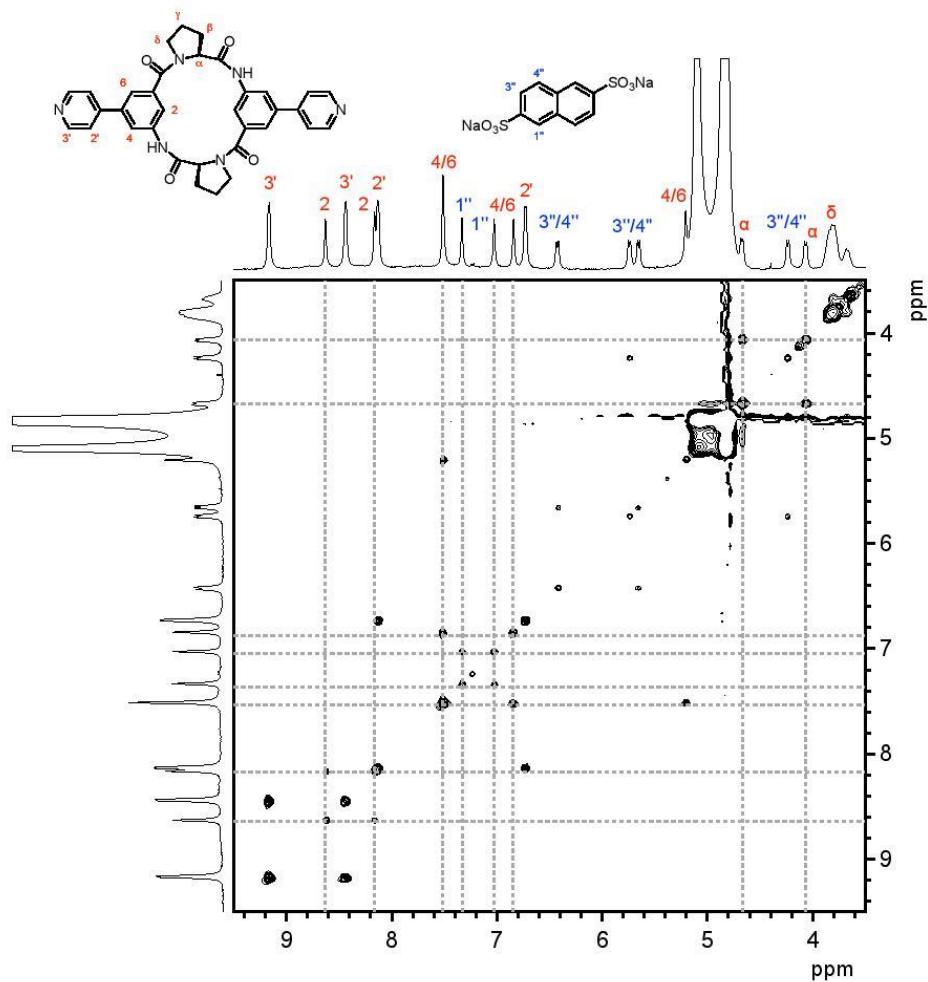


NOESY NMR: **Pd<sub>2</sub>L<sub>2</sub>** + 2.0 equiv of 2,6-naphthalenedisulfonate (400 MHz, CD<sub>3</sub>OD/D<sub>2</sub>O, 1:1 (v/v), 22 °C, mixing time: 200 ms).



(all diagonal peaks and crosspeaks have the same sign)

ROESY NMR: **Pd<sub>2</sub>L<sub>2</sub>** + 2.0 equiv of 2,6-naphthalenedisulfonate (400 MHz, CD<sub>3</sub>OD/D<sub>2</sub>O, 1:1 (v/v), 22 °C, mixing time: 300 ms).



(all diagonal peaks and crosspeaks have the same sign)

## X-Ray Data Collection and Refinement

**General Information.** Single crystal X-ray diffraction studies were performed using a suitable crystal of **L** and **Pd<sub>2</sub>L<sub>2</sub>·2 NDS**. The single crystal was mounted on a MiTeGen Dual Thickness MicroMount™ with Fomblin Y oil and transferred to a N<sub>2</sub> cold stream (100 K) by an OXFORD CRYOSYSTEMS 700 low temperature system. Data were collected at low temperatures (100 K) using  $\phi$ - and  $\omega$ -scans on a BRUKER D8 Venture system equipped with dual I $\mu$ S microfocus sources and a PHOTON100 detector. Cu-K $\alpha$  radiation with wavelength 1.54178 Å and a collimating Quazar multilayer mirror were used. Semi-empirical absorption corrections from equivalents were calculated with SADABS-2016/2.<sup>8</sup> The space groups were determined using *XPREP*<sup>9</sup> through analysis of the Laue symmetry and systematic absences. The structures were solved with *SHELXT*.<sup>10</sup> The structures were refined by full-matrix least-squares based on  $F^2$  using *SHELXL* (Re. 859)<sup>11</sup> and *SHELXL*<sup>12</sup> as a graphical interface. Both structures were checked for a higher symmetry using *PLATON*.<sup>13</sup> All non-hydrogen atoms were located and refined anisotropically. Hydrogen atoms were assigned to idealized positions and given thermal parameters equal to either 1.5 (methyl hydrogen atoms and water hydrogen atoms) or 1.2 (non-methyl hydrogen atoms and nitrogen hydrogen atoms) times the thermal displacement parameters of the atoms to which they were attached. The positions of all NH- and OH-hydrogen atoms were taken from the Fourier synthesis. The bond distances were restrained to idealized distances. Advanced Hirshfeld restraints were applied to all atoms in the structures. Similarity restraints on 1,2 distances were used to model disorder components.  $U_{ij}$  components of disordered atoms were restrained with similar ADP restraints. Restraints for atoms that lie on a common plane were used to model aromatic motifs of **Pd<sub>2</sub>L<sub>2</sub>·2 NDS**.

The cif files have been deposited with the Cambridge Structural Database (CSD).<sup>14</sup> All determined parameters such as bond distances,  $U_{ij}$  components, etc. can be retrieved free of charge from the CSD. General refinement and structure details for both structures are given below.

Table S1. Crystal data and structure refinement for **L** and **Pd<sub>2</sub>L<sub>2</sub>·2 NDS**.

	<b>L</b>	<b>Pd<sub>2</sub>L<sub>2</sub>·2 NDS</b>
CSD entry	1922091	1922090
Empirical formula	C <sub>36</sub> H <sub>37</sub> N <sub>7</sub> O <sub>6</sub>	C <sub>92</sub> H <sub>88</sub> N <sub>16</sub> O <sub>20</sub> Pd <sub>2</sub> S <sub>4</sub>
Formula weight	663.72	2078.82
Temperature	100(2) K	100(2) K
Wavelength	1.54178 Å	1.54178 Å
Crystal system	Tetragonal	Monoclinic
Space group	<i>P</i> 4 <sub>3</sub> 2 <sub>1</sub> 2	<i>P</i> 2 <sub>1</sub>
Unit cell dimensions	a = 11.8117(2) Å c = 24.6045(4) Å	a = 20.4212(9) Å b = 21.4513(9) Å β = 95.124(2)° c = 29.2163(11) Å
Volume	3432.73(13) Å <sup>3</sup>	12747.4(9) Å <sup>3</sup>
Z	4	4
Density (calculated)	1.284 Mg/m <sup>3</sup>	1.083 Mg/m <sup>3</sup>
Absorption coefficient	0.734 mm <sup>-1</sup>	3.372 mm <sup>-1</sup>
<i>F</i> (000)	1400	4272
Crystal size	0.148 × 0.104 × 0.045 mm <sup>3</sup>	0.166 × 0.140 × 0.047 mm <sup>3</sup>
Theta range for data collection	4.152 to 69.995°	2.559 to 80.033°
Index ranges	-14 ≤ h ≤ 13 -14 ≤ k ≤ 14 -29 ≤ l ≤ 29	-25 ≤ h ≤ 26 -27 ≤ k ≤ 27 -37 ≤ l ≤ 37
Reflections collected	36,685	524,580
Independent reflections	3261 [R(int) = 0.0462]	54808 [R(int) = 0.0740]
Completeness to theta = 67.679°	100.0%	100.0%
Absorption correction	Semi-empirical from equivalents	Semi-empirical from equivalents
Refinement method	Full-matrix least-squares on <i>F</i> <sup>2</sup>	Full-matrix least-squares on <i>F</i> <sup>2</sup>
Data / restraints / parameters	3261 / 1190 / 453	54808 / 19217 / 4389
Goodness-of-fit on <i>F</i> <sup>2</sup>	1.043	1.044
Final R indices [I > 2σ(I)]	R1 = 0.0260, wR2 = 0.0664	R1 = 0.0482, wR2 = 0.1264
R indices (all data)	R1 = 0.0285, wR2 = 0.0680	R1 = 0.0518, wR2 = 0.1293
Absolute structure parameter	0.10(7)	0.107(4)
Largest diff. peak and hole	0.143 and -0.114 e.Å <sup>-3</sup>	0.974 and -0.385 e.Å <sup>-3</sup>

### Crystal Structure of **L**

**L** crystallized in the tetragonal space group  $P4_32_12$  with half a molecule **L**, half a free  $\text{CH}_3\text{CN}$  solvent molecule, and one free  $\text{H}_2\text{O}$  solvent molecule in the asymmetric unit. **L** displayed a dynamic whole molecule disorder that was modelled across two positions. The main occupied species refined to 69.6%. The disorder is not resolved well. Four pairs of almost overlapping atoms, namely C6/C6A, C1/C1A, C21/C21A, and C22/C22A, had to be pair wise restrained to show identical thermal displacement parameters. The free  $\text{CH}_3\text{CN}$  solvent molecule was found to be disordered. The disorder was modelled across two positions with the main component refining to 93.0%. Both disorder components lie on a crystallographic two-fold rotation axis, thus, generating an additional symmetry related disorder. The symmetry generated disorder components were suppressed in the refinement model using the PART -1 and PART -2 commands in SHELX. Additional distance restraints were applied to model the linear shape of the solvent molecules.

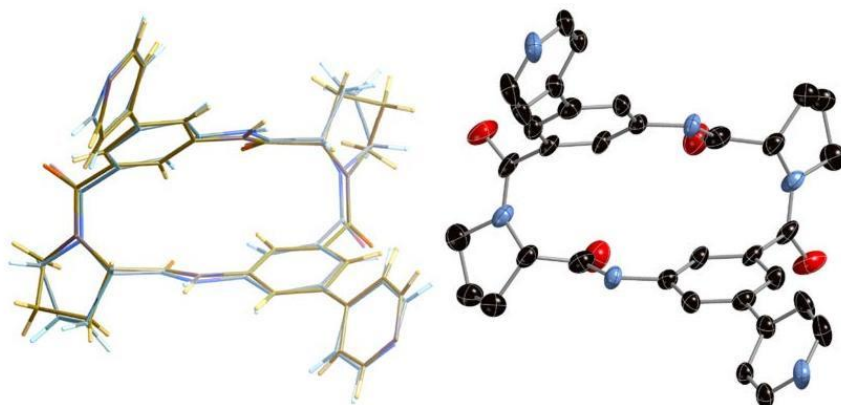


Figure S8: Stick model representation of the disorder components of **L**. The main and minor occupied species are highlighted in blue and yellow, respectively (left). Molecular structure of the main occupied disorder component of  $\text{L}\cdot 2\text{H}_2\text{O}\cdot \text{CH}_3\text{CN}$ . Solvent molecules and hydrogen atoms are omitted for clarity. Thermal ellipsoids are set at 50% probability.



### Crystal Structure of the 2,6-Naphthalenedisulfonate Complex of $\text{Pd}_2\text{L}_2 \cdot 2$ NDS

$\text{Pd}_2\text{L}_2 \cdot 2$  NDS crystallized in the monoclinic space group  $P2_1/c$  with two  $\text{Pd}_2\text{L}_2$  complexes each hosting two 2,6-naphthalenedisulfonate molecules, and several free solvent molecules ( $\text{CH}_3\text{CN}$  and water) in the asymmetric unit. The two  $\text{Pd}_2\text{L}_2 \cdot 2$  NDS complexes are connected via hydrogen bonds between the ethylene diamine hydrogen atoms and the carbonyl oxygen atoms of the peptide bond of **L**. Each  $\text{Pd}_2\text{L}_2$  complex as well as three of the four 2,6-naphthalenedisulfonate molecules displayed a dynamic whole molecule disorder. To facilitate the structure refinement, each  $\text{Pd}_2\text{L}_2$  complex was assigned to an individual residue that is described separately below (Figure S9).

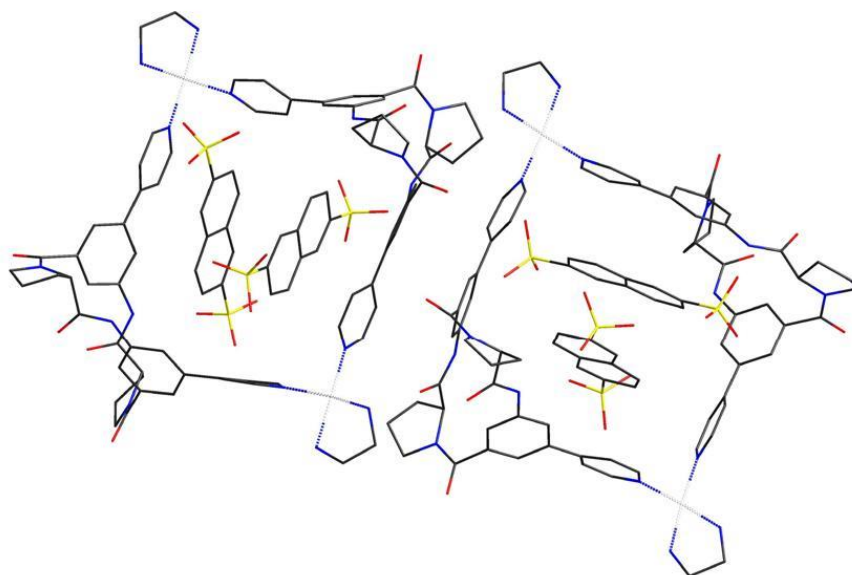


Figure S9: Stick model representation of the asymmetric unit of  $\text{Pd}_2\text{L}_2 \cdot 2$  NDS. Only the main occupied disorder components are shown. Hydrogen atoms are omitted for clarity. The left complex was named residue 1, the right complex residue 2.

Residue 1: The whole molecule disorder of  $\text{Pd}_2\text{L}_2$  was modelled across two positions. The main occupied species refined to an occupancy of 53.4%. Even though both disorder components refine to a stable fashion, there are some pairs of almost overlapping atoms that were restrained to show identical thermal displacement parameters: C43, C44, C44A, C61A, C53, C53A, C54, C54A, C55,

C55A, C56, C56A, C57, C57A, C58, C58A, C59, C59A C61A, C63, C63A, as well as N6, N10, N10A, N11, and N11A. The complex hosts two 2,6-naphthalenedisulfonate molecules, both of which display a dynamic whole molecule disorder. The disorder was modelled across two positions for each guest molecule. The main occupied disorder components refined to 73.9% and 71.4%, respectively. All disordered guest molecules are allowed to form hydrogen bonds with both of the disorder components of the surrounding host complex (Figure S10).

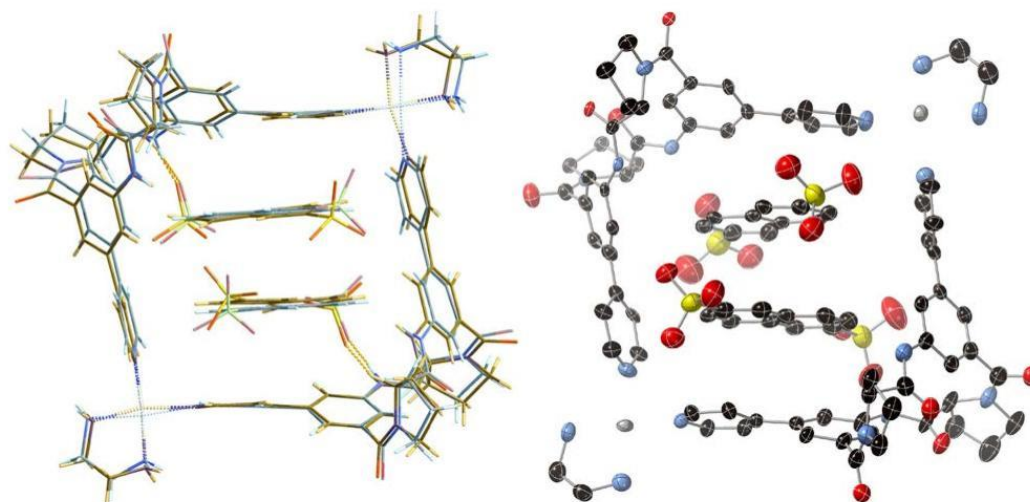


Figure S10: Stick model representation of the disorder components of **Pd<sub>2</sub>L<sub>2</sub>·2 NDS** (residue 1). The main and minor occupied species are highlighted in blue and yellow, respectively. Hydrogen bonds are indicated with dotted yellow lines (left). Molecular structure of **Pd<sub>2</sub>L<sub>2</sub>·2 NDS** (right). Hydrogen atoms are omitted for clarity. Thermal ellipsoids are set at 50% probability.

Residue 2: **Pd<sub>2</sub>L<sub>2</sub>** displayed a dynamic nearly complete whole molecule disorder. Only half a molecule **L** was found not to be disordered. The disorder was modelled across two positions. The main occupied species refined to an occupancy of 80.0%. **Pd<sub>2</sub>L<sub>2</sub>** hosts two 2,6-naphthalenedisulfonate molecules, one of which is disordered. The guest molecule disorder was modelled across two positions. The main occupied species refined to an occupancy of 54.4%. One of the sulfonate groups of the minor disordered species was found to further split into disorder components. The resulting disorder within a disorder was modelled across two positions, resulting in an overall threefold disorder of this 2,6-naphthalenedisulfonate molecule. The occupancies of these three

disorder components were restrained to unity with a standard deviation of zero.

Several free and only poorly defined acetonitrile and water solvent molecules were found in the crystal lattice. SQUEEZE as implemented in *PLATON*<sup>13</sup> was used to handle this extensive solvent disorder. SQUEEZE found three solvent accessible voids located at  $-0.152\ 0.320\ 0.185$ ,  $0.491\ 0.047\ 0.870$ , and  $0.509\ 0.547\ 0.130$ . The corresponding volume and number of electrons contained are  $5050\ \text{\AA}^3$  (1405 electrons),  $41\ \text{\AA}^3$  (16 electrons), and  $42\ \text{\AA}^3$  (17 electrons), respectively. In total, 1438 electrons have been found in the solvent accessible voids, corresponding to a maximum number of 66 acetonitrile molecules per cell.

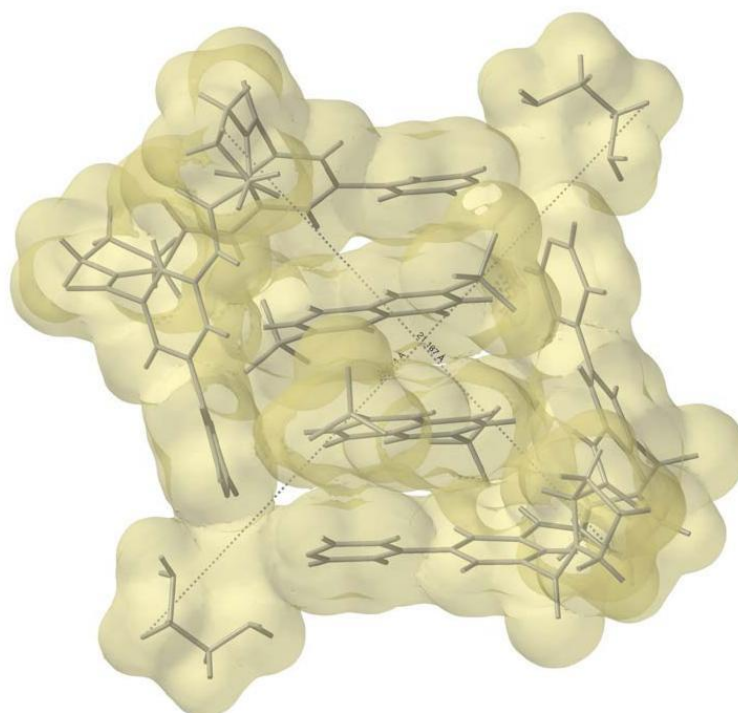


Figure S11: Estimated molecular dimensions of **Pd<sub>2</sub>L<sub>2</sub>·2 NDS** from the crystal structure. From the marked distances of hydrogen atoms, an average diameter of 24.1 Å can be estimated when considering the van-der-Waals radii of hydrogen atoms (1.1 Å).

## References

- 1 Gottlieb, H. E.; Kotlyar, V.; Nudelman, A. NMR chemical shifts of common laboratory solvents as trace impurities. *J. Org. Chem.* **1997**, *62*, 7512–7515.
- 2 Nilsson, M. The DOSY toolbox: a new tool for processing PFG NMR diffusion data. *J. Magn. Reson.* **2009**, *200*, 296–302.
- 3 Evans, R.; Deng, Z.; Rogerson, A. K.; McLachlan, A. S.; Richards, J. J.; Nilsson, M.; Morris, G. A. Quantitative interpretation of diffusion-ordered NMR spectra: can we rationalize small molecule diffusion coefficients? *Angew. Chem. Int. Ed.* **2013**, *52*, 3199–3202.
- 4 Thompson, J. W.; Kaiser, T. J.; Jorgenson, J. W. Viscosity measurements of methanol-water and acetonitrile-water mixtures at pressures up to 3500 bar using a novel capillary time-of-flight viscometer. *J. Chromatogr. A* **2006**, *1134*, 201–209.
- 5 Macchioni, A.; Ciancaleoni, G.; Zuccaccia, C.; Zuccaccia, D. Determining accurate molecular sizes in solution through NMR diffusion spectroscopy. *Chem. Soc. Rev.* **2008**, *37*, 479–489.
- 6 Ganß, A.; Xu, C.; Guenet, A.; Kelm, H.; Kyritsakas, N.; Planeix, J.-M.; Kubik, S.; Hosseini, M. W. Molecular tectonics: homochiral coordination polymers based on pyridyl-substituted cyclic tetrapeptides *CrystEngComm* **2016**, *18*, 7685–7689.
- 8 Zhu, L.; Lu, M.; Qu, D.; Wang, Q.; Tian, H. Coordination-assembly for quantitative construction of bis-branched molecular shuttles. *Org. Biomol. Chem.* **2011**, *9*, 4226–4233.
- 9 Krause, L.; Herbst-Irmer, R.; Sheldrick, G. M.; Stalke, D. Comparison of silver and molybdenum microfocus X-ray sources for single-crystal structure determination. *J. Appl. Cryst.* **2015**, *48*, 3–10.
- 9 Bruker. APEX2, version 4.0, and XPREP, 2nd edition, 2008. Bruker AXS, Inc., Madison, WI, USA.
- 10 Sheldrick, G. M. *SHELXT* - Integrated space-group and crystal-structure determination. *Acta Cryst.* **2015**, *A71*, 3–8.
- 11 Sheldrick, G. M. Crystal structure refinement with *SHELXL*. *Acta Cryst.* **2015**, *C71*, 3–8.
- 12 Hübschle, C. B.; Sheldrick, G. M.; Dittrich, B. *ShelXle*: a Qt graphical user interface for *SHELXL*. *J. Appl. Cryst.* **2011**, *44*, 1281–1284.

- 13 Spek, A. L. PLATON: A Multipurpose Crystallographic Tool. University of Utrecht: The Netherlands, 2008.
- 14 Allen, F. H. The Cambridge Structural Database: a quarter of a million crystal structures and rising. *Acta Cryst.* **2002**, *B58*, 380–388.



# CURRICULUM VITAE

Lígia Margarida Marques Mesquita

## AREAS OF WORK

---

Nanoparticle Chemistry, Peptide Synthesis, Organic Synthesis, Supramolecular Chemistry, Coordination Chemistry, Analytical Chemistry, Host Guest Chemistry, Pharmaceutical Chemistry, Pharmacokinetics, Cell biology, Heterogeneous Catalysis.

## SCIENTIFIC PATH

---

<b>Oct 2020 – Present</b>	<b>Research Scientist</b>
<i>Topas Therapeutics</i>	<u>Field of work</u> : Development of nanoparticles that generate tolerance against bloodborne antigens to address autoimmune diseases, allergies and anti-drug antibodies.
<b>Oct 2015 – Apr 2019</b>	<b>PhD in Chemistry</b>
<i>TU Kaiserslautern</i>	<u>Main Project</u> : Metal Directed Self-Assembly of Cyclopeptide-Containing Macrocycles and Cages
<i>ISIS Strasbourg</i>	Secondment Project: Synthesis and Characterization of Luminescent Neutral Pt(II) Complexes Tethered to Cyclopeptides
<i>Micronit</i>	Industrial Secondment Project: Luminescent Pt(II) Porphyrin Complexes as Oxygen Sensors for Microfluidic Devices
<b>Aug 2013 – Sep 2015</b>	<b>Research Assistant</b>
<i>ITQB-UNL</i>	<u>Field of work</u> : Development of dinuclear Cu(II) and Zn(II) complexes as potential inhibitors of oncogenic protein-protein interactions
<b>Oct 2010 – Feb 2013</b>	<b>MSc in Industrial Pharmaceutical Chemistry</b>
<i>University of Coimbra (FFUC)</i>	<u>Thesis project</u> : New Sustainable Processes Catalysed by Acids with Interest in Pharmaceutical Industry
<b>Sep 2007 – Jul 2010</b>	<b>BSc in Biochemistry</b>
<i>University of Coimbra (FCTUC)</i>	<u>Thesis project</u> : Effect of Silibinin in the cellular death of Acute Lymphoblastic Leukaemia's cells

